Sensorless Control of Motoring/Generating System for Future More-Electric Turboprop Aircraft

Linhui Fan (BEng, MSc)

Thesis submitted to the University of Nottingham

for the degree of Doctor of Philosophy

May 2021

Acknowledgement

Firstly, I would like to express my deepest gratitude to my supervisors, Prof. Serhiy Bozhko and Dr. Tao Yang, for their invaluable advice and expert guidance throughout the course of this research. I would also like to thank Dr. Thomas Cox for acting as my internal examiner and Prof. Alberto Cavallo, from the University of Campania Luigi Vanvitelli, for acting as my external examiner.

Many thanks for a lot of help and support from the knowledgeable research fellows and PhD students in the PEMC group, especially to Dr. Yuzheng Chen. Special mentions to Dr. Seang Yeoh, Dr. Ganeish Velmurugan, Dr. Mi Tang, Dr. Sharmila Sumsurooah ， Dr. Hossein Balaghi Enalou, Dr. Ponggorn Kulsangcharoen, Dr. Muhammad Khowja, Dr. Shajjad Chowdhury, Prof. Hanbing Dan, Dr. Qi Wang, Dr. Fei Gao, Dr. Xiaoyu Lang, Dr. Cheng Wang, Dr. Chen Li, Dr. Xiaochen Zhang, Dr. Xiang Zhang, Dr. Zhen Huang, Dr. Feng Guo, Dr. Yuan Gao, Dr. Xin Wang and all other friends I have met here during my PhD study. My PhD experience has been enhanced by getting to work and know them.

My sincere thanks also go to Dr. Fang Xu, Dr. Subhashisa Swain, Dr. Tianhui Liu, Dr. Dan Zhao, Dr. Weiyao Meng and all other friends I have met here during this journey. You have made my life more pleasant, joyful in the UK. I do appreciate the help and friendship from you and I will cherish our friendship lifelong.

At last but not least, I would like to express my heartfelt appreciation to my parents Mr. Yifan Fan and Mrs. Jianhua Liu for their understanding and support throughout my life.

Also, I would like to thank my husband Dr. Bo Song and puppy Lucky for their love and accompany on the way.

Abstract

Multiphase electrical machines have gained increased attentions recently due to its fault tolerance capability which is of great importance for more-electric aircraft (MEA) application. The object of this research is a dual three-phase permanent magnet synchronous machine (PMSM) motoring/generating system for future more-electric turboprop aircraft. Sensorless control is required because the designed system is fit in a harsh environment with severe volume restrictions for installing mechanical speed/position sensors required for standard control approaches. Another challenge is due to the asymmetric winding structure of the employed machine; hence the well-established machine mathematical models could not be directly transformed from stationary coordinates to *dq* rotating frame complication the field oriented control (FOC) of the machine. To address this issue, an XYZ modelling approach is proposed which not only simplifies the mathematic model but also makes the FOC achievable. Different sensorless strategies are reviewed and compared among which Model Reference Adaptive System (MRAS) is selected as it is robust and simple in implement. The major drawback of this method is the sensitivity to machine parameter variation. To solve this problem, an enhanced MRAS is proposed to identify machine parameter drift. Based on observability analysis, it proves that no more than one parameter could be identified simultaneously for a MRAS based rotor speed sensorless system. After comparison between rotor resistance, rotor inductance and permanent magnet (PM) flux, the last parameter is selected to be the identification subject, and a PM flux estimation based MRAS sensorless system is designed for mid- and high-speed operation. Since MRAS fails at low speed range, an I/F start-up strategy is applied, and

a hybrid sensorless control method is proposed for full-speed range operation. A switching operation is designed for smooth transition between these two methods. Experimental results show good performance of the proposed hybrid approach and verified the key theoretical findings of this research.

Table of Contents

Chapter 1 Introduction 1

1.1 Moving towards More Electric Aircraft 2

1.2 Motoring/Generating System for Future Turboprop More Electric Aircraft 6

1.3 Aims and Objectives 9

1.3.1 Aims 9

1.3.2 Objectives 9

1.4 Structure of Thesis 10

Chapter 2 Sensorless Control of Multi-Three-Phase Machine based Starter/Generator System for More Electric Aircraft 12

2.1 Electric Power System in the More Electric Aircraft 12

2.1.1 Power Generation 12

2.1.2 Power Distribution 20

2.1.3 Power Consumption 23

2.1.4 Starter/Generator System 25

2.2 Review of Multi-Three-Phase Machine Research 29

2.3 Review of Sensorless Control Study 34

2.3.1 Overview of Sensorless Study for Three-Phase PMSM 36

2.3.2 Overview of Sensorless Study for Dual Three-Phase PMSM 38

2.4 ACHIEVE Project 41

2.4.1 Electric Machine 42

2.4.2 Power Converter 44

2.4.3 Thermal Management System 45

2.5 Chapter Summary 46

Chapter 3 Control Strategy of Dual Three-Phase Machine in ACHIEVE with Encoder 47

3.1 Mathematic Model for DTP-PMSM in ACHIEVE 47

3.1.1 Winding structure of ACHIEVE machine 47

3.1.2 Mathematic model in Six-Phase Stator Reference Frame for ACHIEVE Machine 51

3.1.3 Mathematic Model in XYZ Reference Frame for ACHIEVE Machine 52

3.2 Motoring/Generating Control Scheme for DTP-PMSM in ACHIEVE 57

3.2.1 Direct Torque Control 59

3.2.2 Field Oriented Control 60

3.2.3 DC Link voltage Control 63

3.3 PWM Strategy for DTP-PMSM in ACHIEVE 65

3.4 Simulation Results..... 67

3.5 Chapter Summary..... 73

Chapter 4 The State-of-the-Art of Sensorless Control Strategies for PMSM 75

4.1 Sensorless Control Schemes for Medium- and High-Speed Range 77

4.1.1 Direct Calculation Method Based on the Mathematical Equations of Machine 78

4.1.2 Model Reference Adaptive System 86

4.1.3 Observer Method 88

4.2 Sensorless Control Schemes for Zero and Low-Speed Range 91

4.2.1 High-Frequency Signal Injection Method 93

4.2.2 Pulsating Sinusoidal High-Frequency Signal Injection Method..... 97

4.3 Sensorless Control Schemes for Full-Speed Range 104

4.3.1 Closed-Loop Hybrid Sensorless Control Strategy 106

4.3.2 Open-Loop Start-Up Based Hybrid Sensorless Control Strategy.....106

4.4 Chapter Summary.....108

Chapter 5 Model Reference Adaptive System Based Sensorless Control Strategy at Middle- and High-Speed.....111

5.1 Conventional Model Reference Adaptive System Method.....111

5.1.1 The Principle of MRAS.....113

5.1.2 Estimation of PMSM Speed Based on MRAS.....116

5.1.3 Limitation of Conventional MRAS.....121

5.2 Parameter Sensitivity Analysis of Conventional MRAS Based Sensorless Control Method.....122

5.2.1 Current-sensitive Parameters.....122

5.2.2 Temperature-sensitive Parameters.....123

5.3 Model Observability Analysis of Permanent Magnet Synchronous Motor 126

5.3.1 Observability of MRAS Based PMSM Sensorless System with Parameters Identification.....127

5.4 Enhanced MRAS Based Sensorless Control Method Considering Parameter Variation.....129

5.4.1 Principle of Proposed Method 130

5.4.2 Simulation Results 134

5.5 Chapter Summary 143

Chapter 6 Full-Speed Range Rotor Position Estimation Strategy 145

6.1 I/F Open Loop Control as Start-Up Strategy 146

6.1.1 Initial Position Identification of Rotor 149

6.1.2 Acceleration Process of Rotor 150

6.1.3 Analysis of State Switching Operation 151

6.2 Simulation Results of Start-Up Strategy 153

6.3 Chapter Summary 160

Chapter 7 Experimental Validation 162

7.1 Hardware Design and Construction 165

7.1.1 TMS320F28379S DSP 165

7.1.2 Signal Detection Circuit 166

7.1.3 Design of the Power Drive Module 168

7.1.4 Design of Human-Computer Interaction System 170

7.2 Software Design and Construction 171

7.2.1 Design of the Main Program 171

7.2.2 The Design of Interrupt Service Routines 173

7.2.3 Experimental Rig 177

7.3 Experimental Results for Sensorless Position Control System 179

7.3.1 Comparative Study of Conventional and Enhanced MRAS 180

7.3.2 Hybrid Speed Control for Full Speed Range 184

7.4 Chapter Summary 187

Chapter 8 Conclusions and Future work 189

8.1 Conclusions 189

8.2 Future Work 190

8.3 Publications 191

Appendix A Phasor Diagram Transformation 193

Appendix B Simulation Models 194

Reference 197

List of Figures

Figure 1.1. Power sources distribution in conventional aircraft [5]. 3

Figure 1.2. Power sources distribution of MEA [5].....4

Figure 1.3 Comparison of conventional and more electric aircraft [7].....5

Figure 1.4. Electrical power levels generated for various civil aircraft [11, 12]. 6

Figure 1.5. Application background [19].....8

Figure 2.1 Evolution of electrical power need[9]. 13

Figure 2.2 Evolution of Electric generation system [24].....13

Figure 2.3 A constant frequency generation system using a mechanical gearbox[32]. 15

Figure 2.4 VSCF system using DC-link [4].....17

Figure 2.5 VSCF system using AC/AC converter [4]. 17

Figure 2.6 A variable frequency generation system (with AC distribution) [4].....18

Figure 2.7 A variable frequency generation system (with DC distribution) [4].....18

Figure 2.8 Power distribution system in conventional aircraft[35]. 22

Figure 2.9 Power distribution system in a modern aircraft B787[41]. 22

Figure 2.10 Onboard motor applications and their functions[36].....24

Figure 2.11 Electric S/G system in the MEA. (a) interface to a DC distribution system. (b) VSCF AC distribution[43]. 26

Figure 2.12 Torque-speed profile of the aircraft S/G[43]. 27

Figure 2.13 Considered choices for electrical machines in MEA architectures with an AC/DC interface. (a) WFSM. (b) Squirrel-cage IM. (c) PMM.(d) SRM[46]. 28

Figure 2.14 Working principle diagram of photoelectric incremental encoder. 34

Figure 2.15 The principle of absolute encoder. 35

Figure 2.16 Block diagram of general model-based sensorless drive system. 36

Figure 2.17 General block diagram of position/speed estimation procedure for model-based sensorless control. 37

Figure 2.18 Categories for saliency-based position sensorless control. 38

Figure 2.19 DTP-PMSM in ACHIEVE project. 43

Figure 2.20 The SiC based two-level VSC converter in ACHIEVE project. 45

Figure 3.1 Structure of Dual Three Phase Machine. 48

Figure 3.2 Block diagram of two-segment PMSM drive. 50

Figure 3.3 Angle between the two three-phase windings: (a)conventional dual three-phase machine with a displacement ($0 < \alpha < \pi 3$); (b)two-segment machine with no displacement ($\alpha = 0$). 51

Figure 3.4 The assumption of equivalent conversion between XYZ model and Dual Three-phase model. 53

Figure 3.5 Derivation of mutual inductance between virtual X and Y phases. 54

Figure 3.6 Reference frames diagram. 56

Figure 3.7 General control scheme of motoring/generating system (a)motoring mode (b)generating mode. 58

Figure 3.8 Block diagram of DTC system for PMSM. 59

Figure 3.9 Block diagram of FOC system for PMSM 60

Figure 3.10 Block diagram of FOC system for ACHIEVE in motoring mode. 61

Figure 3.11 Block diagram of speed control loop. 62

Figure 3.12 Block diagram of current control loop. 62

Figure 3.13 Block diagram of FOC system for ACHIEVE in generating mode. 64

Figure 3.14 Block diagram of DC link voltage control. 65

Figure 3.15 Block diagram of machine drive architecture. 66

Figure 3.16 Carrier wave phase shift with 0.5 Ts. 67

Figure 3.17 PLECS simulation system of ACHIEVE in motoring mode. 68

Figure 3.18 Simulation results in motoring mode under various load. 69

Figure 3.19 Simulation results in motoring mode under various speed. 70

Figure 3.20 PLECS simulation system of ACHIEVE in generating mode. 71

Figure 3.21 Responses of key variables to various electrical loads iL.....72

Figure 3.22 Edc to a step of $iL = 10$ A for comparison with 540 VDC voltage transient limit from MIL-STD-704F. 73

Figure 4.1 Development for position sensorless drives. 75

Figure 4.2 Categories for position sensorless drives. 76

Figure 4.3 Coordinates reference frame of PMSM. 76

Figure 4.4 General block diagram of fundamental model based sensorless drive system. 78

Figure 4.5 Position and speed estimation procedure. 78

Figure 4.6 Definitions of coordinate reference frames for EEMF based sensorless scheme.....84

Figure 4.7 Equivalent block diagram of least-order observer for estimation of Extended back-EMF. 85

Figure 4.8 Block diagram of position and speed estimation algorithm. 86

Figure 4.9 Block diagram of MRAS based sensorless control system of PMSM. 87

Figure 4.10 Block diagram of SMO based sensorless control system of PMSM. 89

Figure 4.11 The operation of Kalman filter 91

Figure 4.12 Categories for zero to low speed range sensorless methods. 92

Figure 4.13 Block diagram of pulsating sinusoidal high-frequency injection signal method. 97

Figure 4.14 Flux characteristic curve of direct axis flux circuit of surface-mounted PMSM. 99

Figure 4.15 Signal processing in the pulsating sinusoidal high-frequency injection signal method. 102

Figure 4.16 Phase Locked Loop based rotor position observer. 103

Figure 4.17 Determination of weighting coefficient in closed-loop hybrid sensorless control strategy. 105

Figure 4.18 Block diagram of V/F control for PMSM. 107

Figure 4.19 Block diagram of I/F control for PMSM. 108

Figure 5.1 Block diagram of closed loop state observer[252]. 111

Figure 5.2 Configuration of the parallel MRAS[234]. 112

Figure 5.3 Basic structure of nonlinear feedback system[264]. 113

Figure 5.4 The equivalent representation of the MRAS. 115

Figure 5.5 The equivalent presentation of the MRAS for speed estimation [234]. ... 119

Figure 5.6 System schematic of MRAS for speed estimation. 121

Figure 5.7 Resistance of stator winding varying against winding temperature for ACHIEVE machine. 124

Figure 5.8 PM flux under various temperature and stator current for ACHIEVE machine. 125

Figure 5.9 Block diagram of proposed cascaded mras system for ACHIEVE system. 133

Figure 5.10 Process of cascaded MRAS. 134

Figure 5.11 Block diagram of MRAS based sensorless control system for ACHIEVE. 135

Figure 5.12 Simulation results of MRAS under speed variation. 137

Figure 5.13 Simulation results of enhanced MRAS under speed variation. 138

Figure 5.14 Simulation results of MRAS under load variation. 140

Figure 5.15 Simulation results of enhanced MRAS under load variation. 141

Figure 5.16 Simulation results including estimated PM flux and rotor postion estimation error. 143

Figure 6.1 Current vector diagram of PMSM in I/F mode. 146

Figure 6.2 Current vector diagram under load variation..... 148

Figure 6.3 Diagram of I/F based start-up process. 149

Figure 6.4 Process of initial position identification of rotor. 150

Figure 6.5 Diagram of vectors during start-up process..... 151

Figure 6.6 Diagram of state switching operation. 152

Figure 6.7 Block diagram of I/F start-up method. 153

Figure 6.8 q*-axis current iq* during start-up process. 154

Figure 6.9 Angle difference Δθ between dq frame and dq* frame during start-up process..... 154

Figure 6.10 Actual rotor speed during start-up process. 155

Figure 6.11 Δθ under different iq* decreasing rate ki. 158

Figure 7.1 Block diagram of dual three-phase PMSM hardware system in ACHIEVE. 164

Figure 7.2 Operating procedure of DSP1. 166

Figure 7.3 Dual three-phase machine and power electronic box in ACHIEVE. 168

Figure 7.4 Encoder installed on the DTP-PMSM in ACHIEVE 168

Figure 7.5 Envelope provided for converter by the aircraft manufacturer.[281].....169

Figure 7.6 Exploded view of voltage sourced converter including cooling system [281].
.....170

Figure 7.7 SiC based 2L three-phase converter system for ACHIEVE project (a)Envelope of the converter highlighting its radial dimensions. (b)Axial view of the converter showing stack height of gate driver and power board[281].....170

Figure 7.8 Flow chart of main program in two DSPs (a) DSP1 (b) DSP2. 173

Figure 7.9 Flow chart of main interrupt in CPU1.....174

Figure 7.10 Coordinate relationship in I/F control. 176

Figure 7.11 Lab prototype of ACHIEVE project. (a) DTP-PMSM and prime mover;(b)power converter. 178

Figure 7.12 Schematic diagram of experimental platform for ACHIEVE project. ...179

Figure 7.13 TorqueMeter system.....179

Figure 7.14 PM flux reference and estimation value by enhanced MRAS. 180

Figure 7.15 Rotor position sensored by encoder and estimated by enhanced MRAS.
.....181

Figure 7.16 Rotor position estimation error between position sensored by encoder and estimated by enhanced MRAS.....181

Figure 7.17 Rotor speed sensored by encoder and estimated by enhanced MRAS...182

Figure 7.18 Rotor speed estimation error between speed sensored by encoder and estimated by enhanced MRAS.....182

Figure 7.19 Rotor position estimation error for conventional and enhanced MRAS at different rotor speed.....183

Figure 7.20 Flow chart of hybrid control method for full speed range.....184

Figure 7.21 Experimental results for I/F start-up process including q-axis current, rotor speed from encoder and angle error between rotor position from encoder and I/F estimation.....185

Figure 7.22 Experimental results for high-speed operation.....187

Figure B.1 Power system for motoring mode.....194

Figure B.2 Power system for generating mode.....194

Figure B.3 Dual Three-Phase PMSM model.....195

Figure B.4 Converter model.....195

Figure B.5 SVPWM model.....195

Figure B.6 Current Loops model.....196

List of Tables

Table 2-1 Power generation type for recent aircrafts[36]. 19

Table 2-2 Potential Motor Drive Applications for Aircrafts[36]. 25

Table 2-3 Summary of the Electrical Machines for S/G system[43]. 28

Table 2-4 Research team of multiphase machine around the world [62]. 33

Table 2-5 Fault classification and cause analysis of position sensor. 35

Table 2-6 Parameters of the DTP-PMSM in ACHIEVE project. 44

Table 3-1. Machine inductance matrix. 49

Table 3-2 Machine inductance matrix of XYZ model. 55

Table 4-1 Comparison of three common high-frequency signal injection methods [110, 224]. 96

Table 5-1 Lookup table between stator current and dq-axis inductance for ACHIEVE machine. 123

Table 7-1 Experimental parameters of dual three-phase PMSM for ACHIEVE..... 164

List of Acronyms

AC	Alternative Current
ACHIEVE	Advanced meCHatronIcs dEVices for a novel turboprop Electric starter-generator and health monitoring system
ADC	Analogue to Digital Conversion
AEA	All-Electric Aircraft
AEGART	Aircraft Electrical Generation Active Rectifier Technology
AI	Artificial Intelligence
APU	Auxillary Power Unit
ATRU	Automatic Transformer Rectifier Unit
BPF	Band-Pass Filter
CF	Constant Frequency
CFD	Computational Fluid Dynamics
CLA	Control Law Accelerator
CPL	Constant Power Load
CSD	Constant Speed Drive
DAC	Digital to Analogue Conversion
DC	Directive Current
DFIG	Doubly-fed Induction Generator
DG	Distributed Generation
DSP	Digital Signal Processor
DTC	Direct Torque Control

DTP	Dual Three-phase
DTP-PMSM	Dual Three-Phase Permanent Magnet Synchronous Machine
ECS	Environmental Control System
EEMF	Extended back-EMF
EHA	Electro-hydrostatic Actuators
EKF	Extended Kalman Filter
EM	Electrical Machine
EMF	Electromotive Force
EMI	Electromagnetic Interference
EPS	Electrical Power System
ESS	Energy Storage System
EU	European Union
FEM	Finite Element Model
FOC	Field Oriented Control
FPE	Fundamental PWM Excitation
FPGA	Field Programmable Gate Array
FW	Flux Weakening
GaN	Gallium Nitride
HF	High Frequency
HFCI	High-Frequency Current Injection
HFSI	High-Frequency Signal Injection
HFVI	High-Frequency Voltage Injection
HP	High Pressure
I/O	Input/Output

IGBT	Insulated Gate Bipolar Transistor
IM	Induction Machine
INFORM	INdirect Flux detection by On-line Reactance Measurement
IP	Index of Performance
IPM	Interior Permanent Magnet
IPMSM	Interior Permanent Magnet Machines
ISR	Interrupt Service Routine
LP	Low Pressure
LPF	Low-Pass Filter
LUT	Look-Up Table
MEA	More-Electric Aircraft
MOSFET	Metal Oxide Semiconductor Field Effect Transistor
MRAS	Model Reference Adaptive System
PC	Personal Computer
PCB	Printed Circuit Board
PI	Proportional plus Integral
PID	Proportional plus Integral plus Derivative
PLL	Phase-Locked Loops
PM	Permanent Magnet
PMM	Permanent Magnet Machine
PMSM	Permanent Magnet Synchronous Machine
POA	Power Optimised Aircraft
PST	Power System Technology
PWM	Pulse Width Modulation

QEP	Quadrature Encoder Pulse
RAT	Ram Air Turbine
RAT	Ram Air Turbine
S/G	Starter/Generator
SiC	Silicon Carbide
SM	Synchronous Machine
SMO	Sliding Mode Observer
SNR	Signal to Noise Ratio
SPI	Serial Peripheral Interface
SPMSM	Surface-Mounted Permanent Magnet Synchronous Machine
SVM	Space Vector Modulation
SVPWM	Space Vector Pulse Width Modulation
THD	Total Harmonic Distortion
TI	Texas Instruments
TRU	Transformer Rectifier Unit
VF	Variable Frequency
VSC	Voltage Source Converter
VSCF	Variable Speed Constant Frequency
VSI	Voltage Source Inverter
VSVF	Variable Speed Variable Frequency
WBG	Wide Band Gap
WIPS	Wings Ice Protection System
ZOH	Zero Order Hold
ZSCD	Zero Sequence Current Derivatives

List of Symbols

*	Superscript which denotes a reference value
^	The symbol (hat) denotes an estimated value
$\frac{d}{dt}, s$	The symbols denote a derivation function
E_{dc}	DC link voltage
E_{ex}	Extended EMF
$L_{d,q}$	Machine inductance in dq frame
$L_{\alpha,\beta}$	Inductance in $\alpha\beta$ frame
T_L	Load torque
T_e	Electromagnetic torque
T_s	Sampling period
T_{3ph}	The electromagnetic torque generated by one set of three-phase winding
$e_{\alpha,\beta}$	Back EMF in $\alpha\beta$ frame
$e_{\gamma,\delta}$	Back EMF in $\gamma\delta$ frame
f_{sw}	Switching frequency
G_e	compensator
$i_{a,b,c,u,v,w}$	Six phase AC currents
$i_{\alpha,\beta}$	Three phase AC currents in $\alpha\beta$ frame
$i_{d,q}$	Three phase AC currents in dq frame
i_{dc}	DC link current

i_{max}	Maximum current
i_s	Stator current
k_i	Integral gain of PI controller
k_p	Proportional gain of PI controller
k_{Pp}	Proportional gain of PI controller in phase-locked loop
k_{Pi}	Integral gain of PI controller in phase-locked loop
k_t	Torque constant
$s_{a,b,c,u,v,w}$	Six phase switching states
$u_{d,q}$	Three phase AC voltages in dq frame
$u_{\alpha,\beta}$	Three phase AC voltages in $\alpha\beta$ frame
$u_{\gamma,\delta}$	Three phase AC voltages in $\gamma\delta$ frame
u_s	Stator voltage
θ_e	Electrical angle
θ_{sr}	Power angle
$\hat{\theta}_e$	Estimated electric angle
$\Delta\theta$	The angle difference between the real and the estimated rotor position
φ_m	Machine flux linkage
$\varphi_{\alpha,\beta}$	Three phase flux linkage in $\alpha\beta$ frame
ω_e	Electrical speed
$\widehat{\omega}_e$	The estimated electrical rotor speed
ω_m	Mechanical speed
C	DC link capacitor

J	Combined machine and engine inertia
L	Inductive element
R	Resistive element
p	Pole pairs

Chapter 1 Introduction

Recently, the COVID-19 pandemic has been a painful reminder of the vulnerability of the aerospace industry, which is currently facing challenges of small number of passengers, high cost of fossil fuels and requirement of reducing carbon emissions. To recover this industry, regain its competitiveness, and achieve future climate targets, an unprecedented revolution is needed. The aviation sector is at a crossroads, and several international agencies have put forth radical goals for its future. Sectors that were hardest hit by COVID-19 require particular attention and must be prioritized [1].

According to the forecasts from the Archery Strategy Consulting company, the demand for new aircrafts in the world after the COVID-19 pandemic may decrease by 40-60% in the next 5 years, which makes the total number of aircrafts that will be made by 2024 decrease from 8000 to no more than 3000 [2].Nevertheless, at the same time, restrictions on emissions and noise (traditional problems of aircraft manufacturers) are unlikely to be loosed by state regulators. Besides, it is optimistic that after the epidemic recovery, the growth of the aviation industry is expected to reconfirm. Therefore, minimizing harmful emissions and fuel consumption in a difficult economic situation will become the tasks for aircraft manufacturers [3]. To complete this task, several initiatives are being taken by the aircraft industry to promote the use of electrical power to drive most of the aircraft systems and subsystems that are conventionally driven by hydraulic, pneumatic and mechanical power. Development of aircraft designs with improved performance to make them more efficient and environmentally-friendly is the motivation underlying the concept of More Electric Aircraft (MEA) [4].

1.1 Moving towards More Electric Aircraft

To make a comparison of energy utilization between conventional aircraft and MEA, the energy utilization in the conventional aircraft system is introduced initially. There are two types of energy sources operating in conventional aircrafts: the primary source and the secondary source. The primary source comes from the aircraft gas turbine engines in the aircraft. The secondary source consists of electric, hydraulic, pneumatic, and mechanical systems that are powered by the primary source. Figure 1.1 shows the distributions of power sources produced by the gas turbine engine in a conventional aircraft power system. Most of the jet fuel is used for propulsion and a small percentage (up to 4%) of it is used in the form of mechanical, pneumatic, hydraulic, and electrical power for loads on board.

Pneumatic power is used to power the ECS (Environmental Control System) and supply hot air for WIPS (Wings Ice Protection System) [2]. WIPS has two working modes: Anti-Icing and De-Icing. The Anti-Icing mode is pre-emptive and is turned on before the flight enters icing conditions, while the de-icing mode is reactive and used after there has been significant quantity of ice built up. The major drawbacks of the pneumatic power system are low efficiency and difficulty in maintenance and repairing [3].

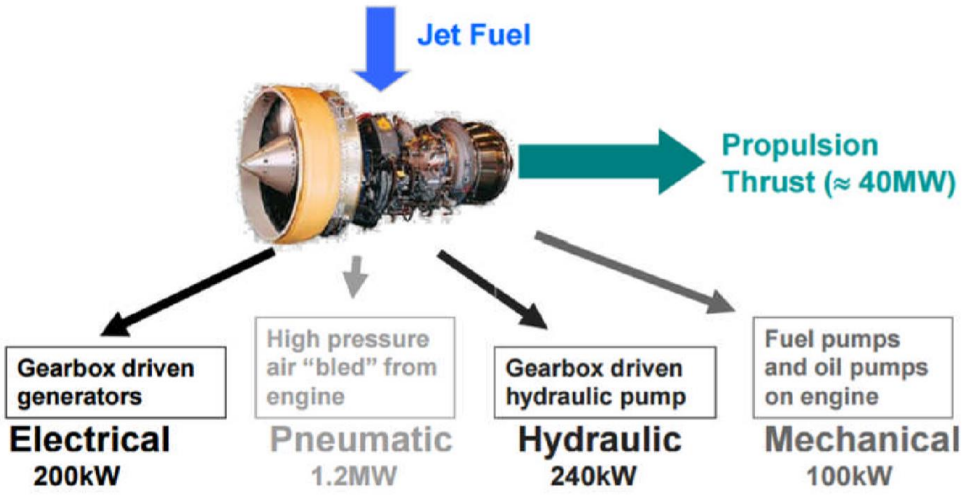


Figure 1.1. Power sources distribution in conventional aircraft [5].

Hydraulic power is transferred from the central hydraulic pump to the actuation systems for flight control and to the landing gear for deployment, reaction, and braking. Hydraulic systems have a large power density and are quite robust. However, heavy and inflexible infrastructures and the potential leakage of dangerous and corrosive liquids are their major illness [3].

Mechanical power is transferred through gearboxes and from engines to the following sites: central hydraulic pumps, local pumps for engine equipment and other mechanically driven subsystems, and the main electrical generator [4]. Disadvantages of the mechanical system are the use of a large and heavy gearbox and its associated maintenance cost [4].

Electrical power in the aircraft is generated by gearbox-driven generators and distributed throughout the aircraft for avionics, cabin electronics, utility actuators, lighting and galleys. It can be seen from Figure 1.1 that the electrical power occupies about 11% among all secondary power sources in the conventional aircrafts.

In contrast with the pneumatic, hydraulic, and mechanical power system, the electrical power system has quite a lot of outstanding advantages such as high efficiency, low maintenance fees, good controllability and advanced diagnostics. Due to these merits of electrical power system, the use of more electrical power has become an inevitable trend on aircraft. The concept of MEA is proposed in modern aerospace engineering to increase the penetration of electrical power in aircraft systems.

As illustrated in Figure 1.2, the idea of the MEA is based on the fact that many devices on board, such as electric pumps, electric heaters, electrically driven air compressors etc, can be driven by electricity.

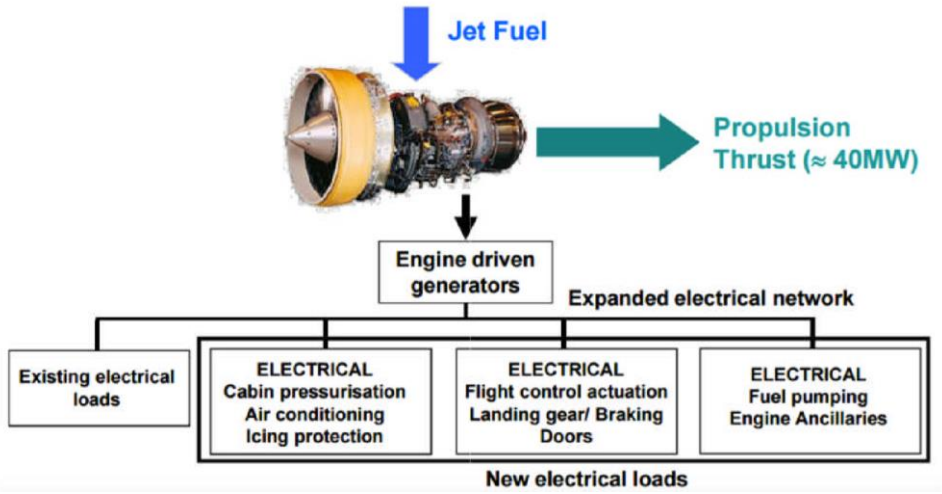


Figure 1.2. Power sources distribution of MEA [5].

Figure 1.3 compares current conventional aircraft systems with the equivalent MEA systems. MEA removes hydraulic and pneumatic systems that are costly, not easily maintained, and susceptible to leakage. This action reduces the weight, cost and complexity of the system and improves the reliability and efficiency of it.

More importantly, electrical systems offer far more options for reconfigurability as well as for advanced prognostics and diagnostics. These prognostics and diagnostics systems could help improve aircraft availability and reduce the need for unscheduled maintenance. There is a potential for equipment on an aircraft to monitor its use and environmental conditions and use profiles of its own failure mechanisms to predict end of life, leading to preventative maintenance based on usage rather than simply age or flying hours [7].

Moreover, a fan shaft generator can be used in MEA for emergency power generation by replacing the ram air turbine (RAT) in conventional aircraft, which also increases the system reliability and robustness when the engine has an emergency accident[6].

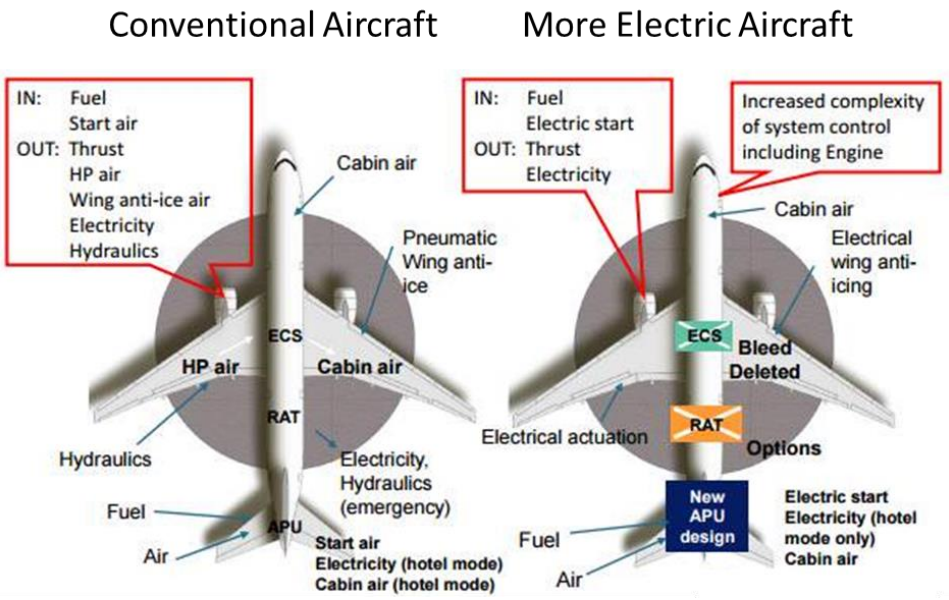


Figure 1.3 Comparison of conventional and more electric aircraft [7].

Over the last few decades, there has been tremendous progress in moving towards MEA [8]. The Boeing 787 is a prime example of an aircraft that has implemented several MEA solutions.

Figure 1.4 shows the electrical power generated by several civilian aircraft in the past decades. It can be seen that the onboard generation power capability of aircrafts has increased over the years. Especially, the electrical power generation capabilities of Boeing 787 reaches up to 1450 KVA, which is a significant improvement when compared with the 300 kVA in Airbus A320 [9]. Taking into consideration the different number of maximum passengers onboard, a 72% increase in terms of power-per-passenger is registered by Boeing 787 (2.78 kVA-per-passenger) versus Airbus A320 (1.61 kVA-per-passenger) [10]. This trend will probably continue as electrical power becomes more important on board in future aircraft.

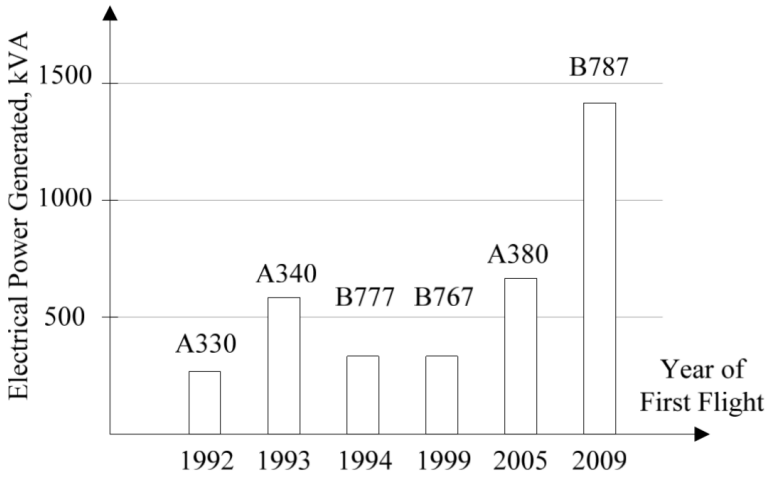


Figure 1.4. Electrical power levels generated for various civil aircraft [11, 12].

1.2 Motoring/Generating System for Future Turboprop More Electric Aircraft

The trend of moving towards MEA has prompted many researchers around the globe to develop related technologies. Several projects were dedicated to expanding research in this field, such as the Totally Integrated More Electric Systems (TIMES) [13] ,Power Optimised Aircraft (POA) [14], More Open Electrical Technologies (MOET) [15],

Clean Sky [16] and Clean Sky2 [17]. These projects are devoted to the research of relevant technologies required to develop the next generation of MEA.

In alignment with the trend towards MEA, Clean Sky 2's ACHIEVE (Advanced meCHatronIcs dEVices for a novel turboprop Electric starter-generator and health monitoring system) project [18] brings innovative thinking to provide green taxiing between the airport terminal and the runway, cleaner on-board power generation, and lowering noise and emissions, which aims to develop a next-generation highly-integrated motor/generator system for turboprop applications.

This project leverages advanced generation systems, integrated power electronics, advanced control systems and intelligent thermal management, in order to develop an innovative advanced integrated mechatronic device for electrical power management in turboprop aircraft. The mechatronic system is composed of three elements: electrical machine, power converter, and controller, aiming to provide improved and greener performing turboprop aircraft that is multi-functional, efficient, reliable, compact and light-weight. For instance, mechatronic device is used in the project to deliver electric power to drive the propeller when the aircraft is taxiing between the airport and the runway (or vice versa), before or after a flight, instead of using power directly from the main turbine engines. This measure saves fuel and reduces noise and emissions, resulting in a cleaner, safer, quieter, and more ecologically compliant environment for those people who work in, or live near, the airport. The success of ACHIEVE will contribute to reducing CO2 and NOx pollution as well as noise emissions. In terms of high-power density, the system is expected to deliver >10kW/L. Additionally, it uses advanced thermal management to operate in a maximum 110°C ambient temperature.

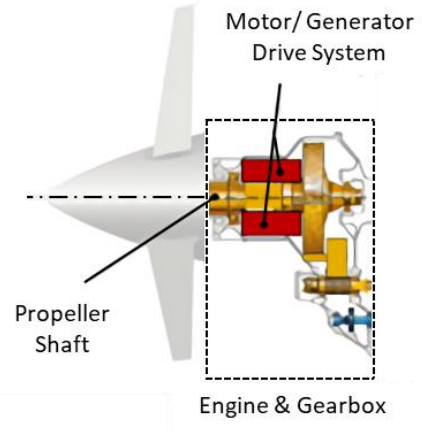


Figure 1.5. Application background [19].

As seen in Figure 1.5, the whole ACHIEVE system is integrated in an aircraft engine gearbox (framed by dashed lines), allowing aircraft to switch off the engines completely and use the battery and motor to drive the propeller which propels the aircraft along the taxiways between the runway and the airport terminal. The electrical machine in this system is a dual three-phase Permanent Magnet Synchronous Machine (DTP-PMSM) that is installed on the propeller shaft and has two operation modes: motoring mode and generation mode. In the green taxing mode, it operates as a motor and is used for taxiing and driving propellers. In the generation mode, it is driven by the engine and operates as an electrical generator.

There are two challenges in the successful application of abovementioned electric machine: first, due to the special structure of the DTP-PMSM [19], traditional vector control of PMSM [20] cannot be applied on it; Second, access of rotor position for the DTP-PMSM is difficult to implement. The high-performance control of machines in MEA, especially the vector control, requires information of rotor position and/or speed to obtain expected control results. Conventionally, the feedback of rotor position and/or speed information is achieved by using mechanical sensors such as photoelectric

encoders and Hall devices. Yet, in this system, the environment temperature could be up to 130 ℃ and such high value may deteriorate the fragile position sensors and bring about its failure. Meanwhile, the gearbox does not have enough space for the instalment of conventional sensors. Therefore, eliminating the position sensor of the DTP-PMSM is complulsory and development of a proper sensorless algorithm for such novel system shall be the core area of research in this Thesis.

1.3 Aims and Objectives

1.3.1 Aims

Following an overview of potential opportunities and challenges of the ACHIEVE project, this work aims to develop a new strategy regarding vector control of DTP-PMSM in both motoring and power generation mode and to investigate solutions of sensorless control for such system.

1.3.2 Objectives

The aim of this research can be achieved through the following objectives:

- Propose a novel modelling method that can apply field oriented control to the special DTP-PMSM system.
- Develop a vector control over the entire speed range covering both motoring and generation modes for the system.
- Investigate the sensorless control of the multi-three-phase PMSM, based on the review of state-of-the-art sensorless strategies for dual three-phase machines.

- Develop simulation models in support of the proposed conventional and enhanced sensorless control methods.
- Prove the key theoretical findings by experiments; this will require developing of a test rig to enable experimental support to the proposed sensorless strategies.

1.4 Structure of Thesis

This Thesis is organized into eight chapters and the structure of it is outlined as follows:

Chapter 2: Explain the research background of this Thesis. An analytic review of existing research on multi-three-phase machine and sensorless control is introduced in detail.

Chapter 3: Analyse the basic structure and mathematical model of the dual three-phase PMSM engaged in this Thesis. Based on the unique asymmetric winding structure of the machine, a new coordinate transformation method is proposed, and the space vector decoupling of the two-phase three-phase machine and the PWM control strategy are introduced.

Chapter 4: Based on the mathematical model of permanent magnet synchronous machine, the principles, and characteristics of the sensorless control algorithm in different speed ranges are introduced.

Chapter 5: Since the application of the DTP-PMSM in this study is mainly in the high-speed stage, the model reference adaptive method based on the machine model is

introduced, and for its sensitivity to machine parameters, an enhanced method with PM flux estimation is proposed. Simulation results verify the effectiveness of this scheme.

Chapter 6: An operation scheme that combines a low-speed I/F control for start-up and high-speed speed-current cascaded closed-loop vector control is proposed and utilized. The hybrid method covers the full-speed range in motoring mode, and it is verified by simulation results.

Chapter 7: The developed experimental platform of the sensorless control system of dual three-phase PMSM permanent magnet synchronous machines is reported. The experimental results of the sensorless control scheme under various operating conditions of zero, low, medium, and high speeds are given, confirming that the full requested speed range (up to max speed) of the PMSM is achieved.

Chapter 8: Summarizes the conclusions obtained in this study and provides a preliminary outlook on the deficiencies of the work and the potential direction of future research.

Chapter 2 Sensorless Control of Multi-Three-Phase Machine based Starter/Generator System for More Electric Aircraft

This chapter provides a literature review of existing knowledge related to this study, covering motoring/generating systems in More Electric Aircraft (MEA), multi-three-phase machine research, etc. The different sensorless control methods have been presented and compared as well. The ACHIEVE project to which this research is aligned is reviewed and the control strategy is explained in detail.

2.1 Electric Power System in the More Electric Aircraft

The aircraft electrical power systems have seen significant changes in recent years as the move towards MEA makes aircraft more and more dependent on electricity. The evolution of aircraft electrical power systems including power generation, distribution and utilisation will be reviewed in detail in this section.

2.1.1 Power Generation

With the advent of the MEA initiative, electric power systems are progressively taking the place of pneumatic, hydraulic, and mechanical power systems [5, 8, 21]. Over time, this trend has led to an increase of required electric power, particularly for larger aircraft [9, 22, 23], as sketched in Figure 2.1. Apparently, power generation plays an important role among the on-board electrical power system. The evolution of electric power generation on-board of aircraft is illustrated in Figure 2.2.

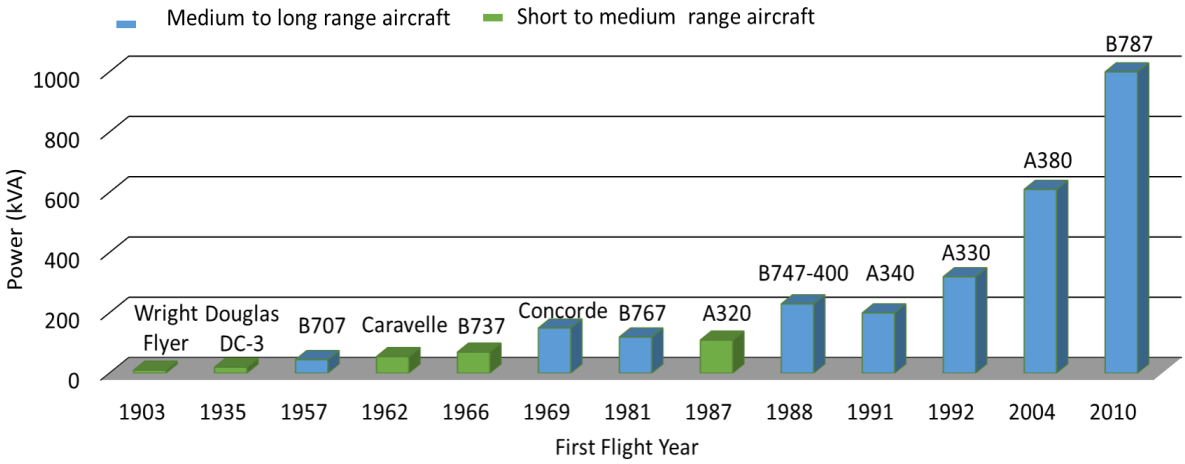


Figure 2.1 Evolution of electrical power need[9].

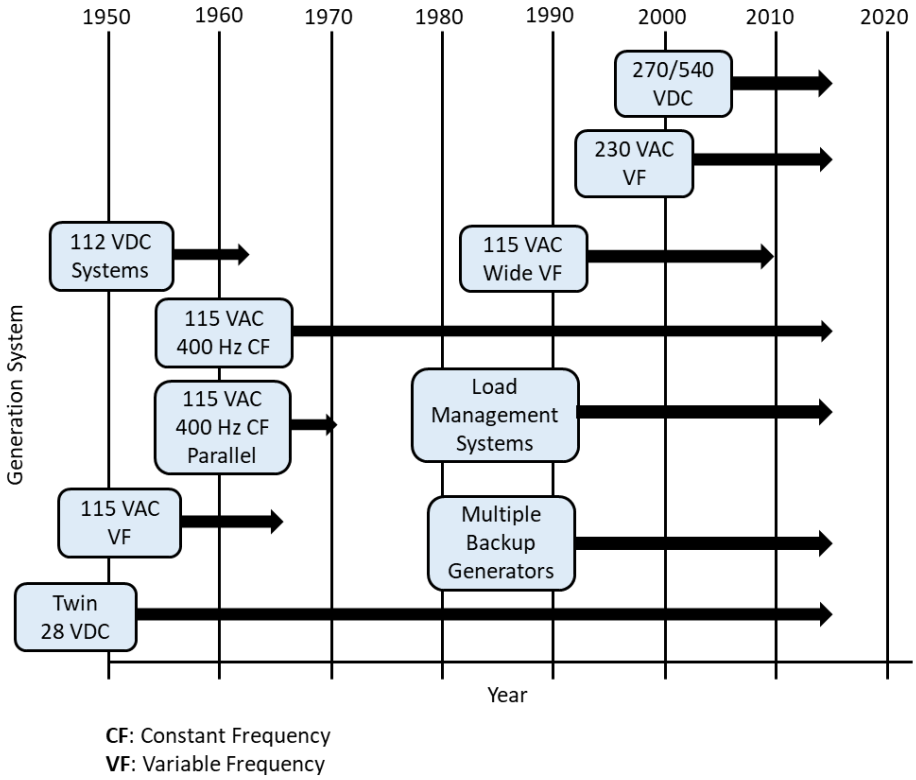


Figure 2.2 Evolution of Electric generation system [24].

2.1.1.1 DC Generation

The DC generators are controlled to supply constant DC voltage even with variable engine speed and electrical loads. This control also needs to satisfy aircraft standards

to ensure compatibility between the aircraft electrical power system and other loads (refer to MIL-STD-704F [25]).

In the early days, electric power on aircraft is mainly used by communication and ignition systems. For instance, the first DC generators are typically rated for less than 500W and usually adopted 6- and 12 VDC voltage levels [26, 27]. The operation of lighting, signalling, and heating systems increased the electric power requirements. Hence, the generator capacity rose up to 1 kW [28], as well as the voltage level, which was increased to 28 VDC. In the early 1950s, a customized DC starter/generator (S/G) was built for the Republic F-84 Thunderjet. This S/G is able to continuously operate at 7500 RPM, while providing a current of 400 A[29]. During the past decade, potential of higher voltage level electrical systems has been investigated, since higher voltage implies lower current for a given power. For instance, 270 VDC system has been developed for military aircraft such as the Lockheed Martin F-22. 270 VDC system is more efficient than conventional methods of power generation due to reduction of required power conversion stages and weight savings. Yet, there are some limits for 270 VDC [11]:

- The peak current cannot exceed 400 A, otherwise, the size of conductors and switchgears to carry the necessary current becomes prohibitive.
- The brush wear on brushed DC generators becomes excessive with resulting maintenance costs if the current exceeds 400 A or the power per channel is over 12 kW.
- Conventional DC circuit breakers cannot be used at such high voltages 270 VDC and as a consequence, 270 VDC protection devices need to be developed.

2.1.1.2 AC Generation

Most aircraft were still DC powered even after World War II. However, from the 1960s' onward, increasing speeds and aircraft size led to an unprecedented increase of required electric power. Furthermore, reliability and power density became ever more critical. For these reasons, a general worldwide trend moving towards AC generation is observed [30, 31]. In the following subparagraphs, the most common AC electric power systems are detailed and analysed.

1) Constant Frequency Power Generation

The 115 VAC at 400 Hz constant frequency (CF) aircraft system initiated in the 1960s. This generation of electrical networks was equipped with fixed frequency (115/200 VAC 400 Hz) integrated drive generators as on the A320, A330, and A340. With this architecture, a complex mechanical gearbox that keeps the mechanical speed, and hence the electrical frequency, constant on the aircraft's electric bus is used, as shown in Figure 2.3.

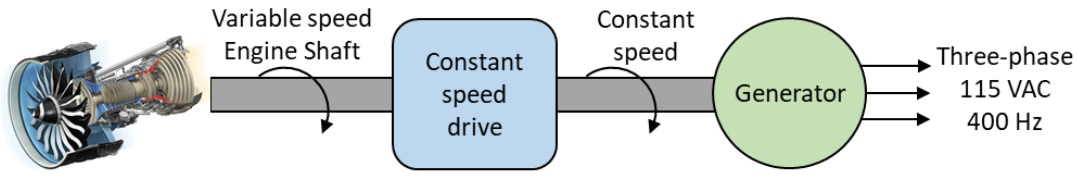


Figure 2.3 A constant frequency generation system using a mechanical gearbox[32].

Yet, the cost of purchase and maintenance of the mentioned gearbox could be high due to the complexity of the hydro-mechanical drive system [33]. In addition, the use of the gearbox reduces the reliability of the entire system. Hence, this topology nowadays

appears not to be the best choice. There are two topologies that are considered as alternatives to CF power generation method.

2) Variable Speed Constant Frequency Power Generation

The variable speed constant frequency (VSCF) topology is similar to the CF topology as three-phase AC power with constant frequency is produced irrespective of the shaft speed. The difference is power electronic converters that could be more efficient are used to regulate the power output. The output of the generator is of a variable frequency related to the speed of the turbine. This electrical frequency, which changes during phases of flight in response to changing engine operational mode, is processed by a regulated AC/AC power converter and filter to produce a fixed frequency supply for the aircraft's Electrical Power System (EPS). The AC/AC power conversion could be realized using various power converter topologies including matrix converters, cycloconverter (Figure 2.4) and back-to-back converters with DC-link (Figure 2.5). The architecture of a VSCF with a cycloconverter is mainly used on military aircraft, such as for the F-18 fighter aircraft, the F-117A stealth attack aircraft, and the V-22 ultrahigh altitude reconnaissance aircraft [11], [34]. The VSCF system using a DC-link was mounted on the MD-90 until 2000 and it is still used on the B777, for the two 20 kVA backup generators [35]. The DC-link is beneficial for feeding high voltage loads and charging batteries through DC/DC converters whilst the bulky DC-link capacitor increases the size and weight of the system. In such a VSCF generation system, no gearbox is needed between the gas turbine shaft and the generator; however, the drawback is that this power converter must process all the generated power and, therefore, must have the full power rating and high reliability to comply with the safety

requirement of aircraft manufacturer. In such systems, the power electronic converters are the bottle-neck of reliability.

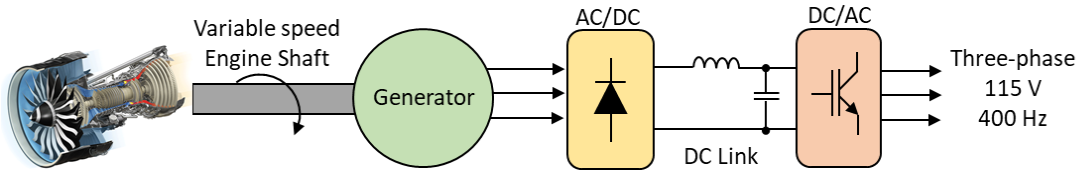


Figure 2.4 VSCF system using DC-link [4].

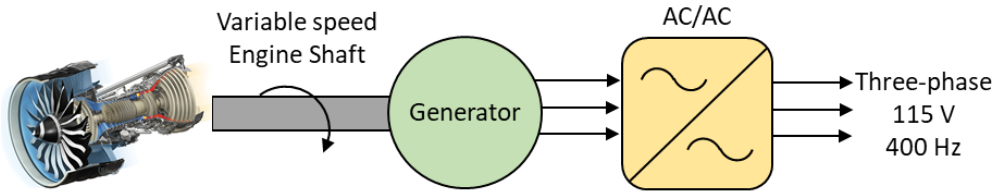


Figure 2.5 VSCF system using AC/AC converter [4].

3) Variable Frequency Power Generation

The third topology is referred to as variable frequency (VF), also known as 'frequency-wild'. This has been getting a lot of attention in the field of future aircraft power generation research as it is a quite promising potential methodology. As sketched in Figure 2.6, the generator is coupled to the engine shaft via a variable speed drive and outputs three-phase VF power ranging between 300 to 900 Hz depending on the engine speed. The key advantage of this layout is that the direct connection between the generator output and the electrical power system provides a simple and very reliable configuration. The drawback is that nearly all aircraft loads will require power converters for control, as the variable-frequency supply cannot be used directly by some onboard loads. However, many loads, for example, actuators, require this power conversion stage for control even when operated from a fixed frequency supply. Having

extra distributed power converters gives more options for a safe aircraft system design as redundancy could be built-in at the system level, avoiding any single points of failure within the design [4] . In new aircrafts such as the Boeing 787, Airbus A380 and A350, this VSVF architecture has been employed [36]. In these aircrafts, while the voltage is regulated at either 115 (A380) or 230 VAC (B787), the frequency changes with the engine speed and typically varies between 320 and 900 Hz [37]. This change in paradigm leads to establishing power conversion for many loads, including motor drives. As a result, power electronic converters are needed locally.

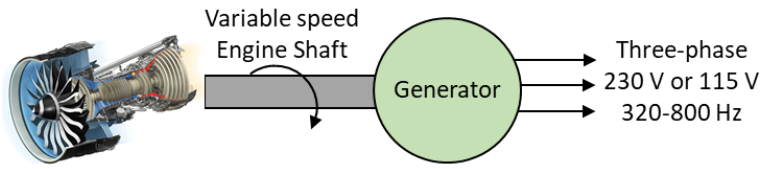


Figure 2.6 A variable frequency generation system (with AC distribution) [4].

Compared with AC systems that are used primarily on military vehicles and military aircraft, variable frequency generation with high voltage DC (HVDC) distribution structure is shown in Figure 2.7. The difference is that the generated electrical power is rectified to the DC bus for further distribution since there is a HVDC bus bar (270 V or 540 V).

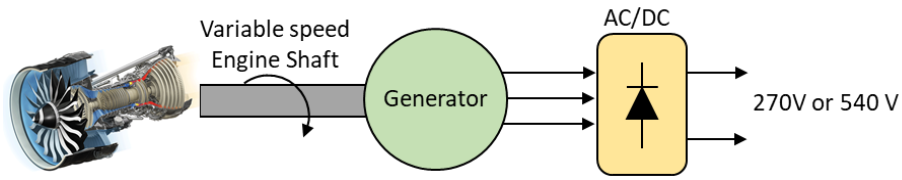


Figure 2.7 A variable frequency generation system (with DC distribution) [4].

As detailed above, the typical power generation system mainly evolves from 115 VAC 400 Hz CF, VSCF, to VSVF. Table 2-1 lists the types of power generation system in recent civil and military aircrafts.

Table 2-1 Power generation type for recent aircrafts[36].

Generation type	Civil aircrafts		Military aircrafts	
CF	B777	2*120kVA	Eurofighter Typhoon	
	A340	4*90kVA		
	B737NG	2*90kVA		
	MD-12	4*120kVA		
	B747-X	4*120kVA		
	B717	2*40kVA		
	B767-400	2*120kVA		
VSCF (cycloconverter) 115 VAC/400 Hz			F-18C/D	2*40/45 kVA
			F-18E/F	2*60/65 kVA
VSCF (DC Link) 115 VAC/400 Hz	B777 (Backup)	2*20kVA		
	MD-90	2*75kVA		
VF 115 VAC/380-760 Hz	Global Ex	4*40 kVA	Boeing JSF	2*50 kVA
	Horizon	2*20/25 kVA		
	A380	4*150 kVA		
VF 230 VAC	B787	4*250 kVA		

AC generation shows several advantages when compared with DC generation. First of all, a significant improvement is achieved in terms of power density. A relevant advantage is the potentially much higher operating voltage. Particularly, a significant cabling weight reduction was achieved since increasing the operating voltage means increasing the current for the same power. With respect of the reliability, the absence of commutators on AC generators improves its lifetime maintenance and reduce the

maintenance requirement [38]. However, the advent of AC generators also introduced new challenges, mainly due to the following issues [32]:

- The parallel operations.
- The need to manage reactive power.
- The choice of an appropriate frequency.

AC generators could be operated in parallel, when the developed voltages have the same amplitude, phase, and frequency. Conversely, only the same voltage amplitude is needed for DC generators. Furthermore, unlike AC systems, the DC ones do not involve reactive power; hence, the related issues (e.g., power factor correction) are avoided. The control of AC generator systems is similar, except for the addition of a separate DC power source for field excitation. Additional regulators are also required to control this DC power source which makes the control slightly more complex.

2.1.2 Power Distribution

Electrical power is distributed throughout the aircraft after being produced by the generators. In the traditional aircraft model, all of the electrical power is produced from engines-driven major generators (next to the engines) and APU-driven generator (in the aft area). The generated electrical power is then routed to the front of the aircraft for control. In the event that one generator fails it is automatically isolated from its respective busbar and all busbar loads are then taken over by the alternative generator. As shown in Figure 2.8, in conventional aircraft systems, the synchronous generator supplies AC voltage at constant frequency to the AC loads through the aircraft. AC/DC

rectifiers are used to convert the AC voltage with fixed frequency at the main AC bus to DC voltage at the secondary buses which provides electrical power to DC loads.

For modern MEA, the new solid-state power controllers and contactors with communication function allow for the possibility to eliminate the configuration in favour of decentralised distribution [39]. This results in increased efficiency of the power distribution system, as line losses are decreased due to shorter distances between generation and consumption. Moreover, significant weight and volume savings could be realized, as the power rating of the main conductors is reduced. These weight savings and rating reductions contribute both to improved fuel efficiency of the aircraft and a lower total cost, as the lower rated equipment could be purchased at a reduced price. Additionally, the distributed power system configuration realizes maintenance cost savings. The Boeing 787 is an example of this modern network configuration and is shown in Figure 2.9. It has 2x250 kVA S/G per engine, resulting in 500 kVA of generated power per channel. In addition, 2x225 kVA APU S/G are on board. Instead of 115 V 400 Hz (fixed frequency) bus, the main bus is of high voltage (230 VAC) and variable frequency ranging from 360 to 800 Hz [40].

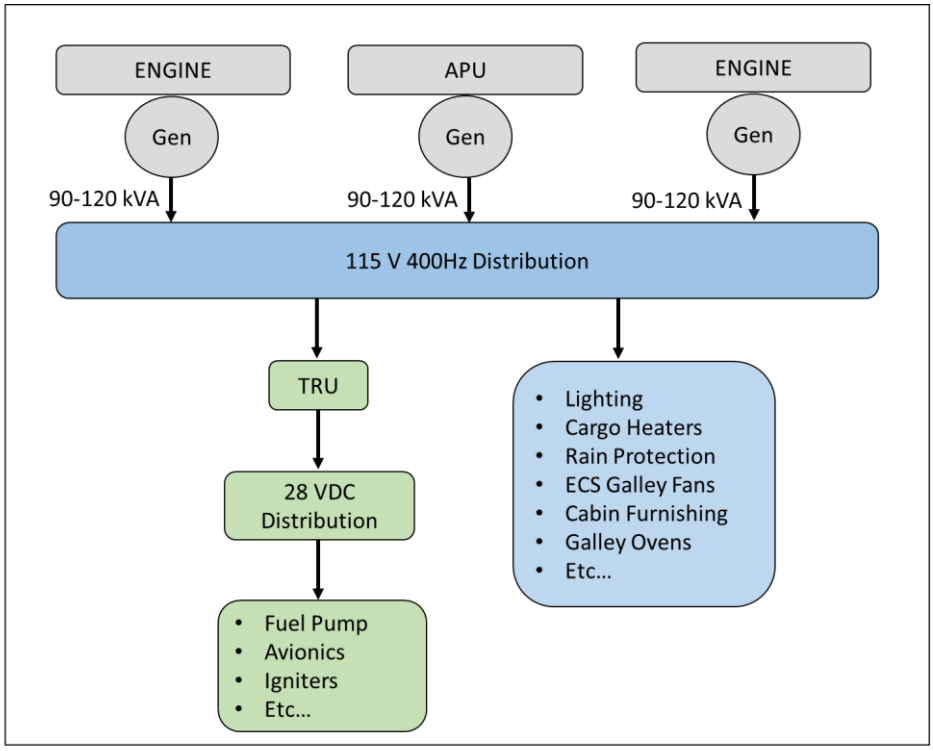


Figure 2.8 Power distribution system in conventional aircraft[35].

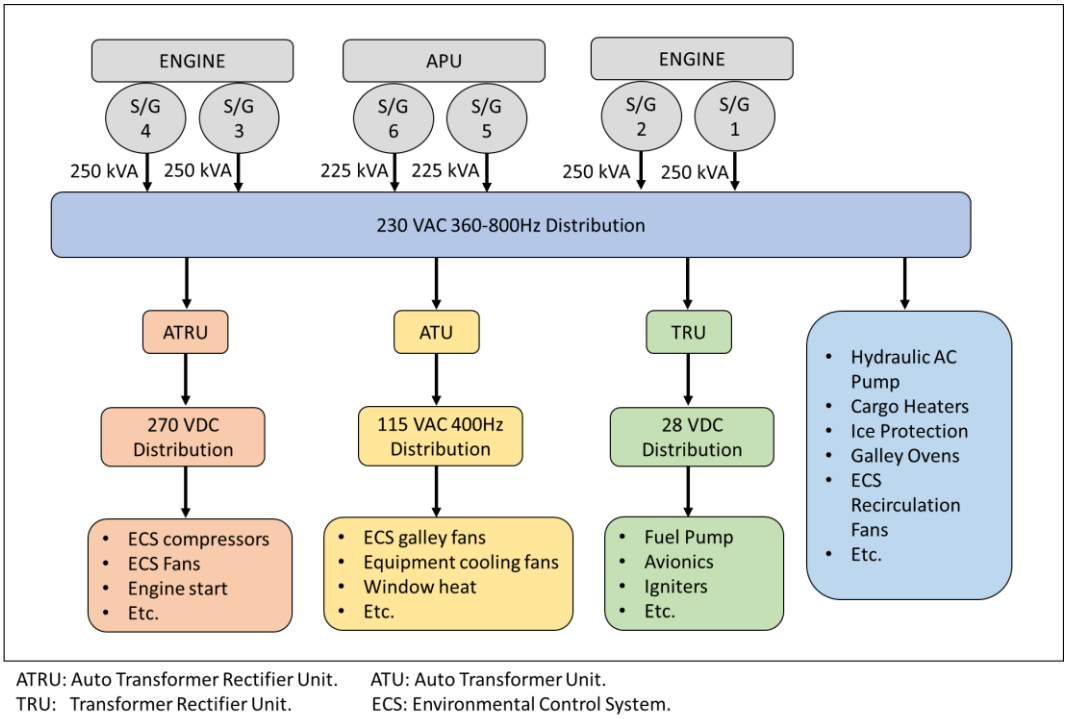


Figure 2.9 Power distribution system in a modern aircraft B787[41].

It is clear that according to the above description, modern MEAs provide the flexibility to aircraft that generating and distributing power to the nearby location where it is being consumed.

2.1.3 Power Consumption

Once the aircraft electrical power has been generated and distributed then it is available to be consumed by the aircraft services. These electrical services cover a range of functions spread throughout the aircraft depending upon their task. While the number of electrical services is legion, they may be broadly subdivided into the following categories [11]:

- Motors and Actuation.
- Lighting Services.
- Subsystem Controllers.
- Avionics Systems.
- Heating Devices.

Various motor applications in the aircraft are shown in Figure 2.10. The number of motors and the power requirement associated with each type of application for existing popular aircrafts are listed in Table 2-2. Large aircraft may have twice as many loads, as well as higher power requirements for each load. The availability of adequate lighting is essential to the safe operation of the aircraft. Lighting systems includes external lighting such as navigation, strobe, landing/taxi, formation, inspection, emergency evacuation and logo lights. Internal lighting includes cockpit/flight-deck, passenger service and emergency/evacuation lighting. The heating load represents the

power needed for anti-icing or de-icing systems which could consume many dozens of kVAs. The actuation load represents the power needed for the operation of electric actuations inside the aircraft. Although electric actuation needs electric machines, power converters and controllers, it provides many advantages over using the hydraulic and mechanical counterparts. These potential benefits may include the following [36]:

- Reduced maintenance due to the modular nature of the system.
- Increased functionality since there is individual control of each surface element.
- Improved fault detection, as all monitoring is electronic and transmitted to the pilot.
- Wear and degradation could be easily monitored by the sensor control systems.
- Reduced mass and higher efficiency than mechanical actuators.

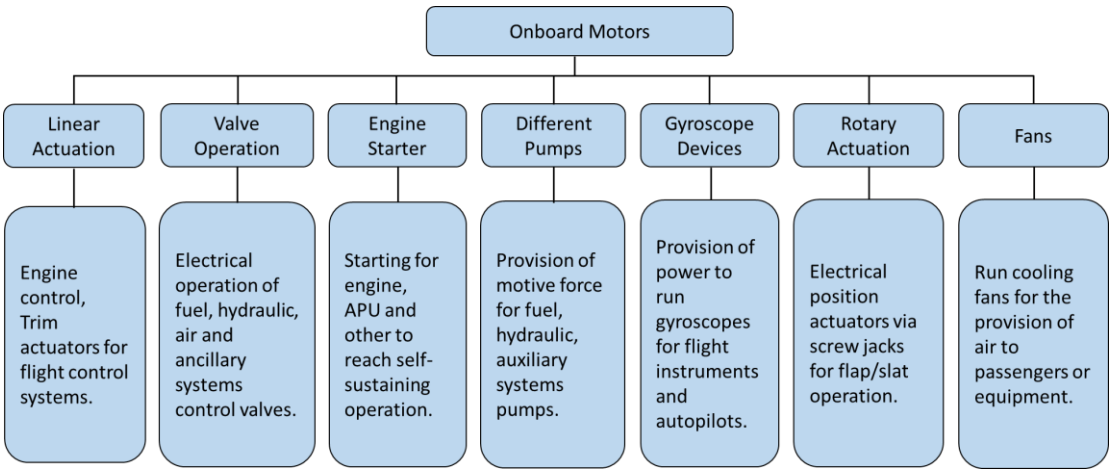


Figure 2.10 Onboard motor applications and their functions[36].

Table 2-2 Potential Motor Drive Applications for Aircrafts[36].

Application	Number of motors	Rating / motor
Air conditioning & cooling fans	11	1-6k VA
Fuel boost pumps	6	3-4k VA
Flaps & slats	2	5-6k VA
Fuel & override pumps	4	9-10k VA
Hydraulic pumps	4	9-10k VA

2.1.4 Starter/Generator System

The integrated S/G is considered as one of the core technologies in the MEA paradigm from the early 1990s. As shown in Figure 2.11, the electric S/G system has two main paradigms in the electrification of aircraft systems, depending on whether the S/G is integrated to an AC or DC distribution grid. A S/G system must be designed for bidirectional power flow and has basically two modes of operation. In the motoring mode, the machine is driven by a bidirectional power converter and uses the power coming from the supply bus to accelerate the aircraft engine. Since the control target in the motoring mode is the machine speed, as can be seen, the speed signal is sensored and the control system regulates the machine speed to its reference value. This mechanical energy could be harnessed to the engine shaft and cause the engine to spool up to a speed where the combustion ignites, and the engine becomes self-sustaining. In the generating mode, the engine acts as a source of mechanical power that is converted by machine and the interface inverter supplies the onboard loads through constant frequency (CF), variable frequency (VF) or DC supply from variable speed (VS) operation. In this way, the S/G is beneficial to facilitate electric engine crank, assist the engine in reaching the desired idle speed, generate power to drive the onboard auxiliaries, and improve the overall system efficiency [42].

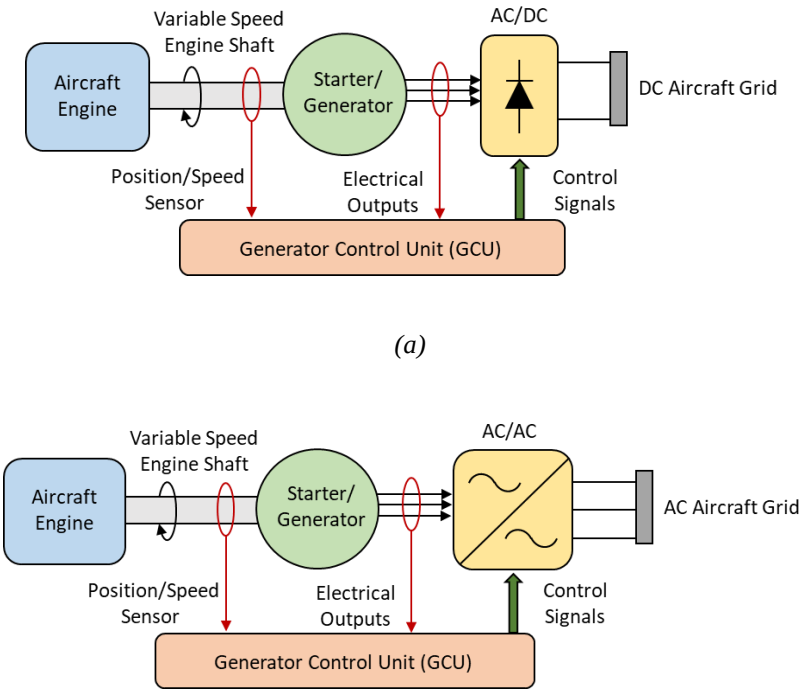


Figure 2.11 Electric S/G system in the MEA. (a) interface to a DC distribution system. (b) VSCF AC distribution[43].

The torque-speed characteristic of the aircraft S/G is shown in Figure 2.12. In the motoring mode, machine runs as a motor and accelerates the engine which is behaving as a load to the self-sustaining speed ω_{start}. From standstill to ω_{base}, the machine operates in the constant torque region where the maximum torque of the machine could be achieved. Between ω_{base} to ω_{start}, the machine provides a constant power to accelerate the engine until the engine is fired and becomes self-sustaining. When the machine reaches ω_{min} the engine is finally self-sustained and the generator operation is initiated. In the generation mode, the machine is required to produce maximum constant power up to a maximum speed (ω_{max}).

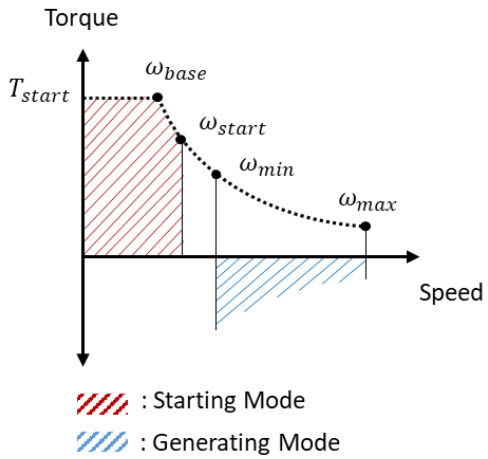
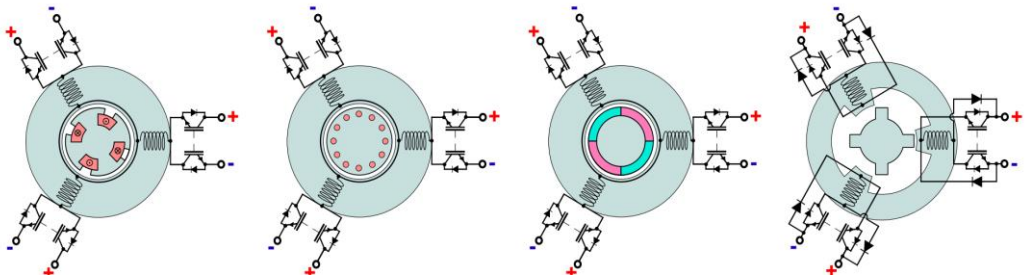


Figure 2.12 Torque-speed profile of the aircraft S/G[43].

Considering that the harsh operating conditions and the high temperatures may push most materials close to their limits, more innovations in materials, thermal management systems design, etc are required. Consequently, various types of electric machines have been proposed for S/G applications, including brushless wound-field synchronous machines (WFSMs), induction machines (IMs), switched reluctance machines (SRMs), and permanent magnet machines (PMMs) [44, 45]. Figure 2.13 illustrates the basic structure and most common power electronic conversion (PEC) interface of each candidate solution assuming an AC/DC interface solution as Figure 2.11 (a). The key points of the different machines are summarized in Table 2-3.



(a) (b) (c) (d)

Figure 2.13 Considered choices for electrical machines in MEA architectures with an AC/DC interface. (a) WFSM. (b) Squirrel-cage IM. (c) PMM.(d) SRM[46].

Table 2-3 Summary of the Electrical Machines for S/G system[43].

Machine	Advantages	Shortages
WFSMs	● High power factor in a wide speed range ● Improved safety due to de-excitation ability	● Limitation of maximum speed ● More complicated control schemes
IMs	● Good fault tolerance ability ● Wide speed range	● Low power density ● Heat generated by rotor side requires thermal management
SRMs	● Good fault tolerance ability ● Robustness in high speed	● Low power factor ● Significant torque pulsations
PMMs	● High efficiency ● High speed ability and power density	● Limited fault tolerance

The brushless WFSM with a rotating diode bridge is the most popular state-of-the-art S/G technology [43]. It enjoys high power factor in a wide speed range and reliable de-excitation ability in case of a failure. Yet, its physical speed limit reduces its potential application in the higher power densities region [47].

The IMs are also a good solution for S/G systems because of their simple structure, low cost, and strong robustness. Extensive feasibility research focusing on using IM as a S/G has been reported in [44, 48-50]. However, induction generators have not been

used in actual aircraft power generation and the use of an IM as an embedded S/G needs to be further explored for aircraft applications.

The SRMs have been considered and investigated as a S/G in [51-55]. The main features of the SRM-based system include fault tolerance, suitability to operate at high speeds and in harsh environments, and relatively high power density [56]. However, SRM has limited high speed capability and a high torque ripple [57]. Due to the acoustic noise and torque pulsations of SRMs, the use of SRMs for aerospace applications is still limited.

The PMMs have been gaining interests for aircraft S/G system over the last few years mainly owing to several merits, including high power density, high efficiency and speed ability[58-60]. Due to these advantages, the focus of this Thesis is on the PMM-based S/G system. However, there are still some limitations of this topology. For instance, the PMMs are not inherently fault tolerant. In order to improve the reliability of system, multi-three-phase machine and sensorless control will be considered and discussed in the following content.

2.2 Review of Multi-Three-Phase Machine Research

Over the past two decades, multi-three-phase machines have received increasing interest in MEA as they achieve notable improvements in various aspects of performance compared with the use of conventional three-phase electric machine drives [61].

Specifically, compared with three-phase drive system, the advantages of multi-three-phase machine are mainly reflected in the following aspects [62]:

- Low-voltage high-power drive is realized. Due to the increase in the number of machine phases, the output power of each phase is greatly reduced when the total output power remains the same, effectively reducing the level of power devices on each bridge leg. Taking surface mounted PMSM as an example, when changing the three-phase winding to multi-three-phase winding, if the torque coefficient of the machine after the modification is unchanged, that is, the same phase current corresponds to the same electromagnetic torque, the Back EMF produced in each phase of the multi-three-phase winding at the same speed will be reduced. In this way, the power supply voltage required for each phase is reduced, thereby high power output of low voltage is obtained.
- Torque ripple is reduced. As the number of machine phases increases, the number of spatial harmonics increases, the torque ripple frequency increases, and the amplitude decreases, thereby reducing the noise and vibration of the machine during operation. The main purpose of the early research on multi-three-phase machines is to reduce torque ripple. Although the current PWM technology is increasingly mature and low-order harmonic currents could be ignored, the air gap harmonic magnetic field which is produced by the non-linear factors such as slotting of the core of the machine, still produce torque ripple through interacting with fundamental current. And the more the number of machine phases, the higher the frequency of torque ripple generated by the fundamental current.
- Fault tolerance ability is improved. When one-phase phase failure occurs in the traditional three-phase machine, the neutral point of the machine must be connected

to the midpoint of the DC bus, otherwise it will be reduced to a single-phase machine and cannot start automatically. For multi-three-phase machines, when one-phase or multi-three-phase faults occur in the stator windings, there is no need to draw out the neutral line or shut down. By using an appropriate fault-tolerant control strategy to make the remaining machine windings synthetic rotating magnetic potential trajectory circular, the machine could be stabilized to run. It should be noticed that as the quantity of power electronic devices increases, the reliability of system might decrease since power electronic devices is much more likely to fail than machines.

- Control resources are enriched. For multi-three-phase machines with concentrated full-length windings, a constant torque could be generated by injecting an appropriate ratio of low-order harmonic currents and corresponding harmonic magnetic fields, thereby increasing the power density of the machine. The space voltage vector of the multi-three-phase inverter increases exponentially, providing abundant control resources for PWM modulation, direct torque control, and predictive current control. For example, dead zone could be compensated through the control of the harmonic sub-plane component and over modulation.

In the 1950s, White. D conducted theoretical research on machines with any natural number of phases, and established the electromechanical energy conversion theory of multiphase AC machines, which laid the theoretical foundation for application of multiphase machine speed control transmission systems [63]. The research of multi-three-phase speed control transmission system could date back to the 1960s when scholars such as Ward. E studied the AC speed control system powered by a five-phase inverter [64]. In the 1980s, T.M. Jahns proposed the concept of phase redundancy to

improve the reliability of the machine drive system [65]. Since 1990s, the rapid development of machine control theory, power electronics technology, PWM technology, and DSP has provided a good platform for the technical improvement of multiphase machines. Meanwhile, in the automobile, ship, rail transit and aerospace propulsion systems, the high-efficiency and high-reliability electrification process has greatly promoted the application of multiphase machine technology.

Research teams about multiphase machine around the world and their research objects, research fields and main representative publications are shown in Table 2-4. Each research team has its own focus. T.A. Lipo's team has engaged in the modelling and fault-tolerant control of multiphase machines since the 1980s, addressing the basic method of multiphase machine analysis. H.A. Toliyat studied the harmonic injection of five-phase machines to improve power density and direct torque control. E. Levi mainly conducted in-depth study on the multiphase-multimotor drive system of the single drive system, analysed its mechanism, and provided a system solution for occasions with high space requirements. F. Barrero and M. J. Duran introduced predictive control into the multiphase machine drive system and optimizes the current loop of vector control and direct torque control. Professor Z.Q. Zhu of Sheffield University started his research of multiphase machines from 2010. By innovatively applying the traditional three-phase vector, direct torque control and sensorless control technologies to multiphase machines, great progress has been made in harmonic current suppression and sensorless control. Jin Huang's research team at Zhejiang University has been conducting intensive study on mathematical modelling, fault diagnosis, fault-tolerant control of multiphase machine and multiphase single-winding bearingless machine control system since the 1990s. In summary, with the demand for high reliability,

electrification, and intelligent development in the fields of aerospace, ship propulsion, electric vehicles, etc., multiphase machines show great advantages in the above fields. The obvious competitive advantage will definitely attract more and more scholars and enterprises to carry out further research and industrialization.

Table 2-4 Research team of multiphase machine around the world [62].

Affinity	Team Leader	Research Objects	Research Area	Sources
University of Wisconsin	T.A. Lipo	5 phase IM 6 phase IM	● Vector control ● PWM modulation Fault tolerance	[66-69]
University of Texas M&A	H.A. Toliyat	5 phase IM 5 phase PMM	● Vector control ● Direct Torque Control ● Fault tolerance ● Sensorless control	[70-73]
University of Liverpool John Moores	E. Levi	5 phase IM DTP IM Multiphase-multimotor drive	● Multimotor series drive ● PWM modulation ● Predictive control ● Fault tolerance	[74-78]
University of Seville	F. Barrero	5 phase IM 6 phase IM	● Predictive control ● Intelligent control Fault tolerance ● Sensorless control	[79-83]
University of Malaga	M.J. Duran	5 phase IM 6 phase IM	● Predictive control ● Intelligent control Fault tolerance ● Sensorless control	[81, 84-87]
University of Sheffield	Z.Q. Zhu	5 phase PMM DTP PMSM	● Vector control ● Direct Torque Control ● Fault tolerance ● Sensorless control	[88-94]
Zhejiang University	J. Huang	5 phase IM 9 phase IM	● Fault diagnosis ● Fault tolerance ● Sensorless control	[95-100]

As shown in Table 2-4, among various research teams of multiphase machine, the sensorless control of DTP-PMSM system is developed by Prof. Z. Q. Zhu's team from the University of Sheffield. However, they basically focus on the zero and low speed range sensorless control system design which has no obvious relevance to this study.

Hence, there is a gap in existing research about the high-speed range sensorless control design for DTP-PMSM system.

2.3 Review of Sensorless Control Study

The high-performance control of electric machines in MEA, especially vector control, requires information of rotor position or speed to obtain expected control results. The feedback of rotor position or speed information is usually achieved by using mechanical sensors such as photoelectric encoders which could be divided into incremental encoder, absolute encoder, and hybrid rotary encoder. The incremental encoder shown in Figure 2.14, utilize the photoelectric signal to convert the mechanical angle of the shaft into a digital signal. Each rotation angle of the shaft produces a pulse signal, so the rotation angle of the rotor could be calculated by counting the pulse signal.

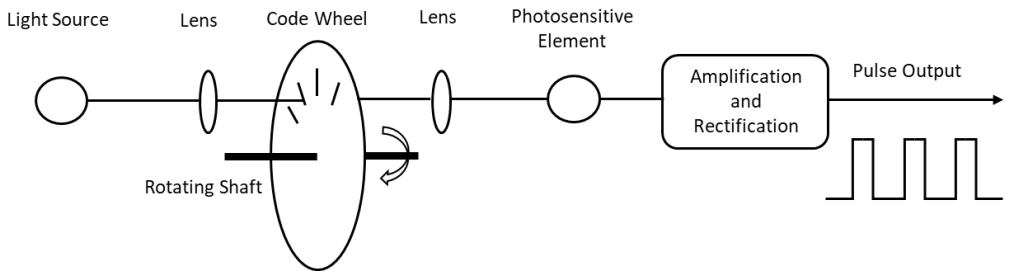


Figure 2.14 Working principle diagram of photoelectric incremental encoder.

The principle of absolute encoder is shown in Figure 2.15. The absolute rotation angle of the machine is read according to the light and dark distribution of the binary dial on the photoelectric signal scanning index plate.

The hybrid rotary encoder which outputs relative rotation angle and absolute rotation angle at the same time combines the flexibility of incremental encoder and the accuracy of absolute encoder.

The position sensors are fragile components which could be easily damaged under harsh environment conditions such as mechanical vibration, high temperatures [101, 102]. The specific fault phenomenon and reason analysis are detailed in Table 2-5.

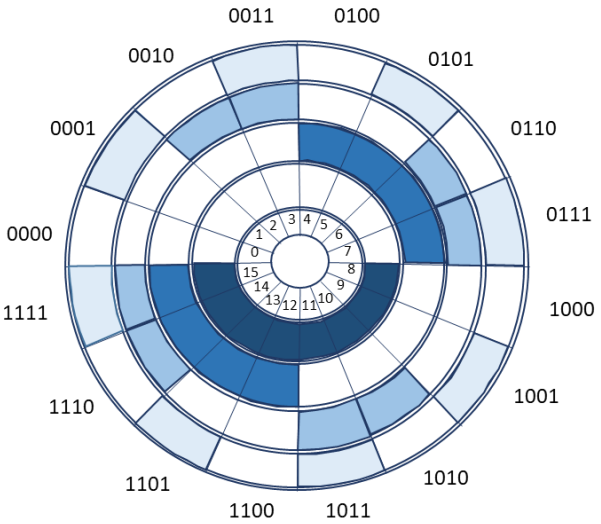


Figure 2.15 The principle of absolute encoder.

Table 2-5 Fault classification and cause analysis of position sensor.

Symptom of failure	Cause of failure	Detailed analysis
The number of output signals is reduced	Duty cycle difference	The gap of grating plate is blocked due to • external object • rubber tube burst
Output signals are not continous	No effective docking	• Cable burst • Vehicle dynamic cable failure
	Bearing fracture	• The installation does not meet the specification. • The grease is infected by foreign matters. • The reinforcement nut is loose. • The preload aggravates the friction damage.
No output signal	Cable Break	• All core wires inside the cable are damaged.
	Coupling Damage	• Insufficient heat treatment technology • The root fillet has a smaller shape.
Output signals are jammed	Photosensitive Element Damage	• Optical pathway is blocked.

As position sensors are vulnerable, their elimination and replacement by application of sensorless algorithm will help to improve system reliability. In the following content, the state-of-art of PMSM based sensorless control research will be reported.

2.3.1 Overview of Sensorless Study for Three-Phase PMSM

In the last few decades, a tremendous effort has been done to develop the sensorless control techniques for a wide speed range [103-105]. Generally, sensorless PMSMs drives method are classified into two categories, i.e., model-based sensorless control typically applied in high-speed range and saliency-based sensorless control applied in low-speed range [106-108]. The PMSM sensorless control block diagram based on the model-based methods is shown in Figure 2.16.

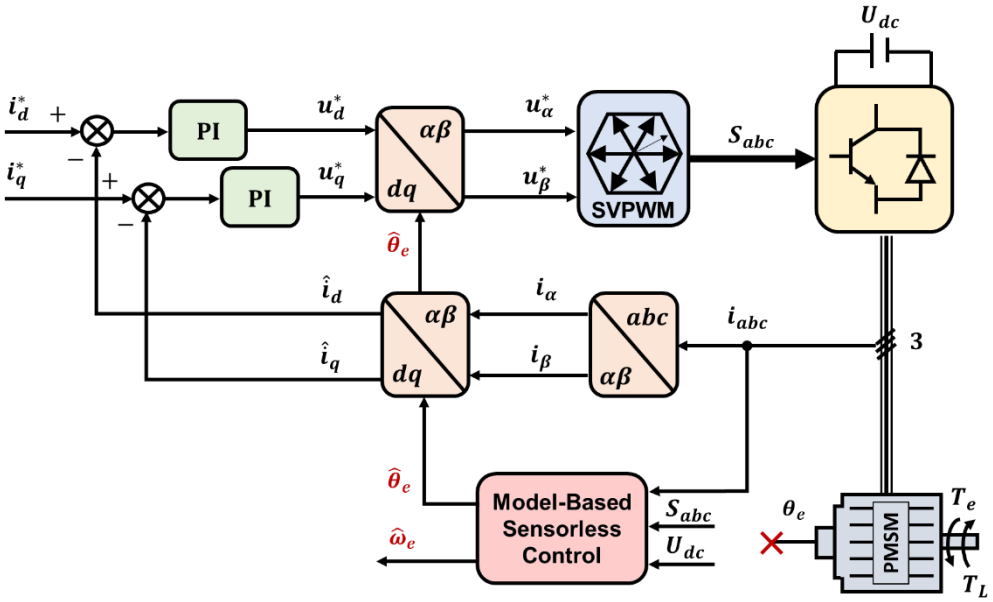


Figure 2.16 Block diagram of general model-based sensorless drive system.

As shown in Figure 2.17 [109], the estimated processes of the rotor position and speed which are based on the model-based methods could be divided into two parts: back EMF or flux estimation, and position/speed observer [110].

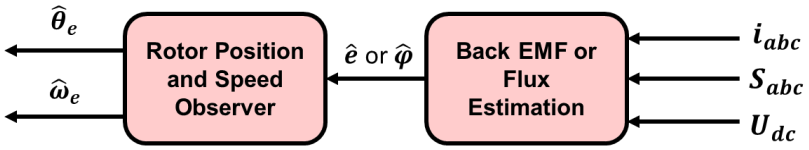


Figure 2.17 General block diagram of position/speed estimation procedure for model-based sensorless control.

According to the observed methods of the back EMF or the flux linkage information, the model-based methods [111-117] could be generally categorized as: model reference adaptive system (MRAS), extended Kalman filter (EKF), flux linkage observer, sliding mode observer (SMO), state observer, artificial intelligence-based estimation method, etc. Although model-based method was proposed and commercialized initially, it fails in the low-speed range due to the low signal-to-noise-ratio caused by modelling uncertainty, inverter nonlinearity, etc [106]. To improve the sensorless control performance at zero-to-low speed, the saliency tracking-based method is developed. As shown in Figure 2.18, it includes two main categories roughly: signal injection-based methods and fundamental pulsewidth modulation (PWM) excitation (FPE)-based methods [118-125].

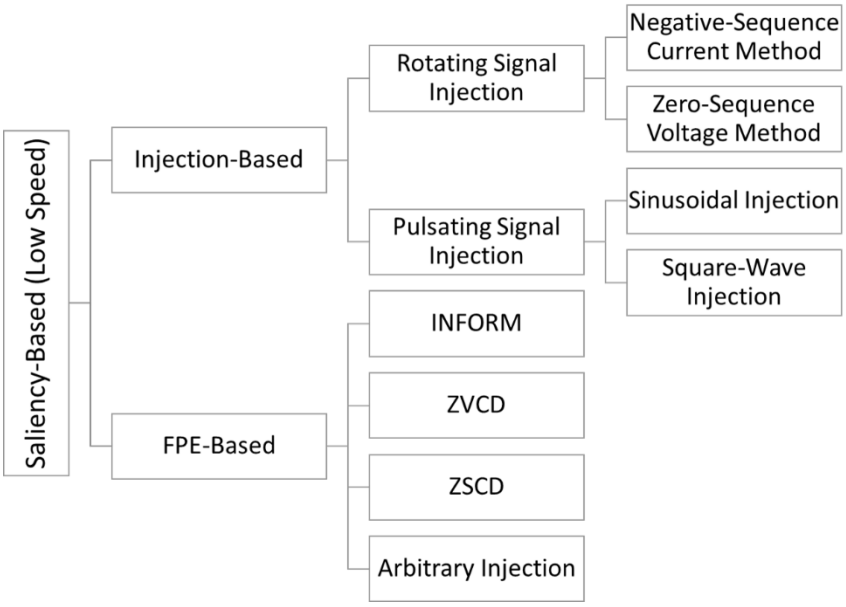


Figure 2.18 Categories for saliency-based position sensorless control.

2.3.2 Overview of Sensorless Study for Dual Three-Phase PMSM

Compared with the traditional three-phase PMSM, the DTP-PMSM has the characteristics of complex structure, high dimension, and strong coupling. Hence, there are relatively few researches of sensorless control of DTP-PMSM. The sensorless control of DTP-PMSM are achieved by adopting the traditional sensorless control method used in three-phase machine to multi-three-phase system. It is divided into two categories roughly: model-based and saliency-based method [126].

Model-based method is mainly used in wind power generation systems, ship propulsion, electric vehicles and other fields that require high-speed machines. [127] proposes to estimate the rotor position of a DTP-PMSM through back EMF with requirement of neither machine parameters information nor high-frequency test signal. In [128], DTP-PMSM is applied in direct-drive wind power generation systems, utilizing model reference adaptive algorithms to estimate generator speed, and obtaining the initial rotor

position by DC excitation of the machine stator. In [129-132], MRAS is applied for DTP-PMSMs in different application scenarios. Especially, in [129, 130], online identification of PMSM parameters is developed by the authors, to obtain accurate machine parameters in ship propulsion filed. In [132], sensorless control algorithm is applied to the aircraft electric S/G system. In [126, 133-135], SMO is applied to dual three-phase machines for electric vehicles. In [136], a sensorless control algorithm is used for DTP-PMSMs based on adaptive sliding mode observer and multiple proportional resonance controllers. Using the hyperbolic tangent function instead of the switching function to weaken chattering, a back-EMF adaptive observer is proposed to avoid the phase and amplitude attenuation problems caused by the use of low-pass filters. [136] studied the effect of back-EMF and current harmonics on the accuracy of position and speed estimation of single and double three-phase PMSM. Two model-based sensorless control strategies namely the flux linkage observer (FO) and the simplified extended Kalman filter (EKF) method , were used and compared. [137] studied the position sensorless control of high-speed DTP-PMSM applied to turboprop aircraft, green taxi motors and engine generators. In this Thesis, two different types of back-EMF based sensorless control methods using phase-locked loop (PLL) and Luenberger observer [138] are compared. In [93], an improved rotor position estimation strategy based on third harmonic back-EMF for single and DTP-PMSM under imbalanced situation is proposed.

Meanwhile, saliency-based methods for DTP-PMSM are developed. [139, 140] introduced a position estimation method for DTP-PMSM based on high-frequency voltage injection at zero-low speed. Compared with traditional three-phase machines, DTP-PMSMs could significantly reduce the torque and current fluctuations caused by

the high-frequency signal injection. This method is increasingly widely used in the fault starting of automotive applications. [92, 94] introduced a method of using zero-sequence carrier voltage to improve the estimation accuracy of rotor position. Due to the additional degrees of freedom of the DTP-PMSM, two high-frequency signals could be injected into two winding devices independently. Therefore, through the optimal phase shift angle between the injected signals, an improved rotating carrier signal injection method based on zero-sequence voltage sensorless position is proposed, which could effectively suppress the position estimation error caused by the 6^{th} harmonic. M. Barcaro *et al* also analyzed the torque component and sensorless position detection capability of DTP-PMSMs equipped with two fractional slot windings. Using permanent magnet torque and reluctance torque to characterize the salient polarity of the rotor, the comparison study of the sensorless rotor position tracking ability of the dual three-phase embedded PMSM under normal and faulty operating conditions was carried out. Even in the fault state, only one set of fractional slot windings has good salient polarity, and the rotor position could be well detected by the high-frequency signal injection method [141].

The DTP-PMSM based motoring/generating system in this study is quite novel and there is a gap in existing research about the sensorless control of such system. According to the review of sensorless control methods for DTP-PMSM system, MRAS is selected for this study since it is relatively robust and simple in implement.

2.4 ACHIEVE Project

The work presented in this Thesis is aligned with the 'Advanced meCHatronIcs dEVices for a novel turboprop Electric starter-generator and health monitoring system' (ACHIEVE) project, a part of the Clean Sky 2 programme [17, 142]. This project has conducted intensive trade-off studies of developing a next-generation highly-integrated motoring/generating system for turboprop applications [18].

The ACHIEVE system is designed to meet the following technical specifications:

1) Machine speed in motoring mode is up to 12.4 krpm, in generating mode is from 12.4 k to 14.2 krpm.
2) In generation mode, the system should provide up to 20 kW of electrical power to the 540 V DC bus.
3) The design of a motor/generator is required to integrate inside the propeller housing.
4) The space for the machine is restricted to 170 mm, 91 mm and 68 mm as outer diameter, inner diameter, and the axial length of the machine respectively, including end windings overhang and housing width on both sides.
5) No space for encoder installation, hence sensorless control is essential.
6) The electric power quality should meet MIL-STD-704F [25] requirements.
7) Good reliability and fault tolerance.

2.4.1 Electric Machine

The DTP-PMSM is designed to integrate inside the propeller housing as shown in Figure 1.5. The space for the machine is restricted to 170 mm, 91mm and 68 mm as outer diameter, inner diameter, and the axial length of the machine respectively, including end windings overhang and housing width on both sides.

The DTP-PMSM for this application is shown in Figure 2.19. It has a surface-mounted topology due to its high power density and the strict volume requirements restricted by the limited housing size. Non-oriented electrical steel (JFE_10JNEX900 [143]) is considered for stator laminations due to its excellent low iron loss profile and high magnetic flux density properties. For the permanent magnet material, Samarium Cobalt (Recoma 33E) was chosen from Arnold Magnetics due to its highest stability and magnetic output at elevated temperatures as compared to neodymium permanent magnets (NdFeB) [144]. The details of the machine design could be found in [145]. A number of design factors were considered, for instance the slot-pole combinations of the machine. Taking into account the power electronic converter losses and switching frequency limitations, an 18S/12P machine was selected for the application since it is the best trade-off between the space requirement, output power, fundamental frequency and cost. The maximum volumetric power density achieved in this project is 17.5kW/L. This value has been calculated by considering the whole envelope covered by the converter and not merely by summing the individual volumes of each component which would otherwise give a quite high power density value.



Figure 2.19 DTP-PMSM in ACHIEVE project.

The DTP-PMSM with asymmetric windings distribution in this research is specifically designed for fault-tolerant requirements and has rarely been studied so far [146-148]. It satisfies all the given requirements, giving output power of 20 kW at 14.2 krpm within the volume of 1407 cm^3. The parameters of the machine relevant in this research are listed in Table 2-6.

Table 2-6 Parameters of the DTP-PMSM in ACHIEVE project.

Parameters	Symbol	Value	Unit
Machine stator resistance	R_s	0.171	Ω
Machine stator inductance	L_d, L_q	530	μH
Permanent magnet flux linkage	φ_m	0.03	Wb
Pole pairs	p_p	6	/
Combined machine and engine inertia	J	0.5	$kgms^2$
Rated speed	ω_{rated}	12400	RPM
Output power at rated speed	P_{rated}	30	kW
Maximum speed	ω_{max}	14200	RPM
Output power at maximum speed	P_{max}	20	kW

2.4.2 Power Converter

The power converter in this study is designed for special aerospace applications in which the envelope is restricted by the aircraft manufacturer. This makes the converter design quite challenging because the geometry of the board is limited which restrains the components locations in terms of position and movement.

Two-level VSC topology is explained in Figure 2.20. The two sets of three-phase windings are named ABC and UVW, respectively. They are star-connected with isolated neutral points. For the first set of windings, V_a, V_b, V_c are the three-phase voltages. S_1 and S_4 are the power switches on one leg of the converter. The same two-level VSC topology is 'copied' for the UVW phases. In this way, the redundancy of the converter is increased to meet the reliability concerns from the aircraft manufacturers.

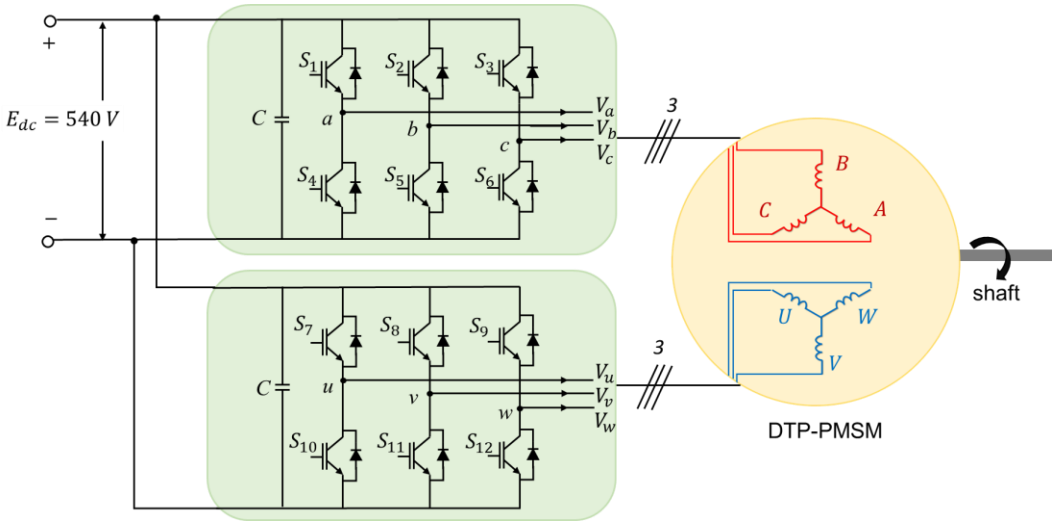


Figure 2.20 The SiC based two-level VSC converter in ACHIEVE project.

From the preliminary design of DTP-PMSM, the converter limits were defined as 32 A Maximum AC current, 540 V DC-link voltage, and 40 kHz switching frequency.

2.4.3 Thermal Management System

The cooling systems of the machine and converter are built together. The engine oil is used as coolant fluid with nominal temperature of 50℃. The oil is supplied from the auxiliary gearbox with fluid flow rate of 6 L/Min. It firstly passes through a gap between the stator conductors to take away the heat generated in the machine stator. This gap is created by reducing the slot fill factor. And then the oil flows through the heat sink of the power electronic boards to dissipate the heat generated by the power converter. This cooling system is validated to maintain the temperature well below the maximum permited value.

The ACHIEVE system offers merits in terms of high power density and efficiency, reduced mass and high velocity. Besides, fault tolerance of system is increased due to redundant converter topology.

2.5 Chapter Summary

This Chapter has discussed solutions offered by the MEA concept including approaches to electric power generation, distribution and consumption. The candidates of the electric machines for the motoring/generating have been presented and compared. The state-of-the-art in the multi-three-phase machine research and sensorless control techniques are reviewed. The ACHIEVE project is introduced in detail. As discussed, the ACHIEVE project targets a novel turboprop electric motor/generator system. This will be based on a surface-mounted DTP-PMSM due to its high power density and reliability. The asymmetric windings configuration and the redundant converter topology are designed to meet the fault tolerance requirement by the aircraft manufacturer. Overall, this Chapter has detailed the key targets of research in this Thesis and established the methodologies and topologies that will be used as a basis for the investigations in the following Chapters.

Chapter 3 Control Strategy of Dual Three-Phase Machine in ACHIEVE with Encoder

As aforementioned in Chapter 2, the electric machine applied in ACHIEVE motoring/generating system is different from the conventional dual three-phase machine. Hence, it is necessary to establish and analyse the mathematical modelling of the machine initially, and then, based on this model - to design a sensorless control system.

3.1 Mathematic Model for DTP-PMSM in ACHIEVE

The DTP-PMSM in this study has two star-connected three-phase stator windings with isolated neutral point. For conventional DTP-PMSM, windings of one three-phases set are always alternated along the stator circumference with equal interval [149, 150], but the machine discussed here is different as each set of windings is placed just on half of the stator. Since distributing multi-three-phases on opposite sides of the machine could lead to significant unbalanced magnetic forces on the rotor in the event of a fault with one three-phase set, most of the previous studies dealing with DTP machine are related to symmetrical windings distribution and there is a gap in the study of such asymmetrical winding machines [146-148].

3.1.1 Winding structure of ACHIEVE machine

Figure 3.1 shows the structure of stator and rotor that has 18 slots and 12 poles. The winding connection and permanent magnet direction are labelled in the figure, showing the machine is split into two parts and each three-phase winding occupies half of stator.

This kind of winding distribution is specifically designed for fault-tolerant machine, which should have the capability of electrical isolation, magnetic isolation and physical isolation [151]. Splitting stator into two parts can achieve minimum mutual inductance between the two three-phase windings. This design is for magnetic isolation, which exhibits lower short circuit current and higher average torque when one three-phase windings is short-circuit [152, 153].

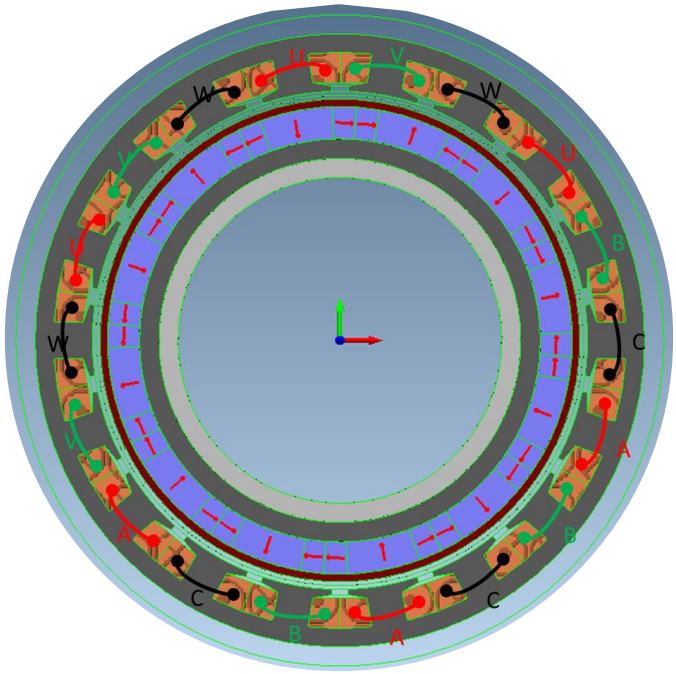


Figure 3.1 Structure of Dual Three Phase Machine.

The symmetrical three-phase windings should be alternated along the stator circumference with same interval. However, each three-phase winding is only displaced on half of the stator, which makes symmetrical displacement impossible. Inductance matrix for 6 windings is calculated from MagNet [154] and listed in Table 3-1.

Table 3-1. Machine inductance matrix.

Unit:μH	A	B	C	U	V	W
A	326	-81	-111	20	50	20
B	-81	326	-111	50	20	20
C	-111	-111	326	20	20	20
U	20	50	20	326	-81	-111
V	50	20	20	-81	326	-111
W	20	20	20	-111	-111	326

Equation (3.1) divides Table 3-1 to four parts, $\boldsymbol{L}$ represents the self and mutual inductance within each set of windings, and $\boldsymbol{M}$ represents the mutual inductance between two sets. Both of them are 3×3 matrixes.

$$L_s = \begin{bmatrix} \boldsymbol{L} & \boldsymbol{M} \\ \boldsymbol{M} & \boldsymbol{L} \end{bmatrix}_{6\times6} \tag{3.1}$$

For a traditional symmetrical dual three-phase machine, both $\boldsymbol{L}$ and $\boldsymbol{M}$ should have one value for diagonal line items and another value for non-diagonal items, but $\boldsymbol{L}$ and $\boldsymbol{M}$ for this design do not meet that standard since $M_{AB} \neq M_{AC}, M_{AV} \neq M_{AW}$ etc. The reason for that M_{AB} is smaller than M_{AC} is that windings A, C are always next to each other but A, B are discontinuous near the boundary of two three-phase windings. If the mutual inductances in one three-phase winding are not equal, it cannot be transferred to diagonal matrix by Clarke-Park transformation [155], which means traditional control methods such as decoupled vector control [156] and vector space decomposition (VSD) control [157] for DTP-PMSM is impossible.

The unusual winding structure makes it difficult to control the machine. In [158], the concept of multisegment machine is proposed and the control model of a two-segment machine is developed as shown in Figure 3.2. For the proposed two-segment machine, the stator windings of the machine are divided into two segments, with each segment fed by one set of VSI, each inverter is controlled independently to provide three-phase current for two segments, respectively. The total power and torque are shared by the two segments of the stator windings.

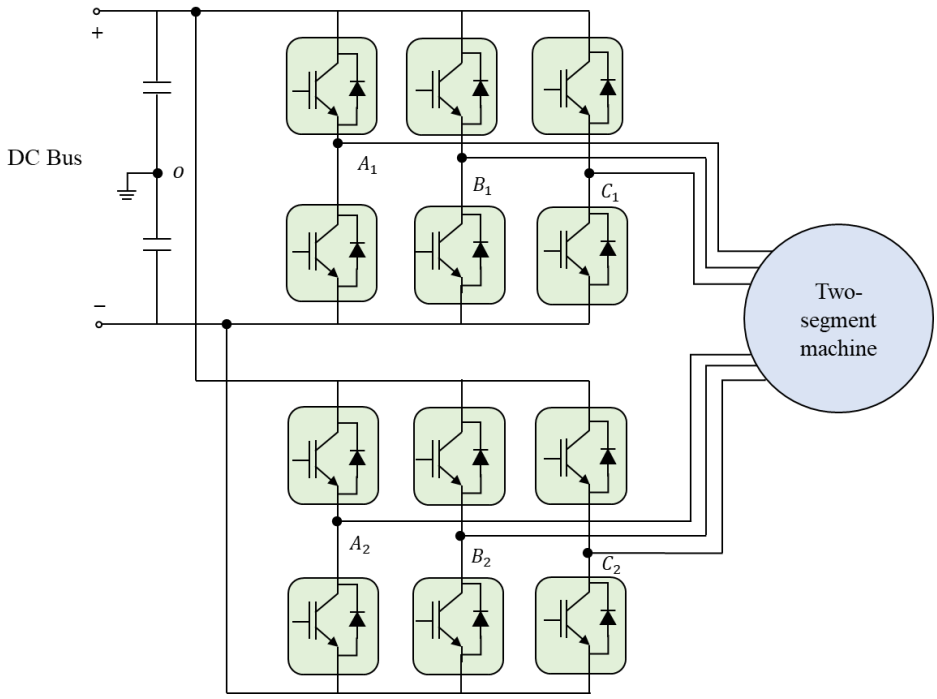
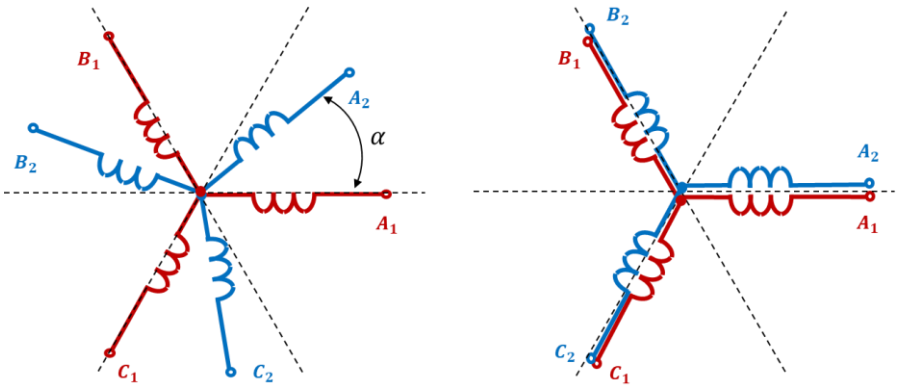


Figure 3.2 Block diagram of two-segment PMSM drive.

A typical two-segment machine is a dual three-phase machine [159], with two groups of windings. For the dual three-phase machine, the three-phase sets are shifted by the angle $\alpha(0 < \alpha < \pi/3)$ shown in Figure 3.3(a). Different from conventional dual three-phase machine, the electrical angle of two sets of windings in a two-segment machine has been kept the same, as shown in Figure 3.3(b).



(a) *(b)*

Figure 3.3 Angle between the two three-phase windings: (a)conventional dual three-phase machine with a displacement ($0 < \alpha < \pi/3$); (b)two-segment machine with no displacement ($\alpha = 0$).

According to the above introduction of the winding structure of the machine in this study, it appears quite similar to the two-segment machine. Actually, it is different from the traditional two-segment machine since the displacement between its two three-phase windings is π (rad). Hence, an equivalent mathematic model which utilizes the unique winding structure of such machine with the aim to design the controls is proposed in the following section.

3.1.2 Mathematic model in Six-Phase Stator Reference Frame for ACHIEVE Machine

Below, equations (3.2) and (3.3) are the voltage and flux linkage expression, and corresponding symbols are defined in (3.1), (3.4)-(3.9) in which all vectors are divided to two parts. The vectors with subscript '1' represent the variables of ABC windings, and the vectors with subscript '2' represent the variables of UVW windings.

$$u_{6s} = Ri_{6s} + \frac{d\psi_{6s}}{dt} \tag{3.2}$$

$$\psi_{6s} = L_{6s} i_{6s} + \psi_m \lambda_{6s} \tag{3.3}$$

$$u_{6s} = [u_a \; u_b \; u_c \; u_u \; u_v \; u_w]^T \tag{3.4}$$

$$i_{6s} = [i_a \; i_b \; i_c \; i_u \; i_v \; i_w]^T \tag{3.5}$$

$$\psi_{6s} = [\psi_a \; \psi_b \; \psi_c \; \psi_u \; \psi_v \; \psi_w]^T \tag{3.6}$$

$$\lambda_{6s} = \begin{bmatrix} \lambda_1 \\ \lambda_2 \end{bmatrix} \tag{3.7}$$

$$\lambda_1 = \left[cos\theta \quad cos\left(\theta - \frac{2\pi}{3}\right) \quad cos\left(\theta + \frac{2\pi}{3}\right) \right]^T \tag{3.8}$$

$$\lambda_2 = \left[\cos(\theta - \pi) \quad cos\left(\theta + \frac{\pi}{3}\right) \quad cos\left(\theta - \frac{\pi}{3}\right) \right]^T \tag{3.9}$$

Substituting (3.3) into (3.2), the voltage expression is governed by (3.10). Because the permanent magnets of the machine are surface mounted, the stator inductance will not change with rotor position and the derivation of $\boldsymbol{L_s}$ is zero.

$$u_{6s} = R i_{6s} + L_{6s} \frac{d i_{6s}}{dt} + \psi_m \frac{d \lambda_{6s}}{dt} \tag{3.10}$$

3.1.3 Mathematic Model in XYZ Reference Frame for ACHIEVE Machine

Due to the fact that $\boldsymbol{L_s}$ cannot be diagonalized using Clarke-Park transformation, an equivalent three phase symmetrical model (XYZ model in Figure 3.4) is proposed here to achieve the decoupled control. In fact, the dual three-phase machine can be transferred to a traditional three phase machine by inversely cascading U/V/W winding with A/B/C winding separately. If the labels 'U/V/W' in Figure 3.1 are replaced by 'A/B/C', A/B/C winding is alternated along the stator circumference with same interval just like the windings distribution of a traditional three phase machine.

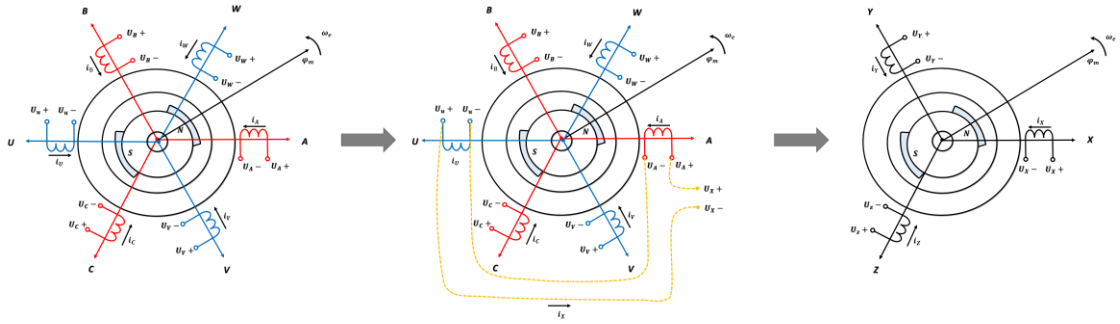


Figure 3.4 The assumption of equivalent conversion between XYZ model and Dual Three-phase model.

The relationship between dual three-phase current and XYZ phase current in Figure 3.4 is presented in (3.11).

$$\begin{bmatrix} i_x \\ i_Y \\ i_Z \end{bmatrix} = \frac{1}{2}\begin{bmatrix} i_a - i_u \\ i_b - i_v \\ i_c - i_w \end{bmatrix} \tag{3.11}$$

The relationship between dual three-phase voltage and XYZ phase voltage is presented in (3.12).

$$\begin{bmatrix} u_x \\ u_Y \\ u_Z \end{bmatrix} = \begin{bmatrix} u_a - u_u \\ u_b - u_v \\ u_c - u_w \end{bmatrix} \tag{3.12}$$

A detailed analysis of the winding structure for the proposed machine could be found in [19]. It is also proved that the dual three-phase current satisfies (3.14) if the dual three-phase voltage meets condition in (3.13).

$$\begin{bmatrix} u_a \\ u_b \\ u_c \end{bmatrix} = -\begin{bmatrix} u_u \\ u_v \\ u_w \end{bmatrix} \tag{3.13}$$

$$\begin{bmatrix} i_a \\ i_b \\ i_c \end{bmatrix} = -\begin{bmatrix} i_u \\ i_v \\ i_w \end{bmatrix} \tag{3.14}$$

Applying (3.13) and (3.14) to (3.12) and (3.11) respectively, gives

$$\begin{bmatrix} i_x \\ i_Y \\ i_Z \end{bmatrix} = \begin{bmatrix} i_a \\ i_b \\ i_c \end{bmatrix} = -\begin{bmatrix} i_u \\ i_v \\ i_w \end{bmatrix} \tag{3.15}$$

$$\begin{bmatrix} u_x \\ u_Y \\ u_Z \end{bmatrix} = 2\begin{bmatrix} u_a \\ u_b \\ u_c \end{bmatrix} = -2\begin{bmatrix} u_u \\ u_v \\ u_w \end{bmatrix} \tag{3.16}$$

Hence, the current and voltage of the XYZ model could be derived from dual three-phase model, and vice versa. The mutual inductance of XYZ model could also be calculated from the relationship between these two models.

Figure 3.5 is an example to show how to determine the mutual inductance M_{XY} from dual three-phase model. In fact, because windings A and U (same with B and V) are regarded as cascaded, M_{XY} should include mutual inductance not only between A&B, but also A&V, U&B and U&V.

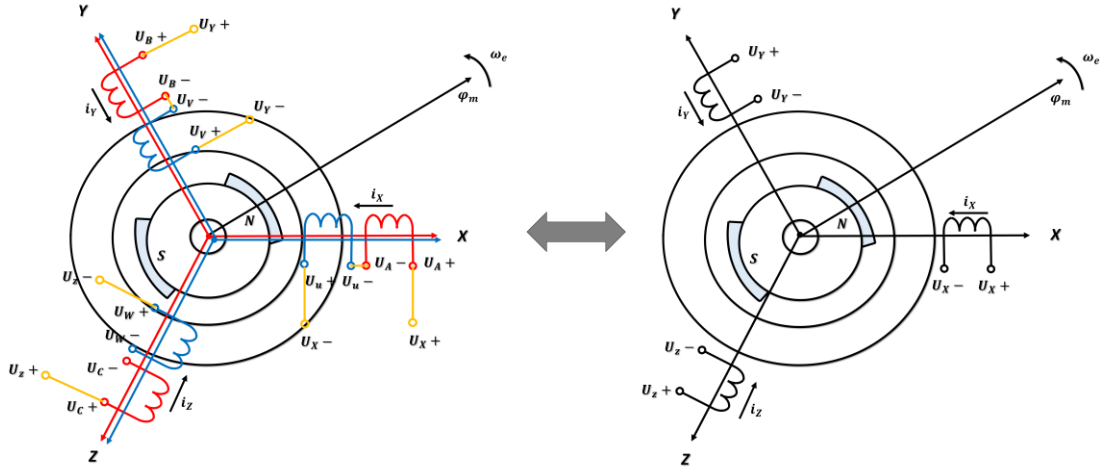


Figure 3.5 Derivation of mutual inductance between virtual X and Y phases.

Table 3-2 shows the inductance matrix of XYZ model which is derived from Table 3-1 by applying (3.17).

Table 3-2 Machine inductance matrix of XYZ model.

Unit: μH	X	Y	Z
X	612	-262	-262
Y	-262	612	-262
Z	-262	-262	612

It can be found that L_{XYZ} is a symmetrical matrix, just as the traditional three-phase surface mounted PMSM. Consequently, the asymmetric inductance matrix in Table 3-1 is transferred to a symmetric one.

$$L_{XYZ} = 2(L - M) \tag{3.17}$$

The voltage equation of XYZ model is shown in (3.18), in which λ_{sin} is defined as (3.19). The coefficient '2' before R and φ_m is due to the cascade of windings. Sufficient work has been done to prove the equivalence between the XYZ model and dual three-phase model.

$$\begin{bmatrix} u_x \\ u_Y \\ u_Z \end{bmatrix} = 2R \begin{bmatrix} i_x \\ i_Y \\ i_Z \end{bmatrix} + L_{XYZ} \frac{d}{dt} \begin{bmatrix} i_x \\ i_Y \\ i_Z \end{bmatrix} - \omega_e 2\phi_m \lambda_{sin} \tag{3.18}$$

$$\lambda_{sin} = [sin\theta \quad \sin(\theta - \frac{2\pi}{3}) \quad \sin(\theta + \frac{2\pi}{3})]^T \tag{3.19}$$

The relationship between different reference frames when it comes to the proposed machine is depicted in Figure 3.6. Appling Clarke-Park transformation in (*A.1*) to (3.18), the *dq* frame voltage is obtained as (3.20).

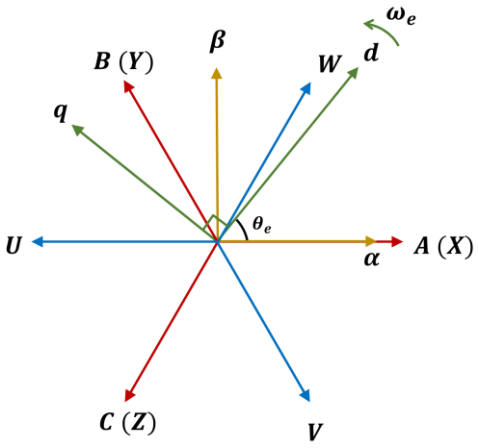


Figure 3.6 Reference frames diagram.

$$\begin{bmatrix} u_d \\ u_q \end{bmatrix} = 2R \begin{bmatrix} i_d \\ i_q \end{bmatrix} + \begin{bmatrix} L_d & 0 \\ 0 & L_q \end{bmatrix} \frac{d}{dt} \begin{bmatrix} i_d \\ i_q \end{bmatrix} + \omega_e \begin{bmatrix} -L_q i_q \\ L_d i_d + 2\varphi_m \end{bmatrix} \tag{3.20}$$

The electromagnetic torque generated by one set of three-phase winding can be derived as (3.21) [160].

$$T_{3ph} = 1.5p(2\varphi_m i_q + i_d i_q (L_d - L_q)) \tag{3.21}$$

where $p = 6$ is pole pair numbers, $L_d = L_q = 874\ \mu H$. According to the law of conversation of energy, the total machine torque T_e is double of T_{3ph}:

$$T_e = 2T_{3ph} = k_t i_q \tag{3.22}$$

$$k_t = 6p\varphi_m \tag{3.23}$$

The machine speed is controlled by the equation [161]:

$$J \frac{d\omega_m}{dt} = T_e - T_L \tag{3.24}$$

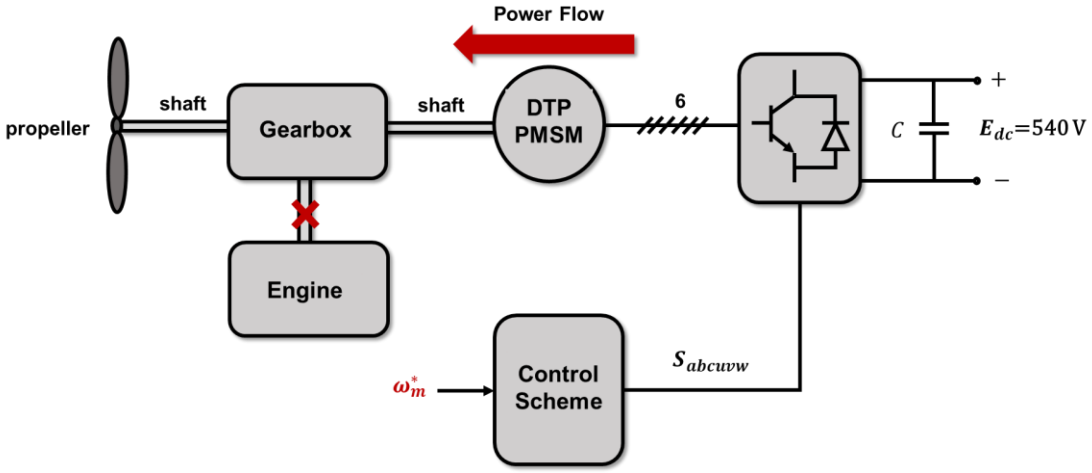
where T_e is electromagnetic torque, T_L is load torque, J is a total inertia and ω_m is a mechanical speed.

$$\omega_m = \frac{\omega_e}{p} \tag{3.25}$$

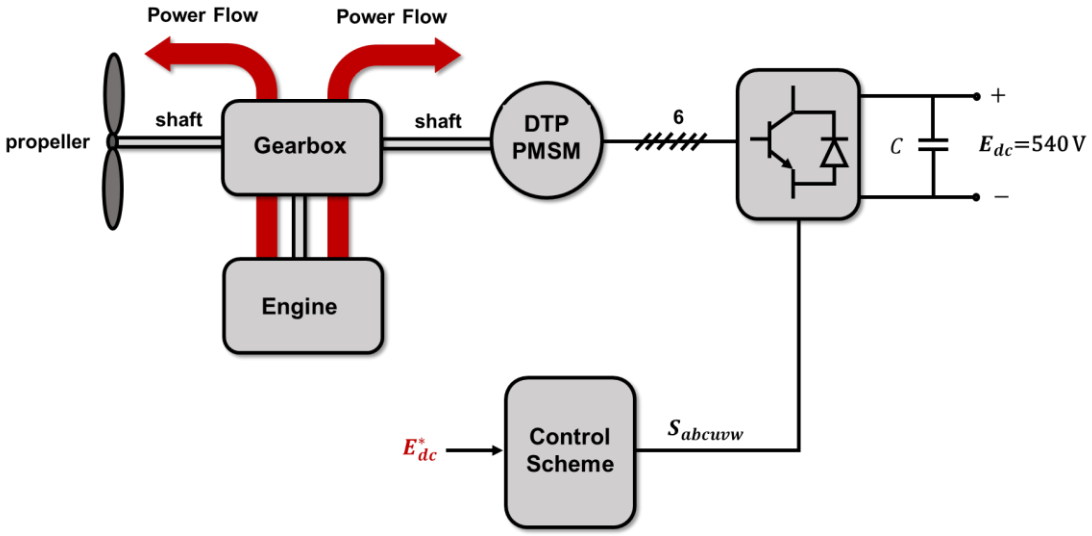
3.2 Motoring/Generating Control Scheme for DTP-PMSM in ACHIEVE

The general control aspects of DTP-PMSM in ACHIEVE could be determined based on motoring/generating operation control strategy of conventional three-phase machine. In motoring mode, electrical power flows from main bus to DTP-PMSM, and machine speed is controlled to drive the propeller. In generating mode, the speed of the engine is controlled externally, and control of the DC link bus power is the primary objective. Both motoring and generating modes are separate and there is no need to control them both at the same time. In generating mode, the control of the DC link voltage is fixed at 540V DC to ensure the uninterrupted operation of the electrical loads. Moreover, in aerospace and automotive sectors applications, flux weakening (FW) is a common control method that enables electric machines to achieve a wider speed range above their rated value. Yet, it is not applied in this Thesis because the machine in ACHIEVE is sufficient to meet the speed requirements within nominal operation.

The general control scheme for the motoring/generating system of ACHIEVE is presented in Figure 3.7. The ACHIEVE machine is interfaced with a controllable power converter that is connected to an electrical power source. The six-phase switching signals S_{abcuvw} derived from the drive controller are sent to the power converter. All variables with the notation denote the reference value of controlled variable.



(a)



(b)

Figure 3.7 General control scheme of motoring/generating system (a)motoring mode (b)generating mode.

Most widely used control strategies of three-phase PMSM system is Direct Torque Control (DTC) and Field Oriented Control (FOC). In this Thesis, both of them are briefly explained and one shall be selected for this motoring/generating system.

3.2.1 Direct Torque Control

The general DTC configuration is described in Figure 3.8. In DTC, the torque T_e and stator flux ψ_s are estimated from the measured voltage E_{dc} and current i_{abc}. These estimated variables are compared to their reference values and are regulated as fast as possible if the error between them exceeds a tolerance band. $H_\psi$and H_T are the control output signals for each control variable. The control signals are then interpreted within a voltage vector look-up table (LUT) to output appropriate switching states for the converter [162].

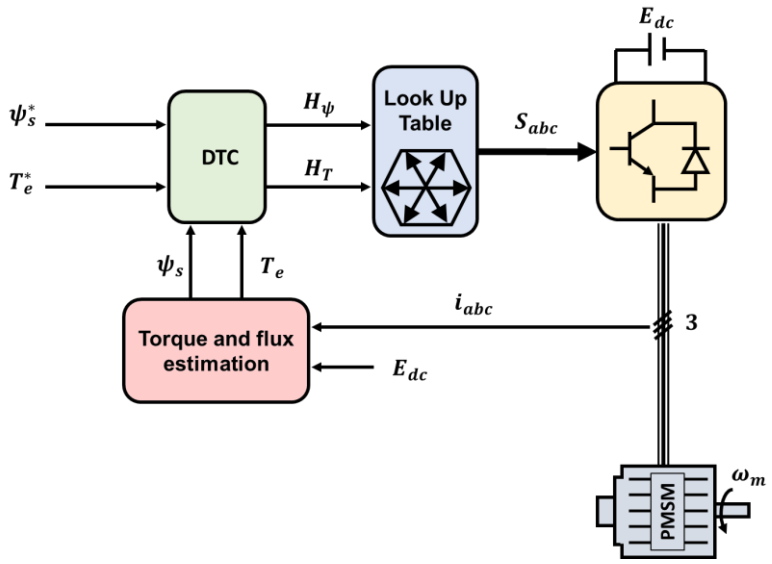


Figure 3.8 Block diagram of DTC system for PMSM.

The advantage of using DTC is that it has quite fast dynamic response and does not require PI regulators, coordinate transformations, or pulse width modulation (PWM) signals for control operation [163, 164]. Yet, due to the use of hysteresis control within the core structure [165, 166], there can be significant current ripple in the outputs from the power converter. The ripples can affect the torque performance of the machine,

especially during motor mode, and hence provide less smooth engine acceleration. The power quality of the main bus is also damaged due to the current ripple. Hence, this type of control is not considered for this motoring/generating system.

3.2.2 Field Oriented Control

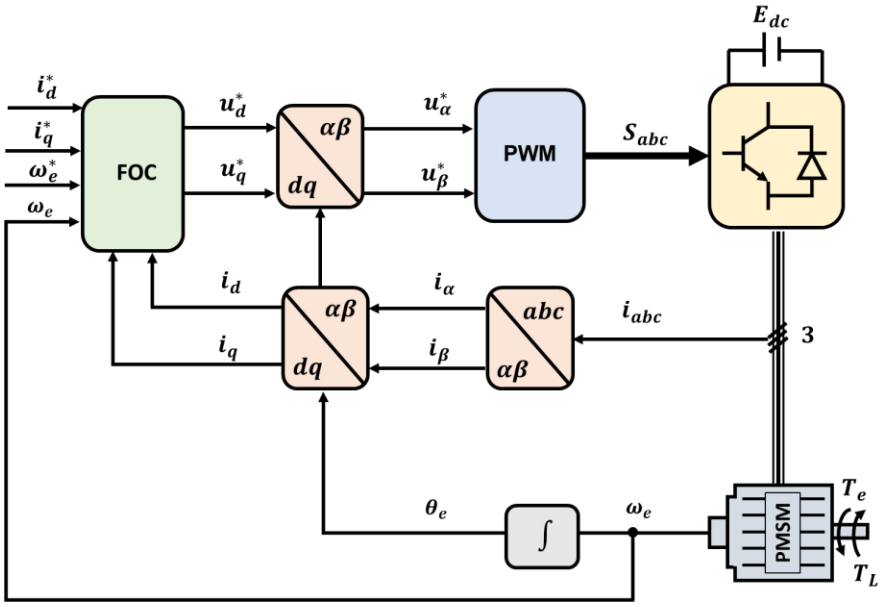


Figure 3.9 Block diagram of FOC system for PMSM .

The general control structure of FOC is presented in Figure 3.9. FOC is based on utilisation of a rotating *dq* reference frame, which is aligned with the machine excitation flux [162, 167]. The rotating *dq* reference frame is the result of direct quadrature transformation that attempts to simplify time varying AC variables into DC type constant steady state values. According to the Lorentz force law [168], the machine torque T_e is directly proportional to the current component orthogonal to the excitation flux, i.e., i_q. PI regulators are usually utilised to control *dq* currents i_d, i_q and output corresponding *dq* voltage reference u_d^*, u_q^*. The voltage references are converted back into the three-phase frame and are passed through a PWM scheme which synthesises

switching signals for the converter. An outer control loop is added to regulate speed or torque and outputs the necessary current references i_d^*, i_q^*. for the *dq* currents.

FOC may be more complex than DTC by having a cascaded loop structure, but the controlled current quality is better compared to DTC with properly tuned PI controllers [162]. Moreover, it is more convenient to control the *dq* currents directly rather than going through an estimation process to determine the stator flux. The cascaded loop of FOC enables the secondary control to be conveniently changed according to motoring/generating operational mode; hence FOC is chosen as the main control scheme. The block diagram of FOC system for ACHIEVE in motoring is presented in Figure 3.10.

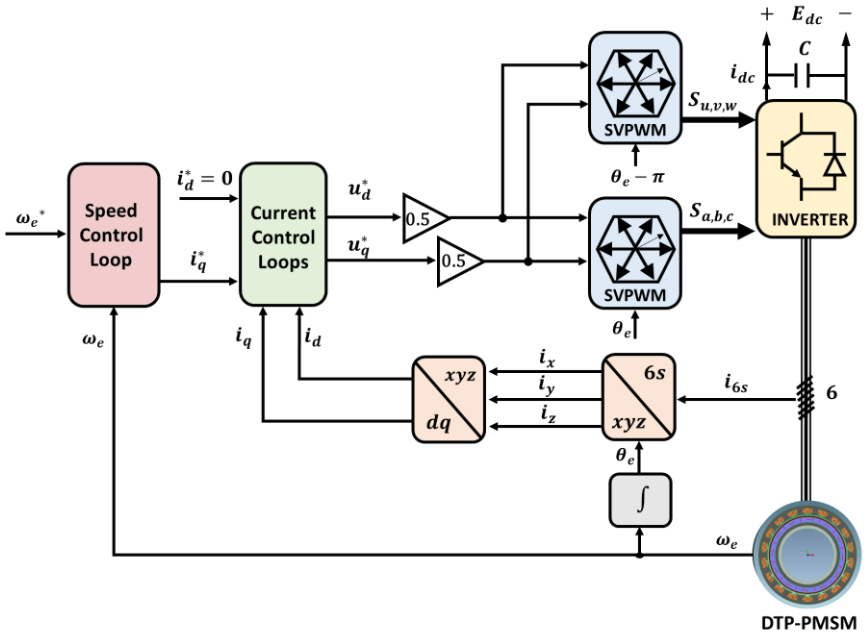


Figure 3.10 Block diagram of FOC system for ACHIEVE in motoring mode.

In Figure 3.10, the reference frame transformation between six-phase and 'XYZ' three-phase has been introduced in (3.11) and the transformation between 'XYZ' three-phase and *dq* frame is achieved by Clarke transformation presented in (*A.1*).

The cascaded control is applied including the outer speed loop and the inner current loop to realize the electromechanical energy conversion of the machine drive system. The detail of the speed control loop and current control loop is depicted in Figure 3.11 and Figure 3.12, respectively.

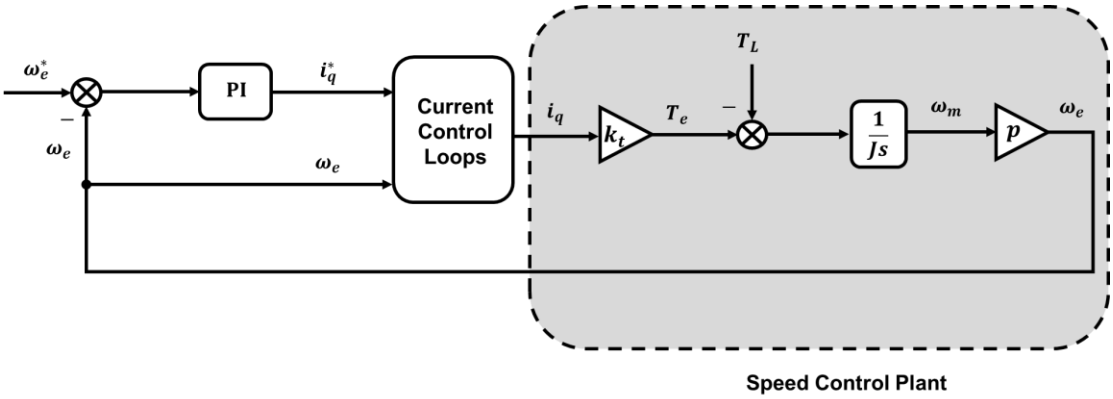


Figure 3.11 Block diagram of speed control loop.

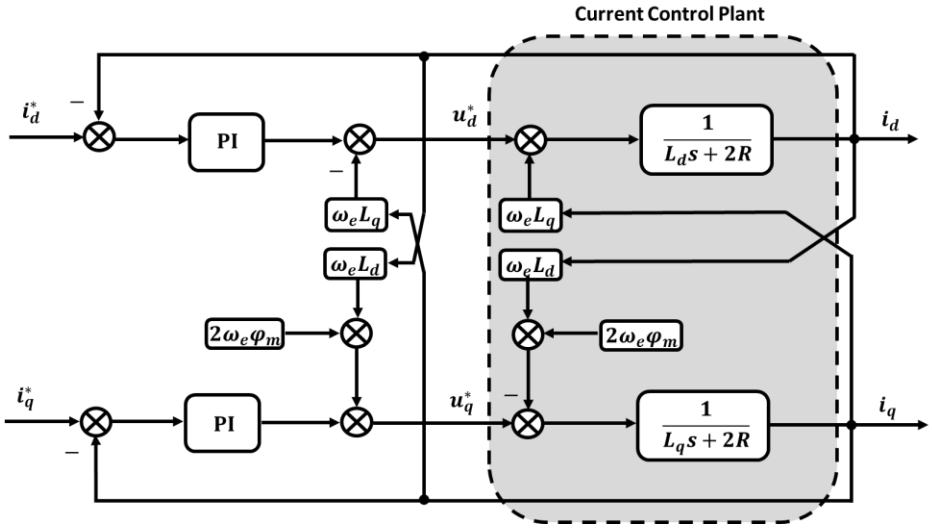


Figure 3.12 Block diagram of current control loop.

The PI type regulator of both control loop could be designed based on the control plant and the specific design process follows the method in [162] which will not be covered here. The coefficient k_t in (3.9) is illustrated in (3.23). It should be noted that the value of u_d^* and u_q^* is halved when utilized in SVPWM. The reason could be explained by (3.16) which presents the relationship between six phase model voltage and XYZ model voltage. Moreover, the torque generated by XYZ model is two times that of a three-phase set in (3.22). Therefore, halving operation is required in terms of the energy conservation.

3.2.3 DC Link voltage Control

In generating mode, the electrical machine functions as a generator, the output voltage has to be controlled to maintain appropriate voltage levels for the electrical loads [169]. In addition to that, the voltage transient has to reach steady state within a limited amount of time while not exceeding the voltage limits as defined in MIL-STD-704F [25].

The block diagram of FOC system for ACHIEVE in generating mode is presented in Figure 3.13. E_{dc} is controlled on the outer loop during generator mode to regulate changes caused by load changes. Compared with system in motoring mode that utilises separate controllers for current and speed control, the speed controller is replaced with a DC link voltage controller for system in generating mode.

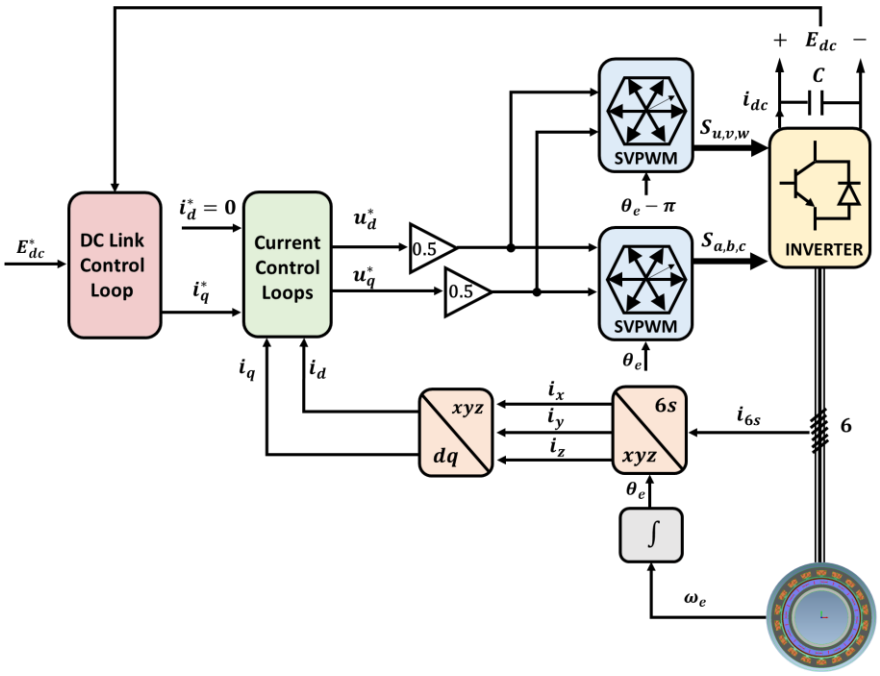


Figure 3.13 Block diagram of FOC system for ACHIEVE in generating mode.

The average model equation of a power converter can be represented by a complex power equation in the *dq* frame [170]:

$$E_{dc} i_{dc} = -1.5(u_d i_d + u_q i_q) \tag{3.26}$$

The negative sign denotes the direction of i_{dc} when it is measured. Positive i_{dc} is defined as power supplied to the DC link bus while negative is towards the machine side. The DC link bus equation can be equated as:

$$C \frac{dE_{dc}}{dt} = i_{dc} - i_L \tag{3.27}$$

where i_L is the general notation for electrical loads connected to the DC link bus.

The block diagram of DC link voltage control is depicted in Figure 3.14.

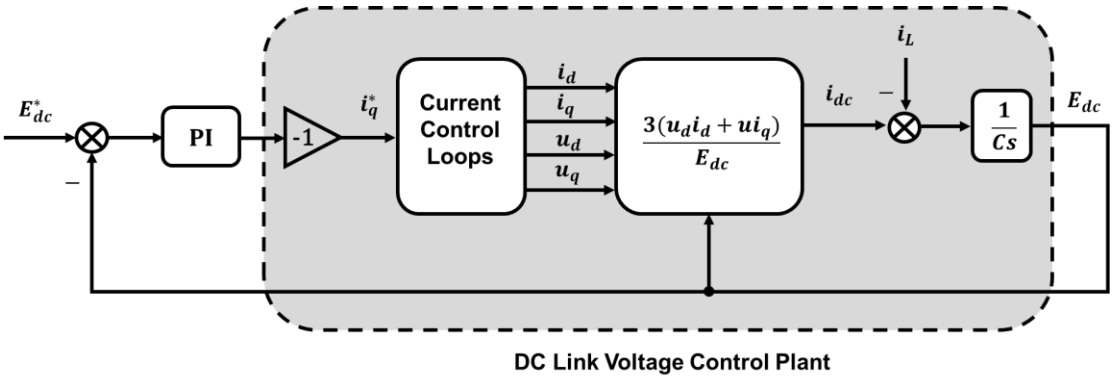


Figure 3.14 Block diagram of DC link voltage control.

3.3 PWM Strategy for DTP-PMSM in ACHIEVE

In ACHIEVE, the two sets of independent stator windings can be regarded as two independent three-phase machines. In Figure 3.10 and Figure 3.13, the voltage reference vectors u_α^* , u_β^* are obtained from current regulator and coordinate transformation, and PWM modulation can be carried out according to the position of the two vectors. This modulation strategy can learn from the traditional three-phase machine SVPWM, which is a relatively mature modulation scheme. The two sets of stator windings can be regarded as mutually independent in the control process, so the *q*-axis currents of each three-phase can be separately controlled. However, to keep the output power of the two sets of windings close, the *q*-axis currents of each three-phase are regarded to be identical, which simplifies the current control loop and also maximizes the efficiency of the system.

In modern motor drive system, pulse width modulation (PWM) is usually used to control the output voltage of inverter, i.e., a series of pulse width is modulated to obtain the required voltage waveform. Compared with square wave inverter, PWM control can effectively reduce the harmonic of input voltage, improve current waveform and reduce

torque ripple. The conventional PWM algorithms of traditional three-phase machines include carrier-based pulse width modulation technology (CPWM) and space vector pulse width modulation technology (SVPWM). Similarly, the PWM control of DTP-PMSM is also divided into these two types. Specifically, CPWM [171] can be divided into PWM with zero-sequence voltage injection [172] and sinusoidal PWM without zero-sequence voltage injection (SPWM) [173]. Compared with SPWM, SVPWM [174] has been widely used in practical system because of its higher voltage utilization and easy digital implementation.

For the $3 \times n$ multi-phase machine with isolated neutral points, each three-phase winding can be modulated by independent three-phase SVPWM [175]. As shown in Figure 3.15, the machine in this study is driven by two drive units to generate the required torque. Each group of windings is excited independently with symmetrical three-phase voltage by VSI. Two conventional three-phase SVPWM modulators are used for modulation.

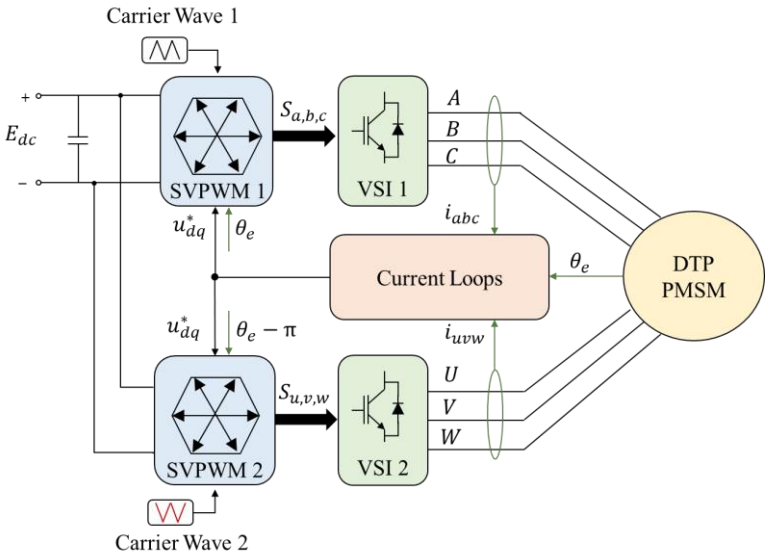


Figure 3.15 Block diagram of machine drive architecture.

It should be noted that for the major 2nd-order harmonics torque ripple cancellation, carrier-wave phase has been shifted with 0.5 T_s, as shown in Figure 3.16. The switching frequency is 40 kHz, thus the period T_s is 25 μs. The switching signal can be obtained through the comparison between the duty cycle and the carrier. Then these phase-shifted switching signals are given to two inverters to drive the motor.

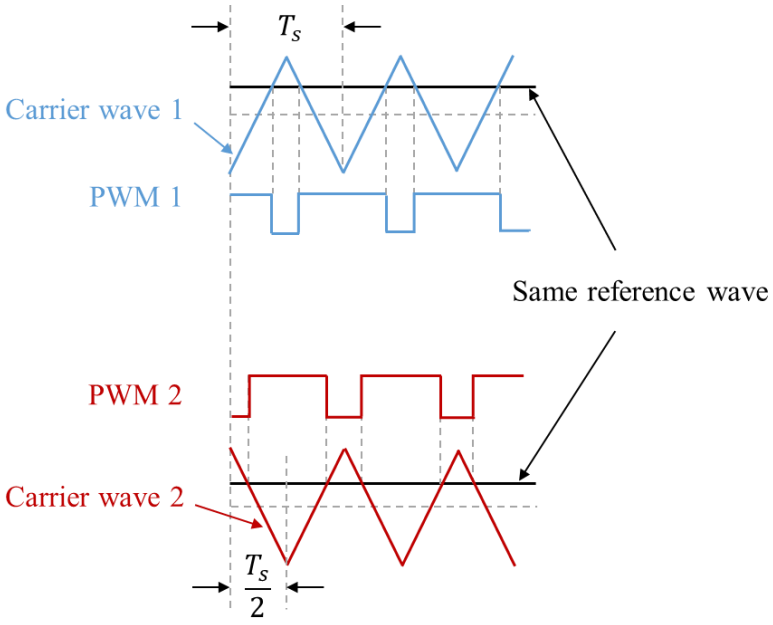


Figure 3.16 Carrier wave phase shift with 0.5 T_s.

3.4 Simulation Results

The control of the DTP-PMSM was initially investigated through simulation by PLEXIM®/PLECS® [176]. The simulation models are provided in Appendix B. Experimental support could be found in Chapter 7. The block diagram of the drive system in motoring mode is presented in Figure 3.17.

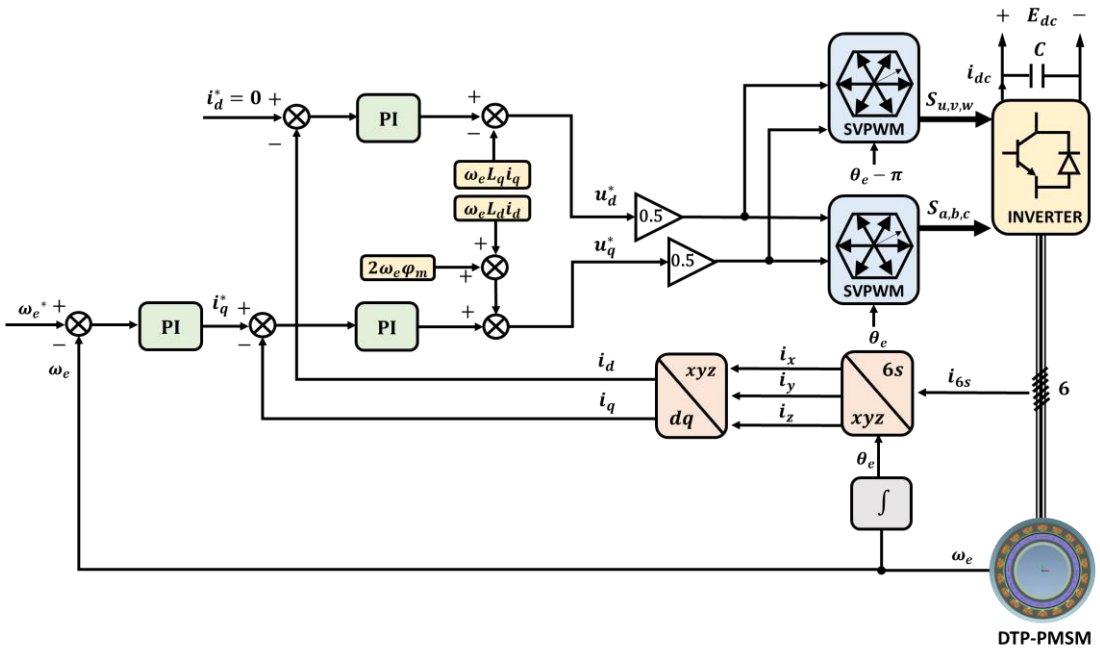


Figure 3.17 PLECS simulation system of ACHIEVE in motoring mode.

There are two scenarios that are discussed. The first one is shown in Figure 3.18. In this scenario, step changes of load torque (±20% of rated value) is applied to the DTP-PMSM running at 12.4 krpm. Current and speed show fast dynamic response within 0.15 s in the presence of load variation.

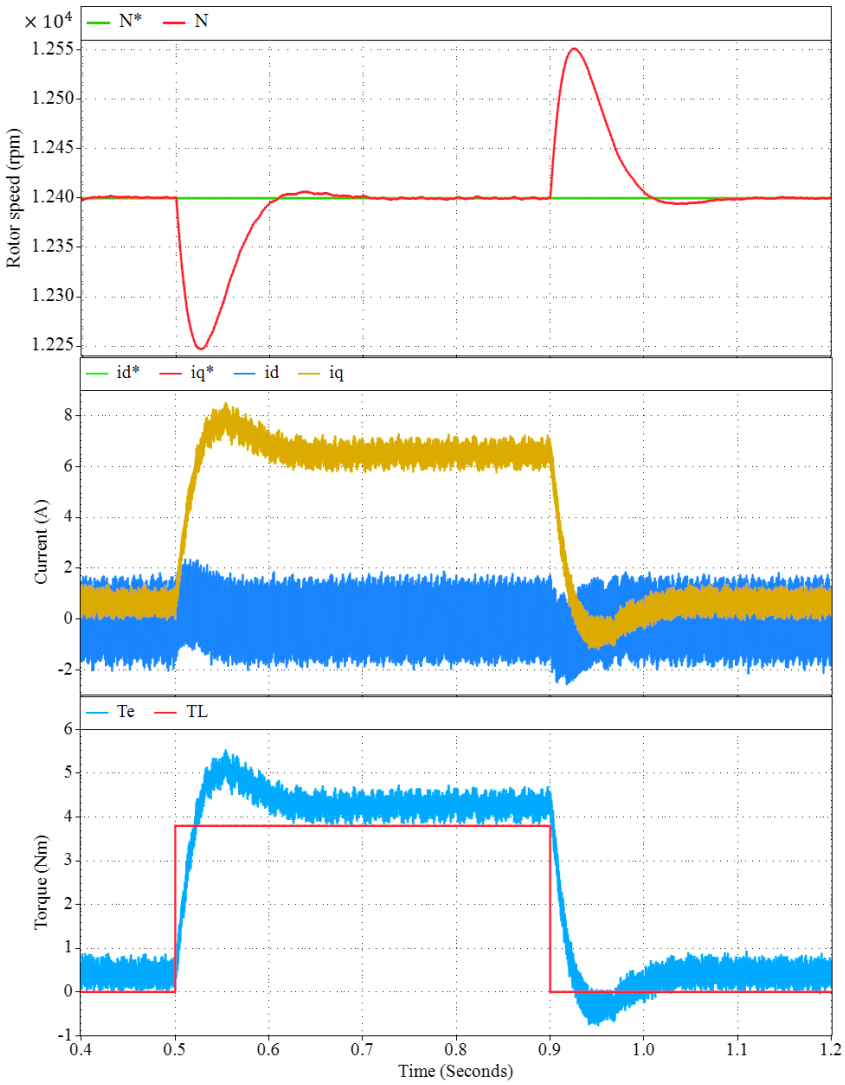


Figure 3.18 Simulation results in motoring mode under various load.

The simulation results of the second scenario is shown in Figure 3.19. The machine runs at 10 krpm initially with no load. Then a step increase of speed reference is applied and the machine accelerates to 12.4 krpm. After an interval of 0.4 s, a reverse step change is applied to the speed reference. It could be seen that the *dq* axis currents and torque are properly controlled and have good dynamic response to the speed variation.

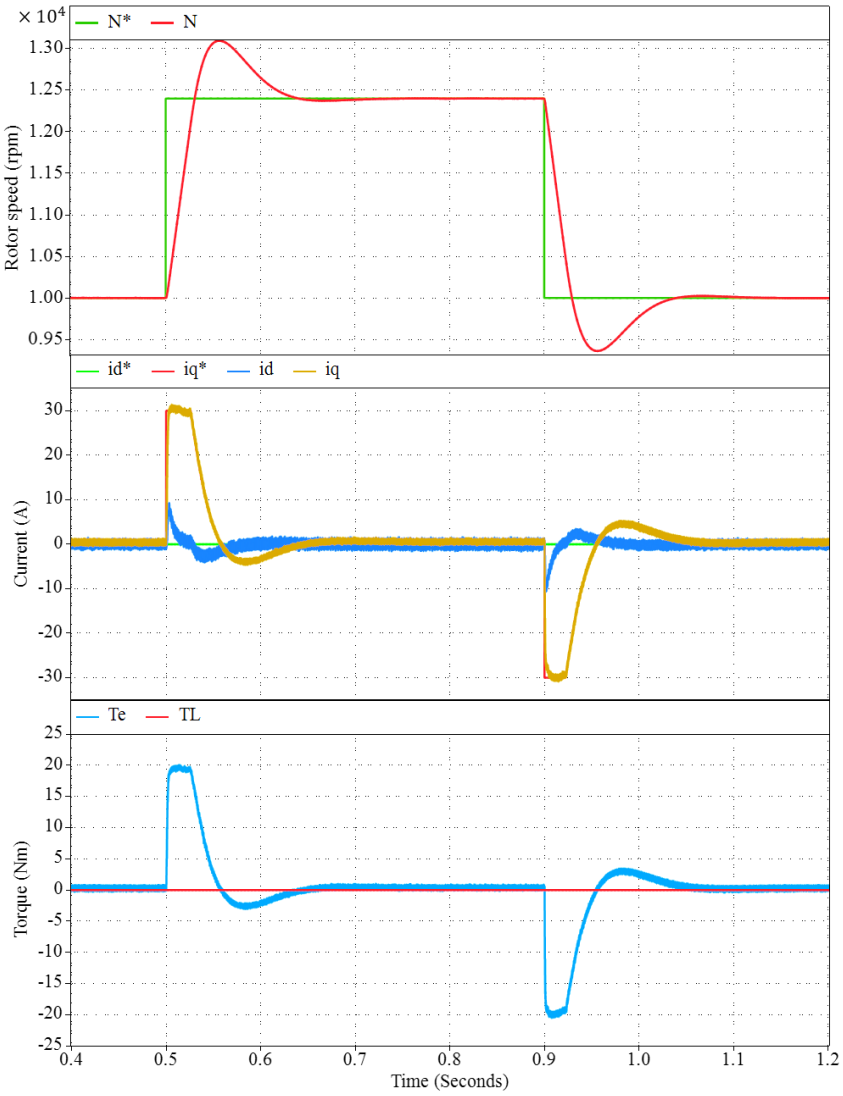


Figure 3.19 Simulation results in motoring mode under various speed.

The block diagram of the drive system in generating mode is presented in Figure 3.20.

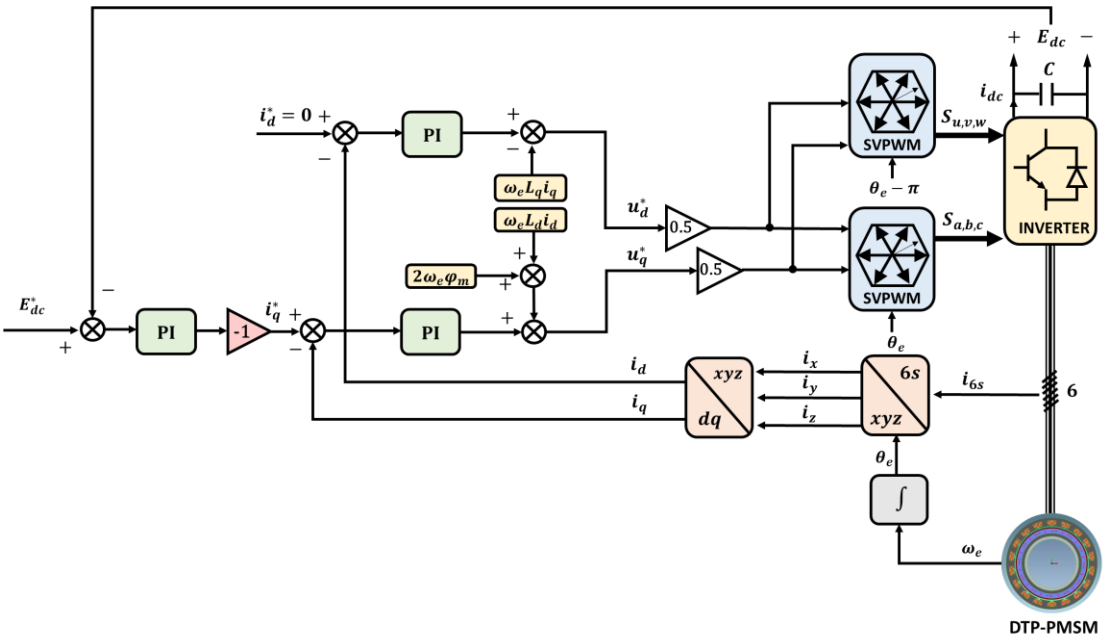


Figure 3.20 PLECS simulation system of ACHIEVE in generating mode.

Figure 3.21 shows a time domain simulation of the motoring/generating power system with the DC link voltage controller.

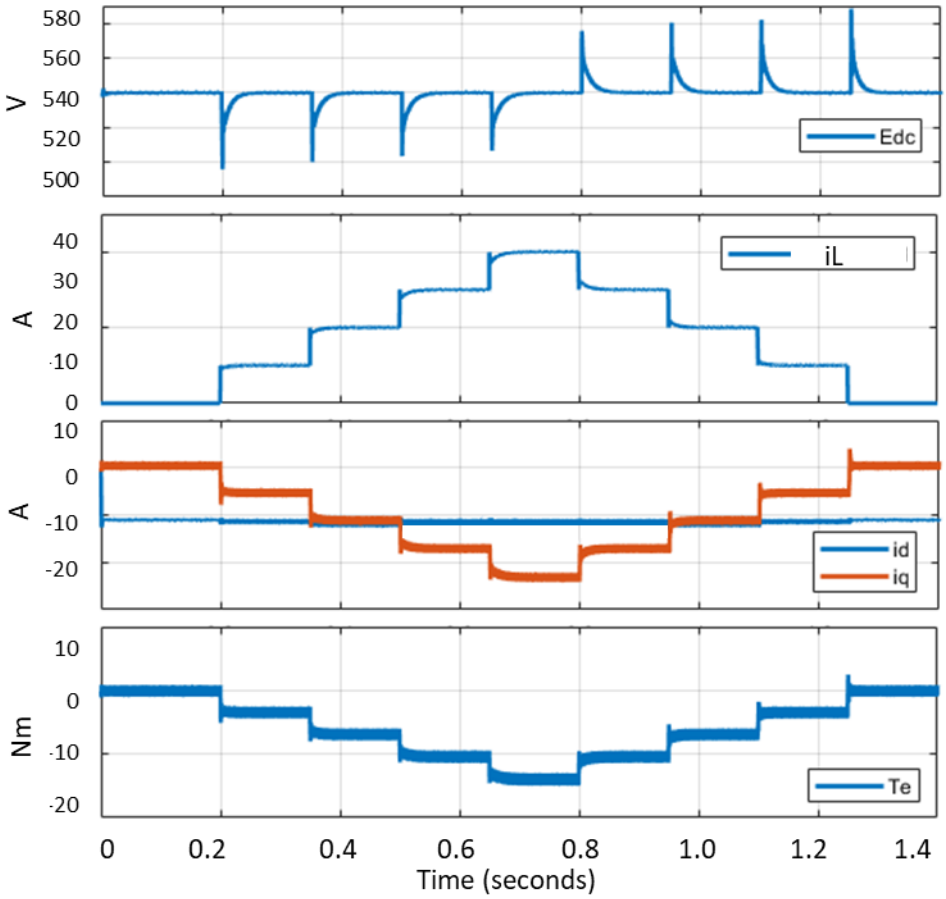


Figure 3.21 Responses of key variables to various electrical loads i_L.

During the simulation the machine speed is set at 14.2 krpm and initially the power system is not subjected to any load. At 0.2 s intervals, i_L was increased to 10 A, 20 A, 30 A and 40 A respectively and then removed in reverse order. It can be seen that E_{dc} reduces to 495 V, 500 V, 505 V and 510 V for each step increase of load respectively. Negative i_q is observed due to the power flow direction being towards the DC bus. The DC link voltage controller is tested with a full step load of 30A as this is the worst case scenario. This test is carried out in order to determine if the E_{dc} response complies with MIL-STD-704F.

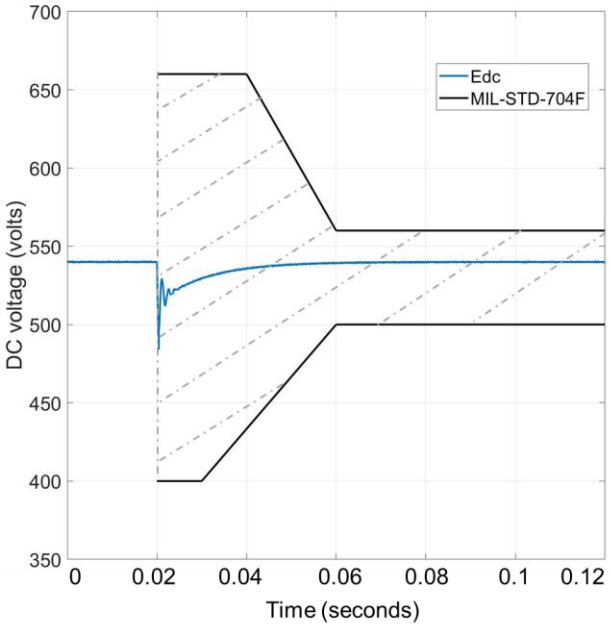


Figure 3.22 E_{dc} to a step of $i_L = 10$ A for comparison with 540 VDC voltage transient limit from MIL-STD-704F.

It can be seen from Figure 3.22 that E_{dc} initially drops from 540 V to 485 V when the load step is applied at t = 0.02 s. It is obvious from Figure 3.22 that DC link voltage control response to a full load step is well within the limits specified by MIL-STD-704F. This shows that the designed controllers are able to work properly even at the highest operating speed and load for this generating system.

3.5 Chapter Summary

This Chapter details the control strategy that is specially designed for the ACHIEVE motoring/generating system. The main finding of this chapter can be summarised as follows:

- The structure of the machine in ACHIEVE is introduced. It is shown that due to the asymmetric winding structure, the mathematical model of machine could

not be directly transformed from six-phase stator reference to rotating *dq* frame. Hence, the conventional space vector control becomes is not directly applicable. To address this issue, the XYZ model is proposed which not only simplifies the mathematical model but also allows for the design and implementation of vector control.

- Based on the motoring/generating operation, the general control requirements have been outlined in this Chapter i.e., speed has to be controlled in motoring mode while DC link power is controlled in generating mode. Different control strategies such as FOC, DC link voltage control have been introduced and applied to the motoring/generating system.
- The PWM control strategy for ACHIEVE is proposed after comparison among various control schemes. The DTP-PMSM in ACHIEVE is designed to be driven by two drive units. Each group of windings is excited independently with symmetrical three-phase voltage by VSI. Two conventional three-phase SVPWM modulators are used for modulation.
- The effectiveness of the control system with encoder in motoring and generating mode is verified through simulation by PLECS. Different scenarios have been discussed to observe the performance of the system under speed variation, load torque variation and electric load variation. This lays the foundation of the sensorless strategy for PMSM in the following chapters.

Chapter 4 The State-of-the-Art of Sensorless Control Strategies for PMSM

As shown in Chapter 3, according to the principle of field oriented control, the position of the orientation field is required to facilitate the control algorithm. It can be measured by dedicated sensors or derived from the machine model and the rotor speed/position. All these methods require additional sensors mounted directly on the machine. This is highly undesirable since these sensors may also subject to quite harsh working conditions where the machine sits. Besides, reliability is decreased further a the additional wiring of these sensors is required which decreases further the reliability since cables and connectors are additional potential fault sources. Therefore, it is highly desirable to estimate the machine rotor position without mechanical sensors. As shown in Figure 4.1, there has been a tremendous effort to develop the sensorless control techniques for a wide speed range from low to high speeds in the last few decades.

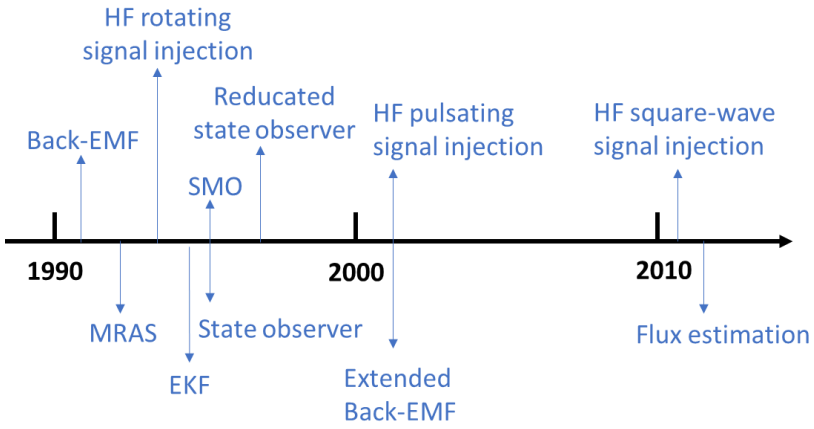


Figure 4.1 Development for position sensorless drives.

With the observability analysis performed [177], the full speed sensorless control strategy has been developed in academia and industry. As shown in Figure 4.2, there are two main categories of sensorless control schemes roughly: model-based sensorless control applied at high-speed range and saliency-based sensorless control applied in low-speed range [178].

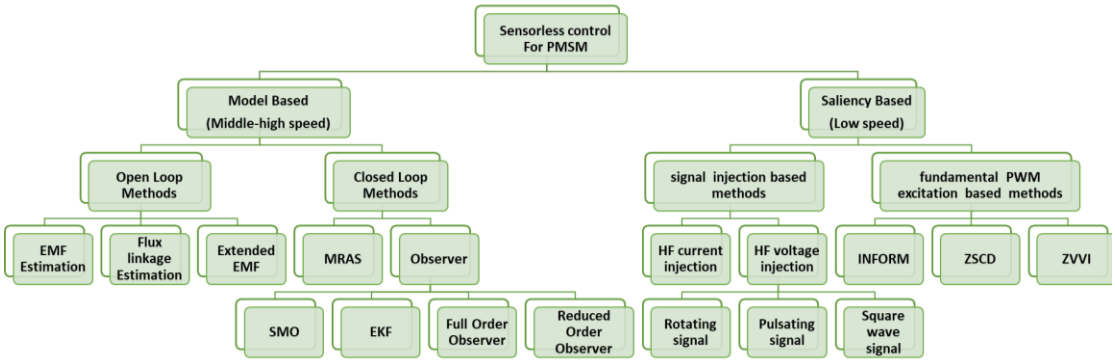


Figure 4.2 Categories for position sensorless drives.

The model based sensorless control could be implemented either in the stationary $\alpha\beta$ frame or in the synchronous dq frame. Figure 4.3 shows the space-vector diagram of PMSM, which indicates the relations of coordinates reference frame used in the mentioned paper.

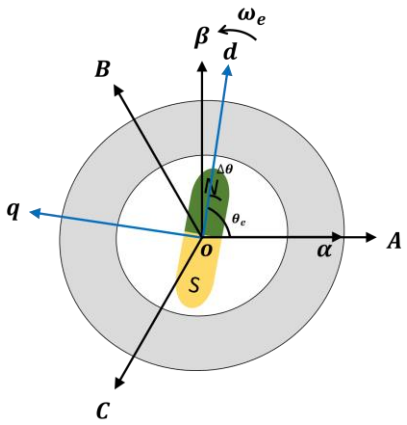


Figure 4.3 Coordinates reference frame of PMSM.

In (4.1), $x_{a,b,c}$ represent the three phase frames, $x_{d,q}$ represent the synchronous rotating dq frames, and θ_e is the electrical angle between them. The stationary $\alpha\beta$ frame is fixed to the stator winding and the α axis coincides with the phase A axis. The frame transformation from three phase to dq can be interpreted into a set of mathematical equations. If the d-axis is aligned with phase a as a reference point for both frames, then:

$$\begin{bmatrix} x_d \\ x_q \end{bmatrix} = k_{dq} \begin{bmatrix} x_a \\ x_b \\ x_c \end{bmatrix} \tag{4.1}$$

$$k_{dq} = \frac{2}{3} \begin{bmatrix} cos\theta_e & \cos\left(\theta_e - \frac{2\pi}{3}\right) & cos\left(\theta_e + \frac{2\pi}{3}\right) \\ -sin\theta_e & -sin\left(\theta_e - \frac{2\pi}{3}\right) & -\sin\left(\theta_e + \frac{2\pi}{3}\right) \end{bmatrix} \tag{4.2}$$

$$\begin{bmatrix} x_\alpha \\ x_\beta \end{bmatrix} = \begin{bmatrix} cos\theta_e & -sin\theta_e \\ sin\theta_e & cos\theta_e \end{bmatrix} \begin{bmatrix} x_d \\ x_q \end{bmatrix} \tag{4.3}$$

The transformation that is used for this control assumes balanced three-phase components. Peak notation is used where the dq peak values are equal to the variable three phase magnitudes. The coefficient $2/3$ in front of the matrix in (4.2) is due to reason that the power calculated in the dq frame is $2/3$ of the power in three-phase frame. The inverse transformation between these three frames can be found in Appendix A.

4.1 Sensorless Control Schemes for Medium- and High-Speed Range

At the medium and high-speed electric machine operation range, the Back-EMF or flux linkage of the PMSM contains a large amplitude of the fundamental wave electrical signal, hence the position detection methods of this speed range are generally based on

the detection of the fundamental signal. The position/speed estimation procedure is presented in Figure 4.4 [109]. As shown in Figure 4.5, the position and speed estimation block can be divided into two parts conventionally, i.e., EMF or flux estimation and position/speed observer.

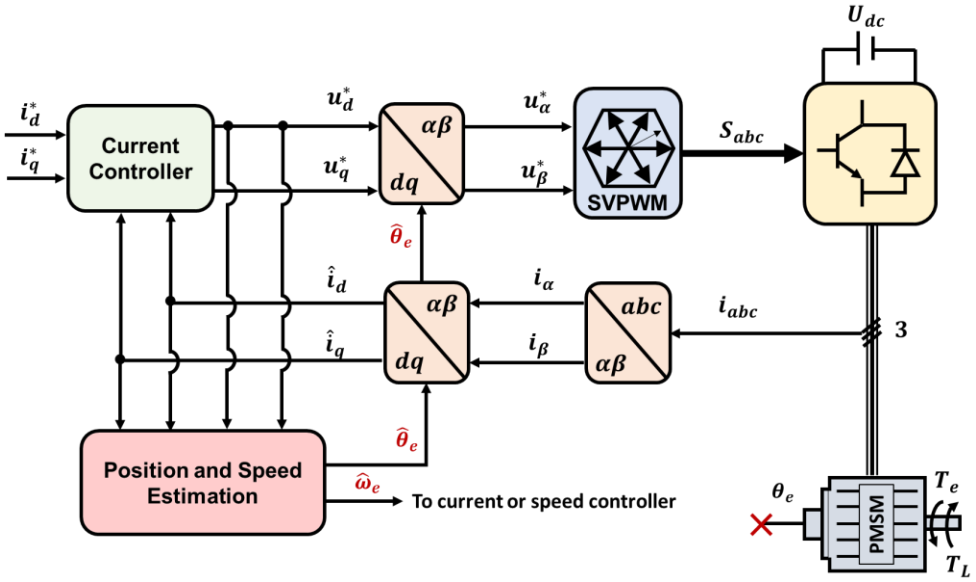


Figure 4.4 General block diagram of fundamental model based sensorless drive system.

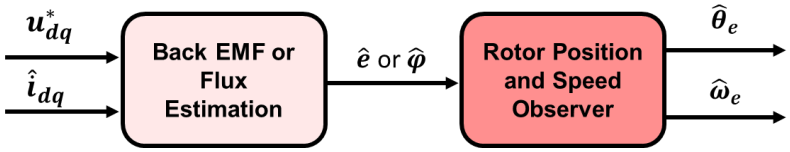


Figure 4.5 Position and speed estimation procedure.

4.1.1 Direct Calculation Method Based on the Mathematical Equations of Machine

The method starts with the mathematical equation of the machine. By detecting the speed-related values such as voltage, current, flux linkage, back electromotive force, etc., the speed and position information are obtained through a direct calculation method. According to the different mathematical equations that are used, it is divided

into back-EMF estimation method, extended back-EMF method and flux linkage estimation method.

4.1.1.1 Back-EMF Estimation Method

The back-EMF estimation method directly uses the voltage equation of the fundamental signal of the machine to directly calculate the back-EMF under the $\alpha\beta$ axis system according to the parameters of the machine voltage, current, resistance and inductance, and then solves the rotor position through the arc tangent operation [179]. The voltage equations of surface-mount PMSM under dq frame is given by [180, 181]:

$$\begin{bmatrix} u_d \\ u_q \end{bmatrix} = \begin{bmatrix} R + sL & -\omega_e L \\ \omega_e L & R + sL \end{bmatrix} \begin{bmatrix} i_d \\ i_q \end{bmatrix} + \begin{bmatrix} 0 \\ \omega_e \varphi_m \end{bmatrix} \tag{4.4}$$

where u_d, u_q are voltages in dq axis, respectively. i_d, i_q are currents in dq axis, respectively. R and L are stator resistance and inductance, respectively. ω_e and θ_e are electrical angular speed and position of rotor, respectively. φ_m is permanent magnet flux linkage. s is differential operator.

The first term on the right side of (4.4) is the voltage drop on the machine's impedance, and the second term is a back-EMF term. By applying transformation (4.3) to (4.4), the voltage equations under $\alpha\beta$ axis are derived as [181]:

$$\begin{bmatrix} u_\alpha \\ u_\beta \end{bmatrix} = \begin{bmatrix} R + sL & 0 \\ 0 & R + sL \end{bmatrix} \begin{bmatrix} i_\alpha \\ i_\beta \end{bmatrix} + \omega_e \varphi_m \begin{bmatrix} -sin\theta_e \\ cos\theta_e \end{bmatrix} \tag{4.5}$$

u_α, u_β are voltages in $\alpha\beta$ axis, respectively. i_α, i_β are currents in $\alpha\beta$ axis, respectively. The second term on the right side of (4.5) is back-EMF term which (4.6) can be solved as [182]:

$$\begin{bmatrix} e_\alpha \\ e_\beta \end{bmatrix} = \omega_e \varphi_m \begin{bmatrix} -sin\theta_e \\ cos\theta_e \end{bmatrix} = \begin{bmatrix} u_\alpha - Ri_\alpha - Lsi_\alpha \\ u_\beta - Ri_\beta - Lsi_\beta \end{bmatrix} \tag{4.6}$$

According to (4.6), the rotor position can be calculated directly as:

$$\theta_e = arctan\left(\frac{-e_\alpha}{e_\beta}\right) = arctan\left(\frac{-u_\alpha + Ri_\alpha + Lsi_\alpha}{u_\beta - Ri_\beta - Lsi_\beta}\right) \tag{4.7}$$

4.1.1.2 Flux Linkage Estimation Method

The implementation process of the flux estimation method [183-185] is similar to that of the back-EMF estimation method. It uses the detected stator voltage and current to calculate the back-EMF of the machine and integrates the back-EMF to obtain the stator flux linkage. According to the mathematical relationship among the stator flux linkage, stator current and rotor position, the position, and speed of the machine could be obtained.

The flux linkage can be calculated using:

$$\begin{bmatrix} \varphi_\alpha \\ \varphi_\beta \end{bmatrix} = \varphi_m \begin{bmatrix} cos\theta_e \\ sin\theta_e \end{bmatrix} = \begin{bmatrix} \int_0^\tau (u_\alpha - Ri_\alpha)dt - Li_\alpha \\ \int_0^\tau (u_\beta - Ri_\beta)dt - Li_\beta \end{bmatrix} \tag{4.8}$$

φ_α, φ_β are flux linkage in $\alpha\beta$ axis, respectively. Then the rotor position can be directly obtained as:

$$\theta_e = arctan\left(\frac{\varphi_\beta}{\varphi_\alpha}\right) = arctan\left(\frac{\int_0^\tau (u_\alpha - Ri_\alpha)dt - Li_\alpha}{\int_0^\tau (u_\beta - Ri_\beta)dt - Li_\beta}\right) \quad (4.9)$$

The flux estimation method is also an open-loop estimation like the previous two methods. The algorithm is simple, but it is only suitable for surface-mounted PMSM, and it is sensitive to changes in machine parameters. The position detection accuracy under different operating conditions also fluctuates.

In the model based sensorless control, both the EMF or flux information could be directly calculated with the open loop method. They do not require much signal processing or calculation process and are simple to implement. However, the accuracy of variables detection depends on the accuracy of the machine parameters. Under different operating conditions such as multiple loads and variable speeds, the ambient temperature and the internal temperature rise of the machine will cause the stator resistance to change, and the saturation of the magnetic circuit also affects the stator inductance. These effects make it difficult to obtain higher detection precision by using this method. More accurate parameters could be obtained through online identification of machine parameters [186], thereby improving the position detection accuracy of such methods. However, the introduction of parameter identification increases the complexity of the system and the difficulty of implementation, so that the direct back-EMF estimation method has lost the advantages of being simple and easy.

To overcome the shortages brought about by the open loop methods, the closed loop methods have been developed and the control algorithms of them are constructed to force the estimated-measured output error to zero. Hence, the robustness and accuracy of the estimation system are improved. Generally, the closed loop methods are

categorized as: model reference adaptive system observer, observer method, and artificial intelligence-based estimation method, etc.

4.1.1.3 Extended back-EMF method

If the machine has salient pole characteristics, not only the back-EMF in $\alpha\beta$ axis is related to the rotor position, but the inductance in $\alpha\beta$ axis is also a function of the rotor position. Therefore, it is difficult to find the accurate rotor position using the back-EMF estimation method and it is necessary to extend the sensorless control scheme of SPMSMs to that of IPMSMs. To realize this idea, [181] proposes an extended back-EMF method, which transfers the part of the inductance to the back-EMF to form an Extended back-EMF (EEMF).

The voltage equation of the IPMSM on dq rotating coordinate is given by:

$$\begin{bmatrix} u_d \\ u_q \end{bmatrix} = \begin{bmatrix} R + sL_d & -\omega_e L_q \\ \omega_e L_d & R + sL_q \end{bmatrix} \begin{bmatrix} i_d \\ i_q \end{bmatrix} + \begin{bmatrix} 0 \\ \omega_e \varphi_m \end{bmatrix} \tag{4.10}$$

where L_d, L_q are the inductance of d-axis and q-axis respectively.

Transforming (4.10) into $\alpha\beta$ fixed coordinate, (4.11) is derived:

$$\begin{bmatrix} u_\alpha \\ u_\beta \end{bmatrix} = \begin{bmatrix} R + sL_\alpha & sL_{\alpha\beta} \\ sL_{\alpha\beta} & R + sL_\beta \end{bmatrix} \begin{bmatrix} i_\alpha \\ i_\beta \end{bmatrix} + \omega_e \varphi_m \begin{bmatrix} -sin\theta_e \\ cos\theta_e \end{bmatrix} \tag{4.11}$$

Where

$$L_0 = (L_d + L_q)/2 \tag{4.12}$$

$$L_1 = (L_d - L_q)/2 \tag{4.13}$$

$$L_\alpha = L_0 + L_1 cos2\theta_e \tag{4.14}$$

$$L_\beta = L_0 - L_1 cos2\theta_e \tag{4.15}$$

$$L_{\alpha\beta} = L_1 sin2\theta_e \tag{4.16}$$

Comparing (4.11) with (4.5), the reason for the presence of $2\theta_e$ terms can be concluded as that the impedance matrix in (4.11) is asymmetrical. The impedance matrix is rewritten symmetrically as

$$\begin{bmatrix} u_d \\ u_q \end{bmatrix} = \begin{bmatrix} R + sL_d & -\omega_e L_q \\ \omega_e L_q & R + sL_d \end{bmatrix} \begin{bmatrix} i_d \\ i_q \end{bmatrix} + \begin{bmatrix} 0 \\ E_{ex} \end{bmatrix} \tag{4.17}$$

where

$$E_{ex} = \left(L_d - L_q\right)\left(\omega_e i_d - \dot{i}_q\right) + \omega_e \varphi_m \tag{4.18}$$

The second term on the right side of (4.17) is defined as an Extended EMF (EEMF) by (4.18)[187]. It is a general form of mathematical model for all synchronous machines. When $L_d = L_q$, it evolves into the equation of SPMSMs. And when $\varphi_m = 0$, it becomes the equation of Synchronous Reluctance Machines (SRMs). There is a differential term of i_q in the EEMF. This means that even when machine speed is near to zero, if the q-axis current i_q is varying, the EEMF E_{ex} is not zero.

If the EEMF can be estimated, the position of magnet can be obtained from its phase just like EMF in SPMSMs. However, in the sensorless drive system, such dq model cannot be utilized because the rotor position is not detected. The mathematical model in the estimated rotating $\gamma\delta$ frame, which lags $\Delta\theta$ from the dq reference frame as

shown in Figure 4.6 is derived as follows by transforming (4.17) into the estimated $\gamma\delta$ frame:

$$\begin{bmatrix} u_\gamma \\ u_\delta \end{bmatrix} = \begin{bmatrix} R + sL_d & -\omega_e L_q \\ \omega_e L_q & R + sL_d \end{bmatrix} \begin{bmatrix} i_\gamma \\ i_\delta \end{bmatrix} + \begin{bmatrix} e_\gamma \\ e_\delta \end{bmatrix} \tag{4.19}$$

where

$$\begin{bmatrix} e_\gamma \\ e_\delta \end{bmatrix} = E_{ex} \begin{bmatrix} -sin\Delta\theta \\ cos\Delta\theta \end{bmatrix} + (\hat{\omega}_e - \omega_e) L_d \begin{bmatrix} -i_\delta \\ i_\gamma \end{bmatrix} \tag{4.20}$$

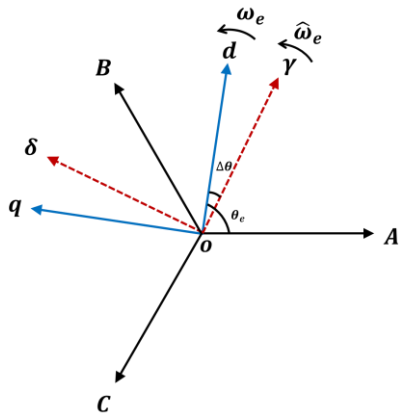


Figure 4.6 Definitions of coordinate reference frames for EEMF based sensorless scheme.

The EEMF in the estimated rotating $\gamma\delta$ reference frame as shown in (4.20) includes the information of estimation position error $\Delta\theta$. It is utilized for the estimation of rotor position and speed. A least-order observer is used to estimate EEMF[187]. Figure 4.7 shows the equivalent block diagram of the least-order observer.

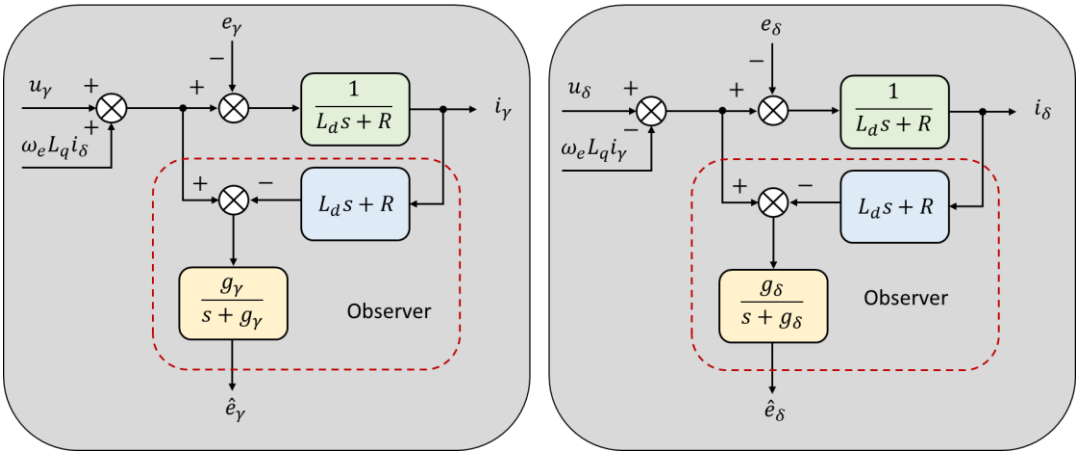


Figure 4.7 Equivalent block diagram of least-order observer for estimation of Extended back-EMF.

Assuming the error between the estimated speed $\hat{\omega}_e$ and the actual speed ω_e is sufficiently small, the EEMF is estimated as follows:

$$\begin{bmatrix} \hat{e}_\gamma \\ \hat{e}_\delta \end{bmatrix} = E_{ex} \begin{bmatrix} -sin\Delta\hat{\theta} \\ cos\Delta\hat{\theta} \end{bmatrix} \tag{4.21}$$

From the estimated extended EMF (e_γ and e_δ), the estimation position error $\Delta\hat{\theta}$ can be derived through the following way:

$$\Delta\hat{\theta} = arctan\left(\frac{-\hat{e}_\gamma}{\hat{e}_\delta}\right) \tag{4.22}$$

The estimated speed $\hat{\omega}_e$ and the estimated position $\hat{\theta}_e$ are compensated by a PI type compensator $G_e(s)$ to ensure the position error maintain zero. The position and speed estimation algorithm are summarized as shown in Figure 4.8. Practically, the estimated speed is filtered through a low-pass filter to reduce the interference of noise. The filtered estimated speed is used to the machine control and the estimation of Extended back-EMF.

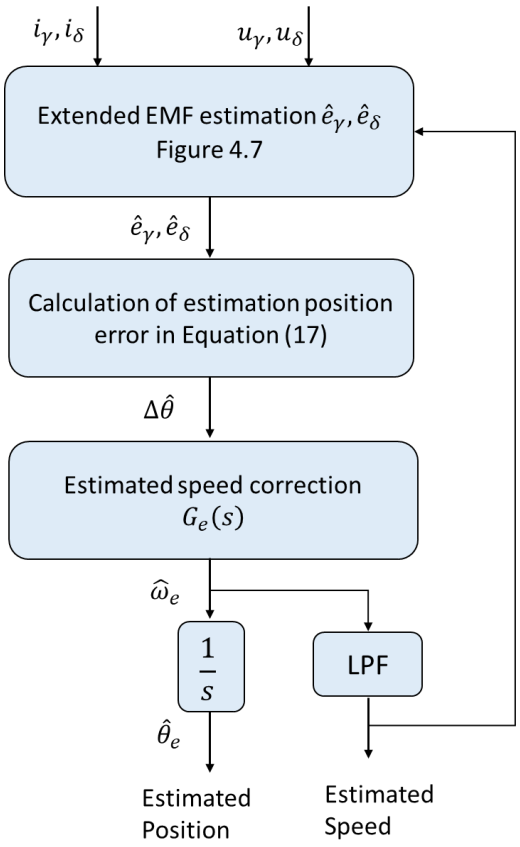


Figure 4.8 Block diagram of position and speed estimation algorithm.

The proposed algorithm is of simple structure and the process of design is clear and easy. The extended back-EMF method expands the back-EMF calculation method to salient PMSM [188], and brings about disadvantage of being sensitive to changes in machine parameters.

4.1.2 Model Reference Adaptive System

Model reference adaptive system [189] is a widely used estimation method and of its principle block diagram is shown in Figure 4.9.

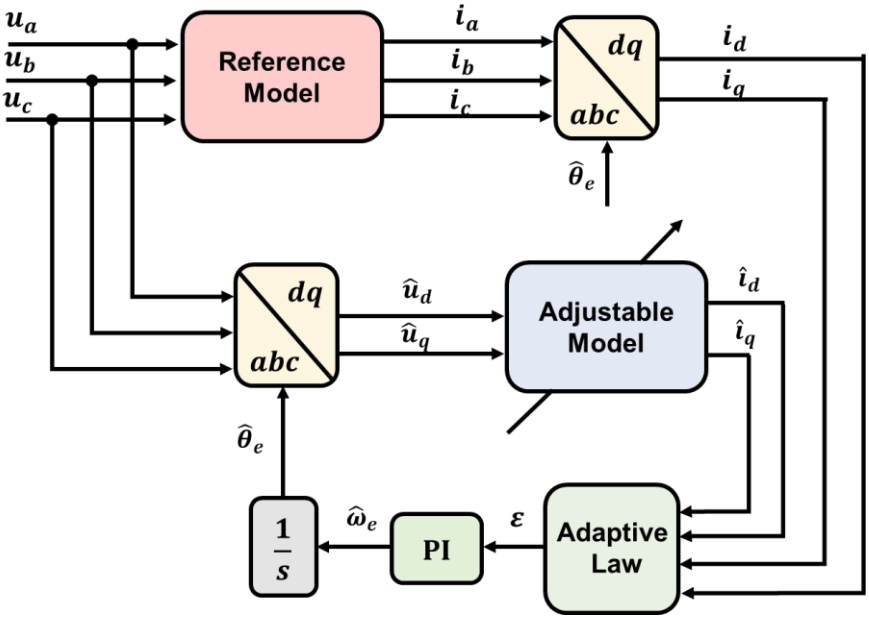


Figure 4.9 Block diagram of MRAS based sensorless control system of PMSM.

It is composed of three basic parts, namely adaptive algorithm, reference model and adjustable model. The voltage equation using the estimated speed as a parameter is an adjustable model, and the machine itself is used as a reference model. The input and output of these two models have the same physical meaning: the input is three-phase voltage u_a, u_b, u_c and the output is dq axis current i_d, i_q. As shown in Figure 4.9, the adaptive algorithm constructs an error term ε based on the difference between the output currents of the reference model and the adjustable model and uses the PI regulator to adjust the error term to zero to obtain the estimated rotor angular speed $\hat{\omega}_e$ and integrate it to obtain the estimated rotor position $\hat{\theta}_e$. When the outputs of the reference model and the adjustable model tend to be consistent, it indicates that the estimated rotor angular speed $\hat{\omega}_e$ and the estimated rotor position $\hat{\theta}_e$ are also essentially the same as the actual rotor position. The MRAS is a closed-loop structure, which is proved to be asymptotically convergent by stability theory. It enjoys simple structure and high stability. When the adjustable model is constructed accurately, the position

detection accuracy of the method is high. However, the accuracy of the adjustable model depends on the resistance, inductance, and permanent magnet flux linkage of the machine, hence the method is sensitive to parameter variations.

4.1.3 Observer Method

According to the state equation of the actual system, an estimated system is reconstructed, and the relevant electrical signals in the actual one is imported into the estimated one. Under certain conditions, the output of the estimated system can be equal to the state of the actual system, which is the basic idea of the observer method. Currently, the main observers used for rotor position detection of PMSM are:

- Full-order or reduced-order state observers
- Sliding mode observers
- Extended Kalman filters

4.1.3.1 Full-order or Reduced-order State Observers

The full-order state observer [190-192] realizes the observation of all state variables by establishing a complete differential state equation of the machine. In the early 1990s, American scholars have applied the full-order state observer to the rotor position detection of PMSM. Since this method observes all states, the model calculation is large, and the solution process is complicated. [193, 194] uses the minimum order state observer to realize the rotor position detection of the PMSM. By reducing the order of the state equation, the system calculation load is reduced to a certain extent.

4.1.3.2 Sliding Mode Observers

Sliding mode control was first proposed by former Soviet scholars Emelyanov and Barbashin in the 1960s. After being developed and improved by Utkin and other scholars, it has gradually become a more important branch in the field of control and is widely used in machine control [195-197]. By the 1990s, Japanese scholar T. Furuhashi introduced sliding mode control theory in the observer, realized the back-EMF estimation of permanent magnet brushless DC machine, and then obtained the estimated rotor position [198]. The principle block diagram of rotor position estimation of PMSM based on the sliding mode observer is shown in Figure 4.10.

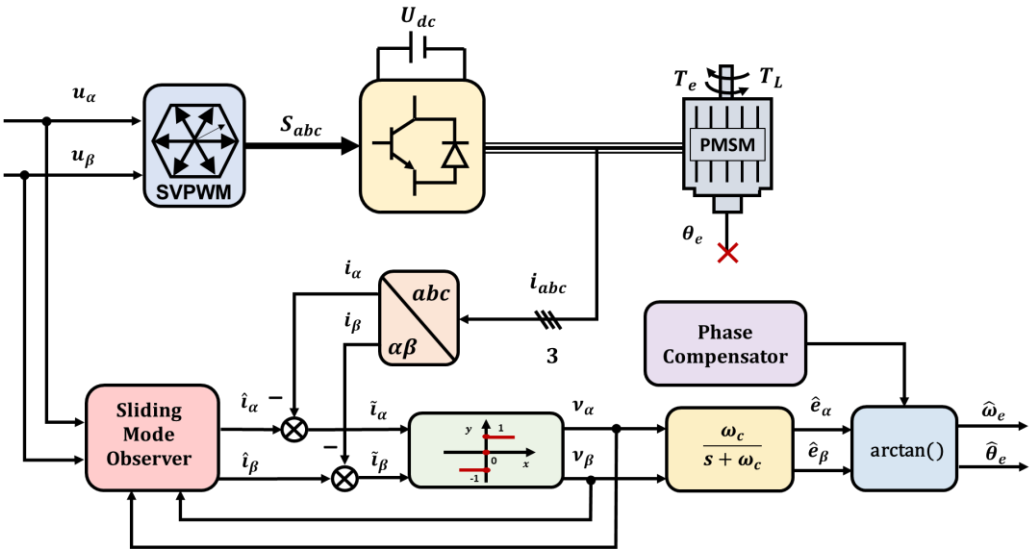


Figure 4.10 Block diagram of SMO based sensorless control system of PMSM.

Compared with the state observer, the sliding mode observer has the advantages of simple structure and high insensitivity to parameter changes. Therefore, it is widely used in rotor position detection of PMSM [199]. Still, for the traditional SMO, the switch function is used as the control function as shown in the green square in Figure 4.10. Due to the switch time and the space lag, the SMO presents serious chattering

[200, 201], which result in high-frequency oscillation components in the estimated signal of the SMO. Due to the discrete switch control in the SMO, chattering becomes the inherent characteristic of the sliding-mode variable structure system, which cannot be completely eliminated and can only be reduced. And various novel ideas such as adaptive SMO and high-order SMO have been proposed [202-204] to find a trade-off between chattering reduction and system robustness.

4.1.3.3 Extended Kalman Filter

The Kalman filter is an optimal linear estimation method, first proposed by American scholar R. E. Kalman in the 1960s [205]. It models the system with rotor speed as one state variable, and the Kalman filter is used to initially predict this variable and then correct it in a recursive manner to achieve the final estimation [206]. The implementation of a discrete Kalman filter can be classified as two procedures, i.e., prediction and correction. Then they are circulated in a closed loop that is shown in Figure 4.11. The first prediction part is responsible for the state predication as its name suggests and the error covariance calculation. As an updating process of initial prediction, the second part is to correct the state using the measurement. The Kalman gain is then calculated, and the error covariance is also updated after the estimation. The detailed equations for both parts are derived in [207]. The basic implementation of the Kalman filter method is only applicable for a linear system, while an Extended Kalman filter (EKF) [114, 208-210] can handle with non-linear systems at the expense of increased computational load. However, this load could be reduced by integrating a predefined look up table [211, 212]. The EKF has poor performance in estimation at zero and low speed but it is suitable for application in a noisy system.

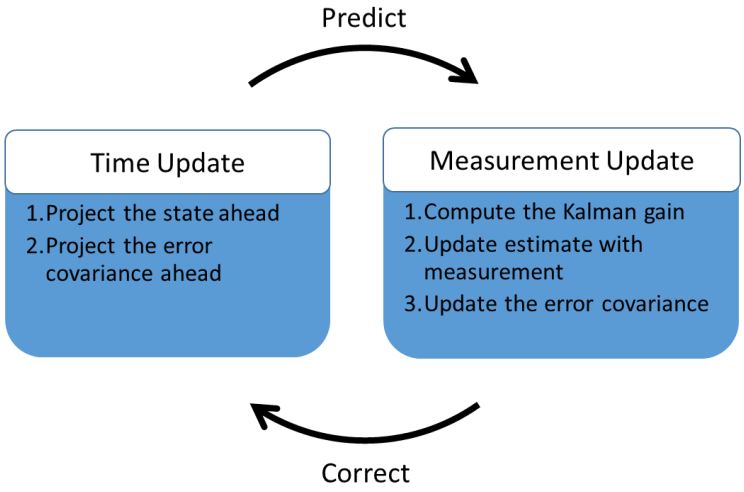


Figure 4.11 The operation of Kalman filter .

Model based method can be implemented using the electromotive force (EMF) or flux associated with the fundamental excitation , and it can be subdivided into open loop ones and closed loop ones. The former is derived through the integration of the back-EMF of the machine without any correction term while the latter makes use of the error between the estimated and measured quantities as feedback to increase their performance in turn [213]. Although model based method was proposed and commercialized initially, it fails in the low-speed range due to the low signal-to-noise-ratio (SNR) that is brought about by the modelling uncertainty, the inverter nonlinearity, etc.

4.2 Sensorless Control Schemes for Zero and Low-Speed Range

To expand the sensorless control into the low- to zero-speed range, the saliency tracking based method is developed, including signal injection-based methods [64-112] and fundamental PWM excitation (FPE)-based methods [40],[113-135], which are shown in Figure 4.12.

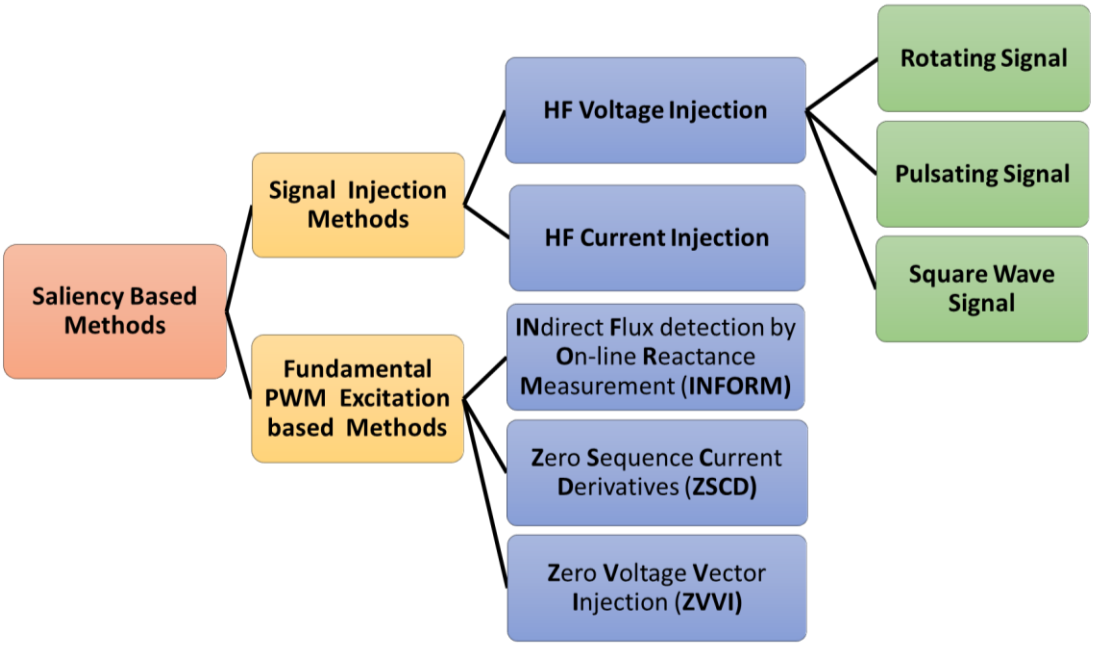


Figure 4.12 Categories for zero to low speed range sensorless methods.

As discussed above in Chapter 1, at zero and low -speed range (generally 0-10% of rated speed [214]), the sensorless schemes are mainly based on the saliency of machine, which can be roughly categorized into fundamental PWM excitation (FPE) method and HF (high-frequency) signal injection method.

The saliency-based method utilizes saliency of machine to calculate the position information of the machine rotor. The saliency of machine mainly includes the geometric saliency caused by the salient structure of the rotor [215-217], the saturation saliency caused by the magnetic saturation of some sections of machine iron core [218-220], and the hysteresis saliency results from the hysteresis of magnetically conductive material of machine stator [221-223]. Geometric saliency are often seen in interior permanent magnet machines (IPMSM), saturation saliency are usually found in surface-mounted permanent magnet machines (SPMSM) with high stator magnetic density, and hysteresis saliency are typically seen in surface-mounted permanent

magnet machines (SPMSM) with low magnetic density of stators. The degree of saliency caused by geometry, saturation and hysteresis has a strong to weak relationship, which means, the machine whose geometric saliency dominates often contains a certain degree of saturation saliency and hysteresis saliency, while machines dominated by hysteresis saliency usually do not contain obvious geometric saliency or saturation saliency [224].

Three main types of FPE method are: Indirect flux detection by on-line reactance measurement (INFORM)，Zero Sequence Current Derivatives (ZSCD) Measurements ，and Zero Voltage Vector Injection (ZVVI) Method [110]. The INFORM method measures the current response induced by the voltage space vectors that are applied in different directions and obtain rotor position information by detecting the current slope. It is simple to accomplish but require extra hardware devices. The principle of ZSCD method is to calculate the derivative of zero sequence current induced by the test vector signals that are injected to the machine. It has high performance but are not available in certain industrial applications where the zero-sequence component excitation is not accessible. The ZVVI method combines the derivation calculations of current and zero voltage vector. It is insensitive to parameters variation and has not yet been commercialized.

4.2.1 High-Frequency Signal Injection Method

HF signal injection method calculates the rotor position information by injecting a specific high-frequency signal into the stator winding and detecting the response to this

signal. According to different excitation methods, the high-frequency injection method can be roughly divided into [225]:

- High-Frequency Current Injection (HFCI) Method
- High-Frequency Voltage Injection (HFVI) Method
    - Rotating High-Frequency Signal Injection (HFSI) Method
    - Pulsating High-Frequency Signal Injection (HFSI) Method

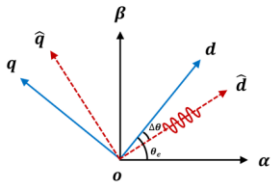
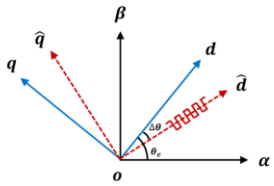
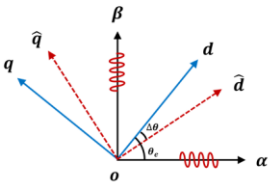
The difference between the HFVI method and HFCI method [122, 226, 227] is the type of injected signals, which mainly depends on the characteristics of the inverter. If the inverter is voltage sourced, it is more appropriate to use the HF voltage signal. While the inverter is current sourced, HF current signal is a better choice. Although the rotating HFCI method extracts the rotor position signal easier than the rotating HFVI method does, the bandwidth of the position observer of the former is smaller than that of the latter. In addition, since typical machine drive systems generally use voltage source inverters (VSI), accurate HFCI can hardly be achieved. Hence, the HFVI method is mainly introduced in the following content.

According to different applicable coordinate systems, the HFVI method can be classified into two categories: Rotating HFSI Method and Pulsating HFSI Method. The Rotating HFSI Method often chooses two sinusoidal signals of equal amplitude, equal frequency, and phase difference $\pi/2$ to be injected separately along the stationary $\alpha\beta$ coordinate axis to generate a rotating voltage space vector. While in the Pulsating HFSI Method, high-frequency signals are injected along the estimated rotating *d*-axis to generate a pulsating voltage space vector.

The concept of high-frequency signal injection was first proposed by R.D. Lorenz in 1993 [228]. In 1998, M.J. Corley and R.D. Lorenz realized the position observation of the interior permanent magnet synchronous machine at zero and low-speed by injecting HF signal into the voltage expressed in terms of rotating *dq* frame [229]. In 1999, S.K. Sul innovated this algorithm and use pulsating sinusoidal high-frequency signal injection for the first time to observe position on asynchronous machines [230]. In 2002, J. Holts achieved the rotor position estimation of surface-mounted PMSM by injecting pulsating sinusoidal high-frequency signal [231]. Around the same time, S.K. Sul not only successfully applied this scheme to the sensorless control of surface-mounted PMSM but also verified the performance even under heavy load conditions [232]. In 2011, Yoon et al. proposed pulsating square wave injection method which can estimate rotor position without a low-pass filter (LPF), and thus has a larger rotor position observation bandwidth [233]. Table 4-1 compares the most common three methods for HFVI method:

- Pulsating High-Frequency Signal Injection method
    - Pulsating Sinusoidal Injection method
    - Pulsating Square Wave Injection method
- Rotating High-Frequency Signal Injection method

Table 4-1 Comparison of three common high-frequency signal injection methods [110, 225].

Injection Scheme	**Pulsating Signal Injection**		**Rotating Signal Injection**
	Pulsating Sinusoidal Injection	Pulsating Square Wave Injection	
Injection Frame and Signal			
Features	• Available for both salient and non-salient machine • Low injection frequency • Affected by inverter nonlinearities effect • Requiring initial position information	• High injection frequency • Small effect of inverter nonlinearities • Requiring initial position information	• Low injection frequency • Small effect of inverter nonlinearities • No initial position information is required

These methods are classified according to what kind of signal and what frames the signals are injected to. This rotating high-frequency signal injection is often called $\alpha\beta$ injection because the rotating voltage signal is applied in a stationary frame. The voltage signal with constant voltage amplitude rotating at the injected high frequency can be represented as:

$$\widehat{U}_{\alpha\beta} = U_h e^{j\omega_h t} = U_h \begin{bmatrix} cos\ (\omega_h t) \\ sin\ (\omega_h t) \end{bmatrix} \tag{4.23}$$

where U_h is the amplitude and ω_h is the frequency of the high-frequency voltage vector $\widehat{U}_{\alpha\beta}$, hence three-phase voltage vector is persistently rotating as an injection signal in the stationary $\alpha\beta$ frame.

Instead of injecting a rotating vector, it is also possible to apply the high-frequency signal in the synchronous frame in a pulsating manner, usually along the *d* axis [234] to minimize the torque ripple [235]. The HF voltage is given in the synchronous *dq* frame as:

$$\begin{bmatrix}\hat{u}_{dh}\\ \hat{u}_{qh}\end{bmatrix} = \begin{bmatrix}U_h cos\,(\omega_h t)\\ 0\end{bmatrix} \tag{4.24}$$

As shown in Table 4-1, a comparison between them is made from various aspects. The scheme of pulsating sinusoidal high-frequency signal injection method is available for both salient and non-salient machine. And an introduction of it will be made in detail in the following content.

4.2.2 Pulsating Sinusoidal High-Frequency Signal Injection Method

This method is usually used for non-salient surface-mounted PMSM. A sinusoidal high-frequency voltage signal is injected into the estimated direct axis to saturate the direct axis magnetic circuit, allowing the machine to show saturation saliency. The block diagram of this method is shown in Figure 4.13.

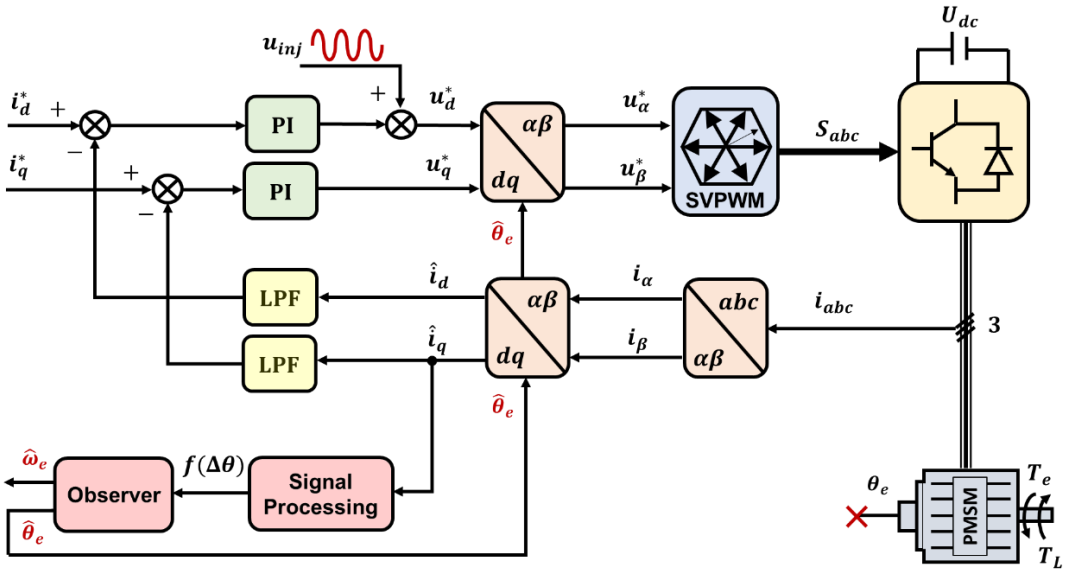


Figure 4.13 Block diagram of pulsating sinusoidal high-frequency injection signal method.

This sensorless scheme can be divided into two steps. The first step is called signal processing that aims to get the error signal $f(\Delta\theta)$ from current feedback in the

estimated q axis. Then an observer is used to obtain the estimated speed and position that are used for coordinate transformation in vector control. Besides, vector control strategy is used to realize the cascade closed-loop control of PMSM speed and current. The space vector pulse width modulation (SVPWM) is used to obtain the drive signal. LPF is added to the dq axis current feedback loop to filter out high-frequency components.

To figure out how this method works, the concept of saturation saliency is explained initially. Normally, the direct axis inductance L_d of surface-mounted PMSM is approximately the same as the quadrature axis inductance L_q, that is, $L_d \approx L_q$. But when the magnetic circuit of the machine is saturated, the direct axis inductance will reduce and thus small saliency is shown, also known as the saturation saliency of machine [227]. Figure 4.14 is the characteristic curve of the flux linkage of the surface-mounted PMSM direct axis magnetic circuit. If there is no current flowing through the direct axis, the amplitude of the flux linkage is similar to the permanent magnet flux φ_m and the working point of the magnetic circuit is A. If negative direction current passes through the direct axis, the operating point changes to B in the linear region where the amplitude of the flux linkage decreases linearly with constant slope and the inductance remains unchanged. If positive current flows in the direct axis, the operating point will move to C in the saturation region where the amplitude of the flux linkage increases nonlinearly, and the slope and inductance decreases as current increases.

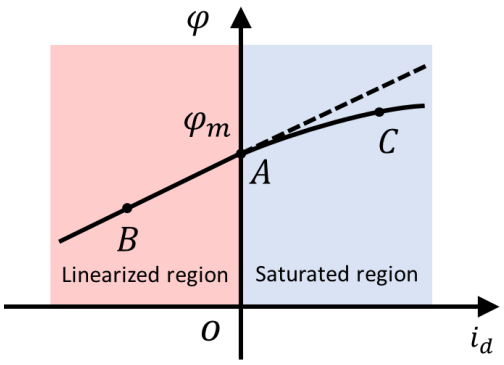


Figure 4.14 Flux characteristic curve of direct axis flux circuit of surface-mounted PMSM.

Due to the absence of permanent magnets in the quadrature axis, the magnetic circuit is in the linear region if current is within the rated current, which means the quadrature axis inductance does not change. Hence, L_d becomes less than L_q and the saturation saliency characteristic can be observed [236]. When high-frequency pulsating voltage is injected, high-frequency components are generated in both voltage and current of the synchronous rotating coordinate system. Only considering high-frequency component in steady-state, the voltage formula can be rewritten as:

$$\begin{bmatrix} u_{dh} \\ u_{qh} \end{bmatrix} = \begin{bmatrix} R_d + j\omega_h L_d & 0 \\ 0 & R_q + j\omega_h L_q \end{bmatrix} \begin{bmatrix} i_{dh} \\ i_{qh} \end{bmatrix} \tag{4.25}$$

In the above formula, u_{dh} and u_{qh} are high-frequency voltage in the actual direct axis and quadrature axis, respectively. i_{dh} and i_{qh} are high-frequency current in the actual direct axis and quadrature axis, respectively. The high-frequency response of current in actual synchronous rotating coordinate system can be solved (4.25) from as:

$$\begin{bmatrix} i_{dh} \\ i_{qh} \end{bmatrix} = \begin{bmatrix} \dfrac{1}{R_d + j\omega_h L_d} & 0 \\ 0 & \dfrac{1}{R_q + j\omega_h L_q} \end{bmatrix} \begin{bmatrix} u_{dh} \\ u_{qh} \end{bmatrix} \tag{4.26}$$

According to the principle of coordinate transformation, the transformation matrix between the actual *dq* frame and the estimated *dq* frame can be expressed as:

$$T_{\hat{\theta}\to\theta}(\Delta\theta) = \begin{bmatrix} cos\Delta\theta & sin\Delta\theta \\ -sin\Delta\theta & cos\Delta\theta \end{bmatrix} \tag{4.27}$$

$$T_{\theta\to\hat{\theta}}(\Delta\theta) = \begin{bmatrix} cos\Delta\theta & -sin\Delta\theta \\ sin\Delta\theta & cos\Delta\theta \end{bmatrix} \tag{4.28}$$

where $\hat{\theta}$ is estimated rotor position, $\Delta\theta = \theta - \hat{\theta}$ is error between actual rotor position and estimated rotor position. Combining (4.26) to (4.28), the high-frequency current response in the estimated *dq* frame is solved as:

$$\begin{bmatrix} \hat{\imath}_{dh} \\ \hat{\imath}_{qh} \end{bmatrix} = T_{\theta\to\hat{\theta}}(\Delta\theta) \begin{bmatrix} \dfrac{1}{R_d + j\omega_h L_d} & 0 \\ 0 & \dfrac{1}{R_q + j\omega_h L_q} \end{bmatrix} T_{\hat{\theta}\to\theta}(\Delta\theta) \begin{bmatrix} \hat{u}_{dh} \\ \hat{u}_{qh} \end{bmatrix} \tag{4.29}$$

Pulsating high-frequency voltage is injected into the estimated *dq* frame as:

$$\begin{bmatrix} \hat{u}_{dh} \\ \hat{u}_{qh} \end{bmatrix} = \begin{bmatrix} U_h cos\,(\omega_h t) \\ 0 \end{bmatrix} \tag{4.30}$$

Substituting (4.25)(4.27)(4.28)(4.30) gives:

$$\begin{aligned} &\begin{bmatrix} \hat{\imath}_{dh} \\ \hat{\imath}_{qh} \end{bmatrix} \\ &= \frac{U_h cos\,(\omega_h t)}{(R_d + j\omega_h L_d)(R_q + j\omega_h L_q)} \begin{bmatrix} \bar{R} + j\omega_h \bar{L} + (\Delta R + j\omega_h \Delta L) cos\,(2\Delta\theta) \\ (\Delta R + j\omega_h \Delta L) sin\,(2\Delta\theta) \end{bmatrix} \\ &= \frac{U_h cos\,(\omega_h t - \varphi)}{|Z|} \begin{bmatrix} \bar{R} + j\omega_h \bar{L} + (\Delta R + j\omega_h \Delta L) cos\,(2\Delta\theta) \\ (\Delta R + j\omega_h \Delta L) sin\,(2\Delta\theta) \end{bmatrix} \end{aligned} \tag{4.31}$$

$\bar{R} = \frac{R_q - R_d}{2}$,$\Delta R = \frac{R_q + R_d}{2}$, $\bar{L} = \frac{L_q - L_d}{2}$, $\Delta L = \frac{L_q + L_d}{2}$,

$$|Z| = \sqrt{(R_d R_q - \omega_h^2 L_d L_q)^2 + \omega_h^2 (R_d L_q + R_q L_d)^2}, \varphi = arctan \frac{\omega_h (R_d L_q + R_q L_d)}{(R_d R_q - \omega_h^2 L_d L_q)}.$$

The high-frequency current response of estimated quadrature axis can be simplified from (4.31):

$$\hat{\imath}_{qh} = \frac{U_h |\Delta Z|}{|Z|} sin(2\Delta\theta)\, cos(\omega_h t - \varphi + \Delta\varphi) \tag{4.32}$$

where

$$|\Delta Z| = \sqrt{\Delta R^2 + \omega_h^2 \Delta L^2} \tag{4.33}$$

$$\Delta\varphi = arctan \frac{\omega_h \Delta L}{\Delta R} \tag{4.34}$$

Since the frequency of the injected signal is high, the resistance value can be ignored when compared with the high-frequency inductance. (4.32) can be approximated as:

$$\hat{\imath}_{qh} \approx \frac{U_h \Delta L}{\omega_h L_d L_q} sin(2\Delta\theta)\, sin\,(\omega_h t) \tag{4.35}$$

From (4.35) it can be seen that the error information of rotor position estimation is contained in the high-frequency current response of estimated quadrature axis. The following diagram shows the signal processing that is used to extract $\Delta\theta$ from estimated quadrature axis current $\hat{\imath}_q$.

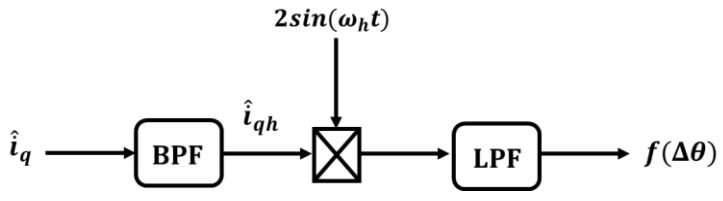


Figure 4.15 Signal processing in the pulsating sinusoidal high-frequency injection signal method.

According to previous introduction, the first thing to obtain the rotor position error information $\Delta\theta$ is to get the high-frequency component of estimated quadrature axis current $\hat{i}_{qh}$. As illustrated in Figure 4.15, this can be achieved by passing estimated quadrature axis current $\hat{i}_q$ through a Band-Pass Filter (BPF) with ω_h as central frequency. In order to get rotor position error information $\Delta\theta$ which is free from high-frequency component, $\hat{i}_{qh}$ is then modulated by making multiplication with signal $2sin(\omega_h t)$.

$$\hat{i}_{qh} \cdot 2sin(\omega_h t) = \frac{2U_h \Delta L}{\omega_h L_d L_q} sin(2\Delta\theta)\, sin^{\,2}(\omega_h t) \tag{4.36}$$

The right side of (4.39) could be rewritten through trigonometric transformation as:

$$\hat{i}_{qh} \cdot 2sin(\omega_h t) = \frac{2U_h \Delta L}{\omega_h L_d L_q} sin(2\Delta\theta) \frac{(1 - cos(2\omega_h t))}{2} \tag{4.37}$$

The modulated signal can be simplified into the sum of two parts, i.e. the DC component and high-frequency component.

$$\hat{i}_{qh} \cdot 2sin(\omega_h t) \tag{4.38}$$

$$= \frac{U_h \Delta L}{\omega_h L_d L_q} sin(2\Delta\theta) - \frac{U_h \Delta L}{\omega_h L_d L_q} sin(2\Delta\theta)\, cos(2\omega_h t)$$

The DC component is the first term on the right side of (4.38) which only contains the error between the actual rotor position and the estimated rotor position. The high-frequency component is the second term on the right side of (4.38). By passing the

modulated signal through a Low-Pass Filter (LPF), the high-frequency component can be filtered out, leaving the DC component as the filtered signal $f(\Delta\theta)$.

$$f(\Delta\theta) = LPF\left[\hat{i}_{qh} \cdot 2sin(\omega_h t)\right] = \frac{U_h \Delta L}{\omega_h L_d L_q} sin(2\Delta\theta) \tag{4.39}$$

If $\Delta\theta$ is small enough, the filtered signal can be linearized as:

$$f(\Delta\theta) \approx k\Delta\theta \tag{4.40}$$

where $k = \frac{2U_h \Delta L}{\omega_h L_d L_q}$

After the first step i.e.,‘ signal processing’ shown in the Figure 4.15, an observer is applied to achieve estimation of rotor speed and position. As shown in Figure 4.16, the commonly used observers are based on the phase-locked loop (PLL).

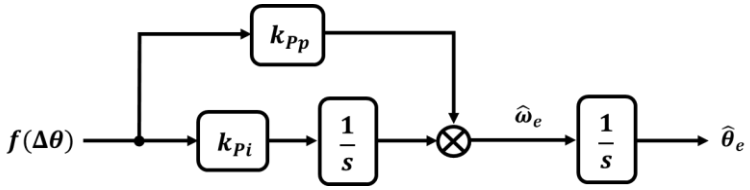


Figure 4.16 Phase Locked Loop based rotor position observer.

PLL is a technology that enables the output signal to track the input signal and is also a negative feedback control system of the phase error. The main idea is to track and adjust the frequency of the output signal through the error value between the input and output signals. When the system reaches steady state operation, the error value between the corresponding signals will tend to be zero, the system no longer has a phase difference. As shown in (4.16), the rotor position error $f(\Delta\theta) \approx k\Delta\theta$ is the input signal, and the estimated electrical angle is the output signal, k_{Pp} and k_{Pi} are the proportional

and integral coefficients of the PI controller, and $1/s$ is the integrator. Through the PI control, $\Delta\theta$ tends to zero, so that the estimated synchronous coordinate system coincides with the actual synchronous coordinate system, and the target purpose of accurately estimating the rotor position is achieved. However, for the PLL technology in digital control mode, the time when the error value reaches a stable state is proportional to the period of the locked input signal, that is, the tracking response speed is slow, and there is a certain degree of lag problem. Therefore, there is a need for a rotor position estimator without lag.

4.3 Sensorless Control Schemes for Full-Speed Range

At present, there is no control method that can realize the sensorless operation of the permanent magnet synchronous machine in the full-speed range. By combining various methods suitable for low speed or medium to high speed, a hybrid method [154] has become a proper solution.

The difficulty of the hybrid control method is the smooth switching between the two types of methods which will affect the stability of the control system. The key to the hybrid control method lies in the smooth switching of the two methods in the transition zone. The currently effective scheme is the weighted average method [237]. As shown in (4.17), the final estimated speed is the weighted average of the speed obtained by the two methods. The upper speed limit n_{max} of the switching interval is determined according to the speed range applicable to the low-speed method, and the lower speed limit n_{min} is determined according to the applicable range of the high-speed method.

The final estimated speed is the weighted average of the speed obtained by the two methods.

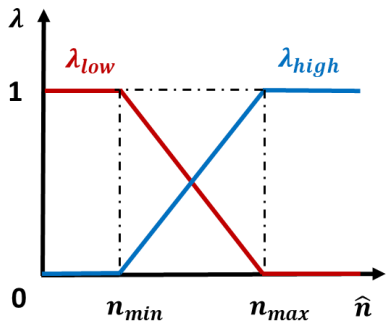


Figure 4.17 Determination of weighting coefficient in closed-loop hybrid sensorless control strategy.

$$\hat{n} = \lambda_{low}\hat{n}_{low} + \lambda_{high}\hat{n}_{high} \tag{4.41}$$

$\hat{n}_{low}$ and $\hat{n}_{high}$ are estimated speed based on low-speed and high-speed schemes, respectively. λ_{low} and λ_{high} are corresponding weighting factors which can be expressed as:

$$\lambda_{low} = \begin{cases} 1 & \hat{n} \le n_{min} \\ \dfrac{n_{max} - \hat{n}}{n_{max} - n_{min}} & n_{min} < \hat{n} < n_{max} \\ 0 & \hat{n} \ge n_{max} \end{cases} \tag{4.42}$$

$$\lambda_{high} = 1 - \lambda_{low} \tag{4.43}$$

According to the different strategies used in the low-speed zone, can be divided into closed-loop hybrid sensorless control method and open-loop start-up based hybrid sensorless control method.

4.3.1 Closed-Loop Hybrid Sensorless Control Strategy

This strategy combines algorithm based on the saliency of the machine for zero and low-speed with methods for medium and high-speed [110, 238, 239]. It utilizes speed and current closed-loop control in the whole speed range, and through the design of appropriate switching strategy, it enables the machine to achieve good performance of sensorless control in the full-speed range[237, 240, 241]. There are many studies that combine high-frequency signal injection method with variable sensorless schemes such as MRAS [241-243], observer [229, 244-246], SMO [246-248], back-EMF estimator [108, 249], extend Back-EMF [166, 249] etc. In [250], an INFORM estimate for low speed is combined with an EMF based observer.

4.3.2 Open-Loop Start-Up Based Hybrid Sensorless Control Strategy

The control strategy mentioned in Chapter 4.3.1 needs to estimate the actual rotor position by detecting the machine state variables and use it in speed and current closed-loop for sensorless control. In some applications where the control accuracy and dynamic response are not high, open-loop start-up has a considerable application prospect, which is usually divided into V/F control and I/F control.

4.3.2.1 V/F Start-Up Strategy

The V/F control mode [251] ensures that the output voltage is proportional to the operating frequency, i.e., V/F is constant in most speed ranges. This kind of control method is not dependent on the machine parameters, the structure is simple, and it is very suitable for the application where the dynamic performance requirements are not high.

Figure 4.18 is the block diagram of V/F open-loop control of PMSM system. The given voltage amplitude U_s is determined according to the pre-set V/F curve, and the reference position of machine control is obtained by integration of ω_e. The two stator phase voltages u_α, u_β are obtained by coordinate transformation, and then three groups of symmetrical complementary PWM signals are generated by SVPWM module. Finally, the inverter outputs three-phase stator voltages to control the machine.

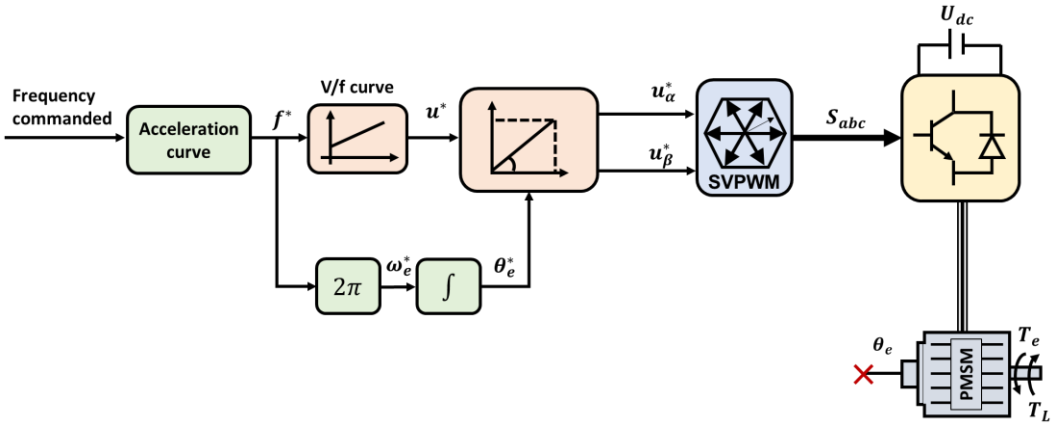


Figure 4.18 Block diagram of V/F control for PMSM.

The core of V/F control is the open-loop V/F curve, which determines the stator voltage amplitude of inverter output at different speeds. The V/F curve is usually set as a straight line with a fixed slope to keep the ratio of voltage to frequency constant. At present, the V/F curve of PMSM is generally a multi-segment polyline so that users can flexibly adjust the dividing points on the curve according to the actual application and produce the most suitable V/F curve.

4.3.2.2 I/F Start-Up Strategy

I/F control realizes the closed-loop control of stator current based on V/F control. The current feedback value is constrained by the expected value to avoid over-current. The

control principle block diagram is shown in Figure *4.19*. A current closed-loop is formed in *dq* coordinate system, and the current error is regulated by PI controller so that the feedback current is constrained by the current command. The position information used in coordinate transformation is provided by the integration of speed command. In this control mode, according to the change of the given angular frequency, the magnetic field of accelerating rotation can be generated in the air gap, and the rotor of the traction machine can be accelerated to start up.

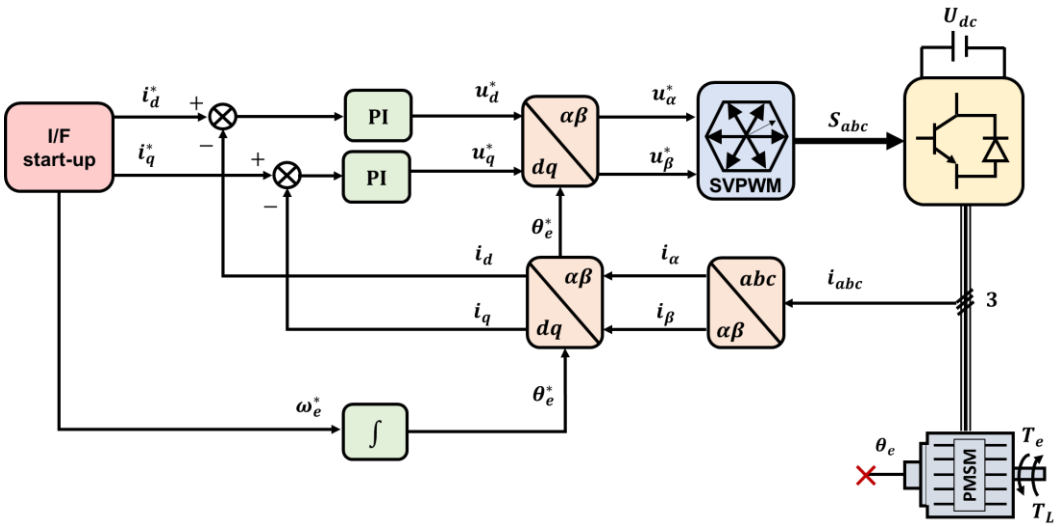


Figure 4.19 *Block diagram of I/F control for PMSM.*

4.4 Chapter Summary

Based on the mathematical model of PMSM, the principles, and characteristics of the sensorless control algorithm in different speed ranges are introduced. The main findings of this chapter can be summarised as follows:

- Several practical sensorless algorithms are overviewed. The first group of sensorless algorithm based on machine mathematic model is suitable for

middle- and high-speed sections, such as back-EMF estimation method, observer based adaptive algorithm, etc. These methods have simple operation, good dynamic characteristics, low requirements for machine construction, good universality for different types of machines, but they are not available for low speed and sensitive to parameter variation.

- The second group based on high frequency response is applicable to zero speed and low speed applications. They need the saliency information of machine, and the speed and position estimation performance are greatly affected by filter parameters, hardware sampling speed and other factors.
- In addition, there is a kind of control strategy, that is, the V/F and I/F open-loop control, which can also realize the sensorless operation of PMSM and usually be applied as a start-up strategy.
- In order to make the permanent magnet synchronous machine drive system run in the full speed range without mechanical sensors, it is necessary to select different sensorless algorithms according to the speed range, and set up a reasonable switch strategy, so that they can be integrated into a full speed scheme suitable for zero speed, low speed, and high speed operation.
- Due to the advantages and disadvantages of different algorithms and control strategies, it is necessary to determine the optimal integration scheme according to the actual operation conditions of PMSM drive system and consider the switching process between different algorithms or control strategies to ensure the smoothness and reliability of switching.

The algorithm theory and performance analysis obtained in this chapter effectively guide the implementation technology in the follow-up research and the operation verification of the actual system. The next two chapters will focus on the sensorless algorithm which is suitable for the DTP-PMSM established in the Chapter 3 and analyse the critical techniques in detail.

Chapter 5 Model Reference Adaptive System Based Sensorless Control Strategy at Middle- and High-Speed

In the previous chapter, various sensorless control strategies have been reviewed. Among them, MRAS is relatively robust and simple in implementation. Hence, in this chapter, the control scheme of MRAS is detailed and different types of MRAS structure are discussed and compared. The shortage of the conventional MRAS is pointed out and enhanced solutions are proposed.

5.1 Conventional Model Reference Adaptive System Method

Among all the strategies to control and estimate the speed of PMSM drives that are discussed in the previous chapter, MRAS is a well-established technique that has attracted much attention because of simplicity and direct physical interpretation [252]. MRAS is classified into closed loop state observer method that is shown in Figure 5.1. If the correction part uses model reference adaptive observer, the closed loop state observer transforms to a MRAS.

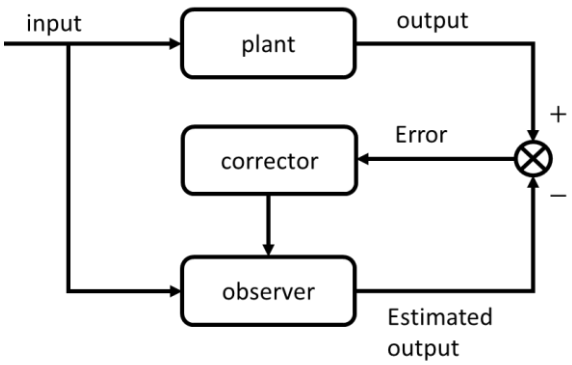


Figure 5.1 Block diagram of closed loop state observer[253].

The preliminary idea of MRAS technique [254] is to adjust the state variables of a system under study using two sub-models (reference model and adaptive model) and find out an adaptation mechanism to minimise the error between these two models in order to estimate a desired physical quantity. The parallel MRAS is most widely used at present, and its configuration is shown in Figure 5.2.

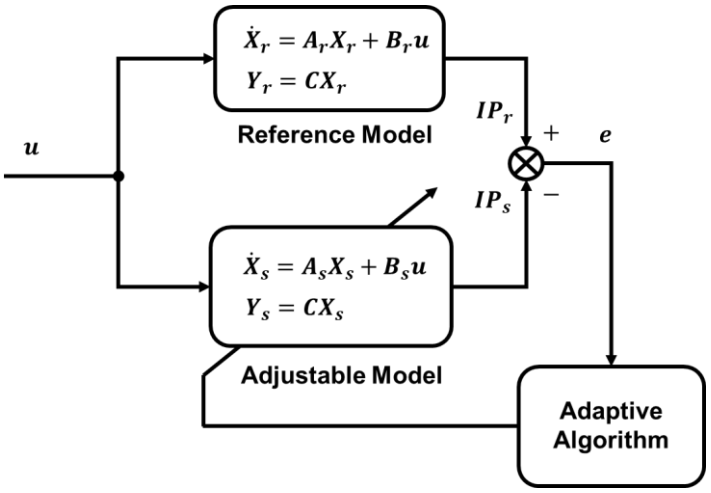


Figure 5.2 Configuration of the parallel MRAS[235].

The reference model is based on a set of equations which does not include the parameter needs to be estimated. On the contrary, the adaptive model is used to observe the same state variables with different sets of equations that employ different inputs among which there are parameters to be estimated. The stability of a drive system is achieved by minimising the error between the two models signals based on either stator current [132, 255] or rotor flux [256, 257] or electromagnetic torque [258, 259], etc. A set of adaptive laws such as Popov's criterion of hyperstability [260, 261], Lyapunov stability theorem [262, 263] and recursive least-square (RLS) algorithm [264] has been widely considered to minimise the error signal. One such adaptation mechanism based on the hyperstability concept with two blocks in the feedback systems is shown in Figure 5.3.

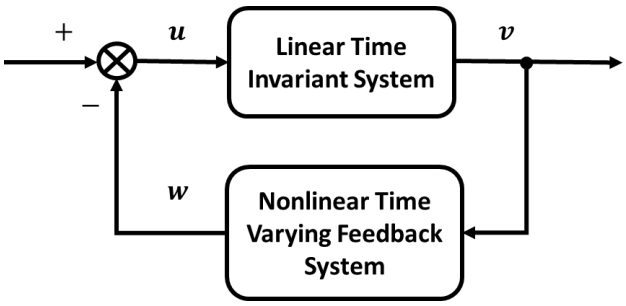


Figure 5.3 Basic structure of nonlinear feedback system[265].

A system is defined as asymptotically hyperstable if the linear time-invariant forward-path transfer matrix is strictly real-positive and that the non-linear feedback (which includes the adaptation mechanism) satisfies Popov's criterion for hyperstability [266, 267].

5.1.1 The Principle of MRAS

In state space, the reference model can be expressed as

$$\dot{X}_r = A_r X_r + B_r u \tag{5.1}$$

$$Y_r = C X_r \tag{5.2}$$

And the adjustable model can be expressed as

$$\dot{X}_s = A_s X_s + B_s u \tag{5.3}$$

$$Y_s = C X_s \tag{5.4}$$

where X_r and X_s are the model state vectors (n×1) of the reference model and the adjustable model, and u is the input vector (m×1) to both models; Y_r and Y_s are the output vectors (r×1) of both models; A_r(n×n), B_r(n×m), A_s(n×n), and B_s(n×m) are time varying matrices; C(r×n) is the output matrix.

The system is dedicated to identify the values of A_r and B_r that vary during operation. The index of performance (IP) of each model can be a function of the output, or a function of the output and the states. The difference between IP_r and IP_s, e, is fed to a block named adaptation mechanism, which modifies the parameters of A_s and B_s until they match those of the reference model so that IP_r and IP_s converge and e becomes zero. Given that the structure of the reference model is known, the identification issue is to design an appropriate adaptation mechanism to ensure the convergence. According to [268], the above system can be represented by an equivalent one. For example, let $e = X_r - X_s$, then subtract (5.1) from (5.3) gives

$$\begin{aligned} \dot{e} &= \dot{X}_r - \dot{X}_s \\ &= A_r X_r - A_s X_s + (B_r - B_s)u \\ &= A_r X_r - A_r X_s + A_r X_s - A_s X_s + (B_r - B_s)u \\ &= A_r e + (A_r - A_s)X_s + (B_r - B_s)u \end{aligned} \tag{5.5}$$

For fast convergence, it is desirable for the adaptation scheme to be able to memorize the previous good values, and therefore one possible form of A_s and B_s is provided [268] as

$$A_s = \int_0^t Y_1(e,t)dt + Y_2(e,t) + A_s(0) \tag{5.6}$$

$$B_s = \int_0^t Z_1(e,t)dt + Z_2(e,t) + B_s(0) \tag{5.7}$$

where Y_1 and Z_1 are n×n and m×n matrices respectively, which denote a nonlinear time-varying relation between A_s, B_s and the values of $e(t)$. Y_2 and Z_2 are matrices of the

same dimensions which denote a nonlinear time-varying relation between A_s, B_s and the values of $e(t)$ and are null for e=0.

From (5.5)-(5.7), one can obtain

$$\dot{e} = A_r e - W \tag{5.8}$$

$$\begin{aligned} W = &\left(\int_0^t Y_1(e,t)dt + Y_2(e,t) + A_s(0) - A_r\right) X_s \\ &+ \left(\int_0^t Z_1(e,t)dt + Z_2(e,t) + B_s(0) - B_r\right) u \end{aligned} \tag{5.9}$$

(5.8) and (5.9) facilitate the construction of the equivalent system shown in Figure 5.4, which is equivalent to that in Figure 5.2.

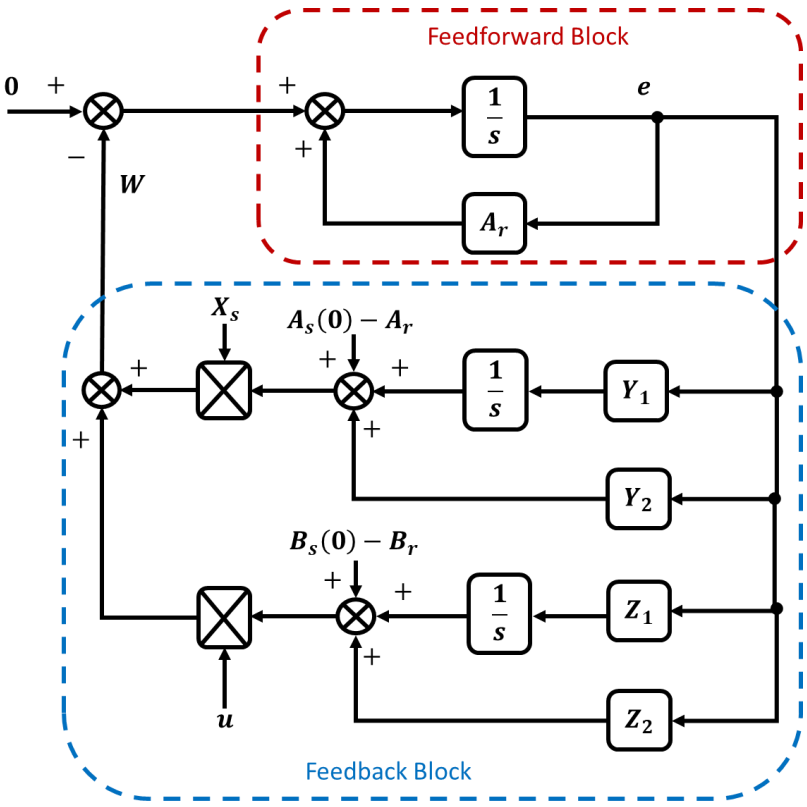


Figure 5.4 The equivalent representation of the MRAS.

The design of the system depends on the suitable selection of Y_1, Y_2, Z_1 and Z_2. This can be achieved with the concept of the hyperstability [254]. If the feedforward block is positive real, and the feedback block satisfies the Popov integral inequality, the system in Figure 5.4 can be claimed to be a hyperstable one that guarantees the convergence of *e* to zero. The Popov integral inequality given in (5.10) leads to the choice of the Y_1, Y_2, Z_1 and Z_2.

$$\eta(t_1) = \int_0^{t_1} e^T W dt \geq -\gamma_0^2 \qquad \text{for all } t_1 \geq 0 \tag{5.10}$$

where γ_0 is a finite positive constant. Once Y_1, Y_2, Z_1 and Z_2 are determined, the adaptation mechanism and hence the MRAS, which is capable of identifying the parameters in the reference model, are defined.

5.1.2 Estimation of PMSM Speed Based on MRAS

There are usually two approaches to establish the reference model of PMSM. One is to use the current equation as the reference model, and the other is to use the flux linkage equation as the reference model. In this section, the former method is introduced. According to the mathematical model of PMSM in (5.11), it can be seen that the current equation contains speed information, so the motor can be viewed as the reference model, and the current model containing the estimated variables is the adjustable model. Stator voltage being the input, the stator current measured by the current sensor is the output of the reference model, and the current solved by the current equation is the output of the adjustable model. Under the effect of the adaptive law, current output of the adjustable model will track the actual current signal, and the coefficient matrix will also

follow the parameter matrix of the reference model. Thus, the speed to be estimated will track the actual speed to achieve the self-adaptation of speed identification.

The stator current formula of PMSM under *dq* rotating frame is:

$$\begin{bmatrix} \frac{di_d}{dt} \\ \frac{di_q}{dt} \end{bmatrix} = \begin{bmatrix} -\frac{R}{L_d} & \frac{L_q}{L_d}\omega_e \\ -\frac{L_d}{L_q}\omega_e & -\frac{R}{L_q} \end{bmatrix} \begin{bmatrix} i_d \\ i_q \end{bmatrix} + \begin{bmatrix} \frac{u_d}{L_d} \\ \frac{u_q}{L_q} - \frac{\omega_e}{L_q}\varphi_m \end{bmatrix} \tag{5.11}$$

To apply Popov hyperstability theory to the system, (5.11) is rewritten by defining like (5.12)-(5.15):

$$i'_d = i_d + \frac{\varphi_m}{L_d} \tag{5.12}$$

$$i'_q = i_q \tag{5.13}$$

$$u'_d = u_d + \frac{R\varphi_m}{L_d} \tag{5.14}$$

$$u'_q = u_q \tag{5.15}$$

Hence, the rewritten model of (5.11) is got in (5.16) which is defined as the reference model in MRAS.

$$\frac{d\boldsymbol{i}'}{dt} = \boldsymbol{A_r}\boldsymbol{i}' + \boldsymbol{B_r}\boldsymbol{u}' \tag{5.16}$$

where

$$\boldsymbol{i}' = \begin{bmatrix} i'_d \\ i'_q \end{bmatrix} \tag{5.17}$$

$$\boldsymbol{A_r} = \begin{bmatrix} -\frac{R}{L_d} & \frac{L_q}{L_d}\omega_e \\ -\frac{L_d}{L_q}\omega_e & -\frac{R}{L_q} \end{bmatrix} \tag{5.18}$$

$$\boldsymbol{B_r} = \begin{bmatrix} \frac{1}{L_d} & 0 \\ 0 & \frac{1}{L_q} \end{bmatrix} \tag{5.19}$$

$$\boldsymbol{u'} = \begin{bmatrix} u'_d \\ u'_q \end{bmatrix} \tag{5.20}$$

The adjustable model in MRAS can be presented in (5.21) according to the reference model in (5.16).

$$\frac{d\hat{\boldsymbol{i}}'}{dt} = \boldsymbol{A_s}\hat{\boldsymbol{i}}' + \boldsymbol{B_s}\boldsymbol{u'} \tag{5.21}$$

where

$$\hat{\boldsymbol{i}}' = \begin{bmatrix} \hat{i}'_d \\ \hat{i}'_q \end{bmatrix} \tag{5.22}$$

$$\boldsymbol{A_s} = \begin{bmatrix} -\frac{R}{L_d} & \frac{L_q}{L_d}\hat{\omega}_e \\ -\frac{L_d}{L_q}\hat{\omega}_e & -\frac{R}{L_q} \end{bmatrix} \tag{5.23}$$

$$\boldsymbol{B_s} = \begin{bmatrix} \frac{1}{L_d} & 0 \\ 0 & \frac{1}{L_q} \end{bmatrix} \tag{5.24}$$

The error of the MRAS current estimator is given as

$$\boldsymbol{e} = \boldsymbol{i}' - \hat{\boldsymbol{i}}' \tag{5.25}$$

Substract (5.21) from (5.16) giving

$$\frac{d\boldsymbol{e}}{dt} = \boldsymbol{A_s e} - \boldsymbol{W} \tag{5.26}$$

where

$$\boldsymbol{W} = (\boldsymbol{A_s} - \boldsymbol{A_r})\hat{\boldsymbol{i}}' = \boldsymbol{J}(\omega_e - \hat{\omega}_e)\hat{\boldsymbol{i}}' \tag{5.27}$$

$$\boldsymbol{J} = \begin{bmatrix} 0 & -\frac{L_q}{L_d} \\ \frac{L_d}{L_q} & 0 \end{bmatrix} \tag{5.28}$$

The equivalent representation of the MRAS for speed estimation is shown in Figure 5.5.

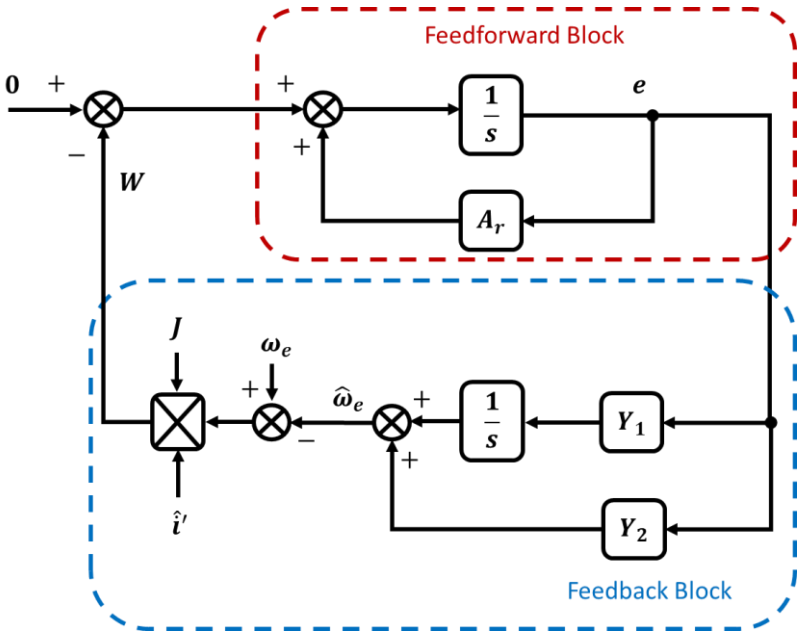


Figure 5.5 The equivalent presentation of the MRAS for speed estimation [235].

Applying (5.10) to this system indicates one possible solution that can ensure the hyperstability [132, 269], which is

$$Y_1 = k_i(\boldsymbol{i}' \times \hat{\boldsymbol{i}}') \tag{5.29}$$

$$Y_2 = k_p(\boldsymbol{i}' \times \hat{\boldsymbol{i}}') \tag{5.30}$$

where k_p and k_i are positive numbers, $\boldsymbol{i}' \times \hat{\boldsymbol{i}}'$ is the inner product between the reference rotor current vector and the estimated rotor current vector.

$$\boldsymbol{i}' \times \hat{\boldsymbol{i}}' = i_d\hat{i}_q - i_q\hat{i}_d - \frac{\varphi_m}{L_q}(i_q - \hat{i}_q) \tag{5.31}$$

The estimated rotor speed is achieved based on the hyperstability theory.

$$\begin{aligned}\hat{\omega}_e &= \frac{Y_1}{s} + Y_2 \\ &= \left(\frac{k_i}{s} + k_p\right)\left(i_d\hat{i}_q - i_q\hat{i}_d - \frac{\varphi_m}{L_q}\left(i_q - \hat{i}_q\right)\right) + \hat{\omega}_e(0)\end{aligned} \tag{5.32}$$

The rotor position is obtained by integrating of rotor speed.

$$\hat{\theta}_e = \int_0^t \hat{\omega}_e dt + \hat{\theta}_e(0) \tag{5.33}$$

One practical realization of the MRAS for the speed adaptation is shown in Figure 5.6.

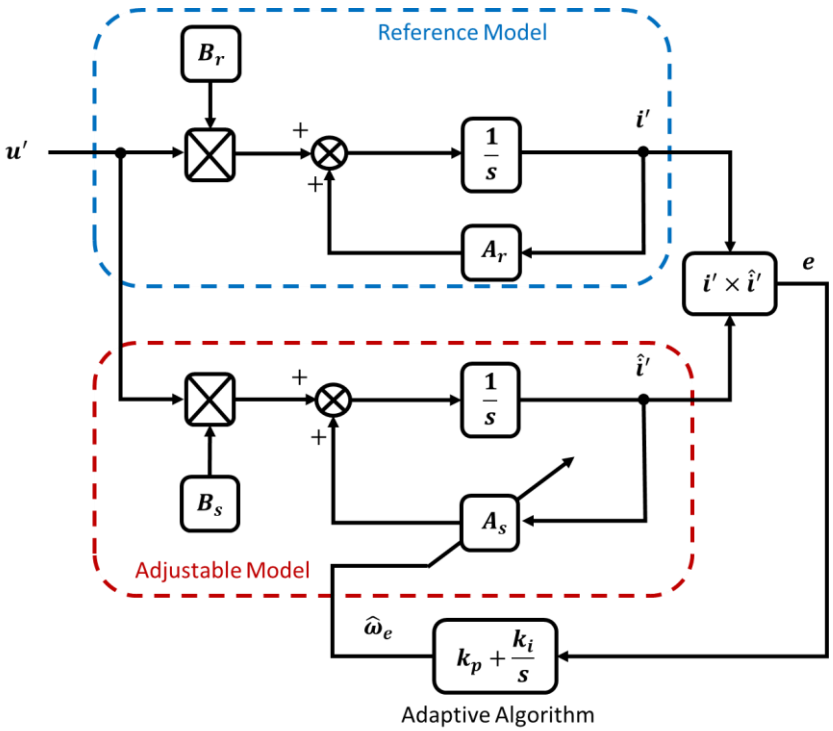


Figure 5.6 System schematic of MRAS for speed estimation.

5.1.3 Limitation of Conventional MRAS

The MRAS is quite simple to implement, sufficiently robust and accurate at higher stator frequencies. However, in most cases, MRAS shows high sensitivity to parameters [270]. The motor parameters are affected by the working environment. For instance, the temperature rises up as the machine running. Consequently, the resistance of the winding increases, the output energy density of rotor permanent magnet decreases, the demagnetization effect occurs, the PM flux amplitude decreases. If the magnetic circuit saturation occurs during the machine running, the inductance amplitude will decrease with the increase of the current [271]. These problems will lead to poor speed estimation performance of MRAS. Therefore, the online tuning of parameters is necessary and important to optimize MRAS sensorless control system.

5.2 Parameter Sensitivity Analysis of Conventional MRAS Based Sensorless Control Method

From the previous derivation, the main parameters in the PMSM model are as follows: stator resistance R, permanent magnet rotor flux linkage φ_m, direct axis inductance L_d and quadrature axis inductance L_q. The sensorless control of PMSM depends on the mathematic model containing these parameters. In general, these parameters can be obtained by off-line measurement. However, they will change with the variation of working condition and working time. The deviation of them brings about the error of position estimation or speed estimation in sensorless control. Errors caused by these offsets will reduce the efficiency of motor operation, and even lead to system instability when the error is too large. In this section, the parameter offset of PMSM is introduced in detail.

5.2.1 Current-sensitive Parameters

The direct and quadrature axis inductances of PMSM are directly related to the stator current. Different from IM, PMSM has no rotor current to counteract the magnetomotive force of stator current. When the current in stator winding is large, a strong armature magnetic field will be generated outside the excitation magnetic field of permanent magnet. Due to the nonlinearity of the B-H curve of the motor core material, when the magnetic field is strong, the core material will enter the saturation state and lead to the decrease of the permeability, resulting in the decrease of the inductance. When the hysteresis in the B-H curve is neglected, the magnetomotive force

generated by the current corresponds to the flux linkage, thereby the inductance and the current also correspond to each other [102].

In the general closed-loop control system of PMSM, the motor current is measured directly through the sensor to perform the current closed-loop control. Since the values of the current sensitive parameters correspond directly to the current, the best way to identify the current sensitive parameters is to establish the lookup tables between current and parameters, and then update the parameters through on-line look-up and interpolation. The lookup table between stator current and inductance in this study is shown in Table 5-1.

Table 5-1 Lookup table between stator current and dq-axis inductance for ACHIEVE machine.

Current RMS (A)	23		11.5		5.75	
Phase Advance	Ld (mH)	Lq (mH)	Ld (mH)	Lq (mH)	Ld (mH)	Lq (mH)
0	0.32335	0.3576	0.31655	0.3584	0.30775	0.358
10	0.36775	0.35175	0.3647	0.35495	0.35125	0.35885
20	0.36405	0.35585	0.3626	0.3587	0.3484	0.36065
30	0.3701	0.35925	0.368	0.362	0.35015	0.3624
40	0.3765	0.3623	0.37395	0.365	0.35355	0.36395
50	0.3821	0.36525	0.379	0.3678	0.3565	0.36535
60	0.3869	0.36775	0.38305	0.3704	0.35865	0.3665
70	0.39075	0.36955	0.3862	0.37245	0.36015	0.3676
80	0.39345	0.37115	0.3883	0.3742	0.36105	0.3697
90	0.38885	0.3803	0.38055	0.3758	0.3373	0.35935

5.2.2 Temperature-sensitive Parameters

Among the parameters of PMSM, the resistivity of copper or aluminium used in stator windings will go up with the rise of temperature, so the stator resistance of motors will

increase with the rise of winding temperature. Therefore, the stator resistance is regarded as a temperature sensitive parameter.

In the ACHIEVE machine, a thermocouple embedded in the stator winding is used to measure the resistance of the stator winding under the variation of the temperature. As shown in Figure 5.7, stator winding resistance is proportional to the winding temperature according to the relationship in (5.34) [272].

$$R_\tau = R_0 * \left(1 + \alpha * (T - T_0)\right) \tag{5.34}$$

where α is the constant determined by the material (for copper, $\alpha = 0.393\%/℃$). $T_0 = 20℃$. R_0 is the resistance value measured at temperature T_0. R_τ is the resistance value at temperature $T(℃)$.

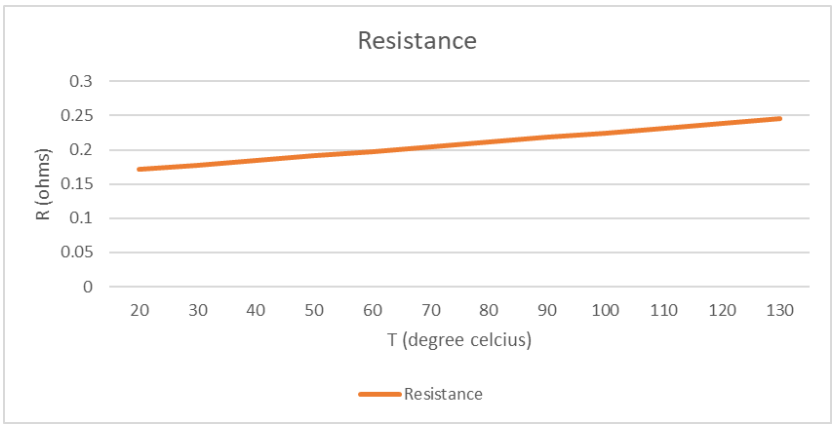


Figure 5.7 Resistance of stator winding varying against winding temperature for ACHIEVE machine.

The rotor flux linkage of PMSM is also considered as a temperature sensitive parameter, and the main heat sources affecting the winding and magnet are different. The temperature rise of stator winding mainly comes from the heat dissipation of the current in the conductor. In contrast, the heating up of permanent magnets is mainly due to the

heat dissipation of eddy current generated when various high-frequency harmonic magnetic fields cut the permanent magnet. Besides, the heat dissipation of permanent magnet is relatively serious at high speed, while that of stator winding is more serious at high current overload.

Although the heat sources of these two components are different, they are not completely independent of each other due to the heat conduction and radiation inside the motor. For example, at low speed and high torque, according to the second law of thermodynamics, the heat dissipation of the stator winding will heat the rotor through thermal radiation. The PM flux of ACHIEVE machine under various stator current against different temperature obtained by Finite Element Analysis (FEA) is depicted in Figure 5.8. The remanence temperature coefficient of permanent materials used in rotor, such as Samarium Cobalt (Recoma 33E) in ACHIEVE is negative [144], so when the temperature of the permanent magnet rises, the excitation capacity of it will decrease hence the rotor flux will decrease as shown in Figure 5.8.

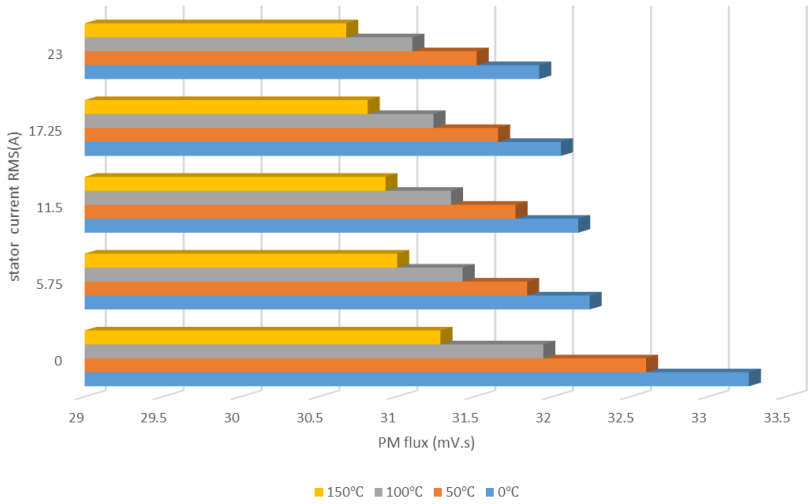


Figure 5.8 PM flux under various temperature and stator current for ACHIEVE machine.

When the operating frequency increases, the stator resistance will also go up due to the skin effect in the winding wires. But the skin effect of the stator winding should not be obvious if the stator winding is carefully designed and manufactured. Moreover, the rotor flux will be reduced by the magnetic field that is induced by the eddy current in the stator core as the frequency increases. However, for the stator core with laminated structure, this effect is very small.

5.3 Model Observability Analysis of Permanent Magnet Synchronous Motor

Since the parameters of PMSM will vary with the change of working conditions, it is necessary to identify the machine parameters in real time for the machine model dependent algorithms such as sensorless control. Besides, parameters of PMSM can reflect the real-time working status of machine. For instance, the rotor flux and stator resistance can reflect the temperature of the rotor and stator, respectively, while the inductance can reflect the saturation degree of the motor core. However, the number of machine parameters that can be simultaneously identified in a steady state machine is limited without signal injection. This is because that the identification of parameters is based on the mathematical model of PMSM. There are only two dimensions of the PMSM in the steady-state, which means that when the current is observable, there are only two degrees of freedom to identify the parameters. When the number of parameters to be identified exceeds the degree of freedom, there is no unique solution. Because the identification of all parameters affects each other and there are infinite combinations, the final identification result cannot converge [102]. The observability matrix can be used to judge the state observability and parameter identifiability of the machine model, which will be applied to the system proposed in the following chapter.

5.3.1 Observability of MRAS Based PMSM Sensorless System with Parameters Identification

The mathematic model of PMSM in $\alpha\beta$ coordinate frame is presented as:

$$\frac{di_\alpha}{dt} = \frac{u_\alpha}{L_q} - \frac{R}{L_q} i_\alpha + \left(2L_1\left(\omega_e i_d + \frac{di_d}{dt}\right) + \omega_e \varphi_m\right)\frac{sin\theta_e}{L_q} \tag{5.35}$$

$$\frac{di_\beta}{dt} = \frac{u_\beta}{L_q} - \frac{R}{L_q} i_\beta - \left(2L_1\left(\omega_e i_d + \frac{di_d}{dt}\right) + \omega_e \varphi_m\right)\frac{cos\theta_e}{L_q} \tag{5.36}$$

where $L_1 = (L_d - L_q)/2$.

If the rotor speed and position are estimated by MRAS，the following two equations can help to improve the degree of freedom of parameter identification.

$$\frac{d\theta_e}{dt} = \omega_e \tag{5.37}$$

$$\frac{d\omega_e}{dt} = 0 \tag{5.38}$$

Considering the identification of the rotor flux, the following equation is supplemented.

$$\frac{d\varphi_m}{dt} = 0 \tag{5.39}$$

Thereby, the rotor flux identification model of sensorless system is built by (5.35)-(5.39). The steady state observability matrix can be expressed as：

$$\begin{bmatrix} \frac{\partial \mathcal{L}_f^0 h_1}{\partial \theta_e} & \frac{\partial \mathcal{L}_f^0 h_1}{\partial \omega_e} & \frac{\partial \mathcal{L}_f^0 h_1}{\partial \varphi_m} \\ \frac{\partial \mathcal{L}_f^0 h_2}{\partial \theta_e} & \frac{\partial \mathcal{L}_f^0 h_2}{\partial \omega_e} & \frac{\partial \mathcal{L}_f^0 h_2}{\partial \varphi_m} \\ \frac{\partial \mathcal{L}_f^1 h_1}{\partial \theta_e} & \frac{\partial \mathcal{L}_f^1 h_1}{\partial \omega_e} & \frac{\partial \mathcal{L}_f^1 h_1}{\partial \varphi_m} \\ \frac{\partial \mathcal{L}_f^1 h_2}{\partial \theta_e} & \frac{\partial \mathcal{L}_f^1 h_2}{\partial \omega_e} & \frac{\partial \mathcal{L}_f^1 h_2}{\partial \varphi_m} \\ \frac{\partial \mathcal{L}_f^2 h_1}{\partial \theta_e} & \frac{\partial \mathcal{L}_f^2 h_1}{\partial \omega_e} & \frac{\partial \mathcal{L}_f^2 h_1}{\partial \varphi_m} \\ \frac{\partial \mathcal{L}_f^2 h_2}{\partial \theta_e} & \frac{\partial \mathcal{L}_f^2 h_2}{\partial \omega_e} & \frac{\partial \mathcal{L}_f^2 h_2}{\partial \varphi_m} \end{bmatrix} = \begin{bmatrix} 0 & 0 & 0 \\ 0 & 0 & 0 \\ cos\theta_e & sin\theta_e & sin\theta_e \\ sin\theta_e & -cos\theta_e & -cos\theta_e \\ \mathcal{O}_1 & \mathcal{O}_2 & \mathcal{O}_3 \end{bmatrix} \tag{5.40}$$

$$\mathcal{O}_1 = \begin{bmatrix} -Rcos\theta_e - \omega_e L_q sin\theta_e \\ -Rsin\theta_e + \omega_e L_q cos\theta_e \end{bmatrix} \tag{5.41}$$

$$\mathcal{O}_2 = \begin{bmatrix} -Rsin\theta_e + 2\omega_e L_q cos\theta_e \\ Rcos\theta_e + 2\omega_e L_q sin\theta_e \end{bmatrix} \tag{5.42}$$

$$\mathcal{O}_3 = \begin{bmatrix} -Rsin\theta_e + \omega_e L_q cos\theta_e \\ Rcos\theta_e + \omega_e L_q sin\theta_e \end{bmatrix} \tag{5.43}$$

Take the third, fourth and fifth rows of the matrix in (5.40) to form a square matrix $\mathcal{O}_4$ as shown in (5.44).

$$\mathcal{O}_4 = \begin{bmatrix} cos\theta_e & sin\theta_e & sin\theta_e \\ sin\theta_e & -cos\theta_e & -cos\theta_e \\ -Rcos\theta_e - \omega_e L_q sin\theta_e & 2\omega_e L_q cos\theta_e - Rsin\theta_e & \omega_e L_q cos\theta_e - Rsin\theta_e \end{bmatrix} \tag{5.44}$$

The determinant of $\mathcal{O}_4$ is solved as：

$$det(\mathcal{O}_4) = \omega_e L_q cos\theta_e \tag{5.45}$$

Similarly, take the third, fourth and sixth rows of the matrix in (5.40) to form a square matrix $\mathcal{O}_5$ as shown in (5.46):

$$\mathcal{O}_5 = \begin{bmatrix} cos\theta_e & sin\theta_e & sin\theta_e \\ sin\theta_e & -cos\theta_e & -cos\theta_e \\ \omega_e L_q cos\theta_e - Rsin\theta_e & 2\omega_e L_q sin\theta_e + Rcos\theta_e & \omega_e L_q sin\theta_e + Rcos\theta_e \end{bmatrix} \quad (5.46)$$

The determinant of $\mathcal{O}_5$ is solved as:

$$det(\mathcal{O}_5) = \omega_e L_q sin\theta_e \quad (5.47)$$

It can be seen that if the machine speed ω_e is not zero, the rotor flux identification under steady-state operation is observable. More study in [102] shows that for MRAS based PMSM sensorless control system, two parameters cannot be identified at the same time during steady state operation due to lack of observability. Besides, it should be note that lack of observability simply prevents the design of a full-order state observer, the lack of identifiability prevents the design of an idenfitication mechanism.

5.4 Enhanced MRAS Based Sensorless Control Method Considering Parameter Variation

According to the analysis aforementioned, the conventional MRAS suffers from parameter sensitivity which will be discussed and solved in this chapter for a more reliable and robust drive system. As the observability analysis of the PMSM using MRAS, just one parameter could be identified online with the speed estimation. To

overcome this challenge, a cascaded MRAS system is proposed which is able to identify flux linkage and estimate rotor speed.

5.4.1 Principle of Proposed Method

The mathematical model of machine is set as the reference model of the MRAS. For the convenience of derivation, the current model of machine in *dq* frame as shown in (5.11) can be rewritten as:

$$\frac{d\boldsymbol{i}}{dt} = \boldsymbol{A}\boldsymbol{i} + \boldsymbol{B}\boldsymbol{u} + C\boldsymbol{l} \tag{5.48}$$

where

$$\boldsymbol{i} = \begin{bmatrix} i_d \\ i_q \end{bmatrix} \tag{5.49}$$

$$\boldsymbol{u} = \begin{bmatrix} u_d \\ u_q \end{bmatrix} \tag{5.50}$$

$$\boldsymbol{A} = \begin{bmatrix} -\frac{R}{L_d} & \frac{L_q}{L_d}\omega_e \\ -\frac{L_d}{L_q}\omega_e & -\frac{R}{L_q} \end{bmatrix} \tag{5.51}$$

$$\boldsymbol{B} = \begin{bmatrix} \frac{1}{L_d} & 0 \\ 0 & \frac{1}{L_q} \end{bmatrix} \tag{5.52}$$

$$C = -\frac{\varphi_m}{L_q} \tag{5.53}$$

$$\boldsymbol{l} = \begin{bmatrix} 0 \\ \omega_e \end{bmatrix} \tag{5.54}$$

From (5.48), an adjustable model with estimated flux and speed can be derived as：

$$\frac{d}{dt}\begin{bmatrix}\hat{i}_d\\ \hat{i}_q\end{bmatrix}=\begin{bmatrix}-\frac{R}{L_d} & \frac{L_q}{L_d}\hat{\omega}_e\\ -\frac{L_d}{L_q}\hat{\omega}_e & -\frac{R}{L_q}\end{bmatrix}\begin{bmatrix}\hat{i}_d\\ \hat{i}_q\end{bmatrix}+\begin{bmatrix}\frac{1}{L_d} & 0\\ 0 & \frac{1}{L_q}\end{bmatrix}\begin{bmatrix}u_d\\ u_q\end{bmatrix}-\begin{bmatrix}0\\ \frac{\hat{\varphi}_m\hat{\omega}_e}{L_q}\end{bmatrix} \tag{5.55}$$

The adjustable model in (5.55) can be expressed as a nonlinear feedback system as:

$$\frac{d\hat{\boldsymbol{i}}}{dt}=\hat{\boldsymbol{A}}\hat{\boldsymbol{i}}+\boldsymbol{B}\boldsymbol{u}+\hat{C}\hat{\boldsymbol{l}} \tag{5.56}$$

where

$$\hat{\boldsymbol{i}}=\begin{bmatrix}\hat{i}_d\\ \hat{i}_q\end{bmatrix} \tag{5.57}$$

$$\hat{\boldsymbol{A}}=\begin{bmatrix}-\frac{R}{L_d} & \frac{L_q}{L_d}\hat{\omega}_e\\ -\frac{L_d}{L_q}\hat{\omega}_e & -\frac{R}{L_q}\end{bmatrix} \tag{5.58}$$

$$\hat{C}=-\frac{\hat{\varphi}_m}{L_q} \tag{5.59}$$

$$\hat{\boldsymbol{l}}=\begin{bmatrix}0\\ \hat{\omega}_e\end{bmatrix} \tag{5.60}$$

The error of the MRAS current estimator is given as:

$$\boldsymbol{e}=\boldsymbol{i}-\hat{\boldsymbol{i}}=\begin{bmatrix}i_d-\hat{i}_d\\ i_q-\hat{i}_q\end{bmatrix} \tag{5.61}$$

The state equation of the current error can be given by subtracting (5.56) from (5.48):

$$\frac{d\boldsymbol{e}}{dt}=\boldsymbol{A}\boldsymbol{i}+\boldsymbol{B}\boldsymbol{u}+C\boldsymbol{l}-\hat{\boldsymbol{A}}\hat{\boldsymbol{i}}-\boldsymbol{B}\boldsymbol{u}-\hat{C}\hat{\boldsymbol{l}} \tag{5.62}$$

$$= \boldsymbol{A}\boldsymbol{i} - \boldsymbol{A}\hat{\boldsymbol{i}} + \boldsymbol{A}\hat{\boldsymbol{i}} - \widehat{\boldsymbol{A}}\hat{\boldsymbol{i}} + C\boldsymbol{l} - C\hat{\boldsymbol{l}} + C\hat{\boldsymbol{l}} - \hat{C}\hat{\boldsymbol{l}}$$

$$= \boldsymbol{A}\boldsymbol{e} - \Delta\boldsymbol{A}\hat{\boldsymbol{i}} - C\Delta\boldsymbol{l} + \Delta C\hat{\boldsymbol{l}}$$

$$= \boldsymbol{A}\boldsymbol{e} - \boldsymbol{W}$$

where

$$\Delta\boldsymbol{A} = \widehat{\boldsymbol{A}} - \boldsymbol{A} \tag{5.63}$$

$$\Delta C = C - \hat{C} = (\hat{\varphi}_m - \varphi_m)/L_q \tag{5.64}$$

$$\Delta\boldsymbol{l} = \hat{\boldsymbol{l}} - \boldsymbol{l} = \begin{bmatrix} 0 \\ \widehat{\omega}_e - \omega_e \end{bmatrix} \tag{5.65}$$

$$\boldsymbol{W} = \Delta\boldsymbol{A}\hat{\boldsymbol{i}} + C\Delta\boldsymbol{l} - \Delta C\hat{\boldsymbol{l}} \tag{5.66}$$

Define

$$\boldsymbol{J} = \begin{bmatrix} 0 & -\dfrac{L_q}{L_d} \\ \dfrac{L_d}{L_q} & 0 \end{bmatrix} \tag{5.67}$$

Hence

$$\Delta\boldsymbol{A} = \boldsymbol{J}(\omega_e - \widehat{\omega}_e) \tag{5.68}$$

To make the adjustment not fail as the error $\boldsymbol{e}$ in (5.61) tends to be zero, the adaptive algorithm is designed in the form of PI regulator. According to the theory of Popov hyperstability in (5.10), the identification of rotor flux can be given in (5.69):

$$\hat{\varphi}_m = (k_{p1} + \frac{k_{i1}}{s})\left(\widehat{\omega}_e L_q(\hat{i}_q - i_q)\right) + \hat{\varphi}_m(0) \tag{5.69}$$

The estimated rotor speed $\hat{\omega}_e$ in (5.69) is calculated in (5.70).

$$\hat{\omega}_e = (k_{p2} + \frac{k_{i2}}{s})\left(i_d\hat{i}_q - i_q\hat{i}_d + \frac{\hat{\varphi}_m}{L_q}(\hat{i}_q - i_q) \right) + \hat{\omega}_e(0) \tag{5.70}$$

Considering that MRAS is sensitive to machine parameters, a cascaded MRAS system is proposed. The block diagram of the proposed system is shown in Figure 5.9.

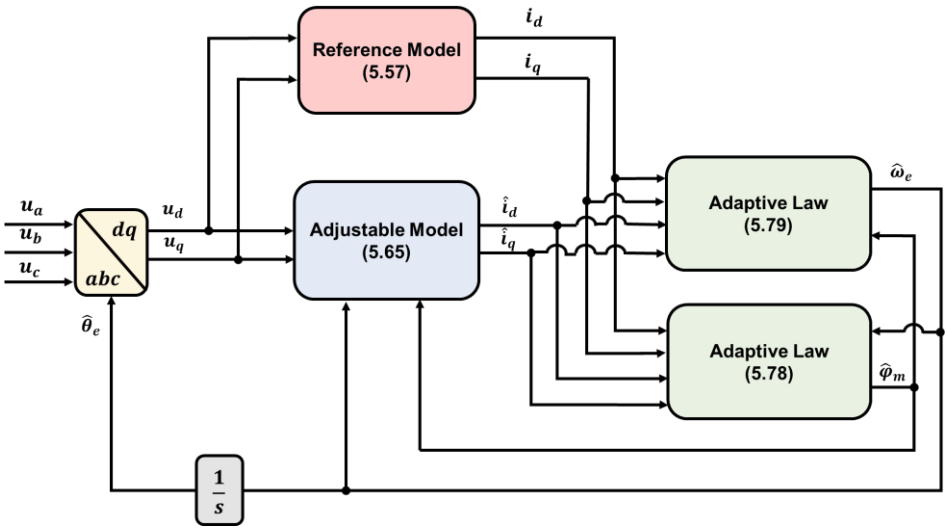


Figure 5.9 Block diagram of proposed cascaded mras system for ACHIEVE system.

The FOC based system consists of a current controller, a speed controller, and a cascaded MRAS observer. The current controller is a standard PI controller with feedforward. The speed controller is also a PI controller. The cascaded MRAS observer estimates rotor position, speed, and rotor flux.

According to (5.69) and the block diagram of MRAS, it is concluded that the rotor speed must be known when identifying rotor flux and the rotor flux must be known when identifying rotor speed. In Figure 5.9, MRAS1 estimates rotor speed while

MRAS2 identifies rotor flux. The step-by-step identification can be described in Figure 5.10.

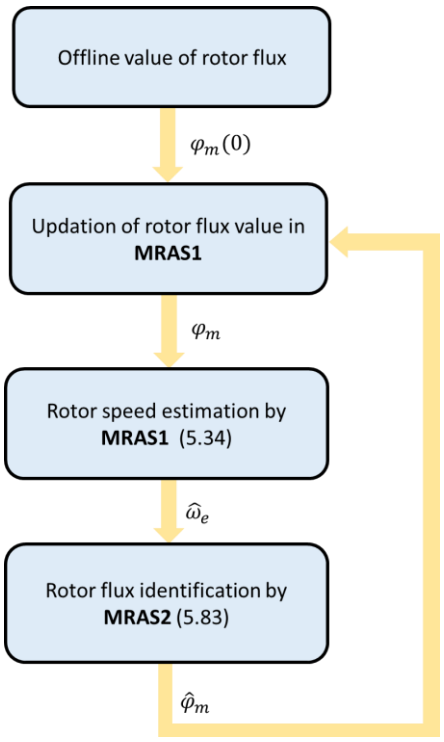


Figure 5.10 Process of cascaded MRAS.

5.4.2 Simulation Results

The simulation verification of proposed sensorless method in Figure 5.11 is carried out in the PLEXIM®/PLECS® environment.

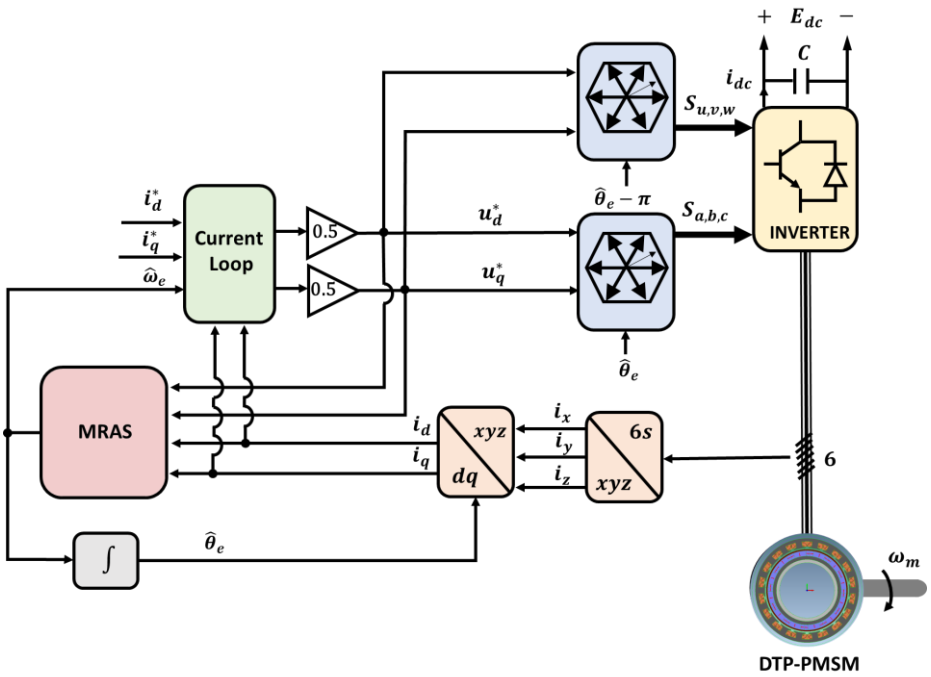


Figure 5.11 Block diagram of MRAS based sensorless control system for ACHIEVE.

During the simulation, machine speed is initially controlled by the given value outside of machine, similar to generating mode. The actual speed and position is applied in the FOC system. This is to avoid MRAS fails in zero- and low-speed range. It should be noticed that in final method, the actual machine speed and position are no longer employed and a hybrid sensorless method covering full-speed range is utilized. When the machine runs into high speed range and sensorless algorithm works properly with satisfactory accuracy, the system becomes working in motoring mode. The machine speed is controlled by the mechanical motion equation of machine in (3.24) and estimated rotor speed and rotor position are applied in the FOC system. Comparison study is made between MRAS and enhanced MRAS. Specifically, there are three scenarios to discuss performance under speed variation, load variation and parameter variation.

In the first scenario, the performance of two methods in terms of speed variation is simulated and compared. The machine runs at 10 krpm initially with no load. Then a step increase of 2.4 krpm is applied to the speed reference N*. After that, a step decrease of 2.4 krpm is applied to the speed reference N*.

In Figure 5.12, the simulation results of MRAS control system are presented. In steady state, the speed estimation error is less than 5 rpm (0.05% of speed) and the rotor position estimation error is about 0.3 degrees which can fully meet the closed-loop speed regulation requirements of machine. During the dynamic response, the accuracy of estimation gets worse, and ripples are observed in estimated variables. For the speed estimation error, the maximum value (absolute value) during dynamic response could go up to 140 rpm (1.4% of speed). For the rotor position estimation error, the maximum value during dynamic response is around 1.1 degrees which is slightly bigger than that of steady state but does not effect good quality of estimate.

In Figure 5.13, the simulation results of enhanced MRAS control system are presented. PM flux is estimated in this system. The flux estimation control has satisfactory performance for both steady state and dynamic response. The flux estimation error in steady state is less than 0.7%. In dynamic response, it takes 0.6 s to arrive steady state with less than 5% overshoot. The estimation of rotor speed and position has as good performance as that of MRAS control system. Hence, both methods have shown satisfactory performance in the presence of speed disturbances.

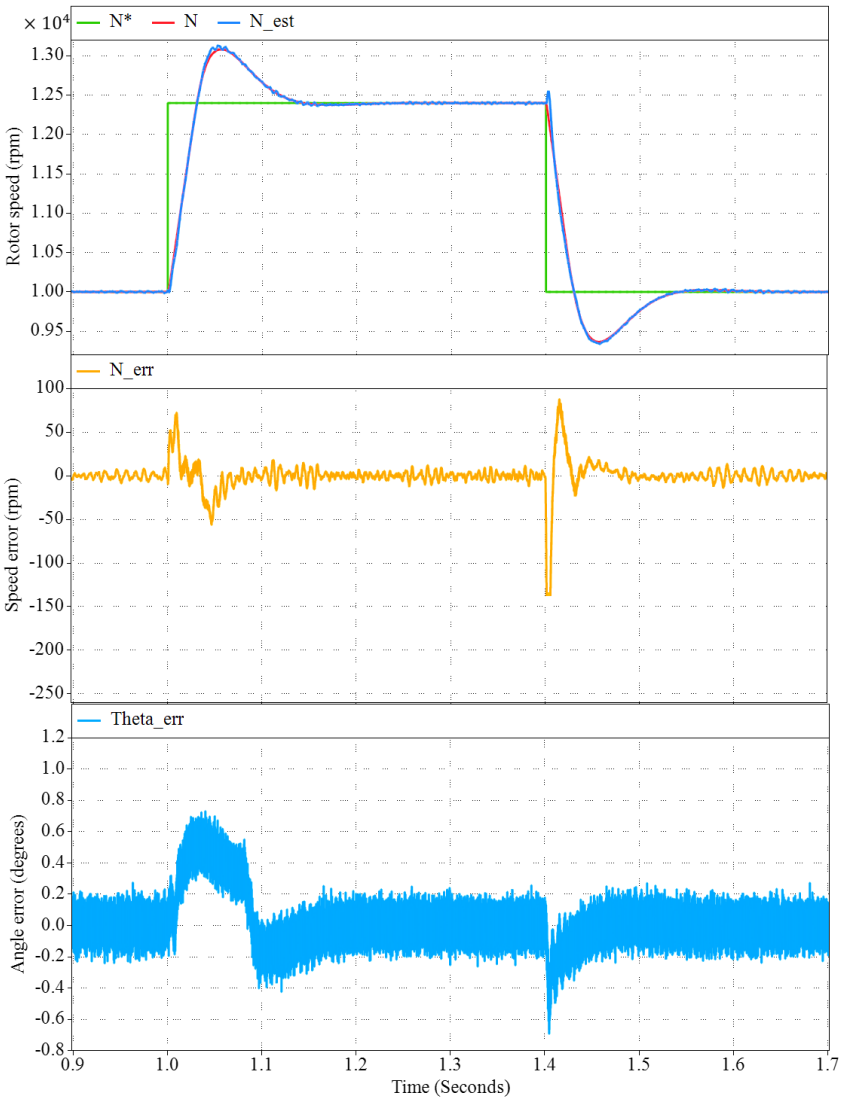


Figure 5.12 Simulation results of MRAS under speed variation.

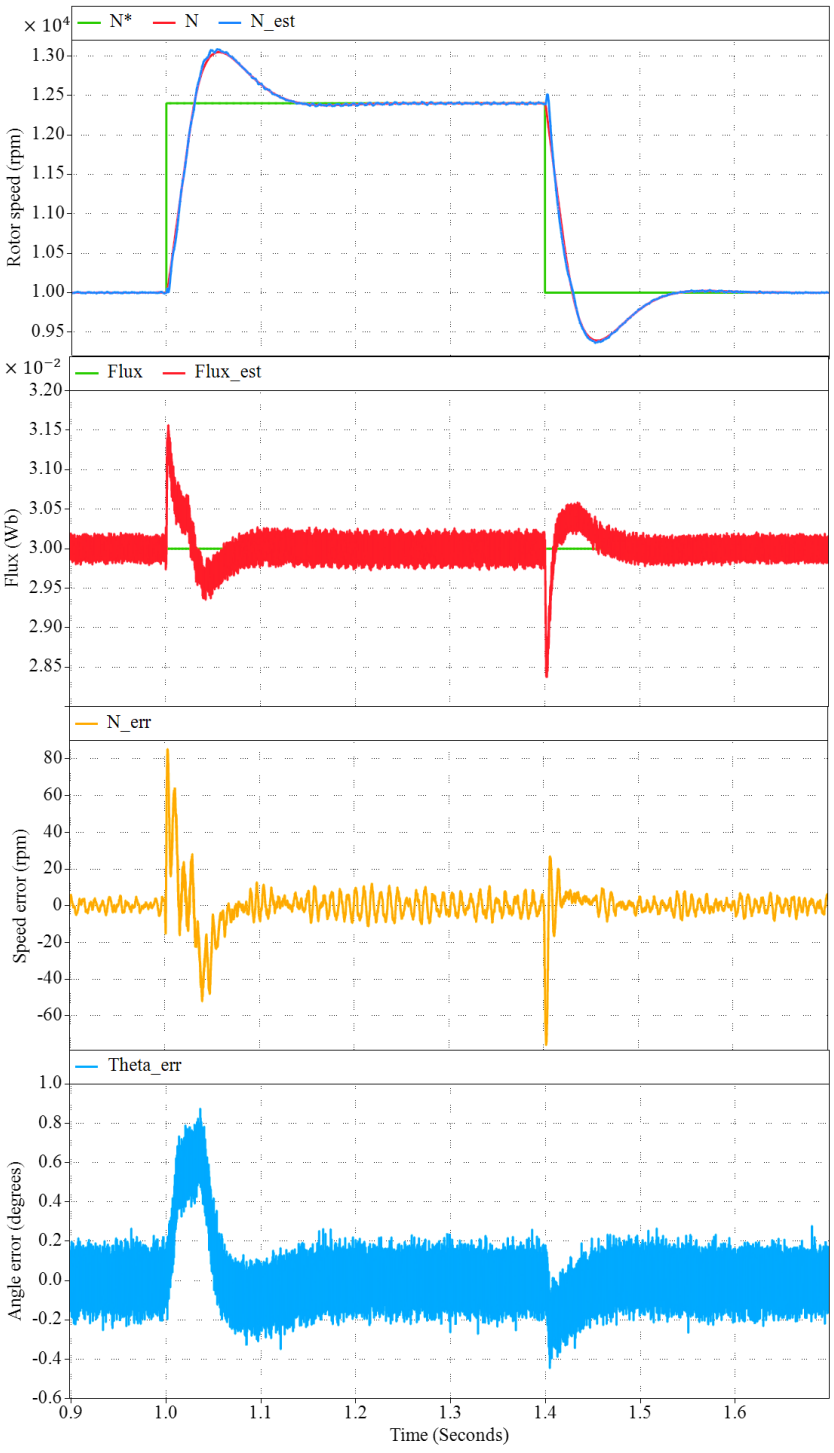


Figure 5.13 Simulation results of enhanced MRAS under speed variation.

In the second scenario, the performance of two methods in terms of load variation is simulated and compared. The simulation results are shown in Figure 5.14 and Figure

5.15. The DTP-PMSM of ACHIEVE runs at 12.4 $krpm$. At t=0.45 s, the load torque has a step increase from 80% to 100%. At t= 0.55 s, the load torque has a step decrease from 100% to 80%.

Figure 5.14 shows simulation results of sensorless system using MRAS. The rotor speed estimation error N_err is around 5 rpm (0.05% of speed) in steady state but fluctuates between -290 rpm (-2.34%) and 270 rpm (2.18%) during dynamic response. The rotor position estimation error Theta_err is within [-1.9 degrees, 1.8 degrees] in steady state while it increases to [-2.3 degrees, 2.2 degrees] during dynamic response.

Figure 5.15 shows simulation results of sensorless system using enhanced MRAS. The flux estimation error is about 0.0015 Wb (5% of flux reference) in steady state. For dynamic response, it takes around 0.05 s for the estimated flux to reach stable and the maximum flux estimation error during this period is 4.7%. The rotor position and speed estimation of enhanced MRAS have quite similar good performances to those of MRAS. The results prove that both MRAS and enhanced MRAS have good performance of speed estimation in the presence of load torque disturbances.

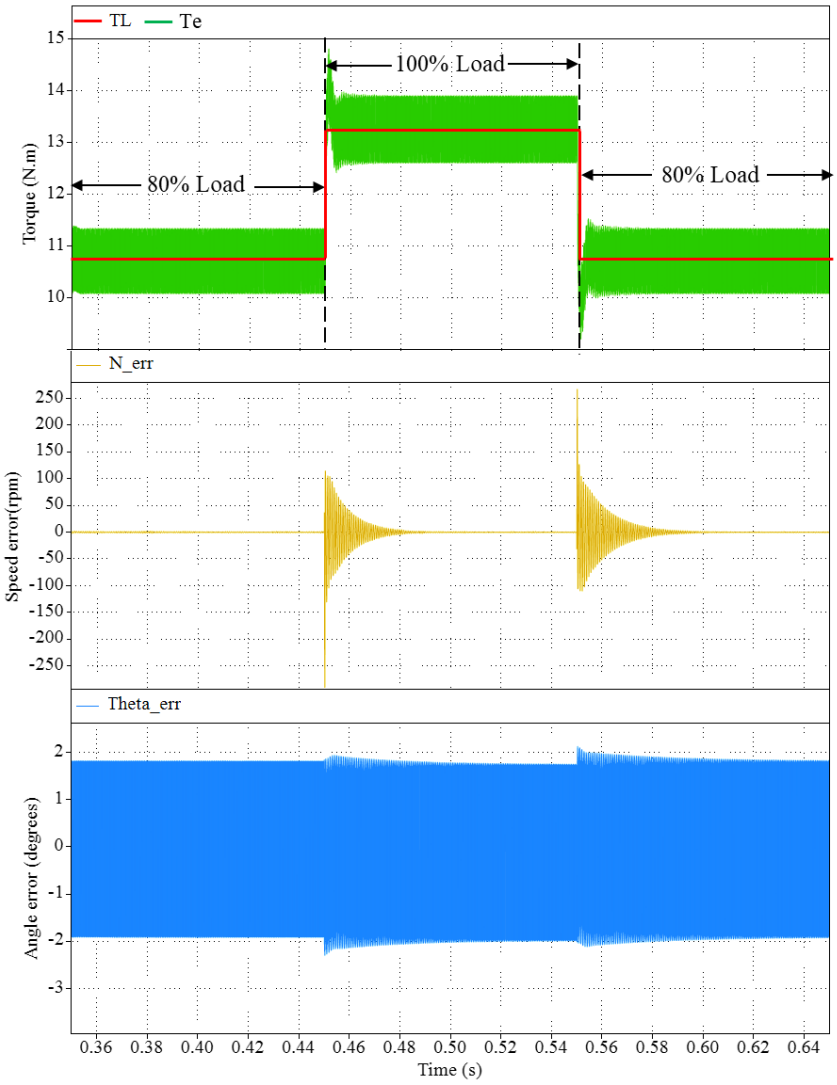


Figure 5.14 Simulation results of MRAS under load variation.

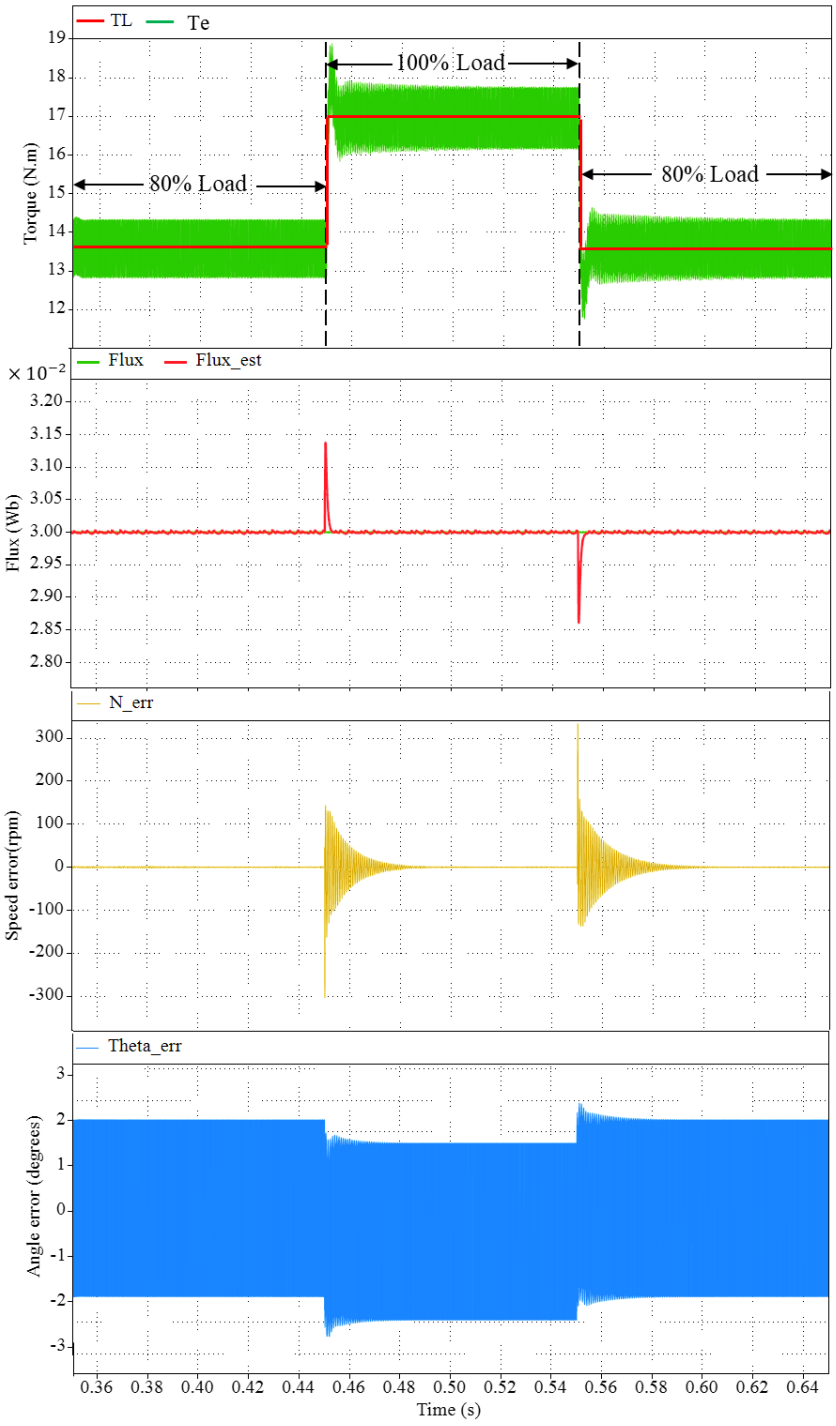


Figure 5.15 Simulation results of enhanced MRAS under load variation.

In the third scenario, the performance of two methods in terms of machine parameter error is simulated and compared. The simulation results are shown in Figure 5.16 . The

DTP-PMSM of ACHIEVE runs at 12.4 $krpm$ with no load. When the machine runs stably, the PM flux of machine has an error and is assumed to drop from rated value to half of rated value. This is just a case to verify the effectiveness of PM flux identification in simulation but not for practical verification because this would represent a catastrophic failure of the machine. The flux estimated by enhanced MRAS has a fast dynamic response in 0.05 s with less than 1% overshoot. The estimation accuracy of both methods suffer from the step change of PM flux. Especially, the rotor position estimation error for MRAS increases from 0.5 degree to 14 degree while for enhanced MRAS, the rotor position estimation error rises from -0.5 degree to 2 degree. Actually, in such step change scenario, the stability of conventional MRAS is lost after a while and consequently, the entire control system goes wrong. But enhanced MRAS still can work properly with satisfactory estimation error. Hence, the superiority of enhanced MRAS over MRAS in case of parameter variation is proved.

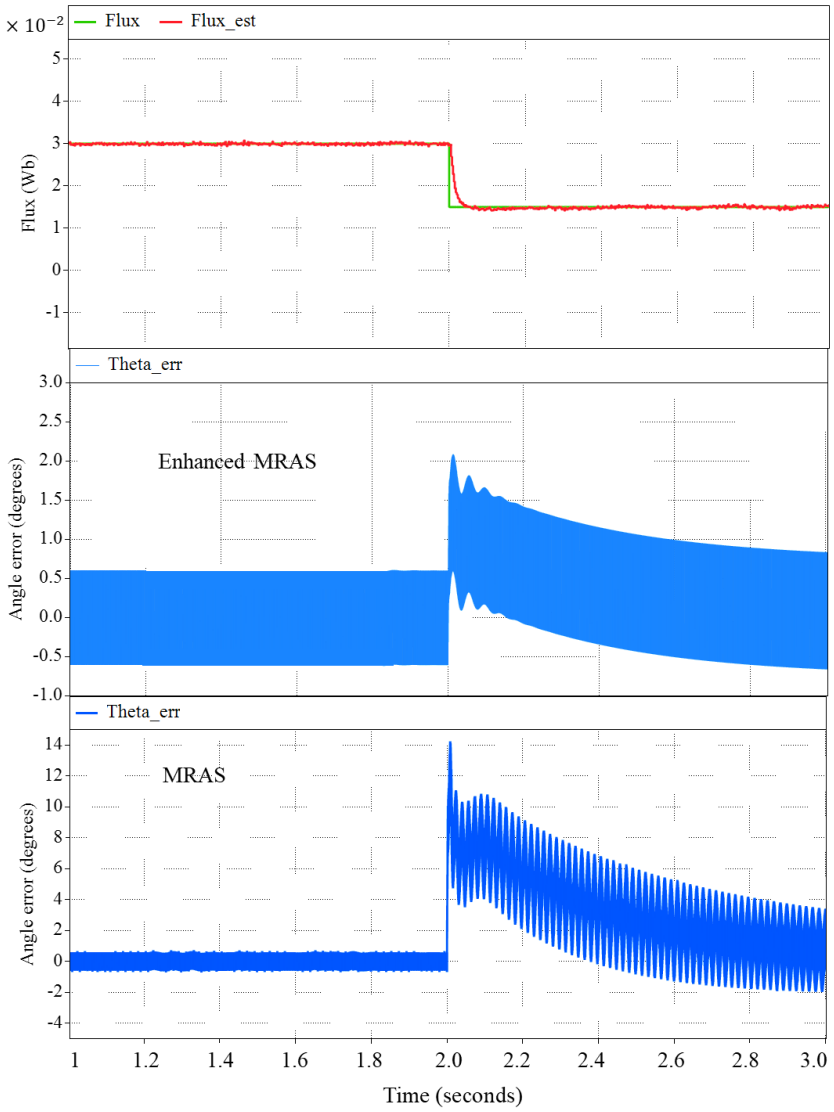


Figure 5.16 Simulation results including estimated PM flux and rotor postion estimation error.

5.5 Chapter Summary

Since the application of the DTP-PMSM in this study is mainly in the high-speed stage, the model reference adaptive method based on the machine model is introduced, and for its sensitivity to machine parameters, an enhanced method with PM flux estimation is proposed to verify the effectiveness of this scheme.

In this chapter, the principle of MRAS method is reviewed. Since the major weakness of MRAS is the sensitivity to the parameters variation, an enhanced MRAS method with PM flux estimation is proposed. The main findings of this chapter can be summarised as follows:

- The parameters of the designed drive system can be categorized into current-sensitive and temperature-sensitive types. The machine inductance can be classified into the former while resistance is regarded as the latter. PM flux is more complexed since it is not only sensitive to temperature but also related to the winding current.
- The number of parameter that could be online identified in a MRAS based sensorless PMSM system could not be more than one. This is proved by observability analysis of the system.
- An enhanced MRAS method is proposed that estimates both rotor speed and PM flux in a cascaded MRAS loop. The principle of the proposed method is illustrated.
- Comparison study has been made between MRAS and enhanced MRAS under different scenario, for instance, speed variation, load variation and PM flux variation. Both methods present good performance in the presence of speed or load variation. The proposed enhanced MRAS shows the priority over MRAS when PM flux has variation.

In the next chapter, an I/F open loop control strategy for start-up will be proposed in order to achieve the full speed range sensorless control.

Chapter 6 Full-Speed Range Rotor Position Estimation Strategy

In Chapter 4, two start-up solutions of PMSM control system are introduced. The first one, such as HF signal injection method, takes advantage of the saliency of the machine. However, its estimator performances are greatly affected by filter parameters, hardware sampling speed and other factors. The second one is the open-loop start-up method, such as V/F and I/F control. Under V/F control mode, the ratio of output voltage to operating frequency is generally constant. The flux of the machine should be kept constant when the frequency conversion is used to obtain the ideal torque-speed characteristics. A core question in such control design is the regulation curve of voltage that varies with frequency, which must satisfy the V/F curve of the machine itself. Otherwise, the error in the configuration of V/F curve will lead to the machine being out-of-step or over-current. Other shortages of this control scheme include: firstly, the reasonable configuration range of V/F curve of PMSM is relatively narrow, so it is difficult to debug the V/F curve; Secondly, this control method does not directly control the torque and thereby is not suitable for the variable load scenario with high dynamic performance requirement; Thirdly, it also has a limitation on the acceleration of start-up and is unable to start quickly; At last, for the V/F control, the absence of current regulation may cause high current and torque ripples during the transition from the start-up stage to the sensorless based Field-Oriented-Control (FOC) stage, which also increases the risk that FOC may not be switched in successfully [273]. To avoid abovementioned problems, I/F control is adopted in this research, which could control the current in a closed-loop control, hence effectively avoids over-current and make the

start-up process smooth and robust. An assumed coordinate system based I/F method is introduced and the analysis of its switching operation are discussed in detail in this chapter.

6.1 I/F Open Loop Control as Start-Up Strategy

As mentioned in Chapter 3, the block diagram of I/F control principle is shown in Fig 3.10. The current is regulated by PI control in *dq* coordinate system, hence the over-current is avoided. In this control mode, the rotor speed is a controlled from the outside of machine. The rotor position applied in the variables transformations between different coordinates is obtained by integration of this speed. According to the change of the given rotor speed, a magnetic field can be generated in the air gap to accelerate the rotation of the rotor. Under the I/F control, the current vector diagram of PMSM is shown in Figure 6.1.

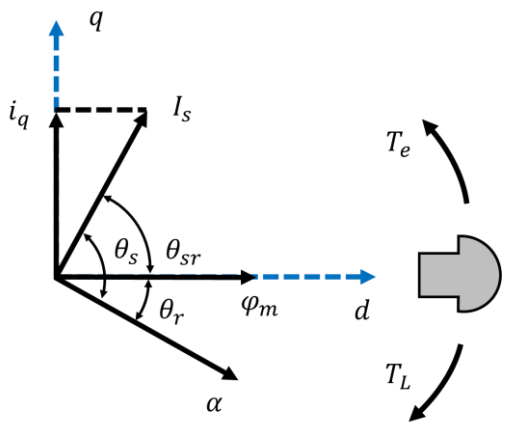


Figure 6.1 Current vector diagram of PMSM in I/F mode.

According to the analysis in Chapter 2, the output torque of the machine is directly proportional to the quadrature axis component i_q of the stator current, so the output torque can be controlled by the stator current. Since only quadrature axis component of

stator current provides electromagnetic torque, when the amplitude of the stator current vector is fixed, the angle θ_{sr} between stator current I_s and rotor flux φ_m determines the output torque, and θ_{sr} is called power angle or torque angle. Under the I/F control scheme, the machine has the characteristics of 'torque-power angle self-balance'. The following is an example of SPMSM to describe such characteristic

When the electromagnetic torque and load torque are balanced, θ_{sr} remains unchanged, the current vector I_s and the rotor flux φ_m remain relatively stationary, and the rotor keeps synchronous rotation. However, when the load torque increases, the electromagnetic torque is less than the load, hence the rotor will decelerate. At this time, the angle θ_{sr} will become larger. Larger θ_{sr} means that the torque component of stator current increases, therefore the machine output torque increases and consequently the machine accelerates. At last, a new torque balance is achieved at a new θ'_{sr}, as shown in Figure 6.2(a). Moreover, if the load torque is less than the electromagnetic torque, when the rotor accelerates, theta θ_{sr} decreases, and the output torque of the machine will decrease. Similarly, the operation of the machine will reach a new balance, as shown in Figure 6.2(b). These two balancing processes in contrasting directions is called 'torque-power angle self-balancing' as mentioned above [274]. It should be noted that if the load torque is too large to be balanced even if the stator current is completely quadrature axis current ($\theta_{sr} = 0.5\pi$), the machine will not be able to achieve balance, because at this time the output torque is the maximum, if θ_{sr} continues to increase, the output torque will not rise and fall, so the 'self-balancing' is broken, resulting in the being machine out-of-step. According to the theory of rotating machinery dynamics and differential equation of SPMSM, it is found that the power

angle range of SPMSM under the traditional I/F control is: $[-0.5\pi, 0.5\pi]$ [275]. To prevent the out-of-step phenomenon mentioned above and ensure that the system can maintain in the power angle stability area, stator current I_s should be large enough so that the output torque controlled by θ_{sr} can keep a certain margin and responds to the load oscillation. Generally speaking, if the given stator current I_s can make θ_{sr} not greater than 0.25π, safe and reliable operation can be guaranteed [276].

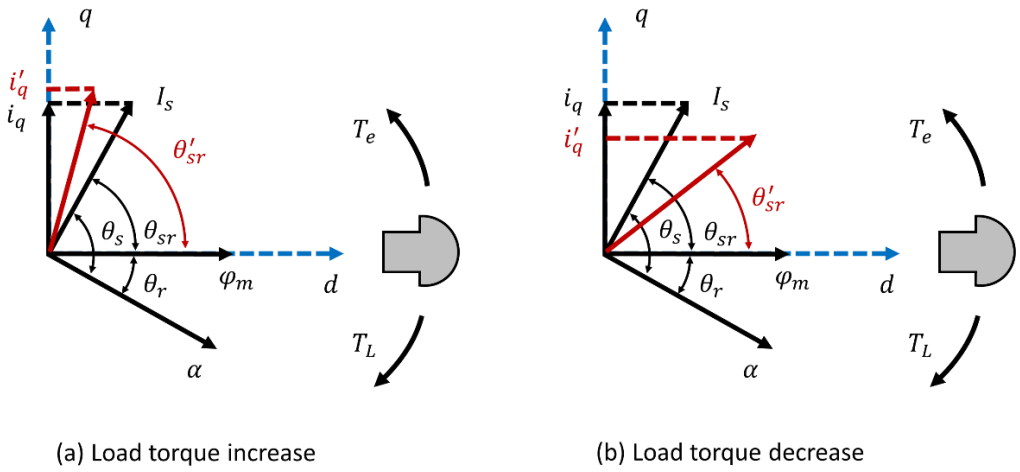


Figure 6.2 Current vector diagram under load variation.

The failure of I/F method often occurs in the following situations: failure due to large load torque or moment of inertia; machine out-of-step caused by the load change before switching to FOC; machine out-of-step result from vibration caused by the non-smooth switching operation. To avoid above situations, a start-up method based on assumed rotating coordinate system is applied in ACHIEVE to realize the smooth switching operation. The specific start-up process can be divided into three steps: initial rotor positioning, accelerated starting, and control mode switching. The start-up process diagram is shown in Figure 6.3. t_1 is the start point, t_2 is the time to switch from

acceleration to constant speed, and t_3 is the time of switching from I/F to sensorless based FOC mode. The start-up process will be described in detail below.

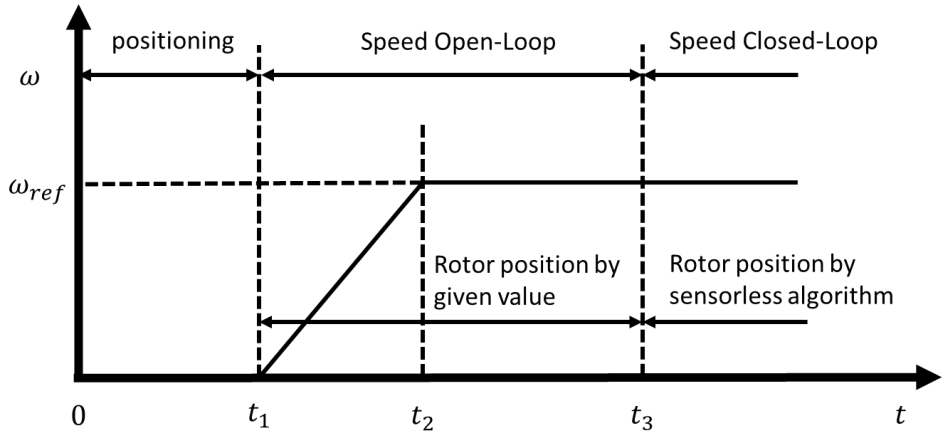


Figure 6.3 Diagram of I/F based start-up process.

6.1.1 Initial Position Identification of Rotor

The machine needs to locate the rotor to a predetermined position before accelerating. Here, a position angle generator is used to generate position signal to complete the current closed-loop operation. The current vector locates at a fixed position through a given position angle and generates a fixed position magnetic field in the air-gap. At the same time, the rotor approaches the magnetic field generated by the current until it coincides with the magnetic field axis.

The identification process is shown in Figure 6.4. Before power is on, the position of the rotor could be arbitrary as shown in Figure 6.4(a). The position signal generated by the position angle generator is the assumed coordinate system dq^*. The current vector locates at the quadrature axis q^* of the assumed coordinate system in the rotor position identification stage, and the synchronous rotating reference frame dq^* is set to be

lagging the real rotor dq frame by 90 electrical degrees, as demonstrated in Figure 6.4(b).

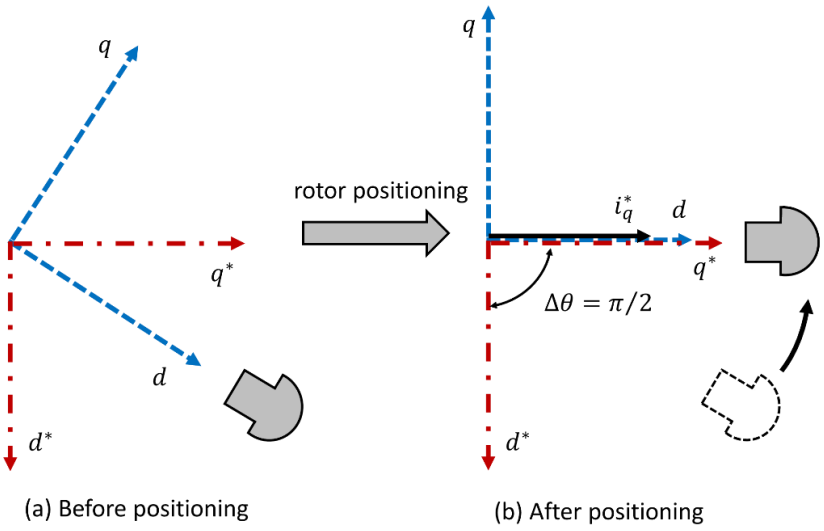


Figure 6.4 Process of initial position identification of rotor.

6.1.2 Acceleration Process of Rotor

Following the initial rotor position identification, the rotor acceleration process begins. During this acceleration process, the current vector rotates with the assumed coordinate system dq^*, and the stator flux generated by the current vector will drive the rotor permanent magnet to rotate synchronously and generate the corresponding effective torque. It can be seen from Figure 6.5 that the current vector will rotate gradually from the d-axis at the given speed ω^*. There is an angle difference $\Delta\theta$ between the actual coordinate system dq and the assumed coordinate system dq^*, which changes with the variation of load. In essence, the purpose of this control process is to control torque and speed by adjusting power angle, i.e., power angle control.

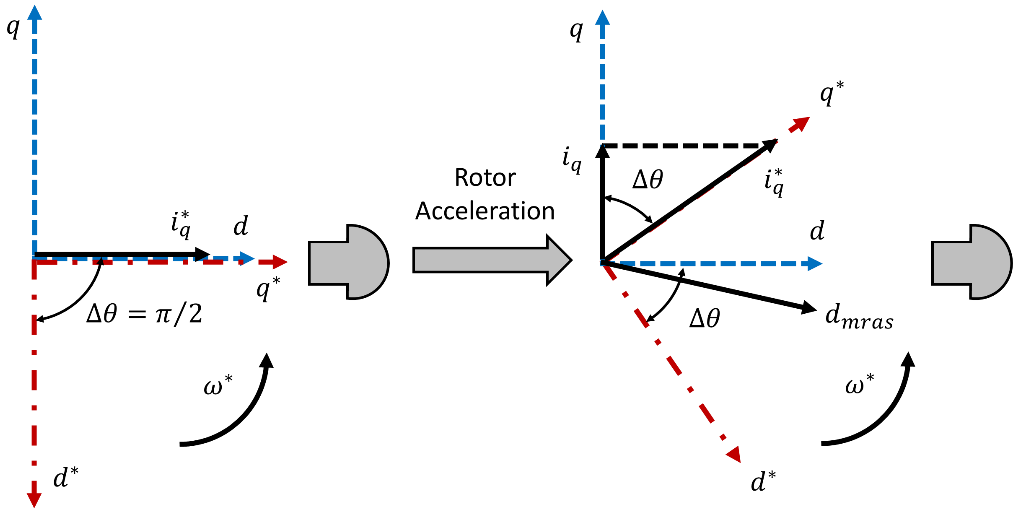


Figure 6.5 Diagram of vectors during start-up process.

6.1.3 Analysis of State Switching Operation

With the increase of machine speed, the Back EMF continuously increases, and MRAS can observe the rotor position and speed accurately. At this time, the machine control mode needs to be switched to the sensorless based FOC control. However, there is still an angle difference $\Delta\theta$ between the given coordinate system and the actual coordinate system, so the control mode cannot be switched directly, and $\Delta\theta$ needs to be eliminated before switching. In this Thesis, a switching transition scheme based on the change of current amplitude is adopted, that is, the value of $\Delta\theta$ is adjusted to zero by reducing the value of i_q^*. As shown in Figure 6.5, the relationship between i_q^* and i_q can be described as:

$$i_q = i_q^* cos\Delta\theta \tag{6.1}$$

The diagram of the self-adjustment process is shown in Figure 6.6. Because the position of the actual coordinate system dq is not available, the angle difference $\Delta\theta$ cannot be

obtained, so $\Delta\theta'$ (the angle difference between the assumed coordinate system and the estimated coordinate system) is used instead of $\Delta\theta$. When $\Delta\theta'$ becomes zero, the command of control mode switching is given. At this time, the direct-axis in the three coordinate system (d, d^*, d_{mras}) are assumed to overlap each other to meet the switching conditions. The speed and position signals estimated by MRAS can be fed back to the control system to complete the cascaded FOC. As shown in Figure 6.7, both software switches are turned from 1 to 2 at the same time.

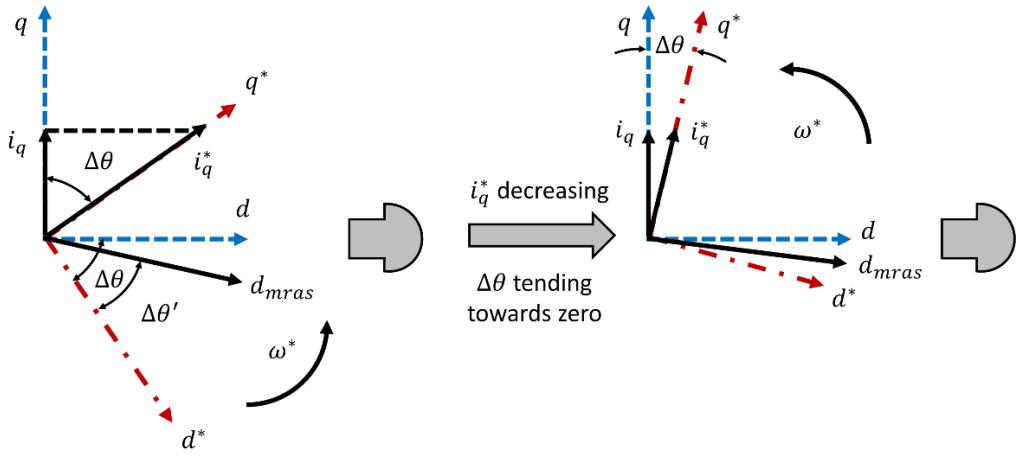


Figure 6.6 Diagram of state switching operation.

When switch 1 is shifted, the initial output value of speed loop PI controller should be equal to the given value of *q*-axis current before switching, so as to prevent failure due to the torque fluctuation brought by the sudden change of *q*-axis command current. The above switching method based on the change of current amplitude actually forces the assumed coordinate system to approach the actual coordinate system according to the principle of 'torque-power angle self-balance'. By reducing the given value of quadrature-axis current i_q^*, the electromagnetic torque of the system machine can automatically adjust the power angle according to the load torque variation.

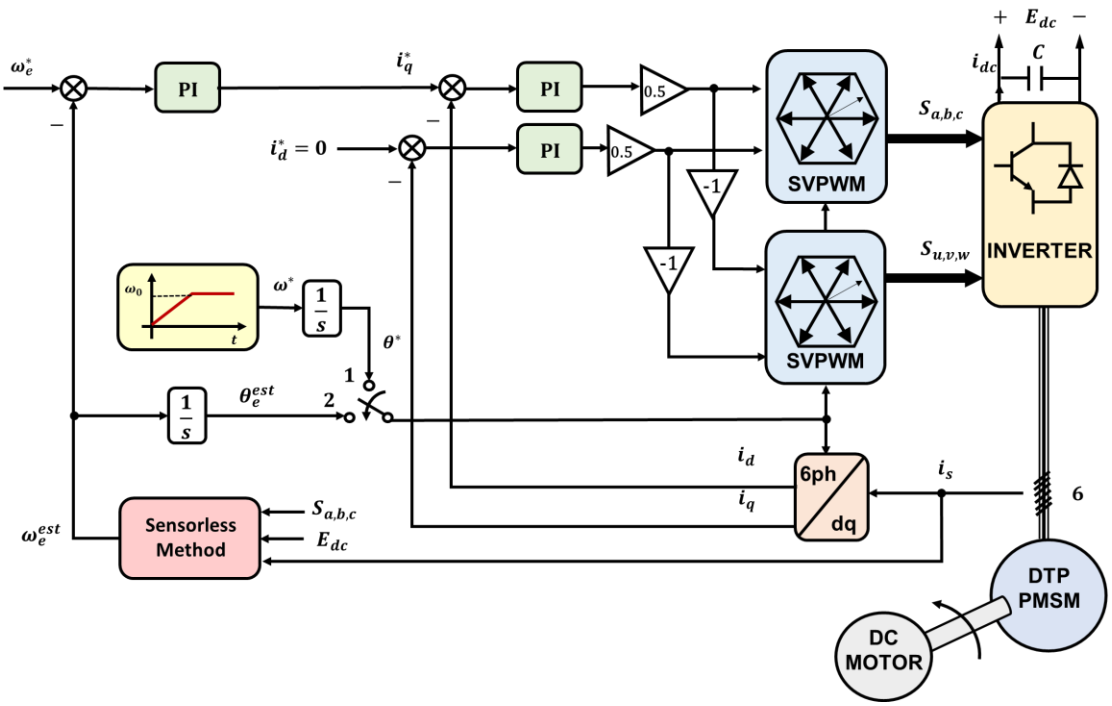


Figure 6.7 Block diagram of I/F start-up method.

6.2 Simulation Results of Start-Up Strategy

For the above start-up method of PMSM sensorless control, this section will build simulation model on the basis of MRAS control system that is established in Chapter 4 for a verification. The simulation includes the accelerating and switching operation of start-up process. The given quadrature-axis current i_q^*, phase angle difference $\Delta\theta$ and actual rotor speed are shown in Figure 6.8-Figure 6.10.

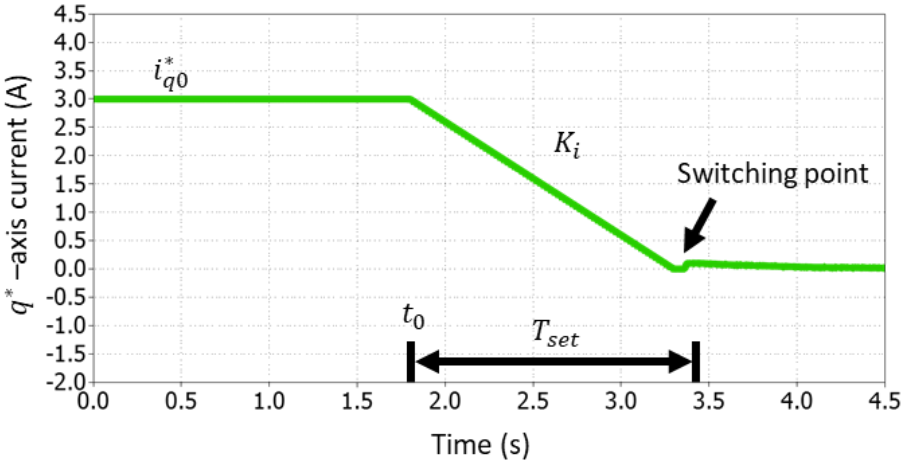


Figure 6.8 q^*-axis current i_q^* during start-up process.

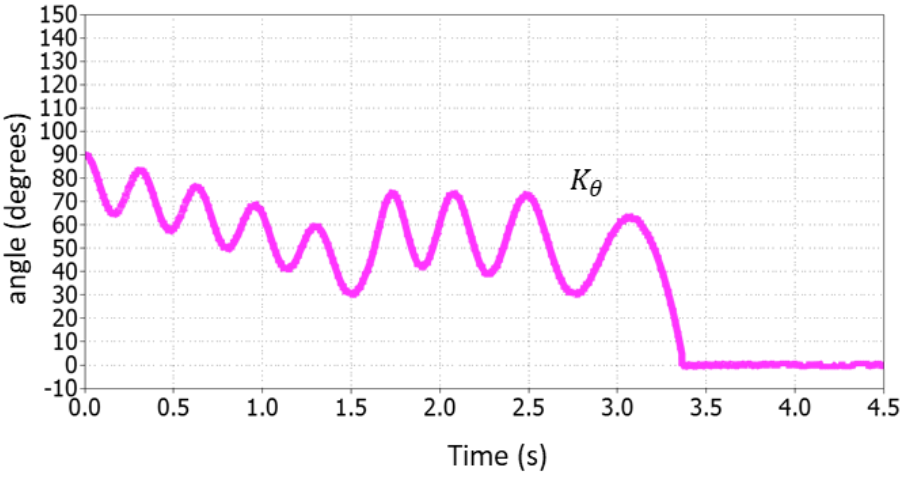


Figure 6.9 Angle difference $\Delta\theta$ between dq frame and dq^* frame during start-up process.

As shown in Figure 6.10, the speed increase ratio used in this simulation is 133.3rpm/s. The load torque used in the simulation is known. According to the results shown in Figure 6.9, the average value of $\Delta\theta$ is around 60° during acceleration. As shown in Figure 6.10, the rotor speed is maintained constant by setting a constant speed reference command after it achieves the required value. Then, the synchronous frame q^*-axis current is decreases and the angle $\Delta\theta$ is correspondingly forced to zero. A small

threshold value for $\Delta\theta$ can be set to control the moment when the FOC scheme should be switched in and take over control. In this simulation, the threshold value of angle $\Delta\theta$ is set to be 5 electrical degrees and the FOC takes over control at 3.4 s. In Figure 6.8, very small current ripple during this switching transient can be observed.

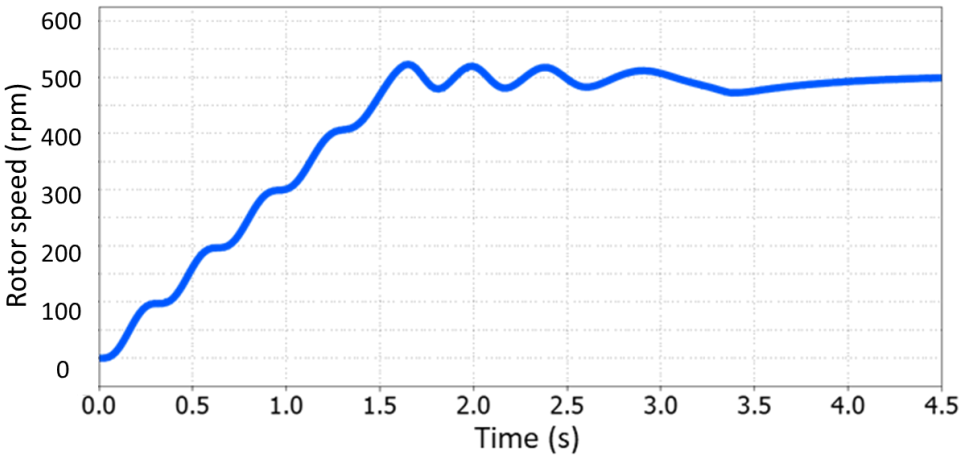


Figure 6.10 Actual rotor speed during start-up process.

It can be seen from Figure 6.9 and Figure 6.10 that the phase angle difference $\Delta\theta$ and rotor speed oscillate during start-up, which is an adaptive adjustment process of 'torque-power angle self-balance' characteristics. This complex dynamic phenomenon can be expressed by following three formulas:

$$T_e = K_T i_q^* cos\Delta\theta \tag{6.2}$$

$$T_e - T_L = \frac{J}{p_p}\frac{d\omega_e}{dt} \tag{6.3}$$

$$\omega_e - \omega_e^* = \frac{d\Delta\theta}{dt} \tag{6.4}$$

(6.2)(6.3)(6.4) constitute a complex nonlinear system with phase difference angle $\Delta\theta$ in dq^* and dq coordinate systems as critical variables. The change of $\Delta\theta$ is not only the

reason of electromagnetic torque variation of PMSM, but also the result of rotor speed and angle change caused by the mechanical response of load. It is a cyclic coupling process, so oscillation of phase angle and speed are produced. Although the three equations cannot be solved mathematically, their oscillation law can be obtained by numerical iteration method. As shown in Figure 6.8, it is assumed that during the transition period from t_0 to $t_0 + t_{set}$, the amplitude of the current command i_q^* decreases gradually with the slope K_i, which is expressed as:

$$i_q^*(t) = i_{q0}^* - K_i(t - t_0) \qquad t_0 \le t \le t_0 + t_{set} \qquad (6.5)$$

According to the principle of 'torque power angle self-balance', with the decrease of current, the phase difference angle $\Delta\theta$ decreases correspondingly. However, the decrease process of $\Delta\theta$ is slow. It can be considered that the rotor speed has not changed significantly in this process. It can also be observed from Figure 6.10 that the speed remains almost constant from the beginning time of 1.7s to the end time of 3.2s. To simplify the analysis, assuming that the torque is fixed due to the constant speed, the torque impulse in the switching process is equivalent to the torque impulse under the original start-up current:

$$\int_{t_0}^{t_0+t_{set}} i_q^*(t) cos\,(\Delta\theta(t)) \cdot dt = i_{q0}^* cos\,(\Delta\theta(t_0)) \cdot t_{set} \qquad (6.6)$$

The average slope of phase difference angle $\Delta\theta$ decrease in the process of switching is defined as $K_\theta = \Delta\theta(t_0)/t_{set}$, therefore:

$$K_\theta = \frac{1}{i_{q0}^*} \cdot \frac{cos\big(\Delta\theta(t_0)\big) - 1}{\Delta\theta(t_0) \cdot cos\big(\Delta\theta(t_0)\big) - sin\,(\Delta\theta(t_0))} K_i \tag{6.7}$$

In equation (6.7), $\Delta\theta(t_0)$ represents the phase difference angle between dq^* and dq coordinate system at the beginning of the switching process. As one can see, when the initial phase difference angle $\Delta\theta(t_0)$ and the current command i_{q0}^* are fixed, increasing the current decline slope K_i can make the phase difference angle $\Delta\theta$ decrease faster, and the transition process time will be shorter. On the other hand, larger load torque has smaller initial phase difference angle $\Delta\theta(t_0)$, which means that the transition time is shorter when the load is large.

The following figure shows the simulation results of the transition process model based on (6.2) (6.3) and (6.4). Given different slope of current falling rate K_i, the change rule of phase difference angle $\Delta\theta$ is shown in Figure 6.11.

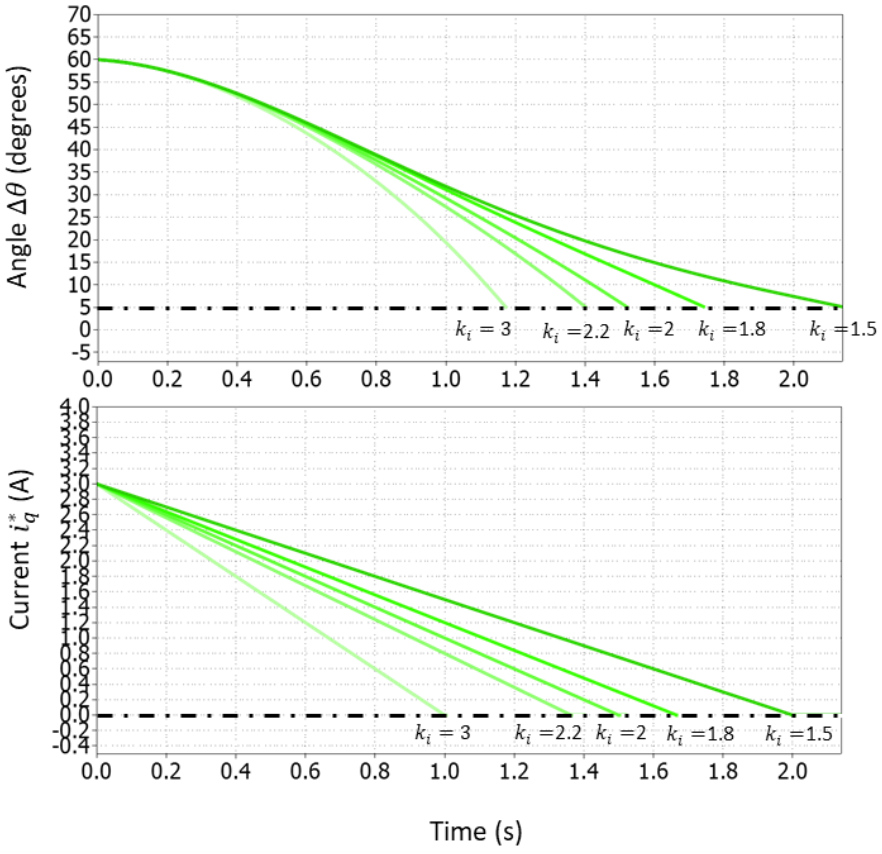


Figure 6.11 $\Delta\theta$ under different i_q^* decreasing rate k_i.

It can be seen from Figure 6.11 that the decreasing process of phase difference angle $\Delta\theta$ lags behind that of slope K_i. This is because the response speed of mechanical system is slower than that of electrical one, which is closely related to the inertia of the system. When the current decline slope K_i is near 2, the phase difference angle and current almost reach the switching point at the same time. At this time, when the system is switched to the sensorless based FOC mode, quite small current ripple and torque ripple can be obtained. If the current decline slope K_i is set too small, the oscillation caused by the self-balancing process is obvious, and it is easy to cause the machine out-of-step when it approaches the switching point. If the current decline slope K_i is set too large, for example, $K_i = 3$, the current will drop below the expected value before $\Delta\theta$

converges to 0°, thus causing current overshoot, torque and speed oscillation during switching operation.

Equation (6.7) can be used as a reference for the design of transition process. In another word, for the system load torque already given, the appropriate current decline slope K_i can be set accordingly, so that the convergence process of $\Delta\theta$ is mild and stable, the current transition is smooth at the switching time, and the torque and speed almost remain constant. According to the mathematical relationship shown in (6.7) and the analysis of simulation results, the value of K_i to ensure the smooth and reliable transition process is $K_i < 2.5$. Another important factor in the transition process is the judgement of the switching point. As shown in Figure 6.7, the best switching point is at the time when dq^* and dq coordinate axes coincide, at this time $\Delta\theta = 0$, so the zero-crossing point of $\Delta\theta$ can be used as the criterion of the switching point. However, the actual rotor position angle during open-loop start-up is unknown, and the $\Delta\theta$ cannot be used directly as the basis of determination, while the angle $\Delta\theta'$ between the d^*-axis and the estimated rotor position d_{mras} can be used as the criterion of the switching point, as shown in Figure 6.6. It should be noticed that in the open-loop start-up stage, due to the large *d*-axis component of the command start-up current i_q^*, a strong magnetic saturation effect is formed on the *d*-axis, which will affect the accuracy of the machine parameters, resulting in the estimated position d_{mras} deviating from the real rotor position by a certain angle, which will reach 20° to 30° in the initial stage of start-up, and gradually reduce with the decrease of *d*-axis current component. Finally, it converges to zero in the vector control mode with $i_d = 0$ to get the accurate estimation result. As shown in Figure 6.6, since the speed loop is bypassed during I/F open-loop

start-up, the initial default value of its output (q-axis command current i_q^*) is set as 0. When the system switches from open-loop mode to vector control mode at the switching point, the initial output value of speed loop PI should be set in advance to prevent torque impact caused by discontinuous change of q-axis command current i_q^* at the moment of switching. At the switching time, the initial value of i_q^* can be expressed as follows:

$$i_q^*(t_0 + t_{set}) = i_q^*(t_0) \cdot cos\Delta\theta(t_0) \tag{6.8}$$

In Chapter 7, experimental work is done to verify the effectiveness of proposed strategy.

6.3 Chapter Summary

As previous chapter discusses the sensorless control method at middle- and high-speed, this chapter mainly introduces sensorless method for zero- and low-speed range to achieve full speed range sensorless control of ACHIEVE machine. The main findings of this chapter can be summarised as follows:

- An I/F open loop control method is proposed as start-up strategy. In the analysis of I/F, the concept of 'torque-power angle self-balancing' is proposed in this research. A mathematical model is used to describe the dynamic oscillation process of 'torque-power angle self-balancing'. The key parameters, current decline rate and phase difference angle decline rate, are discussed in detail.
- The proposed method can effectively prevent the phenomenon of over-current and out-of-step and has certain adaptability to the load variation in the operation process.

- The proposed method is suitable for the application where the operation efficiency is not very high at low speed, which is consistent with the ACHIEVE.
- Appropriate setting of parameters can make the transition process smooth and reliable without big torque fluctuation and current ripple.

Chapter 7 Experimental Validation

In this Chapter, the experimental rig built for the verification tests is described. This rig is a test version of ACHIEVE [18] system developed and kept in the University of Nottingham for continued experimental support of the project developments during periods when the actual ACHIEVE system for customer undergoes testing at the industrial partner facilities. The test rig allows for more extended experiment including advanced concepts and future ideas that are deemed too risky to be performed on the ACHIEVE system. Figure 7.1 shows the block diagram of the test rig. In comparison to the investigated motor/generator system, the role of the aircraft engine is performed by an Induction Machine (IM). A torque meter is connected to the DC machine which controls the machine speed/torque characteristics. The IM can be used to either apply load torque or to drive the dual three-phase ACHIEVE PMSM, depending on its operation mode. The dual three-phase PMSM can be viewed as two sets of three-phase PMSM. Each set is powered by a 2-Level SiC based converter. Two TMS320F28339S Digital Signal Processor (DSP) boards from Texas Instruments® are used to implement the designed control scheme and control the dual three-phase PMSM. A 28V DC power supply is utilized to power both control boards. The debugged code of sensorless control system is written into the flash memory of both DSP through the JTAG interface. Set DSP1 as the master DSP, and DSP2 as the slave DSP. The master and the slave communicate and synchronize PWM signals through Serial Peripheral Interface (SPI). The six-phase current of the machine i_{abcuvw} is sampled by A/D of DSP1. Then DSP1 solves the adopted control method according to the obtained current signal and concludes the stator space voltage vector. After resolving of SVPMW algorithm, the

output switching signals of six-phases are generated by ePWM module of DSP1. As shown in Figure 7.1, s_a, s_b, s_c are sent to the upper inverter to control ABC phases, and s_u, s_v, s_w are transferred to DSP2 through SPI and then sent to the lower inverter to control UVW phases. Meanwhile, if there is any fault in the system such as overcurrent, overvoltage or overtemperature, the fault signal will be sent to GPIO of DSP1. Especially, the fault signal of UVW phases are sent to DSP2 from DSP1 through SPI. After analysing of the fault signal, proper measures are taken to protect the system. During the experiment, the speed of the machine is detected and recorded in real time by the encoder, which can provide a comparison for the speed estimated using sensorless algorithm but does not participate in any feedback loop of the control system. The data obtained from the experiment are all offline plotted by MATLAB® to obtain relevant experimental waveforms. The machine is designed by the University of Nottingham [145] and manufactured by NEMA Ltd [277]. It is a concentrated winding machine with 18 Slots/12 Poles. The relevant parameters of the dual three-phase PMSM used by the offline detection are consistent with the previous simulation, as shown in Table 7-1. The stator resistance, inductance, and Back-EMF constant value in Table 7-1 are measured.

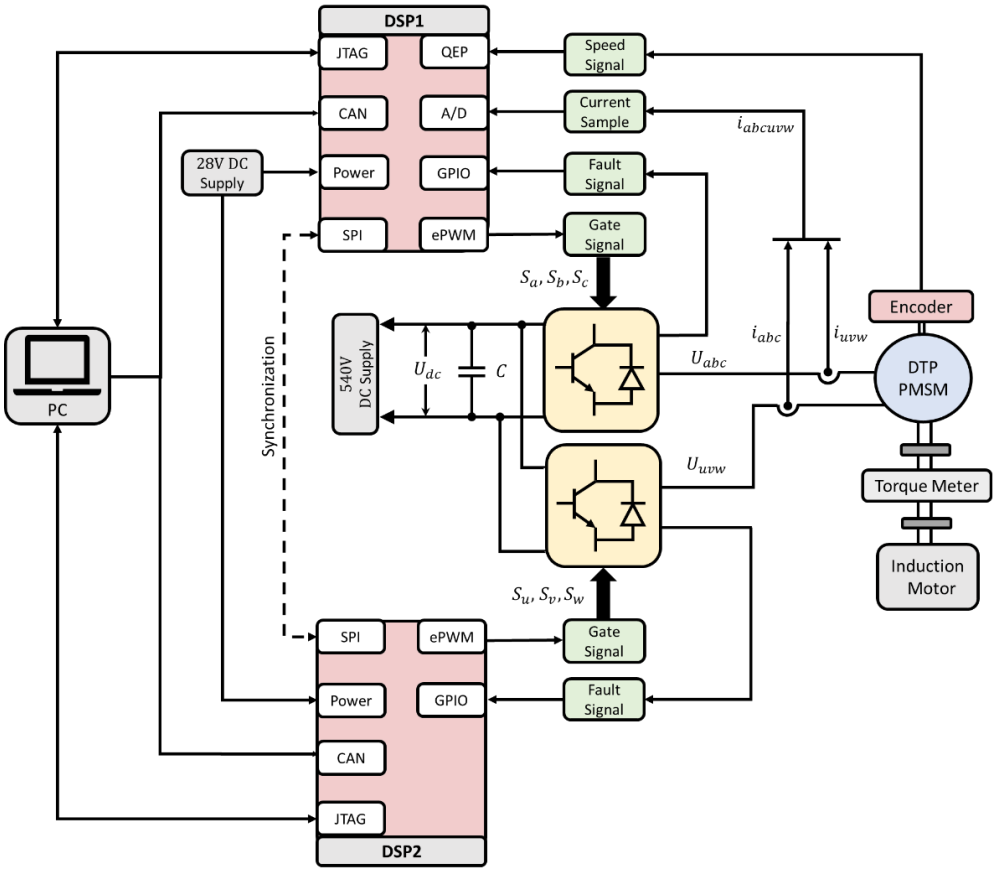


Figure 7.1 Block diagram of dual three-phase PMSM hardware system in ACHIEVE.

Table 7-1 Experimental parameters of dual three-phase PMSM for ACHIEVE.

Parameters	Value	Unit
DC voltage	540	V
Machine stator resistance	0.171	Ω
Machine stator inductance	530	μH
Permanent magnet flux linkage	0.03	Wb
Pole pairs	6	/
Rated power	20	kW
Rated speed	12400	RPM
Switching frequency	40	kHz

7.1 Hardware Design and Construction

7.1.1 TMS320F28379S DSP

The main control chip of the dual three-phase PMSM drive experiment platform is TMS320F28379S DSP [278] from TI. This DSP has a 32-bit floating point CPU that works at 200 MHz, and has an independent Control Law Accelerator (CLA), that can execute code in parallel with the main CPU, thereby improving the real-time nature of the control system and getting better control performance. Considering harsh working conditions that may occur in system application scenarios, two identical DSP are used for control to improve reliability and redundancy of the system.

At the same time, to speed up the processing speed of AD sampling and give full play to the chip performance, CLA module is used in this design. The CLA module is a 32-bit floating-point coprocessor running independently of the main CPU. It has the same working frequency as the main CPU. It can execute code in parallel with the main CPU. It has independent registers, data, program bus and processing unit. It can be directly connected with ADC, ePWM and other peripheral modules. The introduction of CLA increases the real-time performance of the system. Besides, CLA is triggered by peripherals or software to execute tasks. It does not support task nesting; that is, it can only respond to other task requests after the current task is executed.

In this research, the master DSP1 undertakes the majority of control task. and the CLA in DSP1 performs all the machine control algorithm. The operating flow is shown in Figure 7.2. First of all, the initialization of both CPU and CLA is done. Then the CPU and CLA cooperate with each other so that the workload of CPU decrease and

efficiency of entire DSP increases. In each cycle, the CPU samples current, DC voltage and temperature information twice, one at the very beginning, the other at the middle of the counter. Between sampling operation, CPU communicates with PC. In the meantime, the CLA updates machine control algorithm at the start of every cycle. The master-DSP1 and slave-DSP2, as mentioned above, communicate with each other via SPI.

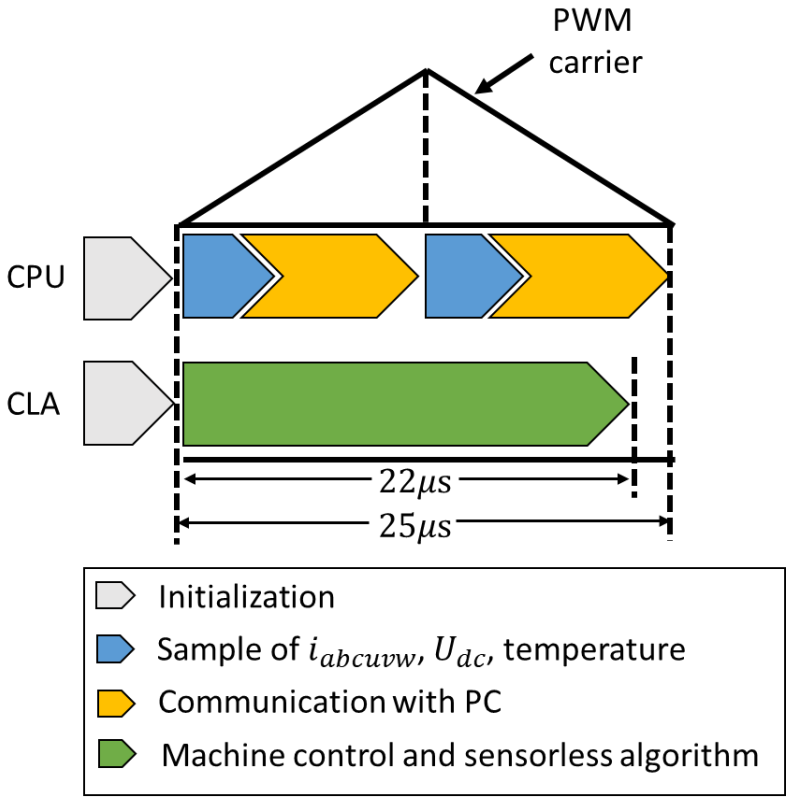


Figure 7.2 Operating procedure of DSP1.

7.1.2 Signal Detection Circuit

The entire control system needs to detect the machine speed and position to compare the estimated rotor speed and position with the actual values, and then check the error of the estimation algorithm. At the same time, a sample stator current is required to

achieve the closed-loop control of the current. Besides, it is necessary to detect the real-time temperature of the motor and the control board to avoid failure caused by excessive heat. As shown in Figure 7.3, speed detection is done by a modular angle encoder with magnetic scanning which is glued to the sleeve coaxial with the rotor. The encoder is ERM 2400 series incremental angle encoder from HEIDENHAIN [279] as shown in Figure 7.4. This encoder consists of a magnetized scale drum and a scanning unit with magnetoresistive sensor. Their MAGNODUR measuring standard and the magnetoresistive scanning principle make them particularly tolerant to contamination. Every time the rotor rotates, the encoder outputs two signals with a phase difference of 90 degrees, 3600 pulses per channel and a zero-pulse positioning signal. The actual speed and direction of the rotor are obtained by the DSP capture unit Quadrature Encoder Pulse (QEP), and then the actual rotor position is calculated. The temperatures of winding, DSP and drive board are detected by the thermocouple so that any overtemperature fault can be detected and reported to PC.

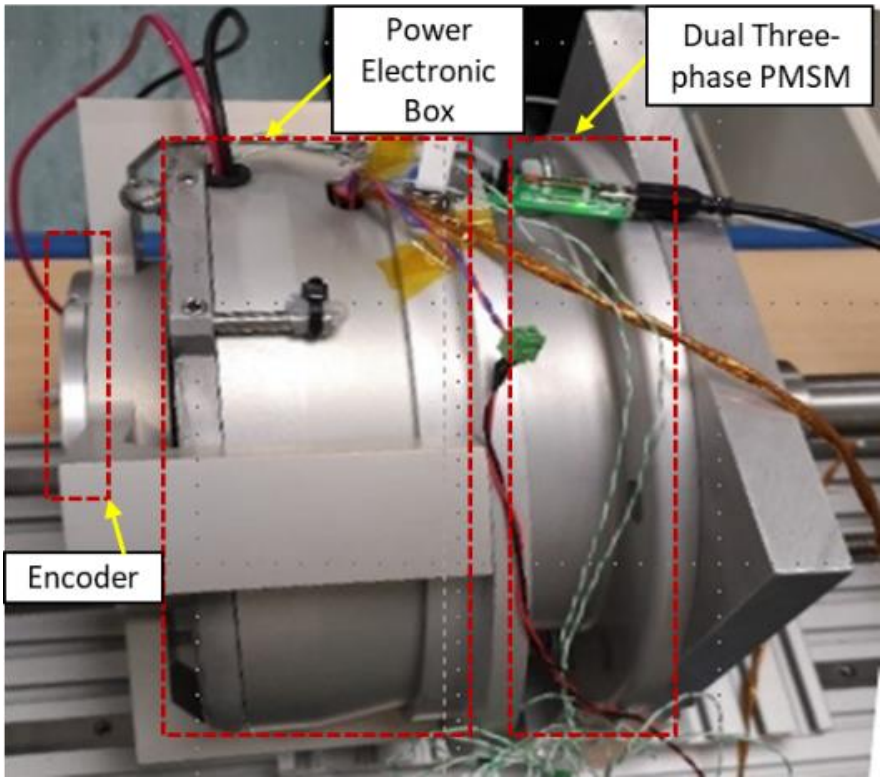


Figure 7.3 Dual three-phase machine and power electronic box in ACHIEVE.



Figure 7.4 Encoder installed on the DTP-PMSM in ACHIEVE .

7.1.3 Design of the Power Drive Module

The design of power drive module is quite challenging since the demanded geometry of the converter system is unique as shown in Figure 7.5. In [280], a SiC based 2-level (2L) voltage sourced converter (VSC) was designed and populated based on the given

envelope. An exploded view showing how various Printed Circuit Board (PCB) boards and cooling system that will fit the envelope is illustrated in Figure 7.6. The power board in the exploded view of Figure 7.6 has a pair of 2L VSCs whose layout is in a semi-circular geometry. The power switching device of this drive platform uses Skiip-packaged26ACM12V17 SiC MOSFET of SEMIKRON [281]. Its withstand voltage up to 1200 V, continuous working current can reach 60 A at 70℃, and its working temperature range is [−40℃, 175℃]. The gate driver board is designed to accept 28 V DC input, thus can directly be connected to the centralised power network of the MEAs[282]. In gate board, the 28V DC are then level-shifted to generate +18 V and -2.3 V to drive SiC MOSFETs using isolated DC/DC converters. Each of the 6 gate driver circuits are supplied using 6 independent isolated and regulated DC/DC converters.

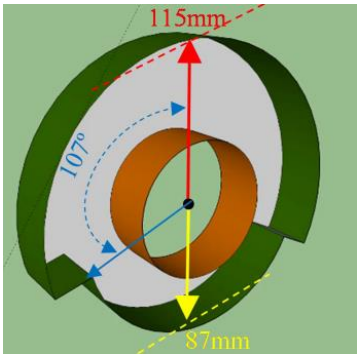


Figure 7.5 Envelope provided for converter by the aircraft manufacturer.[280]

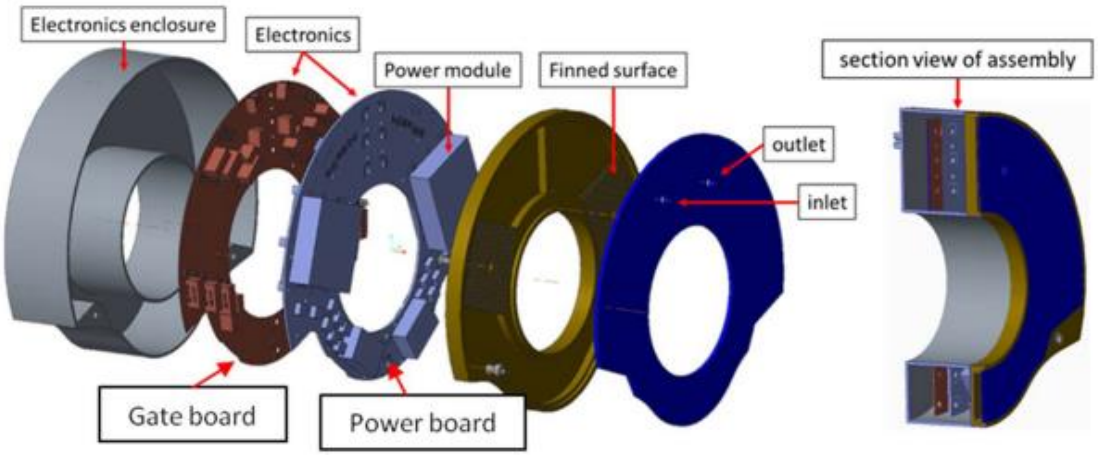


Figure 7.6 Exploded view of voltage sourced converter including cooling system [280].

The power board in the exploded view has a pair of SiC based two-level VSC. Each VSC has a semi-circular shape as presented in Figure 7.7.

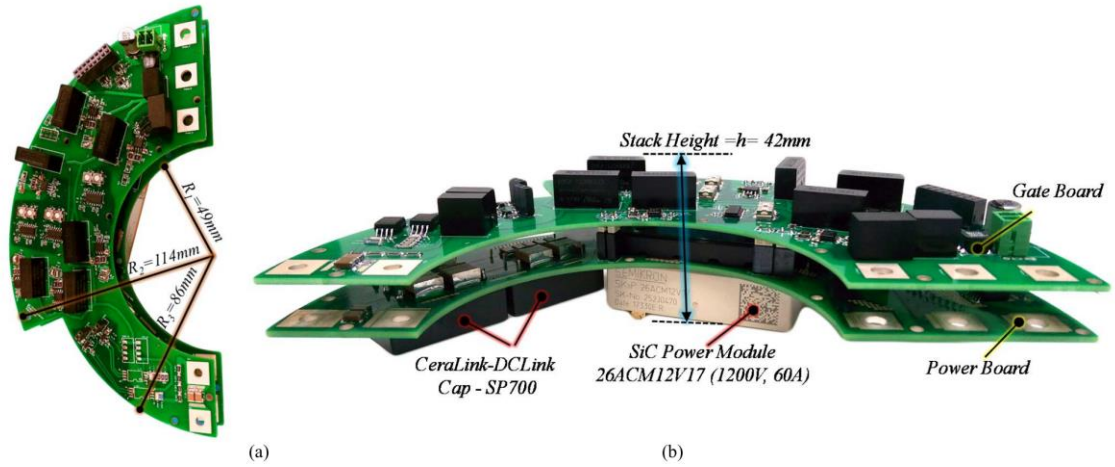


Figure 7.7 SiC based 2L three-phase converter system for ACHIEVE project (a)Envelope of the converter highlighting its radial dimensions. (b)Axial view of the converter showing stack height of gate driver and power board[280].

7.1.4 Design of Human-Computer Interaction System

The host computer control and display interface for the dual three-phase PMSM experiment platform is designed through LabVIEW software. The current signals,

speed signals, real-time temperature, and fault information of two sets of three-phase windings are read. Instructions are given to the machine from LabVIEW interface to make it work in specified functions, such as I/F open-loop start, speed and current closed loop mode, etc.

7.2 Software Design and Construction

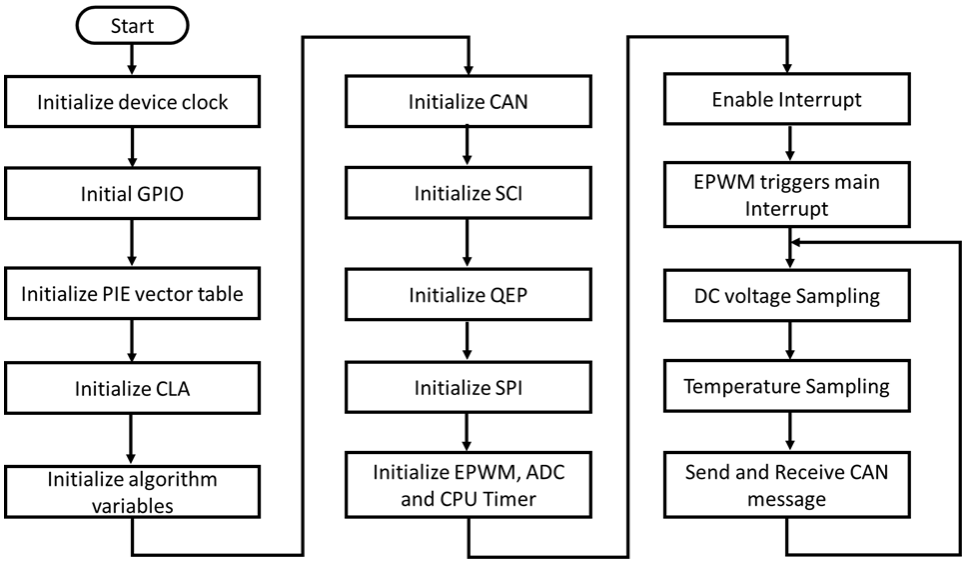
The system program is written in CCS6.0 in the form of C code and burned into the Random Accessory Memory (RAM) or Flash memory of DSP through JTAG bus. The program adopts a modular design, which improves legibility and reduces the difficulty of program modification. The control system includes main program and interrupt service subprogram. The main program is mainly responsible for the initialization of the experimental hardware and variables, the initial detection of the rotor position, the setting of the initial value of the control register and the enabling of the interrupt. The interrupt service subroutine is mainly about the realization of the system control algorithm, including the I/F open-loop start algorithm at low speed and the sensorless control algorithm based on the motor at middle- and high-speed. At the same time, the measurement and calculation of the actual speed and position of the system and the communication between the host PC are also realized through the interrupt service program.

7.2.1 Design of the Main Program

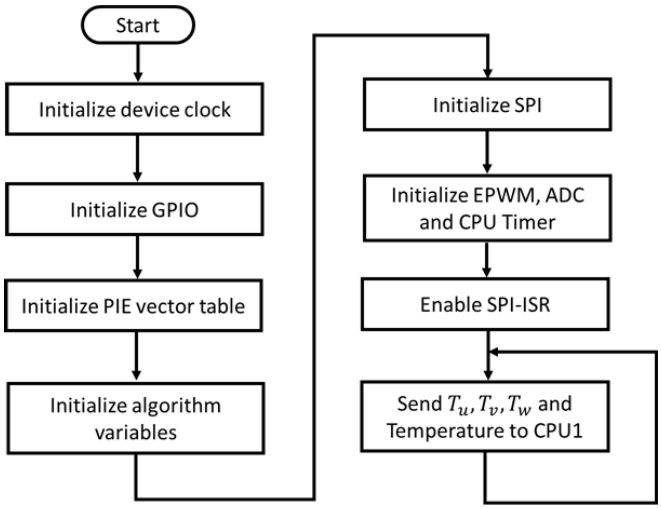
In this experiment, the main interrupt program to execute the motor control algorithm is triggered by the PWM carrier signal of DSP, that is, the main interrupt is triggered at

the time when each carrier counter is reset to zero, and the signals needed for the next cycle of inverter are calculated.

The flow chart of the system main program in DSP1 and DSP2 is shown in Figure 7.8 (a) and (b) respectively. Generally speaking, both main programs roughly contains three steps: initialization of system and variables, trigger interrupt, cycle and wait. Especially, there are some differences between them. For instance, DSP1 takes more roles and functionalities for system control and FOC operation, coordinate transformation and sensorless control algorithm of DTP-PMSM are put in the main interrupt Interrupt Service Routine (ISR) of CLA in DSP1. As contradiction, the main interrupt in DSP2 is only SPI-ISR which is used to communicate with DSP1. Besides, DSP2 do not use CAN, SCI, QEP blocks because DSP1 has already taken care of these.



(a)



(b)

Figure 7.8 Flow chart of main program in two DSPs (a) DSP1 (b) DSP2.

7.2.2 The Design of Interrupt Service Routines

As shown in Figure 7.8, after the system initialization is completed, the CPU performs an interrupt loop waiting state, and then the program cyclically executes the interrupt subroutine at a certain time interval. The main interrupt which is put in CLA-ISR in DSP1, is the core of the whole control program, including coordinate transformation, voltage and current sampling, PI control, SVPWM, motor speed and position calculation, open-loop start-up and MRAS based sensorless algorithm. Besides, the PWM pulse signal is generated and transmitted to the power board to control the operation of the motor. The main interrupt flow chart is shown in Figure 7.9.

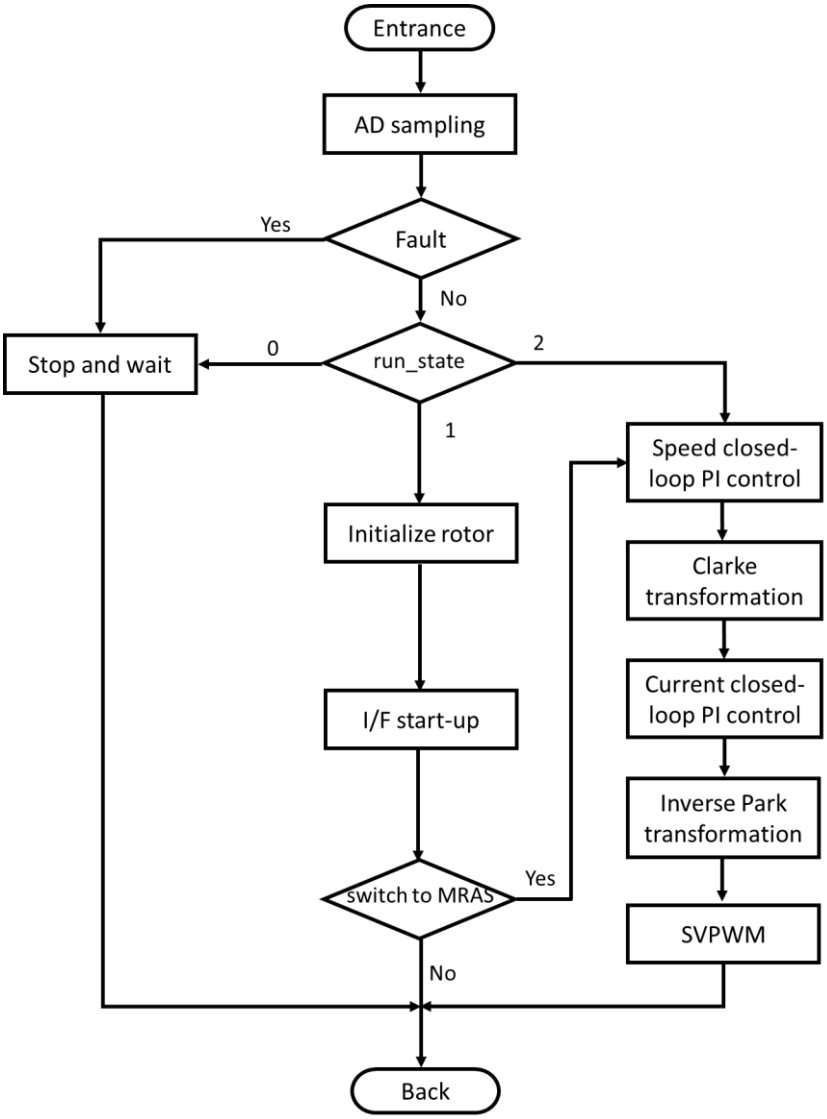


Figure 7.9 Flow chart of main interrupt in CPU1.

After entering the interrupt service routine, the current and voltage are sampled first, and then the fault is detected. Fault detection includes three aspects: on the one hand, detection of overcurrent protection based on the current value obtained by AD sampling; on the other hand, detection of SPI communication; at the same time, detection of whether the CPU timer overflows, that is, whether it exceeds a cycle (25 microseconds). Then, in the case of no fault, the run_state of the motor is judged, and then the program of different scenarios is executed. The three values of the run_state

represent the three operating states of the motor. The other two states are introduced here except for the ‘stop and wait’.

1. Open-loop start-up (run_state=1)

In this Thesis, the DTP-PMSM uses the I/F control in the open-loop acceleration start-up mode. Before the start of PMSM, it is necessary to know the initial position of the rotor. By applying a fixed phase voltage or current vector, the rotor can be forced to rotate to the space where the voltage or current vector is located. In this Thesis, the current vector is applied for rotor initializing. The rotor will rotate to the position where the current vector is under the action of i_q component. The details of this process are introduced in Section 6.1.1. In the experimental test, the machine rotor is located at the zero-angle position which coincides with the A-axis. The difference between this control mode and FOC speed PI control is that the reference value i_q^* of current torque component is directly given, rather than obtained through the PI output of speed loop. As shown in Figure 7.10, the rotor position angle used in vector control is the reference rotor position angle θ_e^* obtained by integrating the given speed, rather than the actual rotor position θ_e. In reference [273, 274], the working principle of I/F start-up in low speed section of permanent magnet synchronous motor is described in detail, and it is proved that the existence of power angle self-balance makes the I/F flow frequency ratio control realize the smooth starting of permanent magnet motor, so this Thesis will not repeat it.

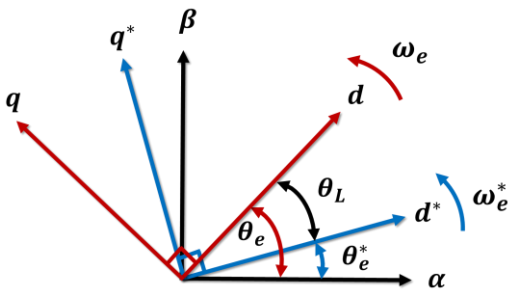


Figure 7.10 Coordinate relationship in I/F control.

With the increase of motor speed, the amplitude of back EMF increases gradually, and the estimation accuracy of MRAS algorithm can meet the needs of sensorless control. Then, it can be switched from I/F control to sensorless control. The process of transferring into sensorless control is a process of reducing the reference value i_q^* of the current torque component. Under the effect of the self-balance of the power angle, the difference θ_L between the actual position of the rotor θ_e and the reference position θ_e^* will gradually reduce. The criteria for transferring into sensorless control is as follows:

a) In the process of reducing the reference value i_q^* of current torque component, if the difference θ_L between the actual rotor position θ_e and the reference rotor position θ_e^* is less than the set threshold value and lasts for a certain period of time, the switching condition is considered to be satisfied.

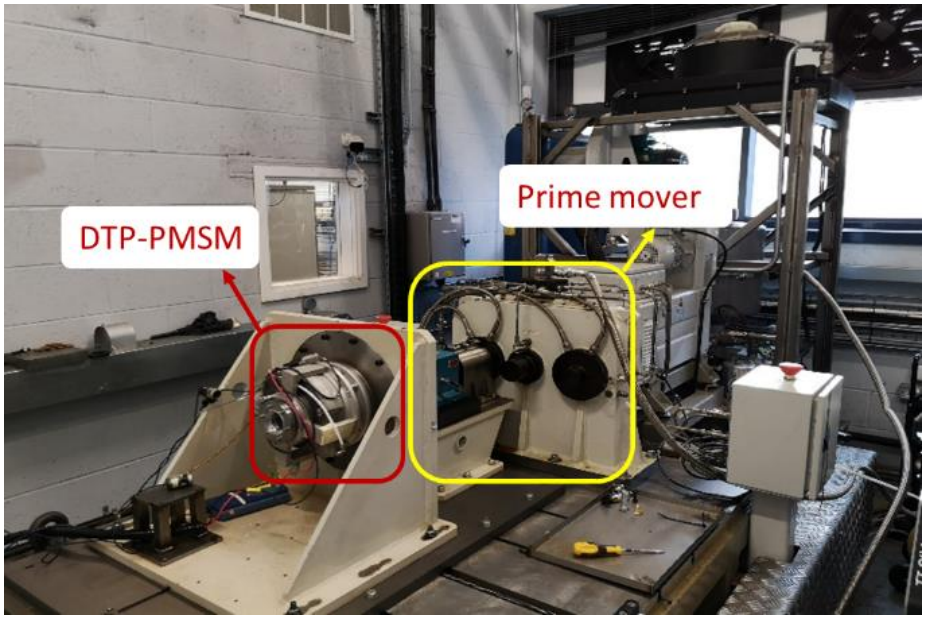
b) If the reference value of the current torque component i_q^* is reduced to the lower limit of the set threshold value, the difference θ_L between the actual position θ_e of the rotor and the reference position θ_e^* can not be less than the set threshold value, the switching is considered to be failed and the shutdown error is reported.

2. Speed and current closed-loop control (run_state=2)

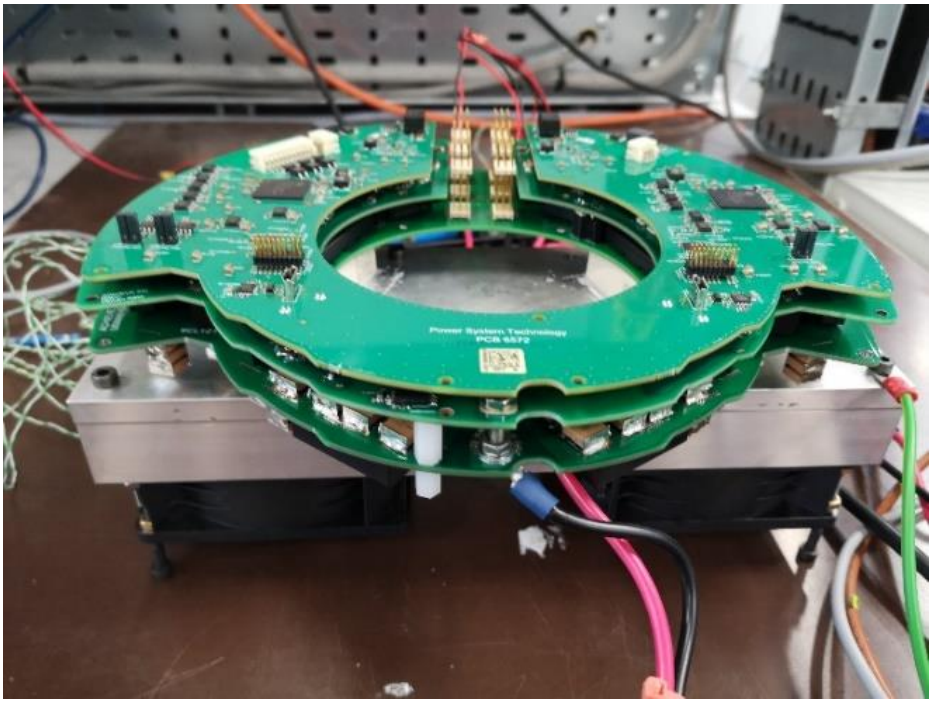
The program completes the whole function of sensorless control of PMSM mentioned above, including extracting the information of speed and rotor position by MRAS, obtaining current torque component i_q^* from PI regulating output of speed loop, getting voltage command from PI regulating output of current loop. In the Chapter 3 and Chapter 5 all these have been described in detail.

7.2.3 Experimental Rig

The experimental rig of ACHIEVE is composed of cooling system, driving system and control system, as shown in the Figure 7.12. The input supply 540 VDC at the converter's input is obtained by a cascade connection of two Delta-Elektronika SM500-CP90 [283]. Each of them supplies $\pm$ 270 VDC and is rated to provide 500 V, 90 A. The cooling system uses oil as coolant to cool down the dual three-phase motor and the converter. In the drive system, the dual three-phase machine is coupled mechanically with the drive machine (dynamometer machine) controlled by the dedicated power electronic converter in all four quadrants of its torque-speed plane. The corresponding torque-speed characteristics of TorqueMeter system as shown in Figure 7.13 covers all the areas required by the designed ACHIEVE system. The control system consists of a host computer and a data acquisition equipment. The drive system transmits signals such as current, speed and temperature to the control system, and the control system transmits measurement commands and fault inquiry commands to the drive system. The completed prototype pictures can be seen in Figure 7.11.



(a)



(b)

Figure 7.11 Lab prototype of ACHIEVE project. (a) DTP-PMSM and prime mover;(b)power converter.

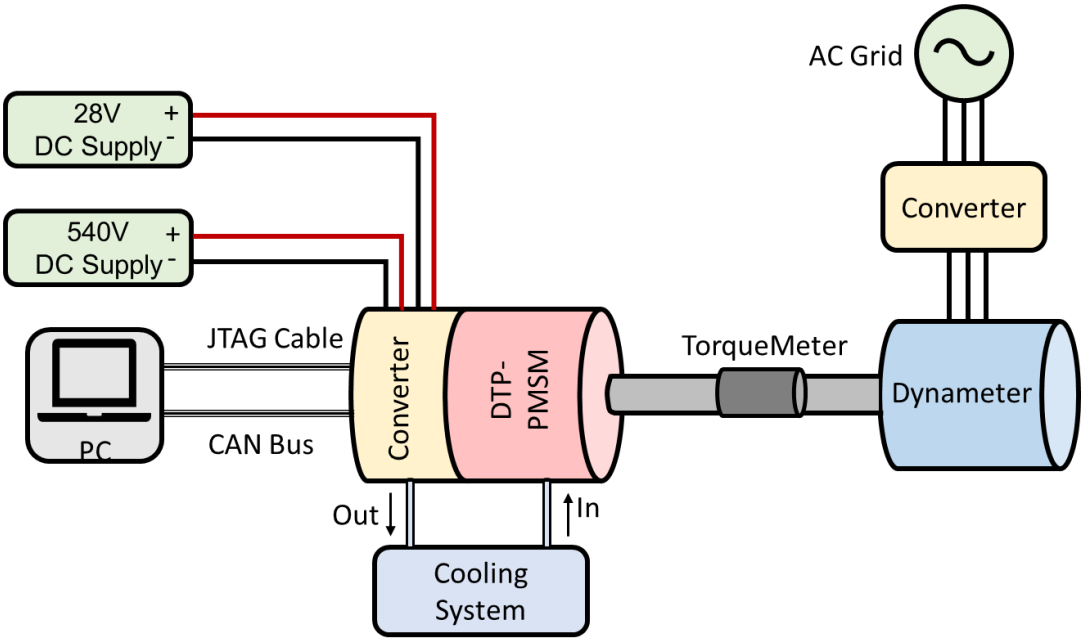


Figure 7.12 Schematic diagram of experimental platform for ACHIEVE project.



Figure 7.13 TorqueMeter system.

7.3 Experimental Results for Sensorless Position Control System

In this section, experimental results for the sensorless position control system are presented. Different tests are designed to exhibit its stability and dynamic performance.

7.3.1 Comparative Study of Conventional and Enhanced MRAS

The speed of machine is controlled by the dynameter which is operating in a constant speed mode 1000 rpm in Figure 7.12. The current is regulated by the current close loop mode using rotor position detected by the encoder. The enhanced MRAS is run to assess its performance and the estimation results are not used for the FOC system. The initial value of PM flux in enhanced MRAS algorithm is set to be 30% of its nominal value 0.03 Wb. As shown in Figure 7.14, it takes around 0.5 s for the estimated flux Flux_est to identify the reference value Flux. The overshoot during this dynamic response is less than 7% which is satisfactory. The rotor position sensored by encoder and estimated by enhanced MRAS are shown in Figure 7.15. The difference between them Theta_err is presented in Figure 7.16. Similarly, the sensored rotor speed N and estimated value N_est are shown in Figure 7.17 and the speed difference between them is shown in Figure 7.18. It can be seen that the performance of the enhanced MRAS is excellent.

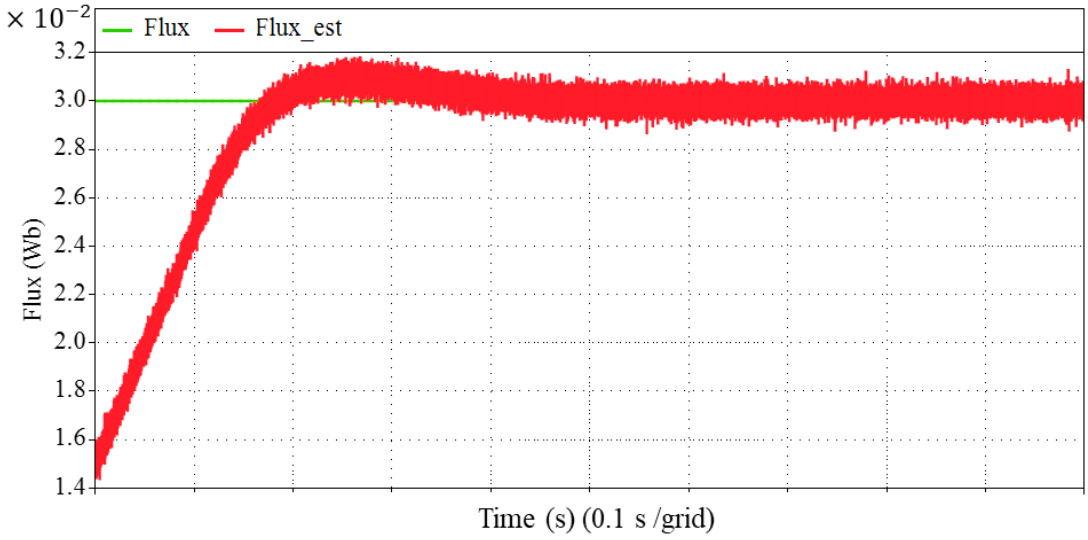


Figure 7.14 PM flux reference and estimation value by enhanced MRAS.

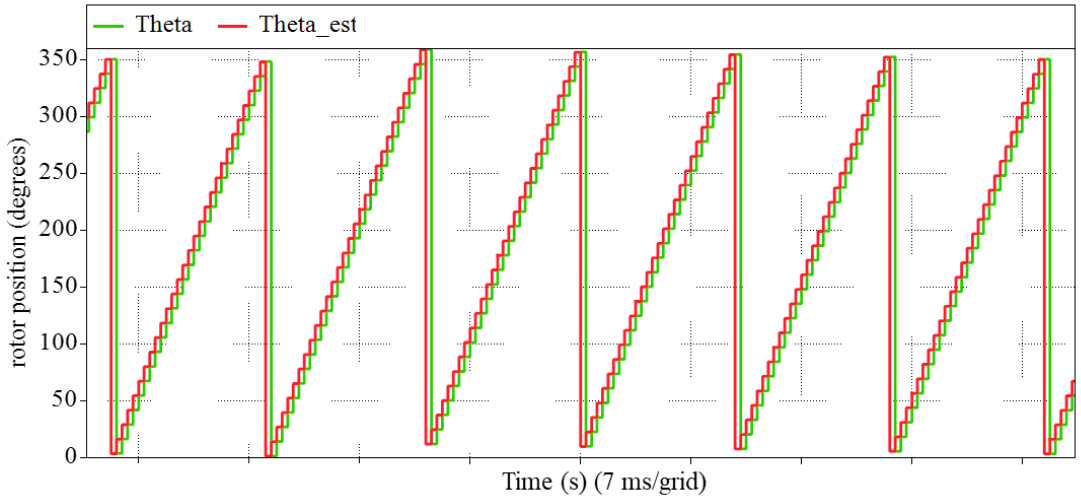


Figure 7.15 Rotor position sensored by encoder and estimated by enhanced MRAS.

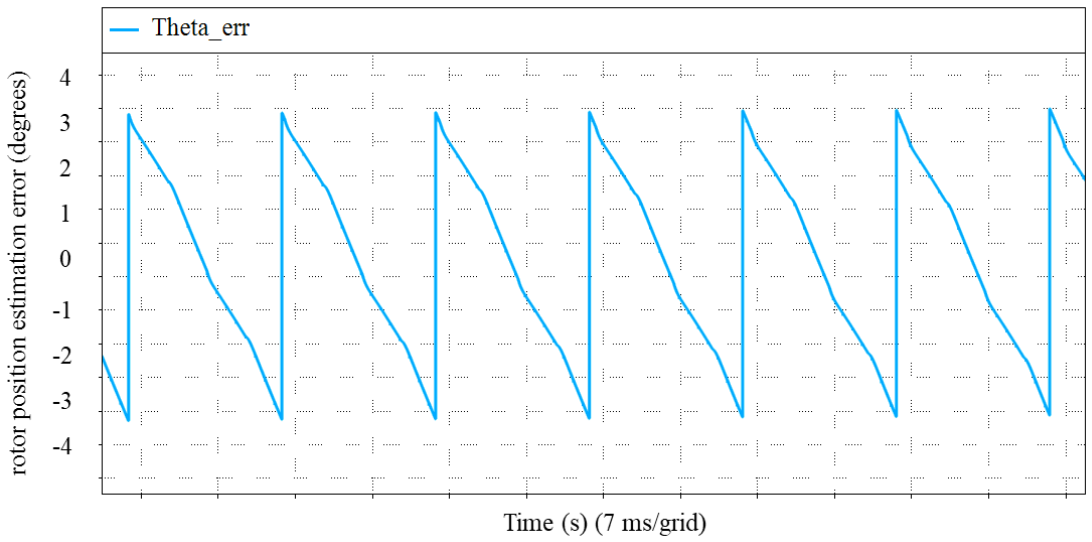


Figure 7.16 Rotor position estimation error between position sensored by encoder and estimated by enhanced MRAS.

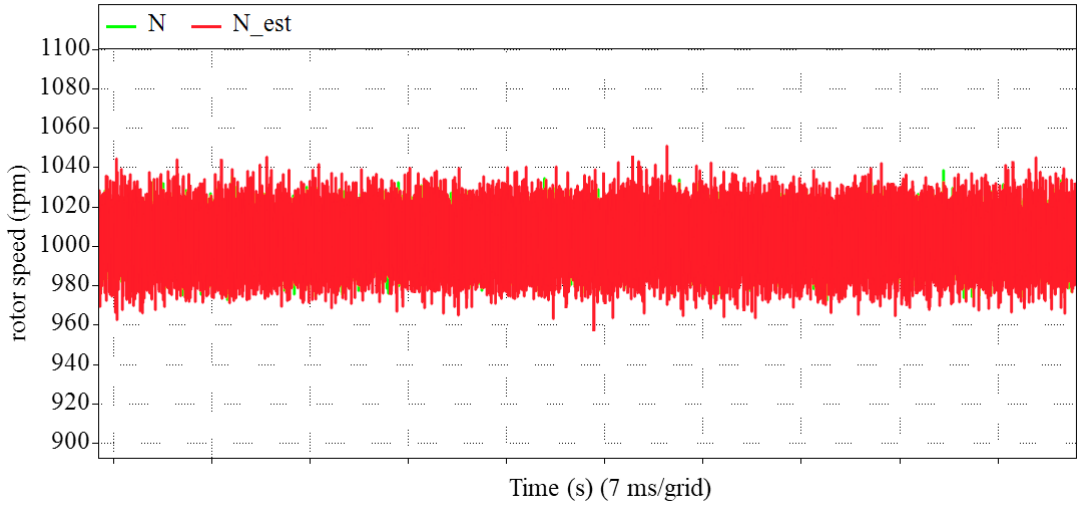


Figure 7.17 Rotor speed sensored by encoder and estimated by enhanced MRAS.

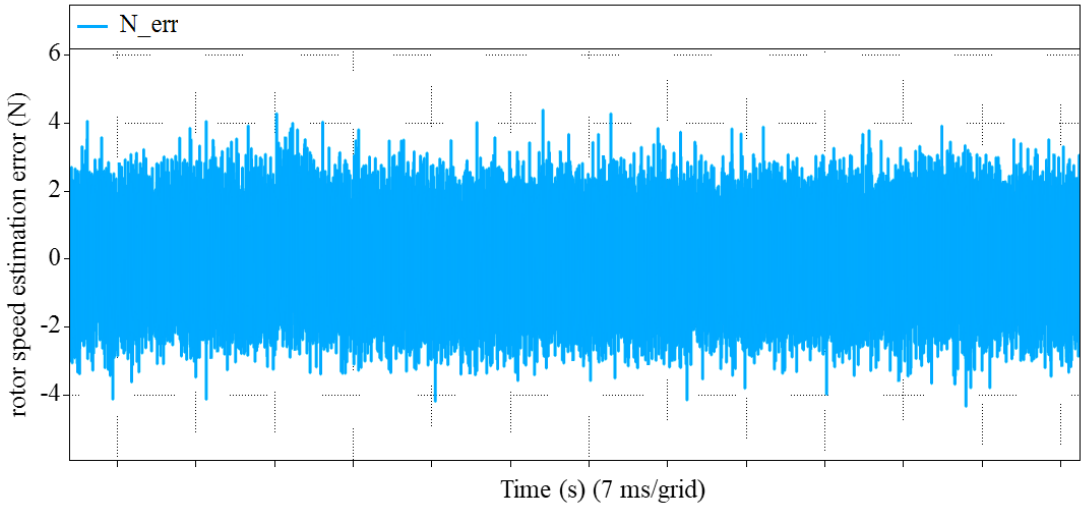


Figure 7.18 Rotor speed estimation error between speed sensored by encoder and estimated by enhanced MRAS.

The same experimental procedure is repeated for both conventional MRAS and enhanced MRAS at different rotor speed. The rotor position estimation error for the two algorithms at different speed are compared in Figure 7.19. The operating speed range covers from 100 rpm to 3000 rpm. The simulation results of these two methods are close to each other and the rotor position estimation error for both methods reduces as

rotor speed increases. In experiment process, for speed range below 100 rpm, the performance of these two sensorless algorithms becomes very poor and even fail at extreme low speed. This is consistent with previous review in Chapter 4 about MRAS method. Besides, the encoder of the machine as seen in Figure 7.4 is no longer available when the machine runs above 3000 rpm. Actually, it will be removed for middle- and high-speed test because there will be high risk of damage due to both limited installation firmness and excessive centrifugal force at high rotating speed. Therefore, the comparative study between the two methods is conducted for the speed range below 3000 rpm. However, this is not an issue for validation of the machine with rated speed of 12400 rpm. The reason is that inherently, MRAS performs better at high speed than low speed. When machine speed goes beyond 3000 rpm, the speed and position information estimated by MRAS have sufficient accuracy for closed loop control, hence there is no problem at all without an encoder.

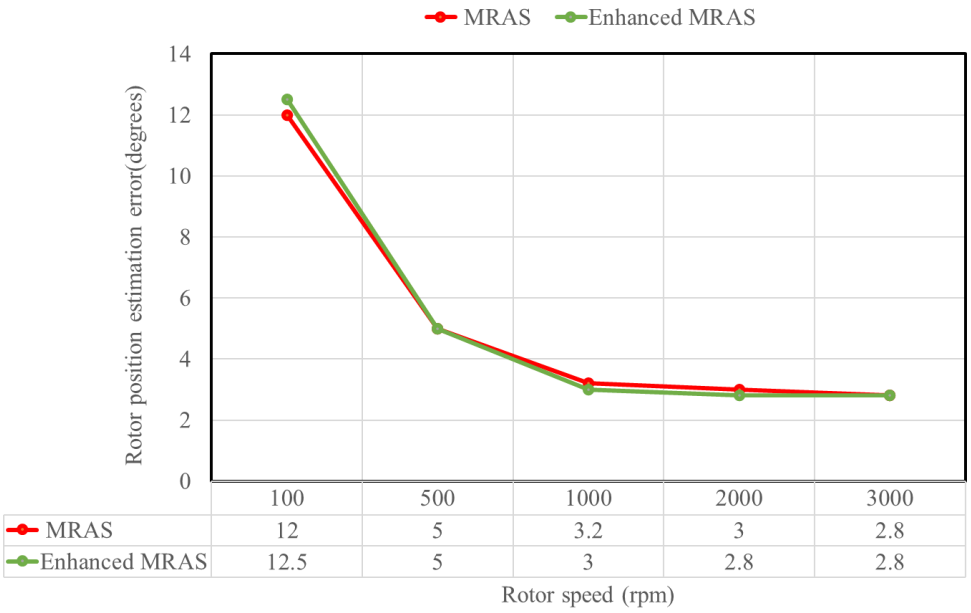


Figure 7.19 Rotor position estimation error for conventional and enhanced MRAS at different rotor speed.

7.3.2 Hybrid Speed Control for Full Speed Range

As the MRAS method does not work for zero and low speed, an I/F strategy is applied to start up the machine with the described switch operation to smoothly switch between these two methods. The flow chart of proposed hybrid control scheme is presented in Figure 7.20. The initialization of rotor and I/F strategy is detailed in Chapter 6. During this stage, the speed goes up from zero to 500 rpm in Figure 7.21 (b) and the q-axis current keeps at 5A firstly and then decrease to zero in Figure 7.21 (a). The error between actual rotor position and I/F estimation rotor position $\Delta\theta$ is depicted in Figure 7.21. $\Delta\theta$ is set to 90 degrees initially and then decreases as the actual rotating frame and the I/F assumption frame becomes closer under the rule of 'torque-power angle self-balance'. As indicated in Figure 7.21(a)-(c), the switching operation appears at the point that machine runs at 500 rpm while $i_q = 0$ and $\Delta\theta$ below five degrees at the same time.

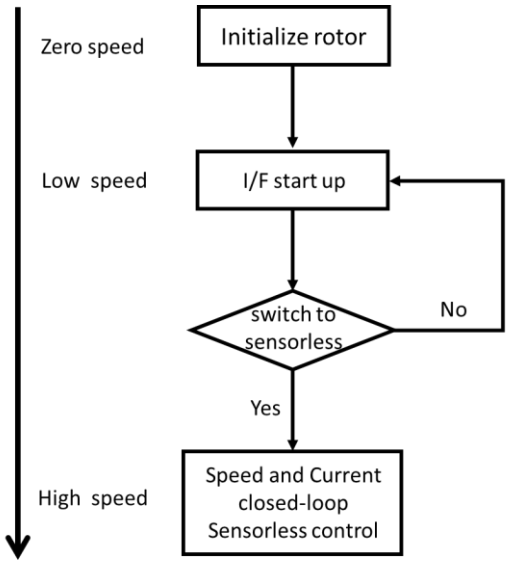


Figure 7.20 Flow chart of hybrid control method for full speed range.

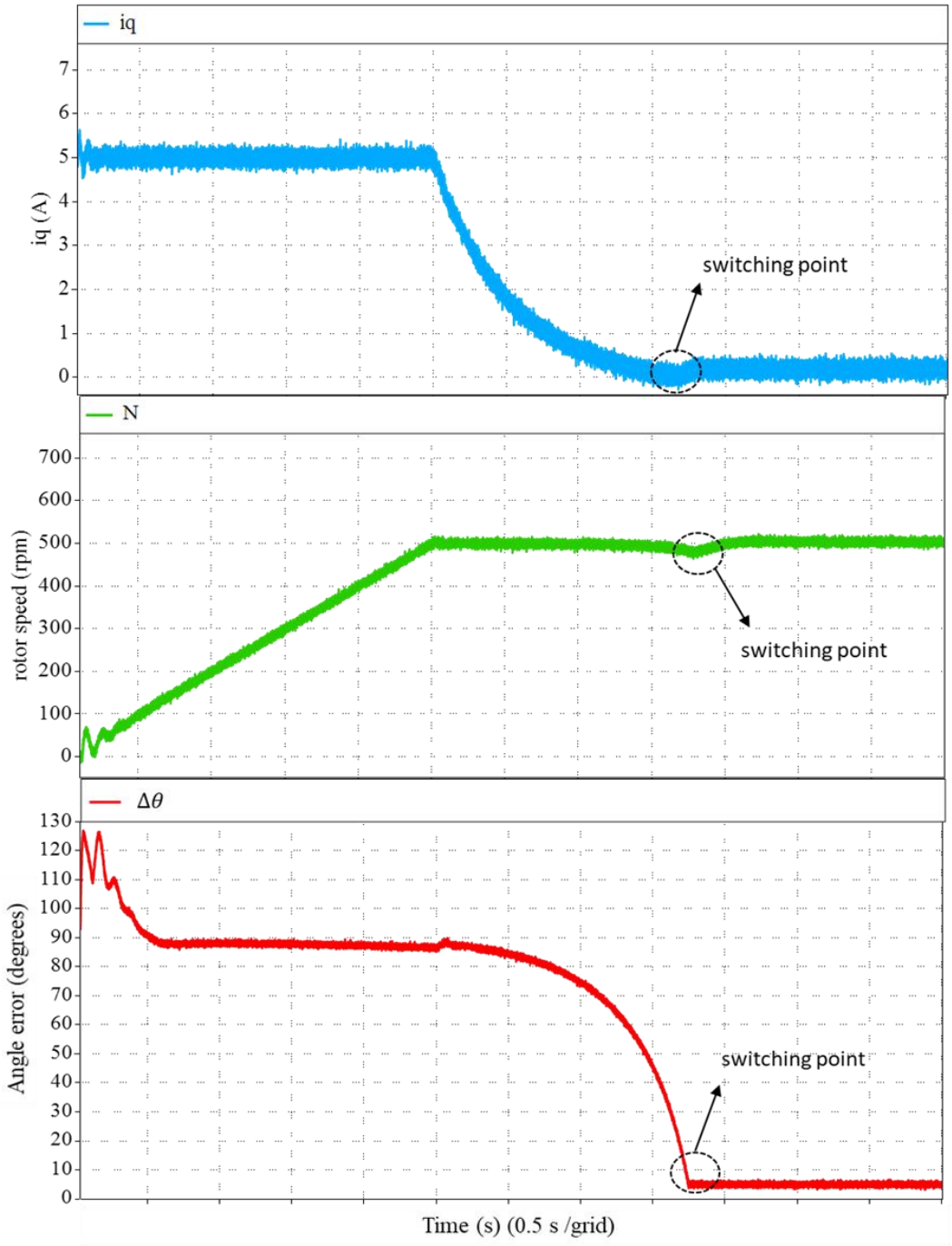
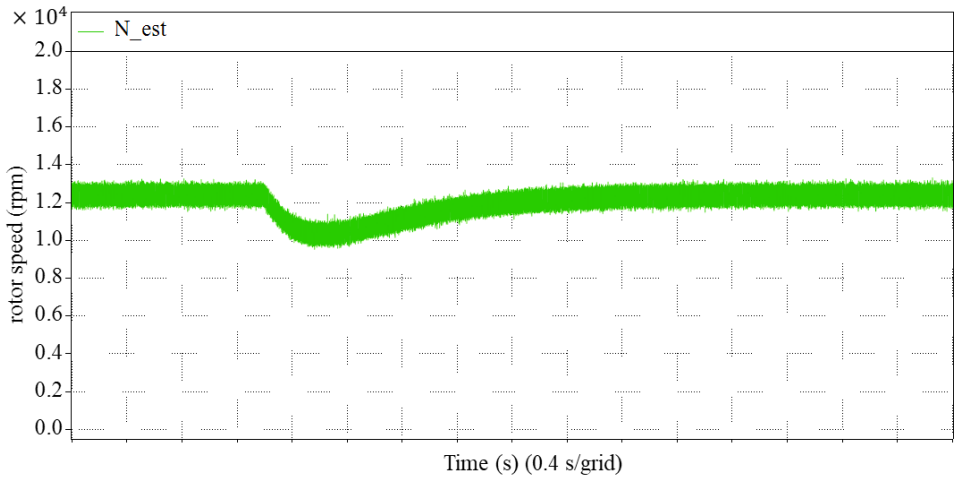


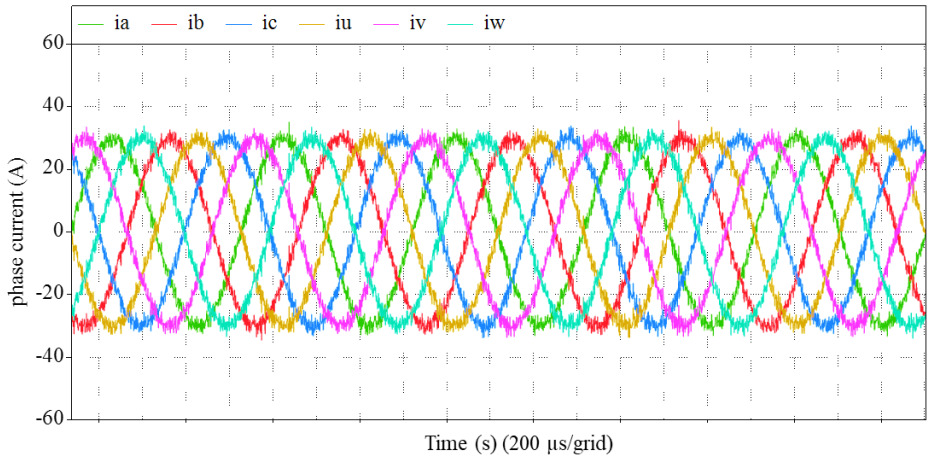
Figure 7.21 Experimental results for I/F start-up process including q-axis current, rotor speed from encoder and angle error between rotor position from encoder and I/F estimation.

After the switching operation, the machine runs in sensorless control mode. The machine speed is controlled to increase to 12.4 krpm. A step change from T_L=0 Nm to 5 Nm is applied to the machine running at 12.4 krpm. As presented in Figure 7.22 (a),

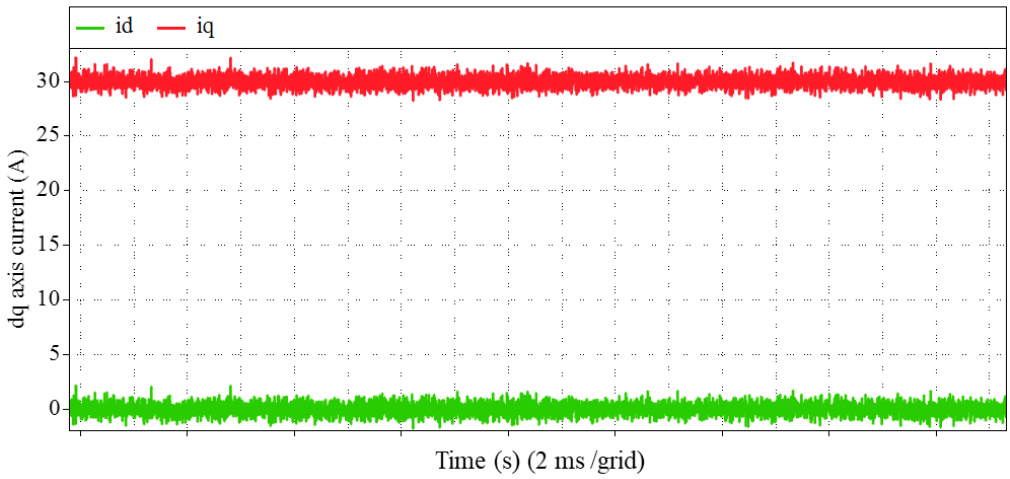
it takes around 2 s for the machine speed to make response with an overshoot under 10%. The rated torque is applied and the corresponding six phase current and *dq* axis currents are shown in Figure 7.22 (b) and (c) respectively. Although the encoder is not available at this scenario and the actual rotor speed and position are not available either, sensorless method could be proved by the good performance of closed loop current and speed control. Hence, the effectiveness of proposed sensorless control system is verified.



(a)



(b)



(c)

Figure 7.22 Experimental results for high-speed operation.

7.4 Chapter Summary

This chapter describes the test platform in the lab and presents experimental results. The reported experimental results have verified the analytical results derived in this Thesis, namely:

- The enhanced MRAS proposed in chapter 5 has fast response to PM flux variation and satisfactory performance in rotor speed and position estimation.
- The I/F start-up strategy proposed in chapter 6 works perfectly and the switch operation between I/F and MRAS is quite smooth.
- The FOC system for ACHIEVE machine that is proposed in chapter 3 shows good performance under load variation.
- Both MRAS and enhanced MRAS show good performance in speed estimation over a wide range. In this project, it can be from 100 rpm to 12400 rpm. The estimation accuracy decreases as the speed goes into very low speed range. In

this study, the rotor position estimation error increases from 2.5 degrees to 12.2 degrees as machine decelerates from 3000 rpm to 100 rpm.

Generally, the experimental work results presented in this chapter are consistence with simulations results in previous chapters. The difference between them is that the comparative study between MRAS and enhanced MRAS is made for a limited speed range. However, as explained in 7.3.1, this does not affect the successful validation of machine for full speed range.

Overall, the investigate of sensorless control for DTP-PMSM proposed by this study is confirmed to be a suitable solution for application in motor/generating system of future more-electric turboprop aircraft. It can also be of interest for general-purpose advanced drive control engineering.

Chapter 8 Conclusions and Future work

This thesis is focused on the sensorless control design for a DTP-PMSM based motoring/generating system. The novelty and contribution of the thesis are summarized as the follows.

8.1 Conclusions

(1) A novel mathematical model of DTP-PMSM specifically designed for ACHIEVE has been built considering the unique asymmetric winding structure. The proposed XYZ model simplifies the mathematic model and is employed for the development of space vector control of the machine.

(2) The control design process for a novel MEA motoring/generating system is introduced which takes into account its control requirements (speed for motoring mode, DC link bus for generating mode). The designed controllers can ensure stable operation of the system throughout the speed and load operating ranges. The effectiveness of the control system with encoder in motoring and generating mode is verified through simulation by PLECS.

(3) An enhanced MRAS is developed to improve reliability of conventional MRAS during parameter variation. The proposed method estimates both rotor speed and flux in a cascaded loop. Comparison study has been made between MRAS and enhanced MRAS under different scenario, for instance, speed variation, load variation and PM flux variation. Both methods present good performance in the presence of speed or load

variation. The proposed enhanced MRAS shows the priority over MRAS when PM flux has variation.

(4) An I/F method is proposed for zero and low speed range operation in order to reach full speed range sensorless control of ACHIEVE. A switching operation is designed to achieve smooth transition between I/F open-loop mode during start-up and MRAS closed-loop in middle- and high-speed.

(5) The experimental test rig to verify the theoretical findings of this study is developed and built. The design and construction of hardware and software are introduced. A hybrid sensorless control system combining I/F start-up and MRAS with switching operation has been implemented. The feasibility of the hybrid algorithm is successfully verified by the experimental results.

8.2 Future Work

The achieved results met all key technical requirements and the research generated multiple possibilities for follow-on studies. The following points outline potential future work that could be expanded from the research presented in this thesis:

(1) In the experimental test, it is found that conventional MRAS based on fixed PI regulator only has good dynamic performance in a certain speed region and is difficult to adapt to variable speed or load in a wide range operation. One of the potential solutions is to develop a self-adaptive PI controller which tunes its parameters adaptively according to the machine speed and load.

(2) Following the previous point of view, it is necessary to explore the stability range of the MRAS based sensorless system which has hardly been deeply dug up to now. The control plant model needs to be derived. This stability range requires to be analysed with respect to operating speed or load. Based on these, the design of the adaptive controller in MRAS will be more effectively and reasonably.

(3) As illustrated in Chapter 5, enhanced MRAS has advantage of simple structure and easy hardware implement. However, it has a limit on the number of parameters that can be estimated at the same time. Hence, alternative strategies could be investigated to achieve multiparameter identification, such as recursive least squares (RLS) algorithms, neural network (NN) technology and extended Kalman filter (EKF), etc.

8.3 Publications

The research work given in this thesis has resulted in the following conference papers:

[1]. Fan, L., et al., Comparative Study of Sensorless Methods Based on Sliding Mode Observer for Dual Three-Phase Permanent Magnet Synchronous Machine. 2021.

[2]. Chen, Y., Bozhko, S., Fan, L., et al. Decoupled model for asymmetrical dual three phase permanent magnet synchronous machine. in 2019 IEEE International Electric Machines & Drives Conference (IEMDC). 2019. IEEE.

[3]. Fan, L., et al. Sensorless control of dual-three phase PMSM based aircraft electric starter/generator system using model reference adaptive system method. in CSAA/IET International Conference on Aircraft Utility Systems (AUS 2018). 2018. IET.

[4]. Fan, L., et al. Comparative study of back EMF based sensorless control methods for dual three-phase PMSM. in 2018 IEEE International Conference on Electrical Systems for Aircraft, Railway, Ship Propulsion and Road Vehicles & International Transportation Electrification Conference (ESARS-ITEC). 2018. IEEE.

Appendix A Phasor Diagram Transformation

The transformation between the two-phase rotating *dq* frames and three-phase frame is as follows:

$$\begin{bmatrix} x_a \\ x_b \\ x_c \end{bmatrix} = k_{abc} \begin{bmatrix} x_d \\ x_q \end{bmatrix} \quad (A.\ 1)$$

where the inverse *dq* transformation coefficient, k_{abc} , is defined as:

$$k_{abc} = \begin{bmatrix} cos\theta_e & -sin\theta_e \\ cos\ (\theta_e - \frac{2\pi}{3}) & -sin\ (\theta_e - \frac{2\pi}{3}) \\ cos\ (\theta_e + \frac{2\pi}{3}) & -sin(\theta_e + \frac{2\pi}{3}) \end{bmatrix} \quad (A.\ 2)$$

Appendix B Simulation Models

Simulation analysis is primarily done with Plexim®/Plecs®. The following are the models created in Plecs to support this study.

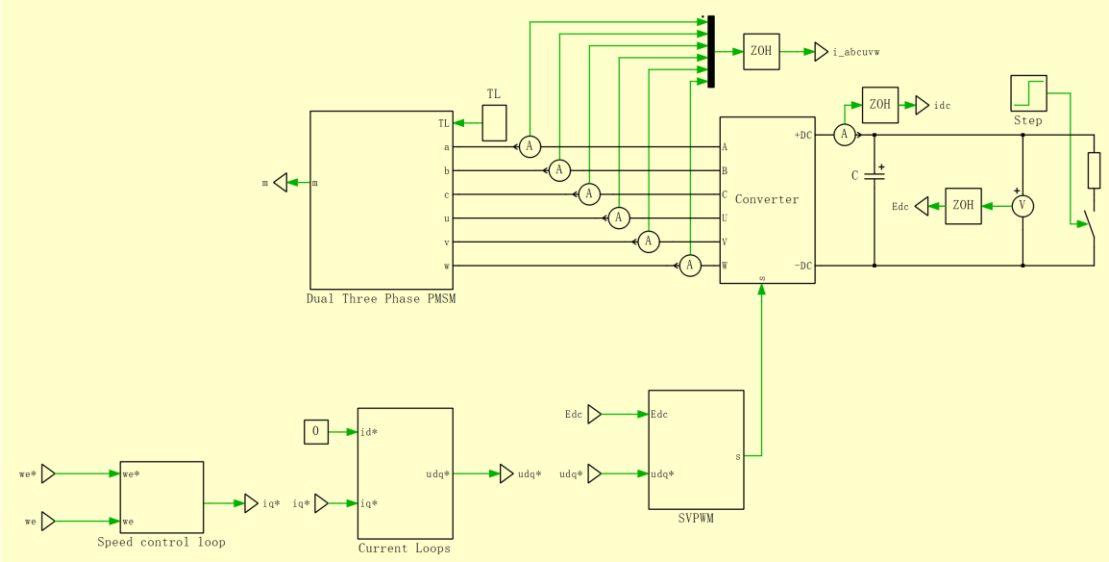


Figure B.1 Power system for motoring mode.

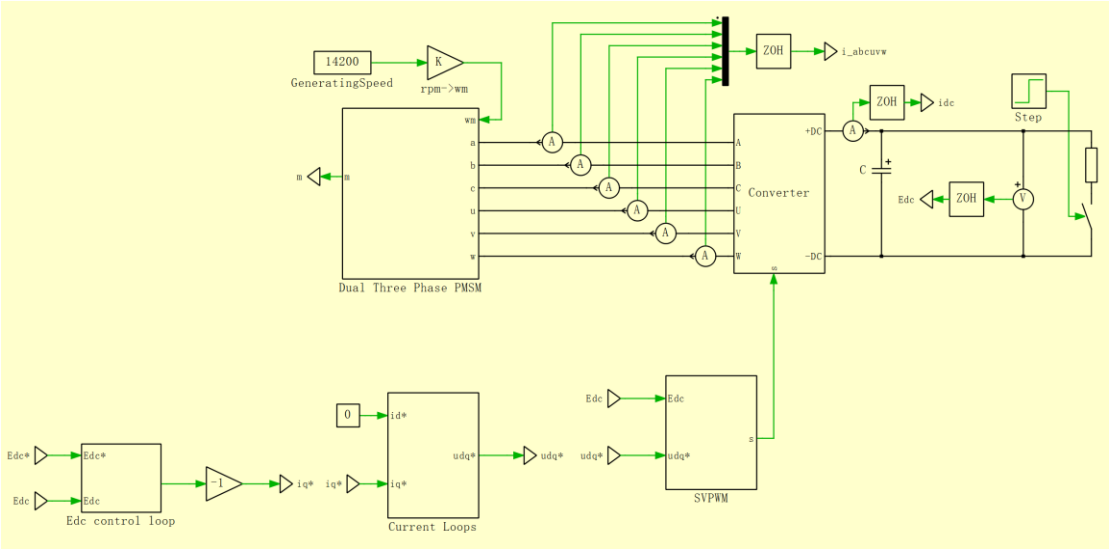


Figure B.2 Power system for generating mode.

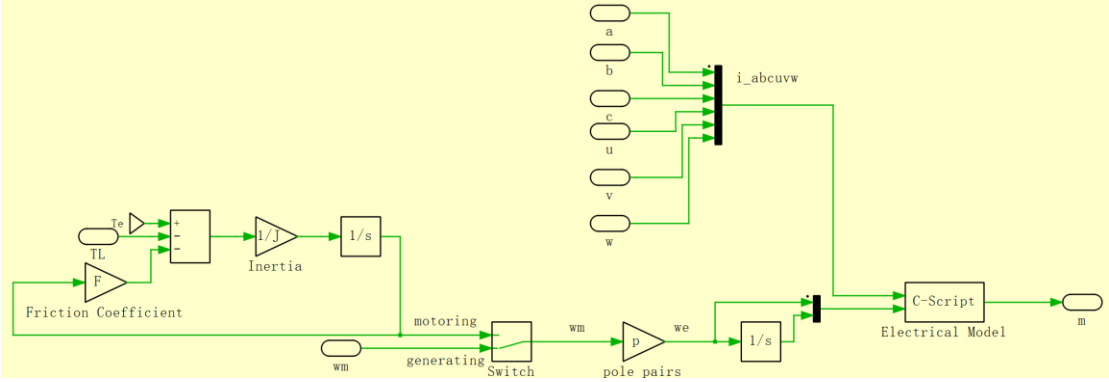


Figure B.3 Dual Three-Phase PMSM model.

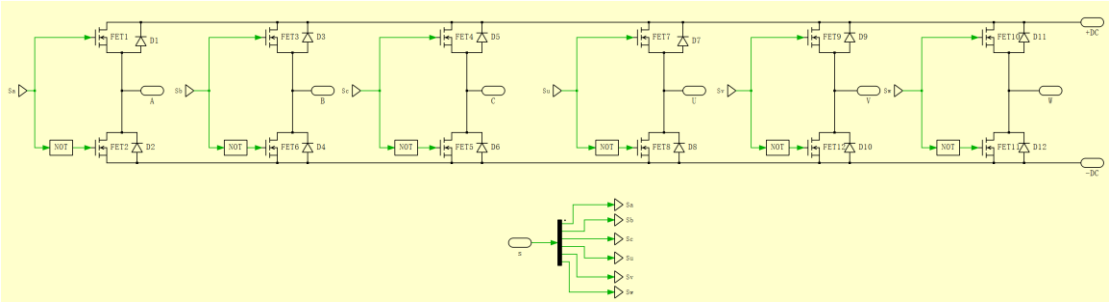


Figure B.4 Converter model.

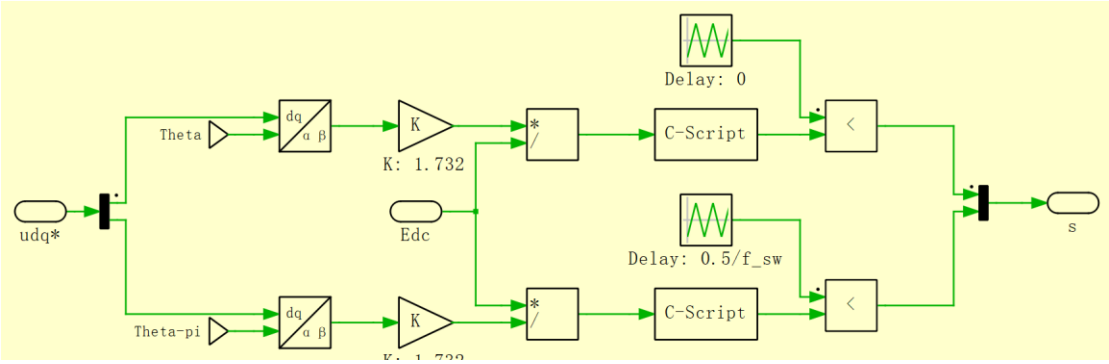


Figure B.5 SVPWM model.

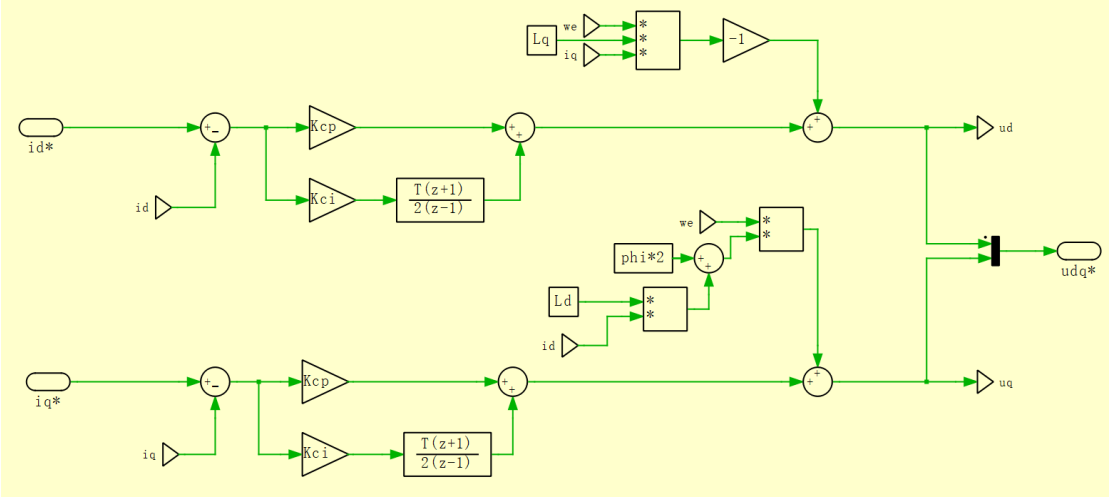


Figure B.6 Current Loops model.

Reference

1. Noland, J.K., *Hydrogen Electric Airplanes: A Disruptive Technological Path to Clean Up the Aviation Sector.* IEEE Electrification Magazine, 2021. **9**(1): p. 92-102.

2. *Archery Strategy Consulting.* . [cited 2021 May]; Available from: http://www.archeryconsulting.fr/.

3. Ismagilov, F., et al. *Electric Machines Development Process for Aviation Hybrid Propulsion Systems*. in *IECON 2020 The 46th Annual Conference of the IEEE Industrial Electronics Society*. 2020. IEEE.

4. Wheeler, P. and S. Bozhko, *The more electric aircraft: Technology and challenges.* IEEE Electrification Magazine, 2014. **2**(4): p. 6-12.

5. Rosero, J., et al., *Moving towards a more electric aircraft.* IEEE Aerospace and Electronic Systems Magazine, 2007. **22**(3): p. 3-9.

6. Gao, F., *Decentralised control and stability analysis of a multi-generator based electrical power system for more electric aircraft*. 2016, University of Nottingham.

7. AirfieldNews.Net. *HOW THE FUTURE OF ELECTRIC AIRCRAFT LIES BEYOND THE ENGINES*. September 10, 2019; Available from: http://airfieldnews.net/news/how-the-future-of-electric-aircraft-lies-beyond-the-engines/.

8. Sarlioglu, B. and C.T. Morris, *More electric aircraft: Review, challenges, and opportunities for commercial transport aircraft.* IEEE transactions on Transportation Electrification, 2015. **1**(1): p. 54-64.

9. Roboam, X., B. Sareni, and A. De Andrade, *More electricity in the air: Toward optimized electrical networks embedded in more-electrical aircraft.* IEEE industrial electronics magazine, 2012. **6**(4): p. 6-17.

10. Lukic, M., et al., *Review, Challenges and Future Developments of Electric Taxiing Systems.* IEEE Transactions on Transportation Electrification, 2019.

11. Moir, I. and A. Seabridge, *Aircraft systems: mechanical, electrical and avionics subsystems integration*. Vol. 52. 2011: John Wiley & Sons.

12. Yang, T., *Development of dynamic phasors for the modelling of aircraft electrical power systems*. 2013, University of Nottingham.

13. Cutts, S., *A collaborative approach to the more electric aircraft.* 2002.

14. Faleiro, L. *Summary of the European power optimised aircraft (POA) project*. in *25th International Congress of the Aeronautical Sciences, ICAS*. 2006.

15. *More Open Electrical Technologies*. [cited 2020 22 April]; Available from: https://trimis.ec.europa.eu/project/more-open-electrical-technologies.

16. *Innovative technologies Clean Sky 1*. [cited 2020 22 April]; Available from: https://www.cleansky.eu/innovative-technologies.

17. *Innovative technologies Clean Sky 2*. [cited 2020 22April]; Available from: https://www.cleansky.eu/innovative-technologies.

18. sky, c. *Electrical taxiing and much more with Clean Sky's ACHIEVE*. [cited 2020 29May]; Available from: https://www.cleansky.eu/electrical-taxiing-and-much-more-with-clean-skys-achieve.

19. Chen, Y., et al. *Decoupled model for asymmetrical dual three phase permanent magnet synchronous machine*. in *2019 IEEE International Electric Machines & Drives Conference (IEMDC)*. 2019. IEEE.

20. Pillay, P. and R. Krishnan, *Modeling, simulation, and analysis of permanent-magnet motor drives. I. The permanent-magnet synchronous motor drive.* IEEE Transactions on industry applications, 1989. **25**(2): p. 265-273.

21. Galea, M., et al. *Design of a high force density tubular permanent magnet motor*. in *The XIX International Conference on Electrical Machines-ICEM 2010*. 2010. IEEE.

22. Avery, C., S. Burrow, and P. Mellor. *Electrical generation and distribution for the more electric aircraft*. in *2007 42nd international universities power engineering conference*. 2007. IEEE.

23. Roboam, X. *New trends and challenges of electrical networks embedded in "more electrical aircraft"*. in *2011 IEEE International Symposium on Industrial Electronics*. 2011. IEEE.

24. Moir, I., A. Seabridge, and M. Jukes, *Civil avionics systems*. 2013: John Wiley & Sons.

25. *MIL-STD-704F*. Aircraft Electric Power Characteristics. United States of America: Department of Defense Interface Standard.

26. Mingos, H., *The Aircraft Year Book for 1938*. 1938: Aeronautical Chamber of Commerce of America, Incorporated.

27. Mingos, H., *The Aircraft Year Book for 1939*. 1939: Aeronautical Chamber of Commerce of America, Incorporated.

28. Bertinov, A., *Aircraft electrical generators*. 1964, FOREIGN TECHNOLOGY DIV WRIGHT-PATTERSON AFB OH.

29. Mingos, H., *The Aircraft Year Book for 1953*. 1953: Aeronautical Chamber of Commerce of America, Incorporated.

30. Boice, W. and L. Levoy, *Basic considerations in selection of electric systems for large aircraft.* Electrical Engineering, 1944. **63**(6): p. 279-287.

31. Holliday, T., *Applications of electric power in aircraft.* Electrical Engineering, 1941. **60**(5): p. 218-225.

32. Madonna, V., P. Giangrande, and M. Galea, *Electrical power generation in aircraft: Review, challenges, and opportunities.* IEEE Transactions on Transportation Electrification, 2018. **4**(3): p. 646-659.

33. Quigley, R. *More electric aircraft*. in *Applied Power Electronics Conference and Exposition, 1993. APEC'93. Conference Proceedings 1993., Eighth Annual*. 1993. IEEE.

34. Moir, I. and A. Seabridge, *Vehicle management systems.* Military Avionics Systems, 2006: p. 399-401.

35. Andrade, L. and C. Tenning, *Design of Boeing 777 electric system.* IEEE Aerospace and Electronic Systems Magazine, 1992. **7**(7): p. 4-11.

36. Abdel-Fadil, R., A. Eid, and M. Abdel-Salam. *Electrical distribution power systems of modern civil aircrafts*. in *2nd International Conference on Energy Systems and Technologies*. 2013.

37. Olaiya, M. and N. Buchan, *High power variable frequency generator for large civil aircraft.* 1999.

38. Adkins, B., W. Philipp, and A. Hossle, *Electrical machines for aircraft.* Proceedings of the IEE-Part A: Power Engineering, 1956. **103**(1S): p. 116-127.

39. Buticchi, G., et al., *On-board microgrids for the more electric aircraft—Technology review.* IEEE Transactions on Industrial Electronics, 2018. **66**(7): p. 5588-5599.

40. Sinnett, M., *787 no-bleed systems: saving fuel and enhancing operational efficiencies*. Aero Quarterly, 2007. **18**: p. 6-11.

41. Nelson, T. *787 systems and performance*. [cited 2021 Feb]; Available from: http://myhres.com/Boeing-787-Systems-and-Performance.pdf.

42. Bhangu, B.S. and K. Rajashekara, *Electric starter generators: Their integration into gas turbine engines.* IEEE Industry Applications Magazine, 2013. **20**(2): p. 14-22.

43. Nøland, J.K., et al. *Electrical machines and power electronics for starter-generators in more electric aircrafts: A technology review*. in *IECON 2019-45th Annual Conference of the IEEE Industrial Electronics Society*. 2019. IEEE.

44. Elbuluk, M.E. and M.D. Kankam, *Potential starter/generator technologies for future aerospace applications.* IEEE Aerospace and Electronic Systems Magazine, 1997. **12**(5): p. 24-31.

45. Yang, Z., et al., *Comparative study of interior permanent magnet, induction, and switched reluctance motor drives for EV and HEV applications.* IEEE Transactions on Transportation Electrification, 2015. **1**(3): p. 245-254.

46. Nøland, J.K., et al., *High-power machines and starter-generator topologies for more electric aircraft: A technology outlook.* IEEE Access, 2020. **8**: p. 130104-130123.

47. Zhang, Z., et al., *Overview and analysis of PM starter/generator for aircraft electrical power systems.* CES Transactions on Electrical Machines and Systems, 2017. **1**(2): p. 117-131.

48. Alan, I. and T.A. Lipo, *Starter/generator employing resonant-converter-fed induction machine. I. Analysis.* IEEE Transactions on Aerospace and Electronic Systems, 2000. **36**(4): p. 1309-1328.

49. Alan, I. and T.A. Lipo, *Starter/generator employing resonant-converter-fed induction machine. II. Hardware prototype.* IEEE Transactions on Aerospace and Electronic systems, 2000. **36**(4): p. 1319-1329.

50. Zhu, Z.-Q. and D. Howe, *Electrical machines and drives for electric, hybrid, and fuel cell vehicles*. Proceedings of the IEEE, 2007. **95**(4): p. 746-765.

51. MacMinn, S.R. and J.W. Sember. *Control of a switched-reluctance aircraft engine starter-generator over a very wide speed range*. in *Proceedings of the 24th Intersociety Energy Conversion Engineering Conference*. 1989. IEEE.

52. Richter, E. and C. Ferreira. *Performance evaluation of a 250 kW switched reluctance starter generator*. in *IAS'95. Conference Record of the 1995 IEEE Industry Applications Conference Thirtieth IAS Annual Meeting*. 1995. IEEE.

53. Jones, S.R. and B.T. Drager, *Sensorless switched reluctance starter/generator performance.* IEEE Industry applications magazine, 1997. **3**(6): p. 33-38.

54. Powell, D.J., et al., *Iron loss in a modular rotor switched reluctance machine for the" More-Electric" aero-engine.* IEEE transactions on magnetics, 2005. **41**(10): p. 3934-3936.

55. Schofield, N. and S. Long, *Generator operation of a switched reluctance starter/generator at extended speeds.* IEEE transactions on vehicular technology, 2008. **58**(1): p. 48-56.

56. MacMinn, S.R. and W.D. Jones. *A very high speed switched-reluctance starter-generator for aircraft engine applications*. in *Proceedings of the IEEE National Aerospace and Electronics Conference*. 1989. IEEE.

57. Song, S., et al., *Model Predictive Control of Switched Reluctance Starter/Generator With Torque Sharing and Compensation.* IEEE Transactions on Transportation Electrification, 2020. **6**(4): p. 1519-1527.

58. Wei, J., et al., *The control strategy of open-winding permanent magnet starter-generator with inverter-rectifier topology.* IEEE Transactions on Industrial Informatics, 2012. **9**(2): p. 983-991.

59. Legranger, J., et al., *Combination of finite-element and analytical models in the optimal multidomain design of machines: Application to an interior permanent-magnet starter generator.* IEEE Transactions on Industry Applications, 2009. **46**(1): p. 232-239.

60. Wang, C.-F., et al., *A permanent magnet integrated starter generator for electric vehicle onboard range extender application.* IEEE Transactions on Magnetics, 2012. **48**(4): p. 1625-1628.

61. Levi, E., *Multiphase electric machines for variable-speed applications.* IEEE Transactions on industrial electronics, 2008. **55**(5): p. 1893-1909.

62. Zhou, C., *RESEARCH ON DRIVE AND FAULT-TOLERANT CONTROL TECHNOLOGIES OF DUAL THREE-PHASE PERMANENT MAGNET SYNCHRONOUS MOTOR*, in *Harbin Institute of Technology*. 2016. p. 1-z.

63. W'iiite, D. and H. Woodson, *Electromechanical energy conversion*. 1959: John Wiley & Sons Inc., New York.

64. Ward, E. and H. Härer. *Preliminary investigation of an invertor-fed 5-phase induction motor*. in *Proceedings of the Institution of Electrical Engineers*. 1969. IET.

65. Jahns, T.M., *Improved reliability in solid-state AC drives by means of multiple independent phase drive units*. IEEE Transactions on Industry Applications, 1980(3): p. 321-331.

66. Zhao, Y. and T.A. Lipo, *Space vector PWM control of dual three-phase induction machine using vector space decomposition.* IEEE Transactions on industry applications, 1995. **31**(5): p. 1100-1109.

67. Zhao, Y., *Vector space decomposition modeling and control of multiphase induction machines*. 1995: University of Wisconsin--Madison.

68. Lyra, R.O. and T.A. Lipo, *Torque density improvement in a six-phase induction motor with third harmonic current injection.* IEEE Transactions on Industry Applications, 2002. **38**(5): p. 1351-1360.

69. Dwari, S., L. Parsa, and T.A. Lipo. *Optimum control of a five-phase integrated modular permanent magnet motor under normal and open-circuit fault conditions*. in *2007 IEEE Power Electronics Specialists Conference*. 2007. IEEE.

70. Xu, H., *Enhanced rotor field oriented control of five-phase induction motor with the combined fundamental and third harmonic currents*. 2001, Texas A & M University.

71. Parsa, L., *Performance improvement of permanent magnet AC motors*. 2005, Texas A&M University.

72. Parsa, L. and H.A. Toliyat, *Sensorless direct torque control of five-phase interior permanent-magnet motor drives.* IEEE Transactions on Industry applications, 2007. **43**(4): p. 952-959.

73. Xu, H., H.A. Toliyat, and L.J. Petersen, *DSP-Based Direct Torque Control (DTC) of Five-Phase Induction Motors.* IEEJ Transactions on Industry Applications, 2001. **121**(12): p. 1256-1262.

74. Levi, E., et al., *Operating principles of a novel multiphase multimotor vector-controlled drive.* IEEE Transactions on Energy Conversion, 2004. **19**(3): p. 508-517.

75. Jones, M., et al., *A six-phase series-connected two-motor drive with decoupled dynamic control.* IEEE Transactions on Industry Applications, 2005. **41**(4): p. 1056-1066.

76. Levi, E., et al., *Steady-state modeling of series-connected five-phase and six-phase two-motor drives.* IEEE Transactions on industry applications, 2008. **44**(5): p. 1559-1568.

77. Levi, E., *Advances in converter control and innovative exploitation of additional degrees of freedom for multiphase machines*. IEEE Transactions on Industrial Electronics, 2015. **63**(1): p. 433-448.

78. Levi, E., et al., *A space-vector modulation scheme for multilevel open-end winding five-phase drives.* IEEE Transactions on Energy Conversion, 2011. **27**(1): p. 1-10.

79. Barrero, F., et al., *A proof of concept study of predictive current control for VSI-driven asymmetrical dual three-phase AC machines*. IEEE Transactions on Industrial Electronics, 2009. **56**(6): p. 1937-1954.

80. Barrero, F., et al., *An enhanced predictive current control method for asymmetrical six-phase motor drives.* IEEE Transactions on Industrial Electronics, 2010. **58**(8): p. 3242-3252.

81. Guzman, H., et al., *Speed control of five-phase induction motors with integrated open-phase fault operation using model-based predictive current control techniques*. IEEE Transactions on Industrial Electronics, 2013. **61**(9): p. 4474-4484.

82. Guzmán, H., M. Duran, and F. Barrero. *A comprehensive fault analysis of a five-phase induction motor drive with an open phase*. in *2012 15th International Power Electronics and Motion Control Conference (EPE/PEMC)*. 2012. IEEE.

83. Martín, C., et al., *Multiphase rotor current observers for current predictive control: A five-phase case study.* Control Engineering Practice, 2016. **49**: p. 101-111.

84. Duran, M.J., et al., *Predictive current control of dual three-phase drives using restrained search techniques.* IEEE Transactions on Industrial Electronics, 2010. **58**(8): p. 3253-3263.

85. Durán, M.J., et al., *Reduction of common-mode voltage in five-phase induction motor drives using predictive control techniques.* IEEE Transactions on Industry Applications, 2012. **48**(6): p. 2059-2067.

86. Guzman, H., F. Barrero, and M.J. Duran, *IGBT-gating failure effect on a fault-tolerant predictive current-controlled five-phase induction motor drive.* IEEE transactions on industrial electronics, 2014. **62**(1): p. 15-20.

87. Munim, W.N.W.A., et al., *A unified analysis of the fault tolerance capability in six-phase induction motor drives.* IEEE Transactions on Power Electronics, 2016. **32**(10): p. 7824-7836.

88. Almarhoon, A.H., Y. Ren, and Z. Zhu. *Sensorless switching-table-based direct torque control for dual three-phase PMSM drives*. in *2014 17th International Conference on Electrical Machines and Systems (ICEMS)*. 2014. IEEE.

89. Liu, J. and Z. Zhu. *Rotor position estimation for dual-three-phase permanent magnet synchronous machine based on third harmonic back-EMF*. in *2015 IEEE Symposium on Sensorless Control for Electrical Drives (SLED)*. 2015. IEEE.

90. Wang, K., Z. Zhu, and G. Ombach, *Torque improvement of five-phase surface-mounted permanent magnet machine using third-order harmonic.* IEEE Transactions on Energy Conversion, 2014. **29**(3): p. 735-747.

91. Ren, Y. and Z.-Q. Zhu, *Reduction of both harmonic current and torque ripple for dual three-phase permanent-magnet synchronous machine using modified switching-table-based direct torque control.* IEEE Transactions on Industrial Electronics, 2015. **62**(11): p. 6671-6683.

92. Almarhoon, A.H., Z. Zhu, and P. Xu, *Improved pulsating signal injection using zero-sequence carrier voltage for sensorless control of dual three-phase PMSM.* IEEE Transactions on Energy Conversion, 2017. **32**(2): p. 436-446.

93. Liu, J. and Z.-Q. Zhu, *Rotor position estimation for single-and dual-three-phase permanent magnet synchronous machines based on third harmonic back-EMF under imbalanced situation.* Chinese Journal of Electrical Engineering, 2017. **3**(1): p. 63-72.

94. Almarhoon, A.H., Z. Zhu, and P. Xu, *Improved rotor position estimation accuracy by rotating carrier signal injection utilizing zero-sequence carrier voltage for dual three-phase PMSM.* IEEE Transactions on Industrial Electronics, 2016. **64**(6): p. 4454-4462.

95. Wu-bin, K., et al., *Comparison of current control strategies based on multiphase motor for electric vehicle.* Electric Machines & Control/Dianji Yu Kongzhi Xuebao, 2019(1).

96. Bingnan, L., *Analysis and identification on the suspension parameters of the multiphase bearingless PM motor with single set of windings*. 2014, zhejiang university.

97. Yumao, B., *Research of direct torque control for nine-phase induction motor*. 2012, zhejiang university.

98. Min, K., *research on multiphase bearingless motors*. 2008, zhejiang university.

99. Jiong, L., *research on stator winding interturn short circuit faults diagnosis of induction motor*. 2007, zhejiang university.

100. Jiaqiang, Y., et al., *Electronic Pole-Changing Speed Adjusting Technology of Multiphase Induction Motors Based on Vector Control* TRANSACTIONS OF CHINA ELECTROTECHNICAL SOCIETY, 2014. **29**(3): p. 96-102.

101. Jilong, L., et al., *Position-Sensorless Control Technology of Permanent-Magnet Synchronous Motor-a Review.* TRANSACTIONS OF CHINA ELECTROTECHNICAL SOCIETY, 2017.

102. Tong, W., *Sensorless Control and Parameter Identification of PM Motors*. 2019, zhejiang.

103. Staines, C.S., C. Caruana, and R. Raute, *A review of saliency-based sensorless control methods for alternating current machines.* IEEJ Journal of Industry Applications, 2014. **3**(2): p. 86-96.

104. Zhang, G., G. Wang, and D. Xu, *Saliency-based position sensorless control methods for PMSM drives-A review.* Chinese Journal of Electrical Engineering, 2017. **3**(2): p. 14-23.

105. Sul, S.-K., Y.-C. Kwon, and Y. Lee, *Sensorless control of IPMSM for last 10 years and next 5 years.* CES Transactions on Electrical Machines and Systems, 2017. **1**(2): p. 91-99.

106. Xu, D., et al., *A review of sensorless control methods for AC motor drives*. CES Transactions on electrical machines and systems, 2018. **2**(1): p. 104-115.

107. Yang, S.-C. and Y.-L. Hsu, *Full speed region sensorless drive of permanent-magnet machine combining saliency-based and back-EMF-based drive.* IEEE Transactions on Industrial Electronics, 2016. **64**(2): p. 1092-1101.

108. Seilmeier, M. and B. Piepenbreier, *Sensorless control of PMSM for the whole speed range using two-degree-of-freedom current control and HF test current injection for low-speed range.* IEEE Transactions on Power Electronics, 2014. **30**(8): p. 4394-4403.

109. Lee, Y., Y.-C. Kwon, and S.-K. Sul. *Comparison of rotor position estimation performance in fundamental-model-based sensorless control of PMSM*. in *2015 IEEE Energy Conversion Congress and Exposition (ECCE)*. 2015. IEEE.

110. Wang, G., M.I. Valla, and J.A. Solsona, *Position Sensorless Permanent Magnet Synchronous Machine Drives—a Review.* IEEE Transactions on Industrial Electronics, 2019.

111. Lee, Y. and S.-K. Sul, *Model-based sensorless control of an IPMSM with enhanced robustness against load disturbances based on position and speed estimator using a speed error.* IEEE Transactions on Industry Applications, 2017. **54**(2): p. 1448-1459.

112. Bolognani, S., et al., *Model sensitivity of fundamental-frequency-based position estimators for sensorless PM and reluctance synchronous motor drives.* IEEE Transactions on Industrial Electronics, 2017. **65**(1): p. 77-85.

113. Zhao, Y., et al., *An extended flux model-based rotor position estimator for sensorless control of salient-pole permanent-magnet synchronous machines.* IEEE Transactions on Power Electronics, 2014. **30**(8): p. 4412-4422.

114. Quang, N.K., N.T. Hieu, and Q. Ha, *FPGA-based sensorless PMSM speed control using reduced-order extended Kalman filters.* IEEE Transactions on Industrial Electronics, 2014. **61**(12): p. 6574-6582.

115. Lee, K.-G., J.-S. Lee, and K.-B. Lee, *Wide-range sensorless control for SPMSM using an improved full-order flux observer.* Journal of Power Electronics, 2015. **15**(3): p. 721-729.

116. Andersson, A. and T. Thiringer, *Motion sensorless ipmsm control using linear moving horizon estimation with luenberger observer state feedback.* IEEE transactions on transportation electrification, 2018. **4**(2): p. 464-473.

117. Bao, D., et al., *Adaptive synchronous-frequency tracking-mode observer for the sensorless control of a surface PMSM.* IEEE Transactions on Industry Applications, 2018. **54**(6): p. 6460-6471.

118. Hofer, M., M. Nikowitz, and M. Schroedl. *Sensorless control of a reluctance synchronous machine in the whole speed range without voltage pulse injections*. in *2017 IEEE 3rd International Future Energy Electronics Conference and ECCE Asia (IFEEC 2017-ECCE Asia)*. 2017. IEEE.

119. Ni, R., et al., *Square-wave voltage injection algorithm for PMSM position sensorless control with high robustness to voltage errors.* IEEE Transactions on Power Electronics, 2016. **32**(7): p. 5425-5437.

120. Wang, G., et al., *Sensorless control scheme of IPMSMs using HF orthogonal square-wave voltage injection into a stationary reference frame.* IEEE Transactions on Power Electronics, 2018. **34**(3): p. 2573-2584.

121. Zhang, X., et al., *Improved initial rotor position estimation for PMSM drives based on HF pulsating voltage signal injection.* IEEE Transactions on Industrial Electronics, 2017. **65**(6): p. 4702-4713.

122. Kim, S.-I., et al., *A new rotor position estimation method of IPMSM using all-pass filter on high-frequency rotating voltage signal injection.* IEEE Transactions on Industrial Electronics, 2016. **63**(10): p. 6499-6509.

123. Hind, D.M., *Current derivative estimation for sensorless motor drives*. 2015, University of Nottingham.

124. Xu, P. and Z. Zhu, *Novel square-wave signal injection method using zero-sequence voltage for sensorless control of PMSM drives.* IEEE Transactions on Industrial Electronics, 2016. **63**(12): p. 7444-7454.

125. Ahmad, M., W. Zhang, and Q. Gao. *Low and zero speed position estimation of dual three-phase PMSMs based on the excitation of PWM waveforms*. in *2017 IEEE 3rd International Future Energy Electronics Conference and ECCE Asia (IFEEC 2017-ECCE Asia)*. 2017. IEEE.

126. Yelu, Z., *Research on sensorless control of dual three phase permanent magnet synchrounous motor*. 2019, zhejiang.

127. Scelba, G., et al. *Compensation of rotor positon estimation errors in sensorless dual-three phase PMSM drives through back-EMF sensing*. in *2017 IEEE International Symposium on Sensorless Control for Electrical Drives (SLED)*. 2017. IEEE.

128. Yanhui, H., et al., *Position sensorless vector control for direct-drive wind power generator.* Electric Machines and Control, 2010(3): p. 7.

129. Ping, Z., et al., *The Control of the Current of Dual Three-phase Permanent Magnet Synchronous Motor for Ship Electric Propulsion System.* Marine Electric & Electronic Engineering, 2014.

130. Zaifa, C., L. Yancheng, and L. Xiangyu, *R esearch on On-Line Parameters Identification Method of Permanent Magnet Synchronous Motor for ship Propulsion.* Electric Machines & Control Application, 2018(10): p. 12.

131. He, Y., et al. *Speed and position sensorless control for dual-three-phase PMSM drives*. in *2009 Twenty-Fourth Annual IEEE Applied Power Electronics Conference and Exposition*. 2009. IEEE.

132. Fan, L., et al. *Sensorless control of dual-three phase PMSM based aircraft electric starter/generator system using model reference adaptive system method*. in *CSAA/IET International Conference on Aircraft Utility Systems (AUS 2018)*. 2018. IET.

133. Dong, W., *Research on double three-phase and sliding mode control of six-phase switched reluctance motor used in electric vehicles* . 2016, Dalian university of technology.

134. Yelu, Z., et al., *Study on Sensorless Control of Dual Three-phase PMSM in Full Speed Range.* MICROMOTORS, 2018. **51**(11): p. 31-39.

135. Fan, L., et al., *Comparative Study of Sensorless Methods Based on Sliding Mode Observer for Dual Three-Phase Permanent Magnet Synchronous Machine.* 2021.

136. Zhang, Y. and G. Junli, *A research on an implementation method of speed sensorless control for dual three-phase permanent magnet synchrounous motor.* Journal of Guangdong University of Technology, 2019. **36**(03): p. 83-90.

137. Fan, L., et al. *Comparative study of back EMF based sensorless control methods for dual three-phase PMSM*. in *2018 IEEE International Conference on Electrical Systems for Aircraft, Railway, Ship Propulsion and Road Vehicles & International Transportation Electrification Conference (ESARS-ITEC)*. 2018. IEEE.

138. Zhang, Y., et al. *A comparative study of Luenberger observer, sliding mode observer and extended Kalman filter for sensorless vector control of induction motor drives*. in *2009 IEEE Energy Conversion Congress and Exposition*. 2009. IEEE.

139. Roetzer, M., et al. *Anisotropy-based position estimation approach for symmetrical dual three-phase permanent magnet synchronous machines*. in *2017 IEEE International Symposium on Sensorless Control for Electrical Drives (SLED)*. 2017. IEEE.

140. Zhongjian, Z. and Z. Chengbao, *Position Sensorless Control of EPS System at Low Speed Based on Dual Three-Phase Permanent Magnet Synchronous Motor.* motor and control application, 2019. **46**(12): p. 99-104.

141. Barcaro, M., et al., *Sensorless rotor position detection capability of a dual three-phase fractional-slot IPM machine.* IEEE Transactions on Industry Applications, 2012. **48**(6): p. 2068-2078.

142. *ACHIEVE*. [cited 2021 May]; Available from: https://www.nottingham.ac.uk/aerospace/projects/cleansky/achieve-project.aspx.

143. *JFE_10JNEX900*. Available from: https://www.jfe-steel.co.jp/en/products/electrical/product/n_core.php.

144. *Samarium Cobalt Magnets*. Available from: http://www.arnoldmagnetics.com/products/recoma-samarium-cobalt-magnets/.

145. Khowja, M.R., et al. *Trade-off Study of a High Power Density Starter-Generator for Turboprop Aircraft System*. in *IECON 2019-45th Annual Conference of the IEEE Industrial Electronics Society*. 2019. IEEE.

146. Demir, Y. and M. Aydin, *A novel dual three-phase permanent magnet synchronous motor with asymmetric stator winding.* IEEE Transactions on Magnetics, 2016. **52**(7): p. 1-5.

147. Kluszczynski, K. and M. Szczygiel. *Study on 3-winding system with angular asymmetry part I-current zero-components and 2-axis transformation*. in *2017 International Symposium on Electrical Machines (SME)*. 2017. IEEE.

148. Kluszczynski, K. and M. Szczygiel. *Study on 3-winding system with angular asymmetry part II-eigenvalues of inductance matrix and transformation αβ0*. in *2017 International Symposium on Electrical Machines (SME)*. 2017. IEEE.

149. Demir, Y. and M. Aydin. *Design, analysis and validation of a dual three-phase 72-slot, 12-pole permanent magnet synchronous motor*. in *2016 XXII International Conference on Electrical Machines (ICEM)*. 2016. IEEE.

150. Xu, P., et al., *Analysis of dual three-phase permanent-magnet synchronous machines with different angle displacements.* IEEE Transactions on Industrial Electronics, 2017. **65**(3): p. 1941-1954.

151. Bianchi, N. and M. Dai Prè, *Use of the star of slots in designing fractional-slot single-layer synchronous motors.* IEE Proceedings-Electric Power Applications, 2006. **153**(3): p. 459-466.

152. Barcaro, M., N. Bianchi, and F. Magnussen, *Faulty operations of a PM fractional-slot machine with a dual three-phase winding.* IEEE Transactions on Industrial Electronics, 2010. **58**(9): p. 3825-3832.

153. Ni, Q., et al., *A new position and speed estimation scheme for position control of PMSM drives using low-resolution position sensors.* IEEE Transactions on Industry Applications, 2019. **55**(4): p. 3747-3758.

154. SIEMENS. *Simcenter MAGNET*. Available from: https://trials.sw.siemens.com/simcenter-magnet/.

155. Chattopadhyay, S., M. Mitra, and S. Sengupta, *Clarke and park transform*, in *Electric Power Quality*. 2011, Springer. p. 89-96.

156. Karttunen, J., et al., *Decoupled vector control scheme for dual three-phase permanent magnet synchronous machines.* IEEE Transactions on Industrial Electronics, 2013. **61**(5): p. 2185-2196.

157. Hu, Y., Z. Zhu, and M. Odavic, *Comparison of two-individual current control and vector space decomposition control for dual three-phase PMSM.* IEEE Transactions on Industry Applications, 2017. **53**(5): p. 4483-4492.

158. Han, X., et al., *Two-segment three-phase PMSM drive with carrier phase-shift PWM for torque ripple and vibration reduction.* IEEE Transactions on Power Electronics, 2018. **34**(1): p. 588-599.

159. Miyama, Y., et al., *Vibration reduction by applying carrier phase-shift PWM on dual three-phase winding permanent magnet synchronous motor.* IEEE Transactions on Industry Applications, 2018. **54**(6): p. 5998-6004.

160. Krause, P.C., et al., *Analysis of electric machinery and drive systems*. Vol. 75. 2013: John Wiley & Sons.

161. Bozhko, S., et al. *Aircraft starter-generator system based on permanent-magnet machine fed by active front-end rectifier*. in *IECON 2014-40th Annual Conference of the IEEE Industrial Electronics Society*. 2014. IEEE.

162. Yeoh, S.S., *Control strategies for the More Electric Aircraft starter-generator electrical power system*. 2016, University of Nottingham.

163. Swierczynski, D. and M.P. Kazmierkowski. *Direct torque control of permanent magnet synchronous motor (PMSM) using space vector modulation (DTC-SVM)-simulation and experimental results*. in *IEEE 2002 28th Annual Conference of the Industrial Electronics Society. IECON 02*. 2002. IEEE.

164. Zordan, M., et al., *Field-weakening in vector controlled and DTC PMSM drives, a comparative analysis*. 2000.

165. Karlis, A., et al., *Comparison of the Field Oriented and Direct Torque Control Methods for Induction Motors used in Electric Vehicles.* Democritus University of Thrace, 2006.

166. Xu, Z. and M.F. Rahman, *An adaptive sliding stator flux observer for a direct-torque-controlled IPM synchronous motor drive.* IEEE Transactions on Industrial Electronics, 2007. **54**(5): p. 2398-2406.

167. Wang, X., N. Liu, and R. Na. *Simulation of PMSM field-oriented control based on SVPWM*. in *2009 IEEE Vehicle Power and Propulsion Conference*. 2009. IEEE.

168. Assis, A. and F. Peixoto, *On the velocity in the Lorentz force law.* The Physics Teacher, 1992. **30**(8): p. 480-483.

169. Yin, M., S. Bozhko, and S.S. Yeoh, *Control design for PMM-based generator fed by active front-end rectifier in more-electric aircraft.* SAE International Journal of Aerospace, 2016. **9**(2016-01-1987): p. 23-29.

170. Yazdani, A. and R. Iravani, *Voltage-sourced converters in power systems*. Vol. 39. 2010: Wiley Online Library.

171. Bojoi, R., et al. *Complete analysis and comparative study of digital modulation techniques for dual three-phase AC motor drives*. in *2002 IEEE 33rd Annual IEEE Power Electronics Specialists Conference. Proceedings (Cat. No. 02CH37289)*. 2002. IEEE.

172. Huang, J., et al. *Extending voltage range and reducing torque ripple of five-phase motor drives with added voltage harmonics*. in *2008 Twenty-Third Annual IEEE Applied Power Electronics Conference and Exposition*. 2008. IEEE.

173. Li, B. and C. Wang. *Comparative analysis on PMSM control system based on SPWM and SVPWM*. in *2016 Chinese Control and Decision Conference (CCDC)*. 2016. IEEE.

174. Zhou, C., et al. *A dual-plane SVPWM strategy for dual three-phase PMSM*. in *2019 22nd International Conference on Electrical Machines and Systems (ICEMS)*. 2019. IEEE.

175. Karttunen, J., et al. *Dual three-phase permanent magnet synchronous machine supplied by two independent voltage source inverters*. in *International symposium on power electronics power electronics, electrical drives, automation and motion*. 2012. IEEE.

176. Plexim. [cited 2021 April]; Available from: http://www.plexim.com.

177. Vaclavek, P., P. Blaha, and I. Herman, *AC drive observability analysis.* IEEE Transactions on Industrial Electronics, 2012. **60**(8): p. 3047-3059.

178. Sul, S.-K. and S. Kim, *Sensorless control of IPMSM: Past, present, and future.* IEEJ Journal of Industry Applications, 2012. **1**(1): p. 15-23.

179. Wu, R. and G.R. Slemon, *A permanent magnet motor drive without a shaft sensor.* IEEE Transactions on Industry Applications, 1991. **27**(5): p. 1005-1011.

180. Ichikawa, S., et al. *Sensorless control of an interior permanent magnet synchronous motor on the rotating coordinate using an extended electromotive*

force. in *IECON'01. 27th Annual Conference of the IEEE Industrial Electronics Society (Cat. No. 37243)*. 2001. IEEE.

181. Chen, Z., et al. *Sensorless control of interior permanent magnet synchronous motor by estimation of an extended electromotive force*. in *Conference Record of the 2000 IEEE Industry Applications Conference. Thirty-Fifth IAS Annual Meeting and World Conference on Industrial Applications of Electrical Energy (Cat. No. 00CH37129)*. 2000. IEEE.

182. Chen, Z., et al., *An extended electromotive force model for sensorless control of interior permanent-magnet synchronous motors.* IEEE transactions on Industrial Electronics, 2003. **50**(2): p. 288-295.

183. Yousefi-Talouki, A., et al., *Combined active flux and high-frequency injection methods for sensorless direct-flux vector control of synchronous reluctance machines.* IEEE Transactions on Power Electronics, 2017. **33**(3): p. 2447-2457.

184. Haines, G. and N. Ertugrul, *Wide speed range sensorless operation of brushless permanent-magnet motor using flux linkage increment.* IEEE Transactions on Industrial Electronics, 2016. **63**(7): p. 4052-4060.

185. Liu, J. and Z. Zhu. *Rotor position error compensation based on third harmonic back-EMF in flux observer sensorless control*. in *2014 International Conference on Electrical Machines (ICEM)*. 2014. IEEE.

186. Wang, Y., Y. Xu, and J. Zou, *Online Multiparameter Identification Method for Sensorless Control of SPMSM.* IEEE Transactions on Power Electronics, 2020. **35**(10): p. 10601-10613.

187. Morimoto, S., et al., *Sensorless control strategy for salient-pole PMSM based on extended EMF in rotating reference frame.* IEEE transactions on industry applications, 2002. **38**(4): p. 1054-1061.

188. Li, Y., et al. *Improved rotor position estimation in extended back-EMF based sensorless PM brushless AC drives with magnetic saliency*. in *2007 IEEE International Electric Machines & Drives Conference*. 2007. IEEE.

189. Chaoui, H., M. Khayamy, and A.A. Aljarboua, *Adaptive interval type-2 fuzzy logic control for PMSM drives with a modified reference frame.* IEEE Transactions on Industrial Electronics, 2017. **64**(5): p. 3786-3797.

190. Masmoudi, M.L., et al., *Amplification of single mechanical fault signatures using full adaptive pmsm observer.* IEEE Transactions on industrial electronics, 2016. **64**(1): p. 615-623.

191. Hasegawa, M. and K. Matsui, *Position sensorless control for interior permanent magnet synchronous motor using adaptive flux observer with inductance identification.* IET electric power applications, 2009. **3**(3): p. 209-217.

192. Hasegawa, M., S. Yoshioka, and K. Matsui, *Position sensorless control of interior permanent magnet synchronous motors using unknown input observer for high-speed drives.* IEEE Transactions on Industry Applications, 2009. **45**(3): p. 938-946.

193. Tuovinen, T., et al., *Comparison of a reduced-order observer and a full-order observer for sensorless synchronous motor drives.* IEEE Transactions on Industry Applications, 2012. **48**(6): p. 1959-1967.

194. Park, E., et al. *Speed-sensorless control for permanent magnet synchronous motor using MRAS method with reduced order observer*. in *2015 18th International Conference on Electrical Machines and Systems (ICEMS)*. 2015. IEEE.

195. Li, S., M. Zhou, and X. Yu, *Design and implementation of terminal sliding mode control method for PMSM speed regulation system.* IEEE Transactions on Industrial Informatics, 2012. **9**(4): p. 1879-1891.

196. Zhang, X., et al., *Nonlinear speed control for PMSM system using sliding-mode control and disturbance compensation techniques.* IEEE Transactions on Power Electronics, 2012. **28**(3): p. 1358-1365.

197. Kim, H., J. Son, and J. Lee, *A high-speed sliding-mode observer for the sensorless speed control of a PMSM.* IEEE Transactions on Industrial Electronics, 2011. **58**(9): p. 4069-4077.

198. Furuhashi, T., S. Sangwongwanich, and S. Okuma, *A position-and-velocity sensorless control for brushless DC motors using an adaptive sliding mode observer.* IEEE Transactions on Industrial electronics, 1992. **39**(2): p. 89-95.

199. Liang, D., J. Li, and R. Qu, *Sensorless control of permanent magnet synchronous machine based on second-order sliding-mode observer with online resistance estimation.* IEEE Transactions on Industry Applications, 2017. **53**(4): p. 3672-3682.

200. Chen, Z., et al., *New adaptive sliding observers for position-and velocity-sensorless controls of brushless DC motors.* IEEE Transactions on Industrial Electronics, 2000. **47**(3): p. 582-591.

201. Tarchala, G. *Influence of the sign function approximation form on performance of the sliding-mode speed observer for induction motor drive*. in *2011 IEEE International Symposium on Industrial Electronics*. 2011. IEEE.

202. Feng, Y., et al., *Hybrid terminal sliding-mode observer design method for a permanent-magnet synchronous motor control system.* IEEE Transactions on Industrial Electronics, 2009. **56**(9): p. 3424-3431.

203. Ezzat, M., et al. *Observer-controller scheme using high order sliding mode techniques for sensorless speed control of permanent magnet synchronous motor*. in *49th IEEE conference on decision and control (CDC)*. 2010. IEEE.

204. Wang, Y., et al., *Position-sensorless hybrid sliding-mode control of electric vehicles with brushless DC motor.* IEEE Transactions on Vehicular Technology, 2010. **60**(2): p. 421-432.

205. Kalman, R.E., *A new approach to linear filtering and prediction problems*. 1960.

206. Holtz, J. *Developments in sensorless AC drive technology*. in *2005 International Conference on Power Electronics and Drives Systems*. 2005. IEEE.

207. Welch, G. and G. Bishop, *An introduction to the kalman filter. Department of Computer Science, University of North Carolina*. 2006, Chapel Hill, NC, unpublished manuscript.

208. Wang, Z., et al., *Position sensorless control of interleaved CSI fed PMSM drive with extended Kalman filter.* IEEE Transactions on Magnetics, 2012. **48**(11): p. 3688-3691.

209. Smidl, V. and Z. Peroutka, *Advantages of square-root extended Kalman filter for sensorless control of AC drives*. IEEE Transactions on Industrial Electronics, 2011. **59**(11): p. 4189-4196.

210. Kim, Y.-R., S.-K. Sul, and M.-H. Park. *Speed sensorless vector control of an induction motor using an extended Kalman filter*. in *Conference Record of the 1992 IEEE Industry Applications Society Annual Meeting*. 1992. IEEE.

211. Bhangu, B. and C. Bingham, *Nonlinear state-observer techniques for sensorless control of automotive PMSM's, including load-torque estimation and saliency.* 2003.

212. Harnefors, L., *A comparison between directly parametrised observers and extended Kalman filters for sensorless induction motor drives*. A '= A, 1998. **11**: p. 5.

213. Foo, G. and M. Rahman. *Evaluation of velocity servo performance of IMPSM drive under high-performance sensorless operation*. in *8th International Conference on Power Electronics-ECCE Asia*. 2011. IEEE.

214. Chen, G., *Research on PMSM sensorless control system based on adaptive luenberger observer*. 2019, zhejiang university.

215. Luo, X., et al., *PMSM sensorless control by injecting HF pulsating carrier signal into estimated fixed-frequency rotating reference frame.* IEEE Transactions on Industrial Electronics, 2015. **63**(4): p. 2294-2303.

216. Qian, W., et al., *Using high-control-bandwidth fpga and sic inverters to enhance high-frequency injection sensorless control in interior permanent magnet synchronous machine.* IEEE Access, 2018. **6**: p. 42454-42466.

217. Tang, Q., et al., *IPMSMs Sensorless MTPA Control Based on Virtual q-Axis Inductance by Using Virtual High-Frequency Signal Injection.* IEEE Transactions on Industrial Electronics, 2019. **67**(1): p. 136-146.

218. Han, B., et al., *Initial Rotor Position Detection Method of SPMSM Based on New High Frequency Voltage Injection Method.* IEEE Transactions on Power Electronics, 2018. **34**(4): p. 3553-3562.

219. Wang, S., K. Yang, and K. Chen, *An improved position-sensorless control method at low speed for PMSM based on high-frequency signal injection into a rotating reference frame.* IEEE Access, 2019. **7**: p. 86510-86521.

220. Lin, T.-C. and Z.-Q. Zhu, *Sensorless operation capability of surface-mounted permanent-magnet machine based on high-frequency signal injection methods.* IEEE Transactions on Industry Applications, 2014. **51**(3): p. 2161-2171.

221. Scaglione, O., M. Markovic, and Y. Perriard. *Exploitation of iron BH local hysteresis for the rotor position detection of a PM motor*. in *2009 IEEE International Electric Machines and Drives Conference*. 2009. IEEE.

222. Scaglione, O., M. Markovic, and Y. Perriard, *First-pulse technique for brushless DC motor standstill position detection based on iron BH hysteresis.* IEEE Transactions on Industrial Electronics, 2011. **59**(5): p. 2319-2328.

223. Iwaji, Y., et al., *Position sensorless control method at zero-speed region for permanent magnet synchronous motors using the neutral point voltage of stator windings.* IEEE Transactions on Industry Applications, 2016. **52**(5): p. 4020-4028.

224. Duan, Y., *A comparison of saliency based sensorless control techniques for a PM machine*. 2012, University of Nottingham.

225. Sun, W., *study of pmsm position sensorless control and high-performance operation strategy*. 2017, zhejiang university.

226. Chen, J., et al., *Initial rotor position detection method of SPMSM based on high frequency current injection method.* Journal of Electrical Engineering, 2019. **12**(4): p. 45-50.

227. Zhou, C., *Reserch on sensorless control technology of permanent magnet synchrounous motor*. 2019, zhejiang university.

228. Jansen, P.L. and R.D. Lorenz, *Transducerless position and velocity estimation in induction and salient AC machines.* IEEE Transactions on Industry Applications, 1995. **31**(2): p. 240-247.

229. Corley, M.J. and R.D. Lorenz, *Rotor position and velocity estimation for a salient-pole permanent magnet synchronous machine at standstill and high speeds.* IEEE Transactions on Industry Applications, 1998. **34**(4): p. 784-789.

230. Sul, S.-k. and J.-i. Ha, *Sensorless field orientation control method of an induction machine by high frequency signal injection*. 1999, Google Patents.

231. Linke, M., R. Kennel, and J. Holtz. *Sensorless position control of permanent magnet synchronous machines without limitation at zero speed*. in *IECON 02 [Industrial Electronics Society, IEEE 2002 28th Annual Conference of the]*. 2002. IEEE.

232. Jang, J.-H., et al., *Sensorless drive of surface-mounted permanent-magnet motor by high-frequency signal injection based on magnetic saliency.* IEEE Transactions on Industry Applications, 2003. **39**(4): p. 1031-1039.

233. Yoon, Y.-D., et al., *High-bandwidth sensorless algorithm for AC machines based on square-wave-type voltage injection.* IEEE Transactions on Industry Applications, 2011. **47**(3): p. 1361-1370.

234. Ha, J.-I. and S.-K. Sul. *Sensorless field orientation control of an induction machine by high frequency signal injection*. in *IAS'97. Conference Record of the 1997 IEEE Industry Applications Conference Thirty-Second IAS Annual Meeting*. 1997. IEEE.

235. Gao, Q., *Sensorless control of induction machines at zero and low frequency using zero sequence currents*. The university of nottingham.

236. Liu, B., *Sensorless control of permanent magnet synchrounous motors based on high frequency pulsating signal injection*. 2018, Nanjing University of Aeronautics and Astronautics.

237. Wang, G., et al., *Hybrid Sensorless Control Strategy for Permanent Magnet Synchronous Motors* Proceedings of the CSEE, 2012. **32**(24): p. 103-109.

238. Wang, G., et al., *Proceedings of the CSEE.* Proceedings of the CSEE, 2010(30): p. 93-98.

239. Wallmark, O. and L. Harnefors, *Sensorless control of salient PMSM drives in the transition region.* IEEE transactions on industrial electronics, 2006. **53**(4): p. 1179-1187.

240. Andreescu, G.-D., et al., *Combined flux observer with signal injection enhancement for wide speed range sensorless direct torque control of IPMSM drives.* IEEE Transactions on energy conversion, 2008. **23**(2): p. 393-402.

241. Qin, F., Y. He, and H. Jia, *Investigation of the Sensorless Control for PMSM Based on a Hybrid Rotor Position Self-sensing Approach.* Proceedings of the CSEE, 2007. **27**(3): p. 12-17.

242. Silva, C., G.M. Asher, and M. Sumner, *Hybrid rotor position observer for wide speed-range sensorless PM motor drives including zero speed.* IEEE Transactions on Industrial Electronics, 2006. **53**(2): p. 373-378.

243. Piippo, A., M. Hinkkanen, and J. Luomi, *Adaptation of motor parameters in sensorless PMSM drives.* IEEE Transactions on Industry Applications, 2009. **45**(1): p. 203-212.

244. Bisheimer, G., et al., *Full speed range permanent magnet synchronous motor control without mechanical sensors.* IET electric power applications, 2010. **4**(1): p. 35-44.

245. Lin, Y., *Research on Sensorless Vector Control of PMSM*. 2016, ZheJiang University.

246. Li, R., *Research on the sensorless control technique of permanent magent synchronous motor*. 2012, zhejiang university.

247. Yu, S., *Research on the Position Sensorless Hybrid Control Strategy for PMSM*. 2017, Zhejiang University.

248. Foo, G. and M. Rahman, *Sensorless sliding-mode MTPA control of an IPM synchronous motor drive using a sliding-mode observer and HF signal injection.* IEEE Transactions on Industrial Electronics, 2009. **57**(4): p. 1270-1278.

249. Lara, J., A. Chandra, and J. Xu. *Integration of HFSI and extended-EMF based techniques for PMSM sensorless control in HEV/EV applications*. in *IECON 2012-38th Annual Conference on IEEE Industrial Electronics Society*. 2012. IEEE.

250. Rieder, U.-H., M. Schrödl, and A. Ebner. *Sensorless control of an external rotor PMSM in the whole speed range including standstill using DC-link measurements only*. in *2004 IEEE 35th Annual Power Electronics Specialists Conference (IEEE Cat. No. 04CH37551)*. 2004. IEEE.

251. Perera, P.C., et al., *A sensorless, stable V/f control method for permanent-magnet synchronous motor drives.* IEEE Transactions on Industry Applications, 2003. **39**(3): p. 783-791.

252. Huang, S., et al. *The vector control based on MRAS speed sensorless induction motor drive*. in *Fifth world congress on intelligent control and automation (IEEE Cat. No. 04EX788)*. 2004. IEEE.

253. Jerome, J., K.E. Vinodh, and S. Ayyappan, *Comparison of four state observer design algorithms for MIMO system.* Archives of Control Sciences, 2013.

254. Landau, Y.D., *Adaptive control: The model reference approach.* IEEE Transactions on Systems, Man, and Cybernetics, 1984(1): p. 169-170.

255. Zhang, W., et al., *Speed Sensorless Control of Hybrid Excitation Axial Field Flux-Switching Permanent-Magnet Machine Based on Model Reference Adaptive System.* IEEE Access, 2020.

256. Schauder, C., *Adaptive speed identification for vector control of induction motors without rotational transducers*. IEEE Transactions on Industry Applications, 1992. **28**(5): p. 1054-1061.

257. Vas, P., *Sensorless vector and direct torque control*. 1998: Oxford Univ. Press.

258. Prabhakaran, K. and A. Karthikeyan, *Electromagnetic torque based MRAS speed estimator for sensorless SMPMSM drive.* IEEE Transactions on Industrial Electronics, 2020.

259. Kojabadi, H.M., *Active power and MRAS based rotor resistance identification of an IM drive.* Simulation Modelling Practice and Theory, 2009. **17**(2): p. 376-389.

260. S.Wu, Z., *Principle and application of adaptive control.* . 2005: Harbin Institute of Technology press.

261. Tan, Z., Y. Li, and Z. Ji. *Speed sensorless DTC and parameter estimation of induction motor based on a full-order MRAS method*. in *Proceedings IPEMC 2000. Third International Power Electronics and Motion Control Conference (IEEE Cat. No. 00EX435)*. 2000. IEEE.

262. Beguenane, R., M.A. Ouhrouche, and A.M. Trzynadlowski. *Stator resistance tuning in an adaptive direct field-orientation induction motor drive at low speeds*. in *30th Annual Conference of IEEE Industrial Electronics Society, 2004. IECON 2004*. 2004. IEEE.

263. Wai, R.-J. and K.-M. Lin, *Robust decoupled control of direct field-oriented induction motor drive.* IEEE Transactions on Industrial Electronics, 2005. **52**(3): p. 837-854.

264. Yang, Q., et al. *An embedded structure of model reference adaptive system*. in *2008 10th International Conference on Control, Automation, Robotics and Vision*. 2008. IEEE.

265. Han, B., et al., *Discrete model reference adaptive control for gimbal servosystem of control moment gyro with harmonic drive.* Mathematical Problems in Engineering, 2013. **2013**.

266. Popov, V.M. and R. Georgescu, *Hyperstability of control systems*. 1973: Springer-Verlag.

267. Kumar, R., et al., *Review on model reference adaptive system for sensorless vector control of induction motor drives.* IET Electric Power Applications, 2015. **9**(7): p. 496-511.

268. Landau, Y.D., *Adaptive control-The model reference approach*. 1979: New York: Marcel Dekker, Inc, . 169-170.

269. Kivanc, O.C. and S.B. Ozturk, *Sensorless PMSM drive based on stator feedforward voltage estimation improved with MRAS multiparameter estimation.* IEEE/ASME Transactions on Mechatronics, 2018. **23**(3): p. 1326-1337.

270. Holtz, J., *Sensorless control of induction machines—With or without signal injection?* IEEE Transactions on Industrial Electronics, 2006. **53**(1): p. 7-30.

271. Yang, T., *PM Synchronous Motors Sensorless Vector Control System Based on MRAS With Parameter Identification* . 2017, HuNan University.

272. Bobek, V. *PMSM Electrical Parameters Measurement*. [cited 2020 15th June]; Available from: https://www.nxp.com/docs/en/application-note/AN4680.pdf.

273. Wang, Z., K. Lu, and F. Blaabjerg, *A simple startup strategy based on current regulation for back-EMF-based sensorless control of PMSM.* IEEE Transactions on Power Electronics, 2012. **27**(8): p. 3817-3825.

274. Wang, Z., *Reserch on the position-sensorless control strategy of PMSM at full speed range*. 2012, zhejiang university.

275. Wang, M., et al., *An I/f Control Method With Closed-loop Regulation of Current Vector for Surface Permanent Magnet Synchronous Motor Drives* Proceedings of the CSEE, 2015. **35**(10): p. 2513-2521.

276. Zhu, W., et al., *Single current loop starting and closed loop transition of sensorless PMSM control.* Journal of Mechanical & Electrical Engineering, 2015. **32**(1): p. 74-77.

277. company, N.; Available from: https://www.nema.ltd.uk/.

278. INSTRUMENTS, T. [cited 2020 25May]; Available from: https://www.ti.com/product/TMS320F28379S.

279. HEIDENHAIN. *Modular Angle Encoders With Magnetic Scanning*. 09/2018; Available from: https://www.heidenhain.com/fileadmin/pdb/media/img/745168-24_Modular_Angle_Encoders_Magnetic_en_01.pdf.

280. Nasir, U., et al. *A SiC based 2-level power converter for shape-and-space-restricted aerospace applications*. in *2019 IEEE 13th International Conference on Power Electronics and Drive Systems (PEDS)*. 2019. IEEE.

281. SEMIKRON. *SKiiP 26ACM12V17*. [cited 2020 31 May]; Available from: https://www.semikron.com/zh/service-support/downloads/detail/semikron-datasheet-skiip-26acm12v17-25230470.html.

282. Liu, R., et al., *230 VAC/28 VDC high-power density power supply for more electric aircraft applications.* The Journal of Engineering, 2018. **2018**(13): p. 499-505.

283. *SM500-CP-90 Datasheet*. [cited 2020 15th June]; Available from: https://telonic.co.uk/v/pdf/delta-elektronika/Delta-Elektronika-SM15K-DC-Power-Supplies-Datasheet.pdf.